MASTERS THESIS

Multi-dimensional simulations of bow shocks of massive, high-velocity runaway stars

by

Katlego Jafta Ramalatswa

Minor Dissertation presented in partial fulfilment of the requirements for the degree of Master of Science

in the

Department of Astronomy
University of Cape Town

11 July, 2022

Supervisor: A/Prof. Shazrene S. Mohamed

Declaration of Authorship

I, Katlego Jafta Ramalatswa, know the meaning of plagiarism and declare that all of the work in the thesis, save for that which is properly acknowledged, is my own.

Abstract

Stellar bow shocks result from the supersonic collision of stellar winds ejected by runaway stars and the interstellar medium (ISM). Studying their properties provides constraints on mass-loss rates, stellar wind velocities and the properties of the ISM. In this work, we study the formation of bow shocks from stars at the tail end of the runaway velocity distribution which we refer to as high-velocity runaway (HVR) stars. We use PLUTO, a magneto-hydrodynamics grid code, to simulate these bow shocks, performing hydrodynamic simulations in 2- and 3-dimensions, while including thermal conduction and detailed radiative cooling/heating.

Extensive 3D freely expanding stellar wind models testing the numerics in PLUTO, e.g., grid geometries, solvers, limiters and convergence with resolution are presented. Further 2D adiabatic, thermal conduction and radiative cooling models for runaways moving at $v_* \sim 40$ km/s were conducted, and verified through comparison with analytic models and the literature. We then present the main focus of this work, our results for HVRs with space velocities of 200 km/s and 400 km/s, for stars in both main-sequence (MS) and red-supergiant (RSG) phases, and moving through different ISM phases: the hot ionized medium (HIM), H II regions (HII), warm neutral medium (WNM) and cold neutral medium (CNM). We demonstrate that the star's evolutionary phase; ISM phase; relative space velocity; thermal conduction and radiative cooling/heating, all have significant impact on the morphology and evolution of the bow shocks.

We studied all the HVR bow shock models focusing primarily on the properties of the reverse shock and the contact discontinuity. We also studied the development of instabilities and numerical artifacts. The latter we suggest is mainly due to the carbuncle phenomenon, while the former are due to the non-linear thin-shell, Kelvin-Helmholtz and Rayleigh–Taylor instabilities. Furthermore, we discuss results from comparing 2D and 3D models to determine the effect of dimensionality on the growth of these instabilities and the carbuncle phenomenon.

This study serves as the foundation of future work in which we will i) investigate the potential of observing these HVR bow shocks by making multi-wavelength estimates using established radiative transfer codes (e.g., TORUS) and producing synthetic images at different wavelengths (e.g., ultraviolet, Hα, infrared and radio), ii) couple these hydrodynamic models to established stellar evolutionary codes (e.g., MESA), and iii) include the effect of magnetic field and stellar rotation.

Acknowledgements

I deeply thank and appreciation my supervisor Assoc. Prof. Shazrene S. Mohamed of the University of Cape Town (UCT) and the South African Astronomical Observatory (SAAO) for her advice and assistance from the start to the end of this Thesis. I also thank the Council for Scientific and Industrial Research (CSIR) for funding my MSc studies. I also thank the Centre for high performance computing (CHPC) for giving us access to their supercomputer (the "Lengau Cluster") for computing all the numerical models presented in this Thesis. I would also like to thank the SAAO staff for all of their support in the interest of the students, such as the writing circles, IT support and the mentorship programs.

Contents

List of Figures

List of Tables

List of Abbreviations

HVR	high-velocity runaway
SES	supernova ejection scenario
DES	dynamical ejection scenario
MS	main-sequence
RSG	red supergiant
ISM	interstellar medium
SOD	stand-off distance
CIE	collisional ionization equilibrium
PI	photoionization
2D	two-dimensions
3D	three-dimensions
HIM	hot ionized medium
HII	H II region
WNM	warm neutral medium
CNM	cold neutral medium
BH	black hole
VMS	very massive star

List of Symbols

$T_{\rm w}$	stellar wind temperature	
$v_{\rm w}$	stellar wind velocity	
$\dot{M}_{\rm w}$	stellar wind mass-loss rate	
$\rho_{\rm w}$	stellar wind density	
$\rho_{\rm ISM}$	ISM density	
$T_{\rm ISM}$	ISM temperature	
v_*	space velocity of the star	
$R_{\rm SOD}$	stand-off distance	
$T_{\rm eff}$	effective temperature	
$\odot$	solar unit	
$M_\odot$	solar mass	1.998×10^{33} g
$R_\odot$	solar radius	6.955×10^{10} cm
$L_\odot$	solar luminosity	3.828×10^{33} erg/s
$k_{\rm B}$	Boltzmann constant	1.381×10^{-16} erg/K
AU	astronomical unit	1.491×10^{13} cm
pc	parsec	3.086×10^{18} cm
$m_{\rm p}$	proton mass	1.673×10^{-24} g
$m_{\rm H}$	hydrogen atom mass	1.673×10^{-24} g

Chapter 1

Introduction

Stars are arguably the most important objects in the Universe; they are the primary sites for nucleosynthesis of elements essential for life (e.g., carbon) and their explosive events such as supernovae also produce many heavy elements (e.g., gold), that are important for the chemical evolution of galaxies (Kippenhahn, Weigert, and Weiss 2012).

1.1 Stellar evolution of massive stars

Stars form in groups or clusters when cold clouds which are part of the interstellar medium collapse under their own weight due to self-gravity (Kippenhahn and Weigert 1990; McKee and Ostriker 2007). During the collapse, the cold fragments and proto-stars are formed at the central regions of these fragments. The centers of the proto-stars heat-up as they accrete material from their surroundings, and when the centre is hot enough, hydrogen fusion starts and a star is born (McKee and Ostriker 2007; Kippenhahn, Weigert, and Weiss 2012). At this stage, a star is regarded as being on the zero age main-sequence (ZAMS), which marks the start of its evolution (McKee and Ostriker 2007; Kippenhahn, Weigert, and Weiss 2012). The mechanism of star formation is still poorly understood, even more so the formation of multiple star systems (e.g., binaries) (Zinnecker and Yorke 2007). However, with ever more advanced observational facilities (e.g., *James Webb Space Telescope (JWST)*) and computational facilities and techniques, star formation has become one of the most popular research areas in stellar astrophysics.

Stars are commonly categorised based on their masses. The Sun is an example of a low-mass star (masses $\lesssim$ 8 $M_\odot$) and they have weak stellar winds (Lamers and Cassinelli 1999; Kippenhahn, Weigert, and Weiss 2012). Low-mass stars typically end their lives expelling their outer envelope via these winds, and forming glowing planetary nebulae with their cores becoming a white dwarf (Lamers and Cassinelli 1999; Kippenhahn, Weigert, and Weiss 2012). High-mass stars, most commonly called massive stars, have masses $\gtrsim$ 8 $M_\odot$; they have a significant impact on their surroundings due to their strong stellar winds with high mass-loss rates (e.g., stellar wind bow shocks and spherical wind bubbles), and they typically end their lives via violent events (e.g., core-collapse supernovae) (Kippenhahn and Weigert 1990; Maeder 2009). Amongst massive stars, those with masses $\gtrsim$ 60 $M_\odot$ are rare and are referred to as very massive stars (VMSs) (Vink 2008a; Vink 2011; Vink et al. 2015; Köhler et al. 2015, and references therein), and at solar metallicity are thought to typically evolve to form Wolf-Rayet (WR) stars (Maeder and Meynet 1987; Lamers and Cassinelli 1999; Meynet and Maeder 2017), for example see Figure 1.1.

Stellar evolution describes the changes a star undergoes during its lifetime. During the evolution, its position shifts on the Hertzsprung-Russell (HR) diagram which tracks the stellar luminosity and temperature. On the main-sequence (MS) is where they spend most of their lifetime (Kippenhahn and Weigert 1990) with different nuclear burning stages as the main indicator of different evolutionary phases (Kippenhahn and Weigert 1990; Kippenhahn, Weigert, and Weiss 2012). The precise evolutionary path of a star, depends on its initial physical properties while on the ZAMS, such as the initial mass, rotation, metallicity and the presence of companions (de Mink et al. 2013; Chieffi and Limongi 2013, and references therein). For instance, stars with initial masses of 8 $M_\odot \lesssim M \lesssim$ 25 $M_\odot$ as shown in Figure 1.1 will evolve to form red supergiant stars (RSG) in their final phase (Davies and Beasor 2018). In this Thesis we focus on single stars with masses in this range at solar metallicity, but neglect the added complexities due to rotation (for example see Brott et al. (2011) and Meynet and Maeder (2017)). The stars we consider will end their lives via core-collapse supernovae, leaving behind a compact object (either a neutron star (NS) or a black hole (BH) for most massive systems) (Kippenhahn, Weigert, and Weiss 2012).

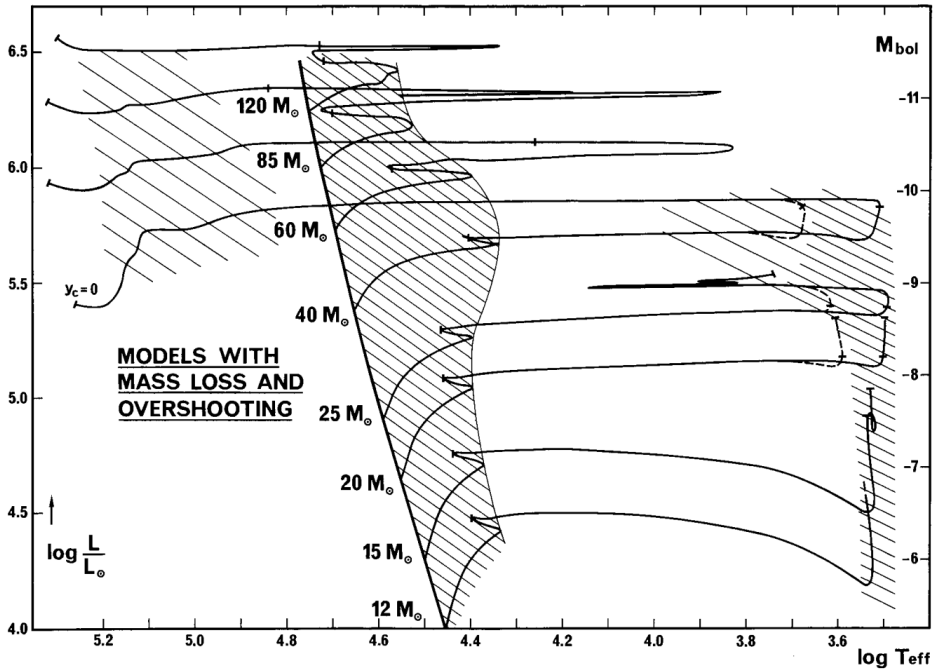

FIGURE 1.1: HR diagram showing evolutionary tracks of massive stars, while taking into account mass loss and moderate convective overshooting (a mechanism which transports material from unstable to stable region in the interior of a star through penetration). The shaded areas indicate where the stars spend most of their lives, which is about 90% on the MS. [Credit: Maeder and Meynet (1987)].

1.2 Stellar winds on the evolution of massive stars

The evolution of all stars is significantly affected by the mass loss, but the effect is particularly important in massive stars as their luminosities are nearer to the Eddington limit (de Jager, Nieuwenhuijzen, and van der Hucht 1988; Vink and de Koter 2002; van Loon 2006; Vink 2006; Vink 2008a; Vink 2008b). Furthermore, the mass-loss rate changes as the star evolves, for example, for a star with initial mass of 10 $M_\odot$, it can increase from $10^{-9.5}$ $M_\odot yr^{-1}$ on the MS to $10^{-6.2}$ $M_\odot yr^{-1}$ in the RSG phase (Brott et al. 2011). Such high mass-loss rates can result in the loss of about 50% or more of the stellar mass (Kippenhahn, Weigert, and Weiss 2012). According to Meynet et al. (1994), a change in mass-loss rate by a factor of 2 can have significant effect on the evolution of a massive star.

Even though stellar winds have been studied for decades, theoretical models and actual values derived from observations are still very uncertain (de Jager, Nieuwenhuijzen, and van der Hucht 1988; van Loon et al. 1999; Mauron and Josselin 2011; Kippenhahn, Weigert, and Weiss 2012; Vink 2008b). Empirical formulae have been developed to describe mass loss using stellar parameters for specific evolutionary phases (de Jager, Nieuwenhuijzen, and van der Hucht 1988; van Loon et al. 2005; Kippenhahn, Weigert, and Weiss 2012), for example Reimers (1975) developed a mass-loss rate formula for red giants which was further modified to rely more on stellar parameters of cool stars by Schroder and Cuntz (2005), which is given as (Kippenhahn, Weigert, and Weiss 2012; Lamers et al. 2000)

$$\dot{M} = -8 \times 10^{-14} \frac{LR}{M} \frac{M_\odot}{L_\odot R_\odot} \left(\frac{T_{\text{eff}}}{4000\,\text{K}}\right)^{3.5} \left(1 + \frac{g}{4300\,g_\odot}\right) [M_\odot yr^{-1}], \tag{1.1}$$

where $\dot{M}$ is the mass-loss rate of the star, which can be obtained from the star's mass M, luminosity L, radius R, effective temperature T_{eff} and surface gravity g. For OB type stars, the formula for estimating their mass-loss rate was derived by Lamers (1981), Vink, de Koter, and Lamers (1999), Lamers et al. (2000), Vink, de Koter, and Lamers (2000a), and Vink, de Koter, and Lamers (2001) and it is given as (Kippenhahn, Weigert, and Weiss 2012)

$$\dot{M} = -1.48 \times 10^{-5} \left(\frac{L}{1000\,L_\odot}\right)^{1.42} \left(\frac{R}{30\,R_\odot}\right)^{0.61} \left(\frac{30\,M_\odot}{M}\right)^{0.99} [M_\odot yr^{-1}]. \tag{1.2}$$

1.2.1 Stellar winds from hot stars

Massive OB-type MS stars with masses $\sim 8 - 25$ $M_\odot$ are an example of luminous hot stars that will evolve into RSGs as mentioned in Section 1.1 (Kippenhahn and Weigert 1990; Lamers and Cassinelli 1999; Vink, de Koter, and Lamers 1999; Vink, de Koter, and Lamers 2000b; Vink and de Koter 2002; Kippenhahn, Weigert, and Weiss 2012). These OB stars have mass-loss rates of $\sim 10^{-9} - 10^{-7}$ $M_\odot yr^{-1}$ and wind velocities of $\sim 1000 - 3000$ km/s which is about three times the value of the escape velocity (v_{esc}), $v_\infty \approx 3v_{\text{esc}}$ (Howarth and Prinja 1989; Kippenhahn and Weigert 1990; Lamers and Leitherer 1993; Puls et al. 1996; Lamers and Cassinelli 1999; Vink, de Koter, and Lamers 1999; Kippenhahn, Weigert, and Weiss 2012; Vink and Gräfener 2012). The driving mechanism of these winds is radiation pressure on lines, which efficiently transfers momentum to the wind materials by photons (Kippenhahn and Weigert 1990; Vink, de Koter, and Lamers 1999; Vink, de Koter, and

Lamers 2001; Vink and Gräfener 2012). Even though radiation driven wind theory is well-developed, there is still some uncertainty in the prediction of mass-loss properties, e.g., due to the inhomogeneities in the winds (Kippenhahn and Weigert 1990; Lamers and Cassinelli 1999; Vink, de Koter, and Lamers 1999; Vink, de Koter, and Lamers 2001).

1.2.2 Stellar winds from cool stars

RSG stars are an example of cool luminous stars which are evolved massive stars with initial MS masses $\sim 8 - 25$ $M_\odot$, and it is the evolutionary phase where stars with ZAMS masses in this range spend most of their post-MS life (Kippenhahn and Weigert 1990; van Loon et al. 2005; Bennett 2010). From observations, it is estimated that RSGs have high mass-loss rates of $\sim 10^{-9} - 10^{-5}$ $M_\odot yr^{-1}$ and slow wind velocities of $\sim 10 - 50$ km/s (de Jager, Nieuwenhuijzen, and van der Hucht 1988; van Loon et al. 1999; Lamers and Cassinelli 1999; van Loon et al. 2005; van Loon 2006; Bennett 2010). It is still not known what mechanisms drives mass loss in RSGs, but decades of research have proposed that radiation pressure on dust particles (Sedlmayr and Dominik 1995; Lamers and Cassinelli 1999; van Loon et al. 1999; van Loon et al. 2005; Bennett 2010; Kippenhahn, Weigert, and Weiss 2012) and also Alfvén Waves (Bennett 2010) are the most likely the driving mechanisms.

1.3 Interstellar Medium

The ISM is the material in galaxies found between stars which is composed of gas, dust, electromagnetic radiation and cosmic rays (Osterbrock 1989; Draine 2011; Klessen and Glover 2016). For example, Figure 1.2 shows the distribution of the ISM in our Galaxy and in the constellation Sagittarius. While stars are the dominating sources of energy in galaxies, the ISM is the material responsible or needed for the formation of stars; this makes the ISM a very important component of galaxies (Draine 2011; Klessen and Glover 2016).

The ISM has different phases, which account for most of its volume and mass in the Milky Way, especially the Galactic disk (McKee and Ostriker 1977; Draine 2011; Klessen and Glover 2016). The first multi-phase structure model of the ISM was proposed by Field, Goldsmith, and Habing (1969), which focused on a two-phase medium consisting of the cold neutral medium (CNM) and warm neutral medium (WNM). The studies by McKee and Ostriker (1977) extended these two-phase models by proposing a hot ISM in an ionized state called the hot ionized medium (HIM). Observations by Hoyle and Ellis (1963) verified the existence of another ionized ISM phase called the warm ionized medium (WIM), the latter is not part of H II regions (Draine 2011; Klessen and Glover 2016). Molecular gas (H_2) is another phase first discovered through observations by Carruthers (1970), it is the coolest and the densest of the ISM phases. The ISM phases, from the hottest to the coolest, have properties as follows:

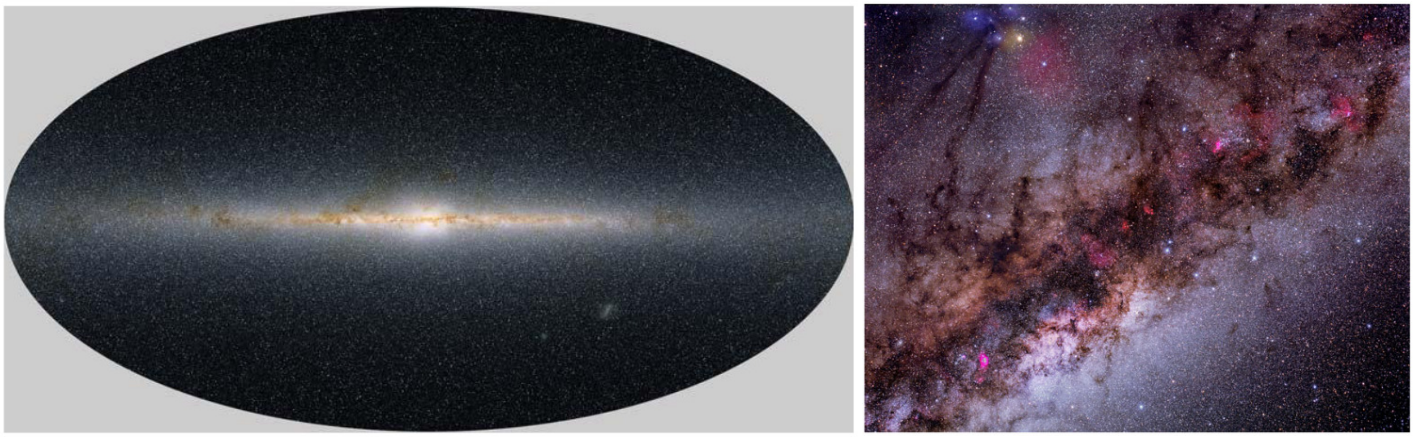

FIGURE 1.2: [Left] All-sky image of stars and the interstellar medium in the Milky Way detected by the 2MASS survey. [Credit: 2MASS/J. Carpenter, T.H. Jarrett, and R. Hurt]. [Right] Dark clouds and stars in Sagittarius. [Credit: John P. Gleason, Celestial Images]

(i) The HIM, also called the coronal gas because it has temperatures comparable to the Sun's corona, is heated to temperatures $T \gtrsim 10^{5.5}$ K by shock waves e.g., supernova explosion blastwaves (McKee and Ostriker 1977; Spitzer 1990; Draine 2011; Klessen and Glover 2016). This medium has low densities of about $\sim 10^{-2.5}$ cm^{-3} and it is observed via ultraviolet, X-ray and radio synchrotron emission (McKee and Ostriker 1977; Draine 2011). In addition, it accounts for about 50% of the volume of the galactic disk in a spiral galaxy (Draine 2011).

(ii) The H II region is photoionized gas which is found around or near newly formed O-type stars (Draine 2011). The latter emit the ultraviolet radiation that is responsible for the photoionization (Draine 2011). The H II gas has number density in the range $\sim 0.3 - 10^4$ cm^{-3} and temperature of about $\sim 10^4$ K, and it is observed via optical line emission (Osterbrock 1989; Draine 2011). The WIM is similar to the H II region, but it refers to the lower density photoionized regions ($\sim 0.2 - 0.5$ cm^{-3}) and it is not considered part of H II regions (Draine 2011; Klessen and Glover 2016).

(iii) The WNM, also referred to as warm H I, consists mainly of atomic gas, whose densities are comparable to the WIM ($\sim 0.2 - 0.6$ cm^{-3}) and it is heated to temperatures of about $\sim 5000 - 10000$ K by photoelectrons from dust and cosmic rays (Field, Goldsmith, and Habing 1969; Wolfire et al. 1995; Draine 2011; Klessen and Glover 2016). It is observed using ultraviolet/visible absorption lines and H I 21-cm emission (Draine 2011). In addition, this medium fills approximately 40% of the Galactic disk's volume (Draine 2011).

(iv) The CNM, also referred to as the cool H I, is mainly composed of atomic gas with low temperatures of about $\sim 50 - 100$ K and densities in the range $\sim 20 - 50$ cm^{-3} (Wolfire et al. 1995; Draine 2011; Klessen and Glover 2016). It is also heated by photoelectrons from dust and, like the WNM, it is also observed via H I 21-cm emission and ultraviolet/visible absorption (Draine 2011). In addition, it occupies about $\sim 1\%$ of the local ISM (Draine 2011).

(v) Molecular gas (H_2), is divided into a lower density ~ 100 cm^{-3} molecular gas also called diffuse H_2, with temperatures of about ~ 50 K, and a higher density $\sim 10^3 - 10^6$ cm^{-3} molecular gas often referred to as dense H_2 with temperatures in the range $\sim 10 - 50$ K (Draine 2011; Klessen and Glover 2016). This medium is correlated with star formation, and it is observed via H I 21-cm & CO 2.6-mm emission and ultraviolet/visible absorption lines (Carruthers 1970; Ferriere 2001; Draine 2011).

These different ISM phases are linked to each other, and there are conversions from one phase to another because of the dynamics of the ISM. For example, high energy photons from hot stars can heat up the cold molecular gas to form hot H II gas, also cooling via the release of radiation by the hot gas can reduce the temperature of ions and electrons which may undergo recombination to form atoms, and the hydrogen atoms can also release radiation and combine to form molecular hydrogen (Draine 2011).

1.4 The origin of high-velocity runaway (HVR) stars

Stars are constantly in motion as they orbit around the centre of their galaxy; those that are moving at supersonic speeds through the ISM with velocities in the range $40 \leq v \leq 200$ km/s are referred to as runaway stars (Blaauw 1961). Hypervelocity stars move at speeds comparable to the Galactic escape velocity ~ 500 km/s (Brown 2015, and references therein). We define HVRs as stars moving at speeds that are at the tail end of the runaway velocity distribution. The supernova ejection scenario (SES) (Blaauw 1961; Stone 1991) (see Section 1.4.1) and the dynamical ejection scenario (DES) (Poveda, Ruiz, and Allen 1967; Gies and Bolton 1986) (see Section 1.4.2), are the two common mechanisms proposed to explain such high stellar velocities (Hoogerwerf, Bruijne, and Zeeuw 2000; Gvaramadze 2009; Peri et al. 2012; Dorigo Jones et al. 2020). The other less common mechanisms are mentioned in Section 1.4.3. In most cases there is not enough evidence to conclude which mechanism is responsible for some runaway stars (Peri et al. 2012, and reference therein), but some studies suggest that runaway and HVR stars are more likely to be produced via the SES (Moffat et al. 1998; Peri et al. 2012), and hypervelocity stars via the DES (Brown 2015).

1.4.1 Supernova Ejection Scenario (SES)

In the SES, see Figure 1.3, a runaway star is produced when a massive binary evolves and the primary explodes as a supernova disrupting the binary by rapidly reducing the gravitational attraction that holds the stars together in their orbit (Blaauw 1961; Stone 1991; Huthoff and Kaper 2002). The secondary is released as a runaway star with a velocity that is comparable to its orbital velocity in the pre-supernova binary (Blaauw 1961; Stone 1991; Huthoff and Kaper 2002).

Blaauw (1961) approximated the possible velocities of the runaway star from the SES as:

$$V_{\mathrm{SES}} \sim 30\left[\frac{M_1}{M_1 + M_2}\right]\left(\frac{M_1}{a_2}\frac{\mathrm{AU}}{\mathrm{M}_\odot}\right)^{\frac{1}{2}} \ \mathrm{km/s}, \tag{1.3}$$

where M_1 is the most massive component in the binary before explosion (the primary star), M_2 is the mass of the secondary before explosion (it will be the runaway star as shown in Figure 1.3), a_2 is the radius of the orbit of M_2 around the common center of gravity, and V_{SES} is the velocity of M_2 around this same point (this is approximately the velocity of the runaway star after M_1 goes supernova). This velocity is in the range $40 \leq V_{\mathrm{SES}} \leq 200$ km/s (Blaauw 1961) or even higher for HVR stars. For example, if M_1 and M_2 have masses equal to $300\,\mathrm{M}_\odot$ and $10\,\mathrm{M}_\odot$, respectively, (so that $\frac{M_1}{M_1+M_2} \sim 1$) and $a_2 = 10$ AU, the velocity of the runaway star will be $V_{\mathrm{SES}} \sim 200$ km/s.

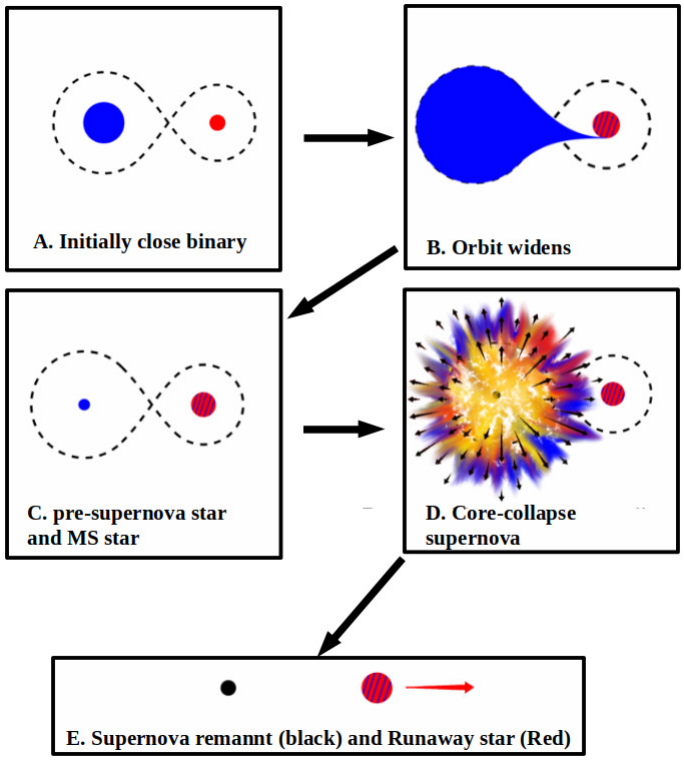

FIGURE 1.3: Schematic representation of how a runaway star can be produced through the SES. The pair of blue and red circular objects represents a binary star system, where the blue circular object is the massive primary, while the red circular object represents the secondary star. A: shows the initial close binary, with the separation in the range 10-100 AU (Kuiper 1935; Blaauw 1961). B: shows that this binary evolves through mass transfer. C: there is no longer mass transfer and the blue circle is now a helium star (O or B type), and the red one is a MS or a blue supergiant (BSG) star. D: the primary explodes as a type II supernova and disrupts the system. E: the secondary star gets released as a runaway star. [Adapted from Figure 1 of Renzo et al. (2018)].

1.4.2 Dynamical Ejection Scenario (DES)

In the DES, a runaway star is produced via strong gravitational interactions between massive OB stars in the core of a young dense cluster (Poveda, Ruiz, and Allen 1967; Huthoff and Kaper 2002). The star that will be released as a runaway can interact with two or more stars in the core of the star cluster (Peri et al. 2012; Gvaramadze 2009). There have been observations of OB runaways with space velocities greater than 100 km/s (Gies and Bolton 1986; Conlon et al. 1990; Blaauw 1993; Gvaramadze et al. 2019), and these velocities are about 10 times the speed of normal OB stars found in the Milky Way (Huthoff and Kaper 2002).

Poveda, Ruiz, and Allen (1967) suggested that there are dynamical interactions between stars that occur due to the collapse of young star clusters. A three-body dynamical interaction is one of the most likely interactions that can explain HVR stars. As shown in Figure 1.4, this process happens when a binary star system encounters a VMS or a BH and the interaction results in a tidal breakup of the binary. One of the binary members becomes bound to the VMS or BH while the other is ejected as a runaway star. The ejection velocity as suggested by Gvaramadze (2009), and

references therein is:

$$V_{\rm DES} \sim 500 \left(\frac{M_{\rm VMS}}{100\,{\rm M}_\odot}\right)^{\frac{1}{6}} \left(\frac{a}{30\,{\rm R}_\odot}\right)^{-\frac{1}{2}} \left(\frac{M_{\rm B}}{10\,{\rm M}_\odot}\right)^{\frac{1}{3}} {\rm km/s}, \tag{1.4}$$

where $V_{\rm DES}$ is the velocity of the runaway star, $M_{\rm VMS}$ is the mass of the VMS or BH, a is the semimajor axis of the binary before disruption and $M_{\rm B}$ is the total mass of the binary. The stars that are released through the DES have velocities in the range $35 \leq V_{\rm DES} \leq 185$ km/s (Poveda, Ruiz, and Allen 1967). If the mass of the VMS is about $200 - 300$ M$_\odot$ (Vink et al. 2015, and references therein), it could result in higher velocities that are $\geq 500 - 600$ km s^{-1} (Gvaramadze 2009; Brown 2015, and references therein).

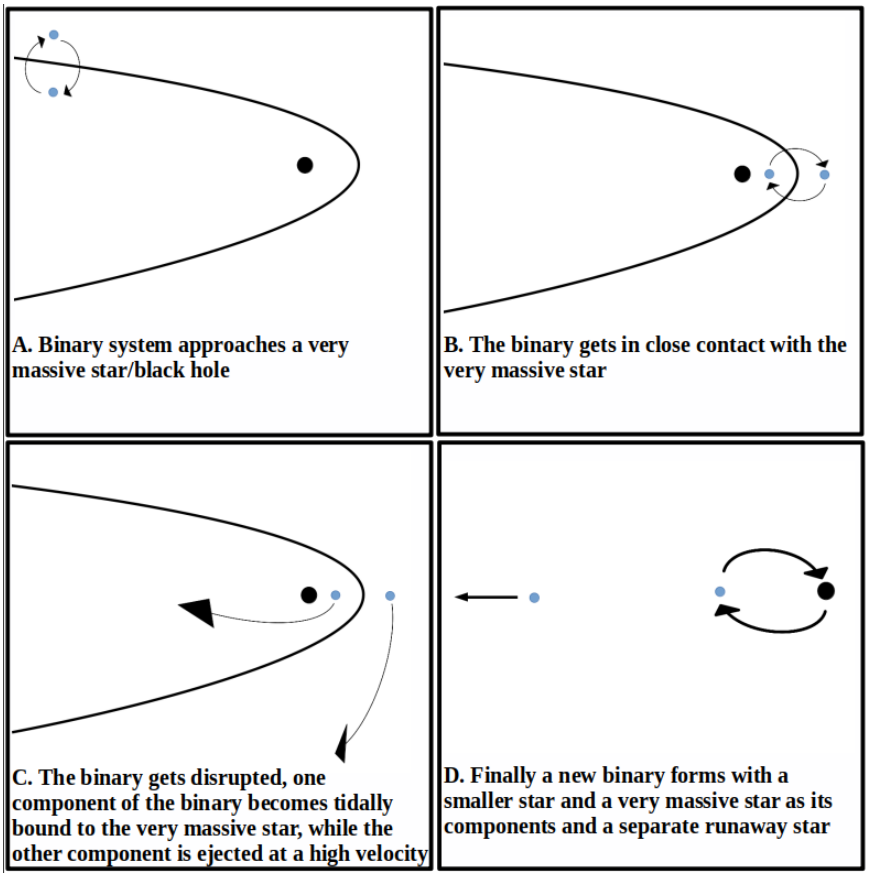

FIGURE 1.4: Schematic representation of how a runaway star can be produced through the DES. The blue circular objects represent OB type stars which are smaller relative to the black circular object which represents a VMS or BH. In A: the tight binary approaches a VMS in a young dense star cluster. B: the binary is in close contact with the VMS. C: the strong gravitational pull of the VMS on the binary results in a tidal disruption of the binary and one star becomes bound to the VMS and the other star is released as a runaway star. [Inspired by Figure 2 of Brown (2015)].

1.4.3 Other Ejection Scenarios

There are various other less common dynamical ways in which HVRs can be produced as discussed by Brown (2015), but because most massive stars exist in binaries, in this subsection, only the ejection scenarios that involve the multiplicity of massive stars are discussed.

Triple system breakup

In this scenario, a runaway star is ejected due to the breakup of an unstable triple star system (Anosova, Colin, and Kiseleva 1996; Gvaramadze 2009). The dissociation of such a system results in a tight binary and a runaway, which is usually the least massive of the three stars (Gvaramadze 2009; Toonen, Boekholt, and Portegies Zwart 2021). According to Toonen, Boekholt, and Portegies Zwart (2021), this mechanism can result in a massive star with high velocities that can reach $\sim 100\,\mathrm{km/s}$.

Binary-Binary encounter

This is a scenario where two binaries interact and eject runaways with velocities that are comparable to the pre-encounter orbital velocity of each component of the systems. This mechanism can result in velocities in the range $\lesssim 200$ km/s (Brown 2015, and references therein).

1.5 Stellar wind bow shocks

1.5.1 Observations of stellar wind bow shocks

Some runaway stars have winds that are powerful enough to form stellar bow shocks, arc-like structures that arise from the shock interaction between the wind and the ISM (Baranov, Krasnobaev, and Kulikovskii 1971; van Buren, Noriega-Crespo, and Dgani 1995; Huthoff and Kaper 2002). Bow shocks can be used to probe the properties of the stellar wind and the local ISM, such as the wind mass-loss rate, the wind velocity and the local ISM density (Hollis et al. 1992; Kaper et al. 1997; Comerón and Kaper 1998; Gvaramadze et al. 2013). In addition, they can also be used to find runaway stars and to determine the clusters from which they originated (Gvaramadze and Bomans 2008). For example, Ueta et al. (2008) derived the space velocity of Betelgeuse relative to its local ISM using the thin-shell approximation by Wilkin (1996), and the stellar wind parameters estimated by previous studies.

Massive MS or BSG stars are the main producers of bow shocks (van Buren, Noriega-Crespo, and Dgani 1995; Peri et al. 2012; Peri, Benaglia, and Isequilla 2015; Dorigo Jones et al. 2020). Approximately $10-25\%$ of O-type stars are runaways (Gies 1987; Blaauw 1993). There are only a few evolved massive stars known to date to have bow shocks around them, for example, a yellow supergiant (YSG) star from the Small Magellanic Cloud (SMC), and three RSG stars (Betelgeuse, μ Cep and IRC-10414) from our Galaxy (Neugent et al. 2018), and references therein.

Bow shocks are ubiquitous and have been detected in systems at different phases of evolution and at different wavelengths, i.e., X-rays (López-Santiago et al. 2012; Rangelov et al. 2019), ultraviolet (Martin et al. 2007; Le Bertre et al. 2012), optical (Gull and Sofia 1979; Bond and Miszalski 2018), infrared (van Buren and McCray 1988; Ueta et al. 2008; Mayer et al. 2011; Gvaramadze et al. 2011; Peri et al. 2012; Gvaramadze et al. 2019; Green et al. 2019) and radio (Benaglia et al. 2010; van den Eijnden et al. 2022). However, most of them have been observed in the infrared (Gvaramadze et al. 2013). Figure 1.5 shows some observed bow shocks with prominent definitions of the arc-like structures.

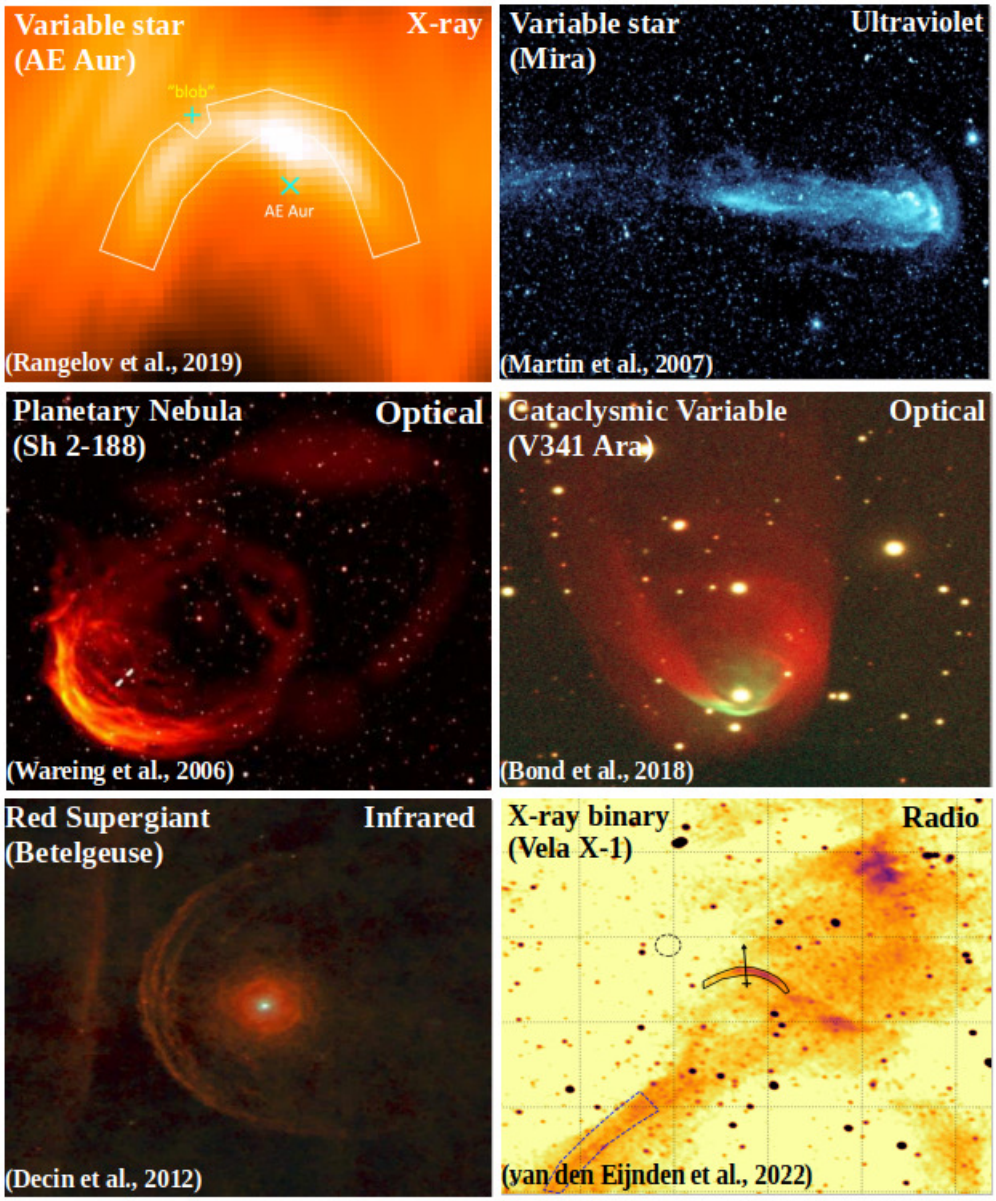

FIGURE 1.5: Some examples of observed bow shocks detected at different wavelengths around different types of systems.

1.5.2 The theory behind stellar wind bow shocks

The work by Baranov, Krasnobaev, and Kulikovskii (1971) was the first to derive the distance characterizing the size of the bow shock called the stand-off distance, R_{SOD}. It is the distance between the star (in the direction of motion), and the point where the ram pressure of the stellar wind $(\rho_w v_w^2)$ and the ISM $(\rho_{ISM} v_*^2)$ are balanced, such that we have:

$$\rho_w v_w^2 = \rho_{ISM} v_*^2, \tag{1.5}$$

where ρ_{ISM} is the density of the ISM, v_* is the velocity of the runaway star with respect to the ISM, ρ_w is the density of the stellar wind and v_w is the velocity of the stellar wind. Assuming spherical mass loss, with mass-loss rate $\dot{M}_w$, then at a radial distance r from the runaway star, we have:

$$\rho_w v_w = \frac{\dot{M}_w}{4\pi r^2}. \tag{1.6}$$

The combination of the Equations 1.5 and 1.6 gives the Baranov, Krasnobaev, and Kulikovskii (1971) (BKK) solution, which is given as:

$$R_{\rm SOD} = \sqrt{\frac{\dot{M}_{\rm w} v_{\rm w}}{4\pi \rho_{\rm ISM} v_*^2}}. \tag{1.7}$$

The thin-shell analytical approximation for the shape of a bow shock, which is assumed to be infinitely thin and whose size is characterized by the $R_{\rm SOD}$ was derived by Wilkin (1996) and its referred to as the Wilkin analytic solution which is given as:

$$R(\theta) = R_{\rm SOD}\left(\frac{1}{\sin\theta}\right)\sqrt{3\left(1-\frac{\theta}{\tan\theta}\right)}, \tag{1.8}$$

where θ is the angle measured in degrees from the axis of symmetry in the direction of motion of the runaway star and extends towards the tail, while tracing the contact discontinuity (represented by the blue line in Figure 1.6). These solutions of Baranov, Krasnobaev, and Kulikovskii (1971) Equation 1.7 and Wilkin (1996) of Equation 1.8 have been used for decades by various authors (e.g., Comerón and Kaper 1998; Mohamed, Mackey, and Langer 2012; Meyer et al. 2014, and many more). However, Scherer et al. (2016) stress that this is a poor approximation, and supports arguments discussed in Zank (1999) about the unreliability of this approximation. This thin shell approximation is poor because in general the shock normal is not parallel to the radius vector and simple geometry cannot reliably describe the contact discontinuity (Scherer et al. 2016). Nonetheless In this Thesis we will also use this Wilkin (1996) analytic solution because of its simplicity and for easier comparison, as it is adopted by the majority of the previous work.

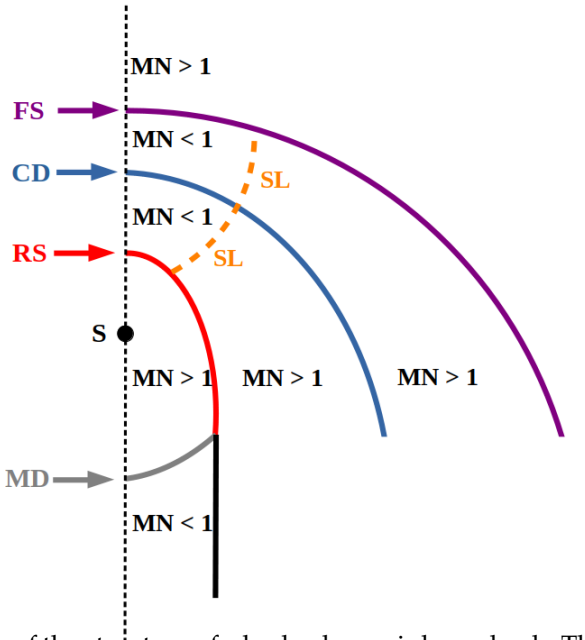

FIGURE 1.6: Sketch of the structure of a hydrodynamic bow shock. The vertical black dashed line is the stagnation line, which is the axis of symmetry of the bow shock, while the solid black dot represents the runaway star at position (S). The abbreviations in this plot denote the following: forward shock (FS), contact discontinuity (CD), reverse shock (RS), Mach disk (MD), sonic line (SL) and Mach number (MN). [Adopted from Scherer et al. (2016)].

Most importantly, if the velocity of the star is subsonic relative to the ISM, we will not have a bow shock, but if it is supersonic we will have a bow shock. In Figure

1.6, FS separates the unshocked and the shocked ISM; CD separates the shocked ISM and the shocked wind, and it acts as a barrier as that of a closed system, which allows through it, the transport of energy but not mass, in addition, pressure on both sides of CD is the same, while the density, temperature and velocity are some of the quantities that are discontinuous; RS separates the shocked wind and the freely expanding wind, MD separates the freely expanding wind and the tail, while SL (MN $= 1$) separates the subsonic (MN < 1) and supersonic (MN > 1) fluid within any of the shocked regions (Scherer et al. 2015; Scherer et al. 2016).

RS extends from the stagnation line where it is categorized as a normal shock to become an oblique shock, which consist of a point where MN $= 1$, which is where the sonic line is found. Further downstream away from this oblique shock surface, the RS becomes parallel to the stagnation line. The velocity of the stellar wind from the star jumps at the RS. When the supersonic freely expanding wind (where MN > 1) transition to the shocked wind, we have a stronger RS when the transition is to the subsonic region of the shocked wind (where MN < 1), and a weaker RS when the transition is to the supersonic region of the shocked wind (where MN > 1), see Scherer et al. (2015) and Scherer et al. (2016) for more details.

1.6 Previous numerical studies of bow shocks

To our knowledge, there has not been any hydrodynamic studies of bow shocks formed by massive HVR stars with velocities $\gtrsim 200$ km/s. Even though such studies have not been carried out, there have been other 2D and 3D hydrodynamic simulations that involved high space velocities, for example ~ 150 km/s by Comerón and Kaper (1998), ~ 70 km/s by Mohamed, Mackey, and Langer (2012) and Meyer et al. (2014), ~ 350 km/s by Li, Bryan, and Quataert (2019) but for a typical asymptotic giant branch (AGB) star, and ~ 160 km/s by Gvaramadze et al. (2019); while others involved relatively lower space velocities, e.g., ~ 30 km/s by Mohamed, Mackey, and Langer (2012) and van Marle, Decin, and Meliani (2014), ~ 50 km/s by Mackey (2012), $\sim 20 - 40$ km/s by Meyer et al. (2014) and Green et al. (2019), $\sim 4 - 16$ km/s by Mackey et al. (2015) and Mackey et al. (2016) and ~ 30 km/s by Mackey et al. (2021).

The 2D hydrodynamic simulations by Comerón and Kaper (1998) and Meyer et al. (2014) included thermal conduction, in addition to cooling. The key results of their study showed that thermal conduction makes the bow shock broader and more stable with very little growth of instabilities, and that thermal conduction is only important for bow shocks around MS stars and not RSGs, because MS stars have higher temperatures. Comerón and Kaper (1998) used cooling and heating proportional to density and energy, while Meyer et al. (2014) used cooling and heating that was interpolated linearly from the tables and/or functions of Hummer (1994), Wolfire et al. (2003), Wiersma, Schaye, and Smith (2009), and Osterbrock (1989). In addition, the growth of the bow shock instabilities agrees with Dgani, van Buren, and Noriega-Crespo (1996) as shown in Figure 1.7 of the Meyer et al. (2014) models.

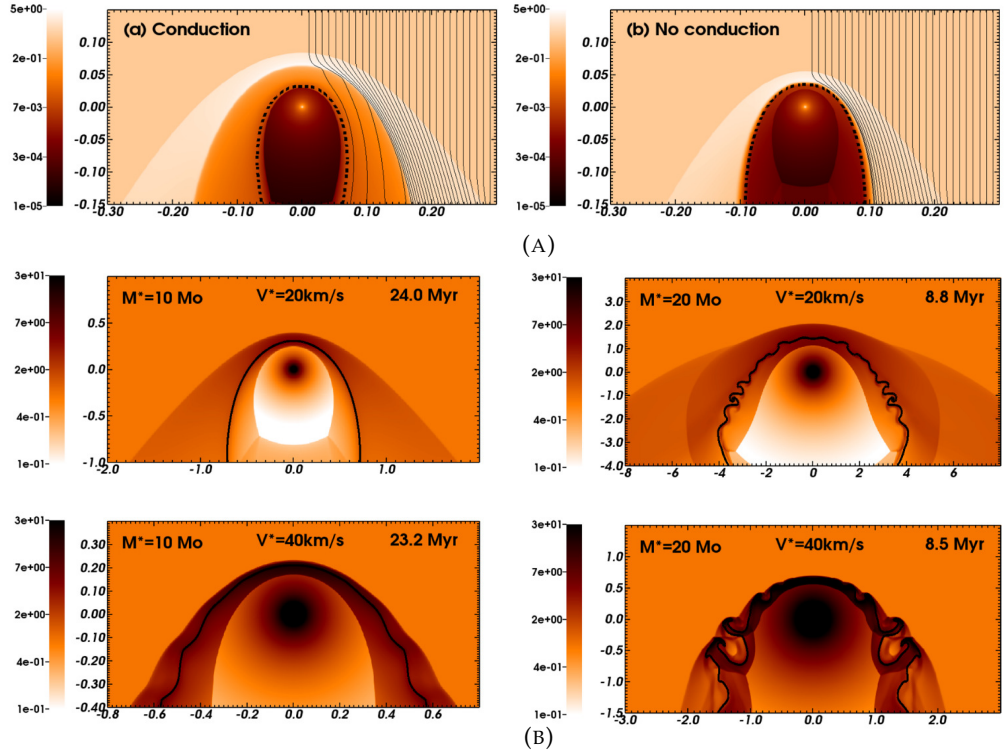

FIGURE 1.7: (A) The effect of thermal conduction on the size, shape and structure of the bow shock around a massive MS star. (B) Effect of mass-loss rate and space velocity of the central star on the bow shock morphology around RSGs. In addition, the colorbar is the number density in logarithmic scale in g /cm^3, while the axes are in pc. [Credit: Meyer et al. (2014)].

The work by Mohamed, Mackey, and Langer (2012) was based on 3D hydrodynamic simulations of Betelgeuse's bow shock as shown in Figure 1.8, they used more detailed cooling at temperatures $\lesssim 10^4$ K which is appropriate for the winds ejected by cool stars such as RSGs. They included processes associated with atoms, molecules, cosmic rays, and dust grains, and studied the 3D morphology of the bow shock, its evolution and the growth of instabilities (Mohamed, Mackey, and Langer 2012).

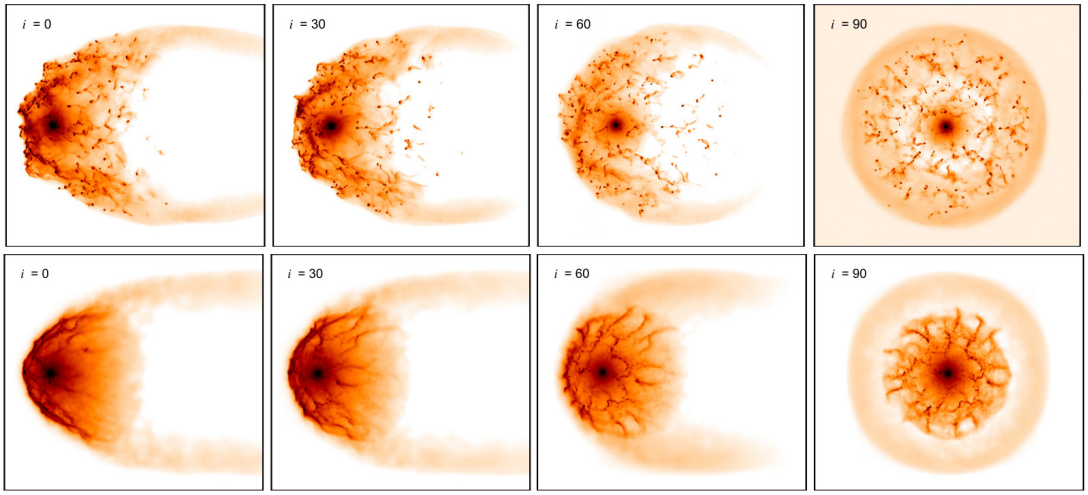

FIGURE 1.8: Bow shock simulations of Betelgeuse in 3D obtained in the same period of time, for the space velocities 32 km/s (top panel) and 72 km/s (bottom panel). The bow shock produced by the faster moving star is much smoother than the one on the top panel. [Credit: Mohamed, Mackey, and Langer (2012)].

The 2D magneto-hydrodynamic simulations of a RSG runaway by van Marle, Decin, and Meliani (2014) included both cooling and the ISM magnetic field. The key results were that the growth of instabilities (i.e., Kelvin-Helmholtz and Rayleigh-Taylor) can be suppressed by the interstellar magnetic field even if it is a weak field (van Marle, Decin, and Meliani 2014) (see Figure 1.9), which might explain why some bow shocks observed around RSGs such as Betelgeuse do not show instabilities. For cooling they used the so-called "exact integration method" from Townsend (2009), and a cooling curve that was obtained using CLOUDY Ferland et al. (1998) for a stellar gas at solar metallicity (van Marle, Decin, and Meliani 2014).

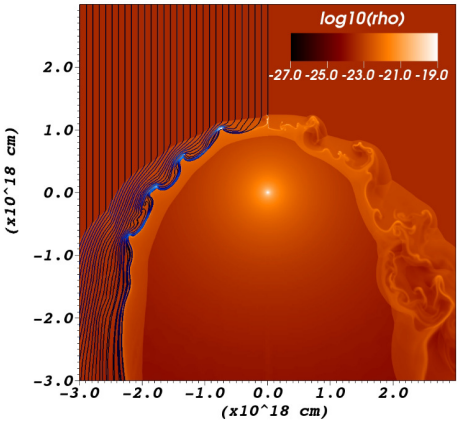

FIGURE 1.9: Density of the circumstellar medium in g /cm^3 of a RSG moving with $\sim$ 30 km/s, showing the case where the instabilities are being suppressed by the interstellar magnetic field (left) and the adiabatic case (right). [Credit: van Marle, Decin, and Meliani (2014)].

The 2D hydrodynamic simulations by Gvaramadze et al. (2019), did not include thermal conduction, even though the simulated bow shock is around an O-type star. Their models of a bow shock around CPD $-$ 64°2731 do not show any growth of instabilities probably because the simulated bow shock is young ($\sim$ 1500 yr) as shown in Figure 1.10, instabilities might develop at a later time. The cooling they included was based on a function by Cowie, McKee, and Ostriker (1981), and cooling due to dust grains was not included because it is less important at temperatures $\sim 10^5$ K where most of the energy is radiated (Cowie, McKee, and Ostriker 1981).

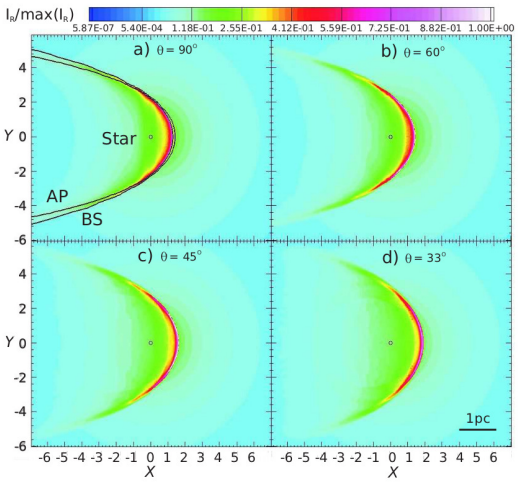

FIGURE 1.10: Synthetic dust emission map of the circumstellar structure of the HVR O-type star, CPD $-$ 64°2731 moving with $\sim$ 160 km/s, with traces of the astropause (AP) and bow shock (BS). [Credit: Gvaramadze et al. (2019)].

The 2D hydrodynamic simulations of a bow shock around a massive O-type star by Green et al. (2019), also did not include thermal conduction and the implemented cooling was similar to that used by Meyer et al. (2014). Synthetic images were produced to estimate the emission and brightness levels at different wavelengths, and one of their key results is that there may be fluid build-up at the apex of the bow shock when using 2D (see Figure 1.11) (Green et al. 2019).

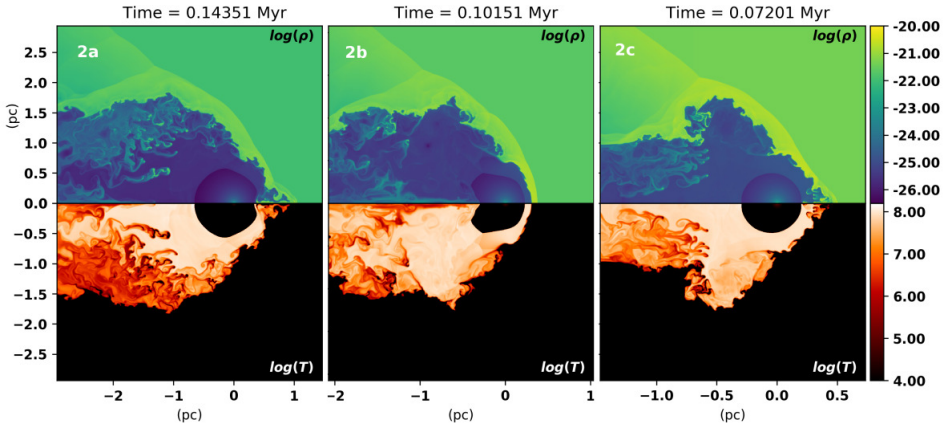

FIGURE 1.11: Density of the bow shock around an O-type star moving with $\sim$ 30 km/s, showing growth of instabilities and fluid build-up in the 2D models at the apex. The density and temperature are in g/cm^3 and K, respectively. [Credit: Green et al. (2019)].

The main results of 2D hydrodynamic models by Li, Bryan, and Quataert (2019) is that high space velocities result in strong instabilities and reduce the size of the bow shocks. In addition, the results also showed that models with cooling show better agreement with observations of the Mira bow shock than the models without it, as shown in Figure 1.12. For temperatures $< 10^4$ K, they did not include cooling due to dust, they used rates based on Rosen and Bregman (1995) which only takes into account neutral hydrogen. In addition, in their simulations, they mention that cooling can drop the gas temperature to a minimum of 10^4 K. However, this is a poor approximation for the stellar winds of cool stars such as AGBs (which is what they are modelling) and RSGs, because the winds of these cool stars have temperatures of, $\sim$ 100s K at a few stellar radii (Lamers and Cassinelli 1999).

The overall consensus from this previous work is that it is important to take into account additional processes such as radiative cooling and thermal conduction in bow shock simulations, because they significantly affect the bow shock morphology, flow characteristics and the development of instabilities. However, most previous studies did not include major processes necessary for cooling at lower temperature $< 10^4$ K, and some did not mention in detail which cooling processes are taken into account. Previous works also focused on lower velocities generally with only a few exceptions like Li, Bryan, and Quataert (2019) and Gvaramadze et al. (2019). However, in looking to better understand runaway star populations and to identify (future) observations of bow shocks around stars with higher velocities, we need to study the tail end of the runaway velocity distribution.

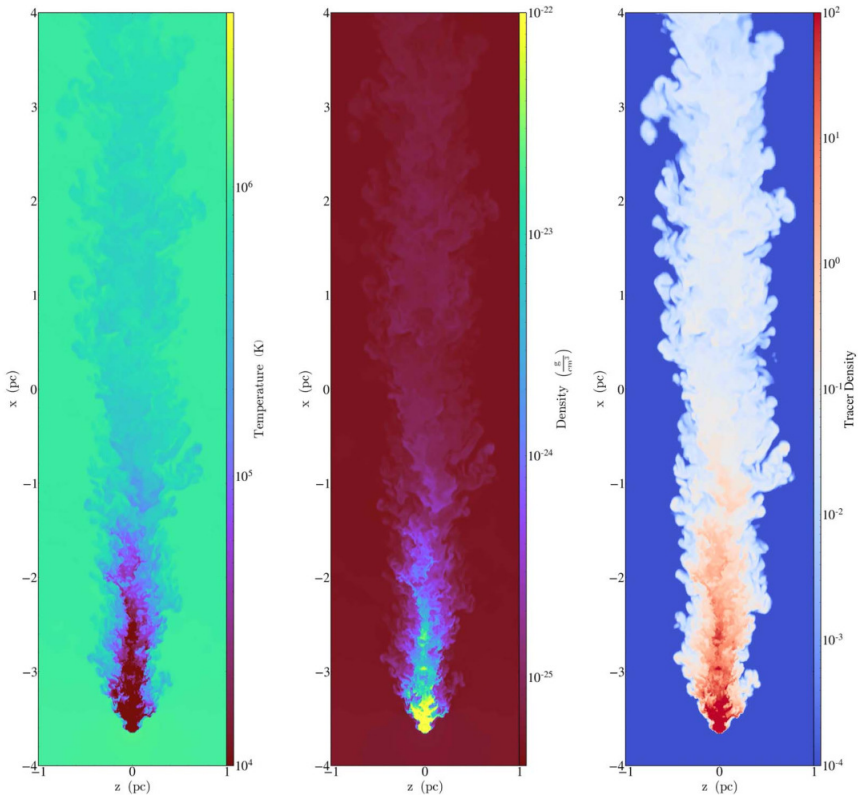

(A) No cooling

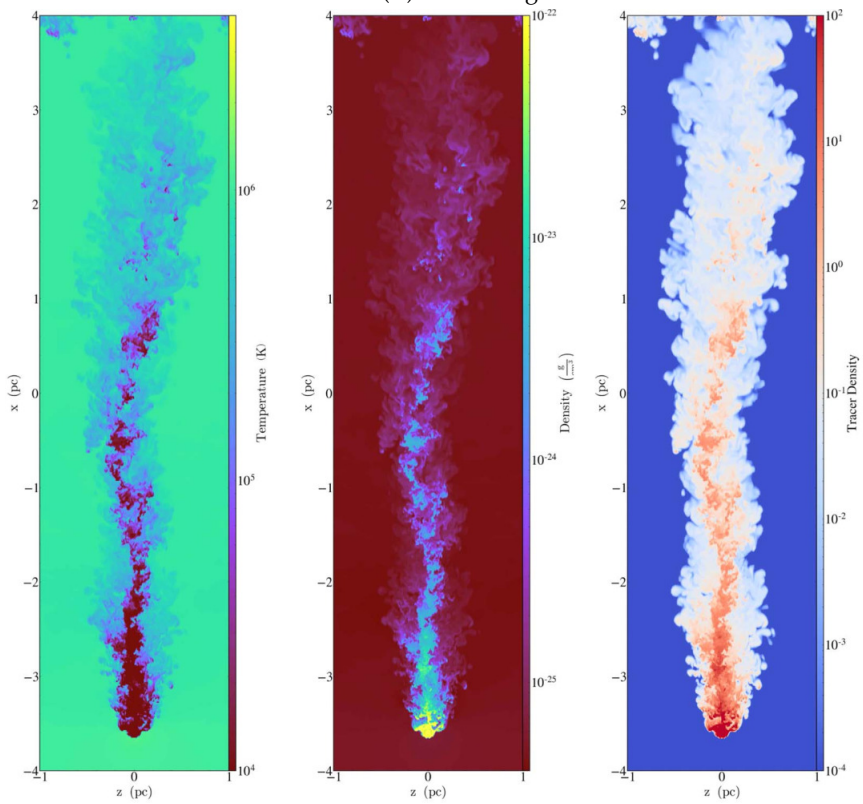

(B) With cooling

FIGURE 1.12: 2D Mira models for space velocity $\sim$ 125km/s without cooling (A) and with cooling (B). [Credit: Li, Bryan, and Quataert (2019)].

1.7 This work

In this work, we study HVRs with velocities $\gtrsim$ 200 km/s, whose origin is supported mainly by the dynamical ejection scenario (DES) as discussed in Section 1.4.2 for a 3-body exchange of a binary with a VMS or BH – basically the Hills mechanism (Brown 2015, and references therein). These space velocities gained through this mechanism depend mainly on how massive the single star/BH is that the binary will interact with, because the more massive the single star/BH, the greater the ejection velocity. The most massive stars have masses in the range $\sim 150 - 300$ $M_\odot$ (Yusof et al. 2010; Vink et al. 2015, and references therein), and there is a possibility of even more massive intermediate mass BHs due to BH mergers (Abbott et al. 2020) in the disks of galaxies, so although they might be rare, the possibility of stars with speeds $\gtrsim$ 200 km/s is interesting to propose and investigate.

The main motivation is to present high-resolution 2D and 3D simulations of bow shocks formed by these HVR stars with well-defined flow characteristics and thorough instability studies. However, for simplicity, the simulations do not include the effect of magnetic fields, stellar rotation and the presence of a companion, i.e., we assume a single star scenario with solar metallicity and constant (non-evolving) stellar and ISM parameters for each model.

In this work, we explore the space velocity by modelling the bow shocks of HVR stars and investigate their morphology while taking into account the different evolutionary phases of massive stars (MS and RSG), and different ISM phases (HIM, HII region, WNM and CNM). We include radiative cooling and thermal conduction similar to the work by Meyer et al. (2014), but implementing the Runge-Kutta Legendre method for the thermal conduction (Vaidya et al. 2017), and a more detailed radiative cooling from Ploeckinger and Schaye (2020) modified to be appropriate for stellar wind bow shocks.

The investigations in this work aim to create the foundation of future work which will involve investigating the possibility of observing bow shocks formed by $\gtrsim$ 200 km/s HVRs. In addition, our simulations will be coupled with the latest evolutionary models, to get more accurate and precise stellar parameters, and to investigate the effect of evolving stellar parameters. Ultimately the goal is to produce synthetic images to guide observational identification of these systems and analysis that will help in constraining the stellar wind and ISM properties.

1.8 Outline

This Thesis is structured as follows: Chapter 2 provides the context and demonstration of the method used, including the details of the implemented radiative cooling and thermal conduction. In Chapter 3, the assumed stellar wind and ISM parameters that are used as initial conditions in the simulations are described. In Chapter 4, test results of the effect of thermal conduction, radiative cooling and space velocity are presented and compared with similar previous work for slower-moving runaway stars. In Chapter 5, the resolution test models and results for HVR stars are presented. In Chapter 6, is the presentation of the results showing the effect of different ISM phases and space velocities on the morphology of HVR bow shocks, in addition to comparison of the 2D and 3D models. Chapter 7 summarises the overall

findings together with concluding remarks. Appendix A, includes a description of how different solvers work, Appendix B provides detailed test results of the effect of the resolution, grid geometry and different solvers using a spherical stellar wind model for exploring the numerics of PLUTO code. Supplementary plots are given in Appendix C.

Chapter 2

Methods

In this chapter, we outline how PLUTO [1] v. 4.3, a magneto-hydrodynamics grid code works, how it is structured and designed, focusing on the most important components including the reconstruction, Riemann solvers and time-stepping, in addition to how additional physics such as radiative cooling and thermal conduction can be included. We outline the background of the physics of fluids, the numerical method that we use to discretize and solve fluid equations, as well as its benefits and drawbacks compared to other methods. We also give a brief overview of our PLUTO numerics test results.

2.1 Hydrodynamics (HD)

In HD, the Newtonian framework is used to approximately describe the flow of fluids. It is commonly used to solve fluid related problems in astrophysics because it can be used to describe large scale processes of interest of astrophysical flows. HD can describe a portion of the fluid system as a complete entity commonly referred to as a fluid element, disregarding the fact that this fluid element is a collection of individual particles (e.g., atoms and electrons). In this work, we assume a fixed frame of reference and an inviscid fluid that flows past this frame is described by the Euler equations, which consist of the (Zingale 2013)

conservation of mass:

$$\frac{\partial \rho}{\partial t} + \nabla \cdot (\rho \mathbf{v}) = 0 \,, \tag{2.1}$$

conservation of momentum:

$$\frac{\partial (\rho \mathbf{v})}{\partial t} + \nabla \cdot (\rho \mathbf{v}\mathbf{v}) + \nabla P = 0 \,, \tag{2.2}$$

conservation of energy:

$$\frac{\partial (\rho E)}{\partial t} + \nabla \cdot (\rho E \mathbf{v}) + \nabla \cdot (P \mathbf{v}) = 0 \,, \tag{2.3}$$

where ρ is the density, $\mathbf{v}$ is the velocity vector, P is the pressure and E is the total energy divided by the mass, and it can be written as

$$E = e + \frac{1}{2}|\mathbf{v}|^2, \tag{2.4}$$

where in Equation 2.4, e is the specific internal energy and the last term is the specific kinetic energy. The addition of an equation of state closes the Euler equations and

[1] http://plutocode.ph.unito.it

the gamma-law equation of state is the most commonly used one (Zingale 2013) and is expressed as:

$$P = \rho e(\gamma - 1), \tag{2.5}$$

where $\gamma = \frac{5}{3}$ for an ideal, monatomic gas.

2.2 Numerical methods

In this section, we explain in detail the numerical methods used at the heart of the PLUTO code (Mignone et al. 2007), the primary simulation tool used in this project. Since PLUTO is a grid code, we will first describe the benefits and drawbacks of grid codes, followed by the description of its numerics.

2.2.1 Grid codes

There are many methods of discretization used in science and engineering, which can broadly be divided into grid-based and gridless methods (Zingale 2013). Below, we discuss the general properties of grid-based methods, followed by discussing some of their strengths and weaknesses, while briefly comparing them to gridless methods.

A grid is used in computations to represent continuous functions in a discrete manner, where each cell/zone represents a fluid element (Zingale 2013). Structured grids (Finite-Volume (FV) or Finite-Difference (FD) grids) are usually used in astrophysics; they make it easy to represent the position of a cell and its variables in the grid by a single integer index in any dimension (Zingale 2013). We can think of this numerical grid as a finite number of zones in space at one or more discrete instances in time used to represent a continuous equation in a discrete form (Zingale 2013). The more zones used to represent the continuous equation, the better the accuracy, but the more computationally intensive (for example, see Chapter 5 and Appendix B for resolution tests). In a FV grid, an average in the cell whose volume is controlled by the grid resolution is used to represent the discrete data (Zingale 2013).

Grid code advantages

- Structured grids are usually cartesian (Zingale 2013), this makes them simple to use as each cell in the domain of the grid can be referenced by an integer index even in higher dimensions (Mignone et al. 2007; Zingale 2013). For example, in 1D the structure of the grid can be represented by a 1D array and in 3D by a 3D array.

- A set of continuous equations such as a system of partial differential equations (PDEs) is transformed into a system of equations that are discretized onto the grid (Zingale 2013). Meaning each cell of a grid represents a fluid element, e.g., each cell in Figure 2.1 represents a fluid element. The FV grid similar to Figure 2.1 is widely used in astrophysics because "conservation is a natural consequence of discretization" (Zingale 2013).

- Eulerian grid methods are able to resolve and treat instabilities such as the Kelvin–Helmholtz or Rayleigh–Taylor instabilities, which are important for dynamical structure formation in astrophysics, whereas gridless methods e.g.,

Smoothed Particle Hydrodynamics (SPH) perform poorly when it comes to these instabilities (Agertz et al. 2007).

- Grid codes can handle shocks and contact discontinuities well, in other words they have good shock capturing ability (Agertz et al. 2007; Zingale 2013). In SPH, for example, large particle numbers i.e., very high resolution is required to do so (Rosswog 2009).
- Some gridless codes require 2-3 times as many particles as the number of zones in a grid code, to have an equivalent resolution of the underlying physics (Hubber, Falle, and Goodwin 2013).

Grid code disadvantages

- Unstructured grids, for example the Adaptive Mesh Refinement (AMR) grids, cannot be easily represented by a multi-dimensional array.
- The grids cannot easily represent domains that are irregularly shaped (Zingale 2013).
- The fluid sometimes follows the shape of the grid (e.g., one can find square stars or square stellar winds, especially at low resolution).
- For high accuracy one should use a Riemann solver which is computationally intensive.

2.2.2 PLUTO code

PLUTO is a magneto-hydrodynamics grid code used for computational astrophysics. It uses a structured grid and a FV method for discretization by default (Mignone et al. 2007). It is designed to determine the solution of hypersonic flows in 1, 2 and 3 spatial dimensions in the following types of coordinate systems: CARTESIAN, CYLINDRICAL, POLAR or SPHERICAL coordinates (Mignone et al. 2007; Mignone et al. 2012). This code has a multi-physics module environment including a HD physics module, along with multiple algorithms designed to treat hypersonic astrophysical fluid flows in the presence of discontinuities (Mignone et al. 2007). This is therefore a code suitable for modelling shock waves, hence its use in this project to model bow shocks.

PLUTO code structure and design

PLUTO is designed in such a way that it integrates a general system of conservation laws which can be written as (Mignone et al. 2007)

$$\frac{\partial \mathbf{U}}{\partial t} + \nabla \cdot \mathbf{F}(\mathbf{U}) = \mathbf{S}(\mathbf{U}), \tag{2.6}$$

where $\mathbf{U}$ is a column vector of conservative variables, $\mathbf{F}(\mathbf{U})$ and $\mathbf{S}(\mathbf{U})$ are both a function of $\mathbf{U}$ and they respectively represent the flux vector and the source terms (e.g., cooling and thermal conduction). This is basically a set of Euler equations in conservative form as shown in Equations 2.1, 2.2 and 2.3; and without the source term, Equation 2.6 can be written as:

$$\frac{\partial \mathbf{U}}{\partial t} + \nabla \cdot \mathbf{F}(\mathbf{U}) = 0, \tag{2.7}$$

with

$$\mathbf{U} = \begin{pmatrix} \rho \\ \rho\mathbf{v} \\ \rho E \end{pmatrix}, \quad \mathbf{F}(\mathbf{U}) = \begin{pmatrix} \rho\mathbf{v} \\ \rho\mathbf{v}\mathbf{v} + P \\ \rho\mathbf{v}E + \mathbf{v}P \end{pmatrix}. \tag{2.8}$$

This is a compact way of representing the conservative laws and it can be solved numerically using a Godunov-type method (Godunov 1959; Zingale 2013). PLUTO code uses the improved version of this method; which is a typical shock capturing method based on the reconstruct-solve-average strategy (Mignone et al. 2007; Zingale 2013). For example, let's consider a 1D Finite-Volume (FV) grid, as shown in Figure 2.1.

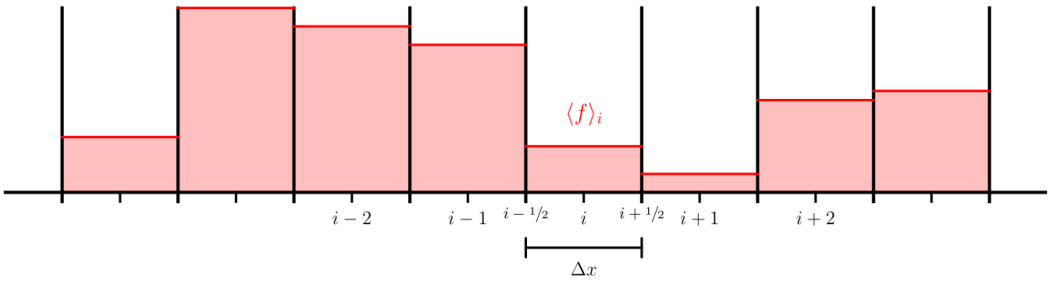

FIGURE 2.1: This is an example of a FV structured grid in one-dimension, where the grid is divided into cells/zones and each zone contains the average value (as the shaded area) of the function that is discretized. In addition, i is the index of the cell, Δx is the width of the cell and $\langle f \rangle_i$ is the average in the zone i represented by the red horizontal line; and the half-integers represents the interfaces of the zone. [Credit: Zingale (2013)].

The integration of Equation 2.7 in a 1D grid, as shown in Figure 2.1 such that $f = \mathbf{U}$, is given as:

$$\mathbf{U}_i^{n+1} = \mathbf{U}_i^n + \frac{\Delta t}{\Delta x}(\mathbf{F}_{i-\frac{1}{2}} - \mathbf{F}_{i+\frac{1}{2}}), \tag{2.9}$$

where

$$\mathbf{U}_i^n = \frac{1}{\Delta x}\int_{x-\frac{1}{2}}^{x+\frac{1}{2}} \mathbf{U}(x, t^n)dx, \tag{2.10}$$

$$\mathbf{F}_{i-\frac{1}{2}} = \frac{1}{\Delta t}\int_{t^n}^{t^{n+1}} \mathbf{F}[\mathbf{U}(x_{i-\frac{1}{2}}, t)]dt, \tag{2.11}$$

$$\mathbf{F}_{i+\frac{1}{2}} = \frac{1}{\Delta t}\int_{t^n}^{t^{n+1}} \mathbf{F}[\mathbf{U}(x_{i+\frac{1}{2}}, t)]dt, \tag{2.12}$$

and where i represents a zone, $(i - \frac{1}{2})$ and $(i + \frac{1}{2})$ represent the zone edges, n is the current time-step and $n + 1$ is the next time step. These fluxes in Equations 2.11 and 2.11 are determined by the Riemann solver; which results in well-behaved treatment of discontinuities with high accuracy, but is computationally expensive (Quirk 1994). In the PLUTO code, modern computationally efficient versions of the Godunov method, e.g., the piecewise LINEAR reconstruction method, an approximate Riemann solver and a Runge-Kutta multi-step time-stepping algorithm are utilized (Vaidya et al. 2018).

In simple terms, Figure 2.1 and Equations 2.7 - 2.12 illustrate that the quantity of a variable within a certain volume in a cell can change only as a result of the fluxes of that variable across the cell interface, which acts as a bounding surface between two different cells (Choudhuri 1998; Agertz et al. 2007). This is one of the things that forms the basis of the Godunov method (Godunov 1959). Figure 2.2 shows the flow diagram of how the Godunov-type code is devised.

Flow diagram for the PLUTO code

To find the state vector of conservative quantities $\mathbf{U}$, and to find its volume average, PLUTO by default uses a Finite-Volume-Method (FVM) (Vaidya et al. 2018) e.g., Figure 2.1. The volume averages of the conservation quantities $\mathbf{U}$ are then converted into primitive variables denoted as $\mathbf{V}$ (i.e., $\mathbf{U} \rightarrow \mathbf{V}$ as shown in Figure 2.2); the right (R) and left (L) states of the cell/zone are then interpolated/extrapolated by the reconstruction technique, this process is called reconstruction ($\mathbf{V} \rightarrow \mathbf{V}_{i+\frac{1}{2},L}, \mathbf{V}_{i-\frac{1}{2},R}$) and it creates a Riemann problem, where $(i-\frac{1}{2})$ and $(i+\frac{1}{2})$ represents the cell's left and right interface, respectively as shown in Figure 2.1.

The Riemann solver then solves the Riemann problem between the left and right states of an interface to compute the flux ($\mathbf{F}$) at the interface of the cell (i.e., $\mathbf{V}_{i+\frac{1}{2},L}, \mathbf{V}_{i+\frac{1}{2},R} \rightarrow \mathbf{F}_{i+\frac{1}{2}}$). Then the solution is advected in time by the time-marching method as follows: $\mathbf{U}^{n+1} = \mathbf{U}^n - \frac{\Delta t}{\Delta x}(\mathbf{F}_{i+\frac{1}{2}} - \mathbf{F}_{i-\frac{1}{2}})$, and then it loops again and again until the last time-step. In this paragraph, $\mathbf{U}^n = \mathbf{U}$, where n is the current time, Δt is the time-step, Δx is the cell size which is determined by the resolution. The FVM can be easily applied in multiple dimensions, and it can handle discontinuities well (Mignone, Plewa, and Bodo 2005; Zingale 2013) .

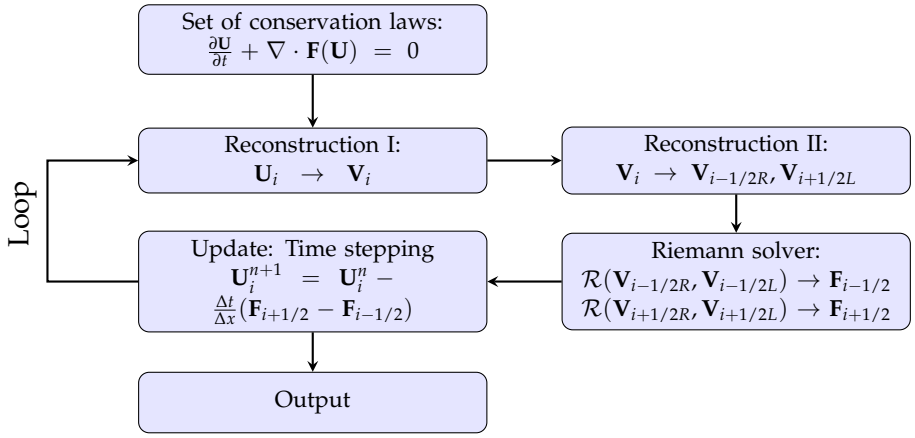

FIGURE 2.2: Flow diagram showing the most important steps PLUTO takes to arrive at the solution. $\mathbf{U}$ and $\mathbf{F}$ are the vector of conservative variables and the corresponding vector of fluxes, Δt is the times-step, Δx is the cell size, n is the current time. The subscript i is the integer that represents the cell and the half-integers represents the cell interface as shown in Figure 2.1, and $\mathcal{R}$ is the operator that represents a Riemann solver. R and L are the left and right interface states, respectively.

2.2.3 Reconstruction

In numerical methods, reconstruction is the process used to convert the conservative variables in the cell to primitive variables, and then use these primitive variables to compute the left and the right states of the cell interface to set up a Riemann problem. This procedure is carried out in each cell for all the cell edges. Since PLUTO uses the FVM, the left and right interface states are predicted via the interpolation and/or extrapolation from the average value of the variable in the cell (Mignone et al. 2007). The available options for reconstruction methods in PLUTO are FLAT, LINEAR, WENO3, LimO3 and PARABOLIC reconstruction (Vaidya et al. 2018). In this work, we focus only on the LINEAR reconstruction method because it is more robust and efficient than the other methods.

Reconstruction sets the spatial order of integration, which may be first-order, second-order or third-order depending on the reconstruction method used (Mignone et al. 2007; Vaidya et al. 2018). It is usually easier to use primitive variables to determine the interface states because of their simpler characteristic structure. While conservative variables can result in unphysical values such as negative densities after applying a limiter (see following subsections) (Zingale 2013), which is why PLUTO converts the conserved variables to primitive variables before computing the interface states, and these predicted interface states are used as inputs to the Riemann solver (Zingale 2013).

LINEAR reconstruction

LINEAR reconstruction is basically a piecewise linear reconstruction applied to primitive variables (Zingale 2013; Vaidya et al. 2018). After converting conservative variables to primitive variables, the average of the data in the cell is approximated by a line (see red lines/curves in Figure 2.3) which has a non-zero slope (Zingale 2013). This method uses a Taylor expansion to construct the interface states, through the use of half of the cell size in order to bring us to the interface and half of the step-size in order to bring us to the midpoint in time (Zingale 2013). From this Taylor expansion we get the interface states, and since the truncated errors in this method are $O(\Delta x^2)$ and $O(\Delta t^2)$, then this reconstruction method is second-order accurate both in space and time (Zingale 2013).

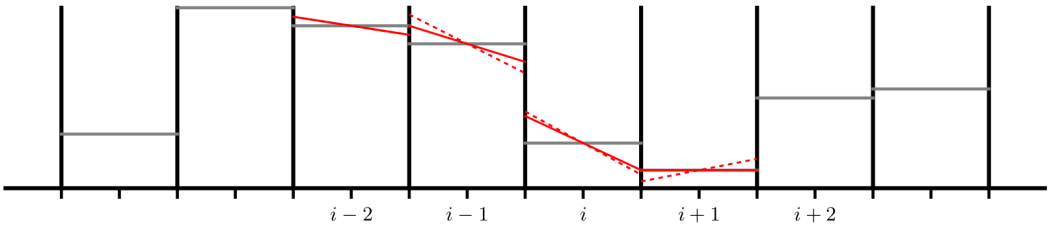

FIGURE 2.3: Linear reconstruction for a FVM, where the gray horizontal line is the cell average, the red lines are slopes obtained after the reconstruction, with the (solid-red-line) and the (dotted-red-line) representing the limited slope and the unlimited slope, respectively. [Credit: Zingale (2013)].

Limiters

A second-order reconstruction method, like the LINEAR reconstruction, is likely to show oscillations in the solution especially when dealing with initial discontinuities.

Applying a limiter makes sure that these oscillations are not introduced during the integration process (Zingale 2013). When dealing with an initial discontinuity without limiting (see Figure 2.4 for a discontinuity that moves from left to right of the grid), there is an overshoot and an undershoot behind and ahead of the discontinuity, respectively, that forms after the first step and this is propagated further away from the discontinuity when more and more steps are added in the integration process (Zingale 2013). We can think of this overshoot and undershoot as the oscillations that develop from using the second-order method, however, when dealing with an initial discontinuity with limiting, the solution is much narrower with less or no oscillations around the initial discontinuity during propagation (Zingale 2013).

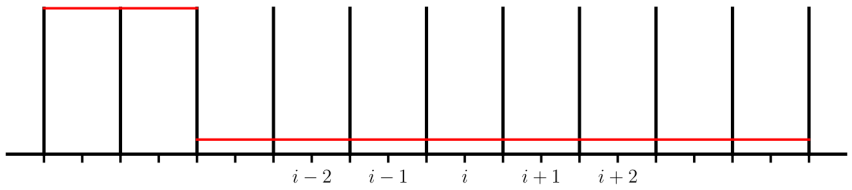

(A) Initial discontinuity arises.

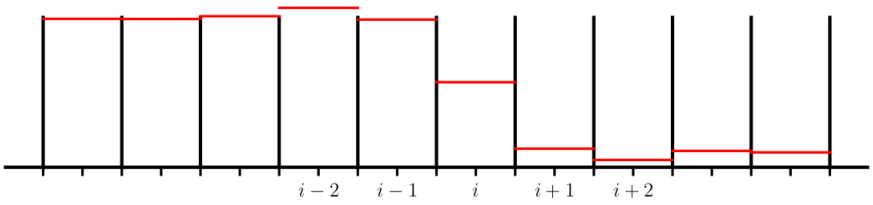

(B) Propagation without limiter

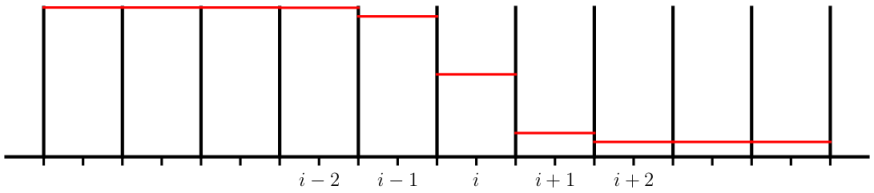

(C) Propagation with limiter

FIGURE 2.4: For a fluid propagating from left to right of this 1D grid. In (A) we see a rise of a discontinuity at regions of cells $i-4$ and $i-3$. In (B) we see overshoot at cell $i-2$ and undershoot at $i+2$ after some step(s) of fluid propagation. In (C) there is no overshoot and undershoot because a limiter is applied. [Credit: Zingale (2013)].

These plots, in Figure 2.4, suggest that when dealing with discontinuities it is best to use limiting, since reducing the slope near the extrema and minimum is its main purpose (Zingale 2013). This is why limiting "kicks-in" near strong gradients (Zingale 2013), which is around where discontinuities form.

In PLUTO, the following limiters are available for LINEAR reconstruction, arranged from most diffusive to least diffusive: FLAT-LIM, MINMOD-LIM, VANALBADA-LIM, OSPRE-LIM, VANLEER-LIM, UMIST-LIM and MC-LIM (Vaidya et al. 2018), and some of these limiters are mentioned in LeVeque (2002) as popular choices of limiters, for example, the MINMOD-LIM.

MINMOD-LIM

In this work we use MINMOD-LIM, one of the most widely used owing to the fact that it is the least expensive limiter that can handle discontinuities well and although it is one of the most diffusive limiters, it is second-order accurate (LeVeque 2002; Zingale 2013; Vaidya et al. 2018). See Zingale (2013) for a detailed description of this limiter.

As an example of how this limiter works, briefly, we first construct the gradients in the interface states of a cell i with width Δx in 1D as shown in Figure 2.3 for a set of conservative variables represented by Equation 2.7 as

$$\left.\frac{\partial \mathbf{U}}{\partial x}\right|_i = \text{MINMOD}\left(\frac{\mathbf{U}_i - \mathbf{U}_{i-1}}{\Delta x}, \frac{\mathbf{U}_{i+1} - \mathbf{U}_i}{\Delta x}\right), \tag{2.13}$$

then we have

$$\text{MINMOD}(m_1, m_2) = \begin{cases} m_1 & \text{if } |m_1| < |m_2| \text{ and } m_1 \cdot m_2 > 0, \\ m_2 & \text{if } |m_2| < |m_1| \text{ and } m_1 \cdot m_2 > 0, \\ 0 & \text{otherwise.} \end{cases} \tag{2.14}$$

If the limiter is not used, the slope for cell i will just be given as

$$\left.\frac{\partial \mathbf{U}}{\partial x}\right|_i = \frac{\mathbf{U}_{i+1} - \mathbf{U}_{i-1}}{2\Delta x}, \tag{2.15}$$

so the solid-red-lines in Figure 2.3 are due to Equations 2.13 - 2.14, while the dotted-red-lines are due to Equation 2.15.

2.2.4 Riemann solver

In numerical methods, a Riemann solver is used to compute the flux at the cell interface, by using the left and right states of that interface computed by a reconstruction method (e.g., LINEAR as described above) (Mignone et al. 2007; Zingale 2013; Vaidya et al. 2018). In other words, in a Godunov-type method as shown in the flow diagram in Figure 2.2, the Riemann solver uses the output information from reconstruction which basically creates a Riemann problem, as inputs, to compute the flux of the interface (Zingale 2013) as shown in Figure 2.5. These fluxes are going to be used to update the solution using a time-stepping algorithm (Mignone et al. 2007; Zingale 2013), for example, see equations 2.9 - 2.12 and the update note in the flow diagram of Figure 2.2.

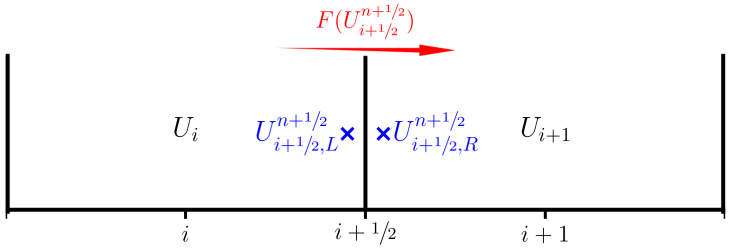

FIGURE 2.5: The Riemann solver uses the left and right interface states $U^{n+\frac{1}{2}}_{i+\frac{1}{2},L}$ and $U^{n+\frac{1}{2}}_{i+\frac{1}{2},R}$ which were found by the reconstruction method to find the interface flux $F(U^{n+\frac{1}{2}}_{i+\frac{1}{2}})$, for a finite volume update of the form $U^{n+1}_i = U^n_i + \frac{\Delta t}{\Delta x}\left(F^{n+\frac{1}{2}}_{i+\frac{1}{2}} - F^{n+\frac{1}{2}}_{i-\frac{1}{2}}\right)$. [Credit: Zingale (2013)].

A Riemann problem is the only non-linear fluid flow problem that is simple enough to allow for the solution to be determined at every cell edge for every time-step (Woodward and Colella 1984). The disadvantage is that a Riemann solver introduces complexity into the Godunov-type method and this complexity can decrease the efficiency of computation, (e.g., a first-order Godunov method requires twice the compute time per cell per time-step when a Riemann solver is used compared to when it is not used) (Woodward and Colella 1984). In addition, the complexity of the Riemann solver is applied in each and every cell of the computational domain, even though it is only needed near the discontinuities (Woodward and Colella 1984).

A Riemann solver is an important element for studying shock waves because one of its qualities is that it allows for narrow discontinuities without unphysical oscillations (Woodward and Colella 1984). The non-linear Riemann solver proposed by Godunov (1959), and further modified by Harten, Lax, and Leer (1983) Toro, Spruce, and Speares (1994) and others, gives the most accurate representation of shocks and their interaction (Woodward and Colella 1984). The PLUTO HD physics module has the following solvers which are arranged from most accurate (i.e., least diffusive) and least robust to least accurate (i.e., most diffusive) and most robust: TWO-SHOCK, ROE, AUSM+, HLLC, HLL, and TVDLF solver (Mignone et al. 2007; Vaidya et al. 2018). All of these available solvers in PLUTO were tested to determine which one gives the best solution for stellar wind models (see test results in Appendix B). The next subsection discusses briefly each of these different Riemann solvers (for a more detailed description of how each solver works, see Appendix A). Some Riemann solvers have a valuable advantage called the positively-preserving property (Miyoshi and Kusano 2005) also known as positively conservative (Batten et al. 1997), which means the solver can maintain the initial positive densities and pressure (Batten et al. 1997; Miyoshi and Kusano 2005).

Even though Riemann solvers yield sharp and monotonic profiles, they are subject to errors (Tóth and Odstrčil 1996). We can think of these errors as the instances where the Riemann solver gives results that are unreliable, these instances include: (1) expansion shocks (this is a non-physical solution which occurs when the entropy condition is not satisfied by the Riemann solver (Quirk 1994)); (2) negative internal energies (this happens when some Riemann solvers want the Riemann problem to be such that the dominant energy is kinetic rather than thermal (Quirk 1994)); (3) slowly moving shocks (which can result in slow convergence to steady state (Roberts 1990; Quirk 1994)); (4) the carbuncle phenomenon (this usually happens when the Riemann solver fails, resulting in a false solution whereby a bump grows ahead of the bow shock along the stagnation line (Quirk 1994)); and (5) kinked Mach stems (is when the Mach stem is inexplicitly kinked when dealing with the reflection of a plane shock wave (Quirk 1994)).

In the following subsections, we describe briefly the properties of the individual solvers, including advantages and disadvantages. In addition, the summary of individual test results which illustrate the performance of each solver is also discussed. How the individual solvers approach and solve the Riemann problem is shown and discussed in Appendix A.

TWO-SHOCK Riemann solver

The TWO-SHOCK solver is the most accurate Riemann solver available in PLUTO. It solves the Riemann problem almost exactly at every interface, and it is usually computationally intensive (Vaidya et al. 2018). This solver uses a two-shock approximation of the Riemann solver to solve the Riemann problem, and Godunov-type codes have largely used this approach (Rider 1999; Mignone, Plewa, and Bodo 2005).

ROE Riemann solver

The ROE solver solves the Riemann problem approximately by making use of the linearized Roe Riemann solver, which is based on the characteristic decomposition of the Roe matrix (Vaidya et al. 2018). This Roe Riemann solver uses a "Property U" matrix to retain features of the exact solution by not altering the interface states before solving the Riemann problem (Roe 1981). It was built to provide information needed for high accuracy, but it does not have a naturally constructed entropy condition, which is one of its theoretical disadvantages (Roe 1981; Quirk 1994). Another disadvantage is that any linearized approximate Riemann solver cannot guarantee a positivity-preserving conservative scheme (Batten et al. 1997; Miyoshi and Kusano 2005), because the linearization of the Riemann problems for Euler equations can sometimes result in negative densities (Miyoshi and Kusano 2005).

AUSM+ Riemann solver

The Advection Upstream Splitting Method Plus (AUSM+) solver (Foo et al. 1995) is a sequel and basically the improvement in accuracy, efficiency and robustness of the original AUSM solver which was first proposed by Liou and Steffen (1993). This solver is only available for PLUTO's HD physics module (which is the assumed physics of this work) (Vaidya et al. 2018), and it is as robust and accurate as the Roe Riemann solver (Liou and Steffen 1993). Without any difficulties (such as the lack of positivity conservative scheme (Batten et al. 1997) by other solvers), it gives the correct solutions for a broad range of flow conditions as well as a wide range of grids (Liou and Steffen 1993). Most importantly the AUSM+ solver is accurate, reliable and can capture stationary shocks (Foo et al. 1995). The improved properties of AUSM+ over the original AUMS are: (I) It can give exact resolution of one-dimensional discontinuities (Foo et al. 1995). (II) It maintains scalar quantities (e.g., density) using its positivity-preserving property (Foo et al. 1995). (III) It does not experience carbuncle phenomenon (Foo et al. 1995). (IV) There are no oscillations for shocks that are propagating at very low velocities (Foo et al. 1995). (IV) The algorithm is much simpler and can be easily extended to handle other hyperbolic systems (Foo et al. 1995).

HLL solver

Harten-Lax-van Leer (HLL) denotes a class of approximate Riemann solvers invented by Hartex, Lax and van Leer for solving the Euler equations of inviscid gas dynamics (Harten, Lax, and Leer 1983; Batten et al. 1997). HLL is a computationally efficient, easy to use solver in a Godunov-type code which does not require a full characteristic decomposition of the equations (Mignone and Bodo 2005), and it assures a positively conservative scheme (Miyoshi and Kusano 2005). The disadvantage of this solver is that it is dissipative and cannot resolve isolated discontinuities (Toro, Spruce, and Speares 1994; Mignone and Bodo 2005), because it uses only one

intermediate state to approximate the Riemann problem, which results in the solution having fewer details (Batten et al. 1997).

HLLC solver

Harten-Lax-van Leer Contact (HLLC) where C represents contact wave is also an approximate Riemann solver like the HLL, but with the ability to handle contact discontinuities better than the HLL solver (Mignone and Bodo 2005; Vaidya et al. 2018). HLLC was constructed by Toro, Spruce, and Speares (1994) improving the original HLL so that it is less dissipative, and it can resolve isolated discontinuities (Miyoshi and Kusano 2005). In addition, its solutions are comparable to the exact Riemann solver solutions (Batten et al. 1997) and like the HLL, the HLLC is also efficient (Miyoshi and Kusano 2005) and positively conservative (Batten et al. 1997; Toro, Spruce, and Speares 1994).

TVDLF solver

The Total Variation Diminishing Lax-Friedrichs (TVDLF) scheme is a solver that uses a simple Lax-Friedrichs scheme to compute the interface flux (Vaidya et al. 2018). TVDLF is the most dissipative solver available in PLUTO (Vaidya et al. 2018) and as a result, it yields solutions that are often smooth (Yee 1994; Tóth and Odstrčil 1996), which makes it poor in resolving discontinuities. TVDLF can be applied to any system of conservation laws because it does not need knowledge of the characteristic wave since it does not use a Riemann solver, this makes it relatively faster (computationally inexpensive) (Yee 1994; Tóth and Odstrčil 1996). In addition, TVDLF is robust, and its solutions are consistent with Riemann solver-type TVD schemes (Tóth and Odstrčil 1996). It may be limited to second-order accuracy and at this accuracy it uses a limiter and the Woodward limiter is preferred (Tóth and Odstrčil 1996), but for consistency in comparison for our simulations the MINMOD limiter will be used.

Summary of the solver test results

Each of the solvers were tested individually using simulations of a spherical stellar wind outflow of an AGB star, at a resolution of $128 \times 128 \times 128$ for a $40 \times 40 \times 40$ AU computational domain (see test results in Appendix B). The simulations were compared to the density, temperature and velocity of the analytical solution of an AGB star's wind from Gawryszczak, Mikołajewska, and Różyczka (2002). The tests were performed for each solver and for each of the coordinate systems, i.e., cartesian, spherical and polar-cylindrical coordinate systems.

Our test results suggest that all these solvers in cartesian and polar-cylindrical coordinates have approximately the same efficiency, but not in spherical coordinates where the ROE and the TVDLF solvers are the least and most efficient, respectively. The 2D density, temperature and velocity maps of the simulations looked the same regardless of the solver used, as such, we used 1D profiles to compare the models obtained using each solver to the analytic solution, and to other solvers.

The results of the 1D profiles showed that all the solvers agree well with the analytic solution at smaller distances and equally diverge from the analytic solution at larger distances. In addition, all these solvers seem to match the analytical solution

to the same degree, but overall, it was clear that the TVDLF solver is the best performing solver with better agreement for the density, temperature and velocity, and it is the most efficient with respect to the spherical coordinate system.

Another thing to note, is that the TWO-SHOCK solver seemed to be inapplicable for these stellar wind models in any coordinate system. It was always returning a negative density while converting between conservative and primitive variables at the beginning of every simulation. The ROE solver was inapplicable for the polar-cylindrical coordinate system because the time-step was too small. See Appendix B for more details about the solver test results.

2.2.5 Time-stepping method

Time-stepping methods are used to advect in time the solution obtained after solving the system of conservation laws (see update node in Figure 2.2). When using a grid code, these time-stepping methods update the solution in time from cell to cell based on the fluxes through the interface of the cells (Zingale 2013). The fluxes were determined by the Riemann solver by using the interface states which were determined by the reconstruction method; so time-stepping is the final step in the Gudunov method (Godunov 1959).

In PLUTO, the time-stepping methods used are explicit forward Euler because the next time solution depends on the previous time solution, which makes them conditionally stable (Vaidya et al. 2018). These methods from least accurate to more accurate, and from least expensive to more expensive are: (1) the EULER method, (2) the second-order Runge-Kutta (RK2) method, (3) the third-order (RK3) method, (4) the HANCOCK methods, (5) the CHARACTERISTIC-TRACING. These methods can be used in a dimensionally split or unsplit grid (Vaidya et al. 2018), however, in our simulations we use a dimensionally unsplit grid because according to Vaidya et al. (2018), it avoids errors that occur due to strong operator splitting (Strang 1968), which is used by the dimensional splitting schemes to solve equations that are in multi-dimensions by a sequence of one-dimensional problems.

It is much more accurate to use the dimensionally unsplit compared to the dimensionally split scheme (Zingale 2013; Vaidya et al. 2018), because in the unsplit scheme, the update is done simultaneously in all the directions, but there is a reduced range of stability (Gottlieb and Shu 1998; Zingale 2013).

Courant Friedrichs Lewy (CFL) condition

The CFL number is used to control the time-step length (Zingale 2013; Vaidya et al. 2018), and in every time-stepping method it must always be less than one, or even lower in higher dimensional systems and/or dimensionally unsplit systems for stability reasons (Beckers 1992; Vaidya et al. 2018), i.e., if the information propagates faster on the computational domain to an extent that it skips some grid elements, then the scheme becomes unstable (Zingale 2013). PLUTO uses an upwind method and in 1D or a dimensionally unsplit grid, the $CFL \leq 1$. This ensures no cells are skipped because with this condition the time-step will be less than the time taken by the information to travel across one cell (Zingale 2013). It is wise to always use $0 < CFL \leq \frac{1}{2}$ to guarantee stability what ever the restrictions (which may be related

to dimensions and/or time-stepping method), but yet this does not guarantee accuracy (Beckers 1992; Mignone et al. 2007; Zingale 2013; Vaidya et al. 2018).

In order to see how the CFL value works, let's again consider an 1D integration equation of the form:

$$\frac{\partial a}{\partial t} + u\frac{\partial a}{\partial x} = 0, \tag{2.16}$$

where $a(x,t)$ is some scalar quantity which is advected at a speed u, then the CFL value will be given as and be stable if (see Zingale (2013) for more details)

$$CFL = \frac{|u|\Delta t}{\Delta x} \leq 1. \tag{2.17}$$

Second-order Runge-Kutta (RK2) time-stepping

RK2 is used to evolve the solutions in all our models because unlike the other time-stepping methods it works in all coordinate systems; in all the different dimensions; in dimensional split or unsplit grids and works with all the different solvers (Vaidya et al. 2018). Like the EULER and RK3 methods, RK2 is a multi-step algorithm which is less diffusive than the EULER but slightly more diffusive than the RK3. Unlike the RK2, the HANCOCK and the CHARACTERISTIC-TRACING methods are single-step methods which involve the use of Taylor expansion and also require the primitive formulation of the equations (Vaidya et al. 2018). These two methods are stable under CFL condition ≤ 0.5 and are more computationally expensive than the RK2 and less diffusive because they are not multi-step algorithms (Vaidya et al. 2018).

RK2 estimates the slopes based on extrapolations of both the midpoint and endpoint of the interval, and it uses the weighted mean of the slopes to evolve the solution (Zingale 2013). RK2's accuracy depends mostly on the time-step choice, the smaller the step-size the better the accuracy (Zingale 2013, and reference therein). The same reconstruction of the interface states and solving of the Riemann problem happens at every stage of this RK2 integrator (Zingale 2013). The time-step is more restrictive when using Runge-Kutta for the time-discretization of a multidimensional system which requires $0 < CFL \leq 1/N_{\rm dim}$, where $N_{\rm dim}$ is the number of dimensions in an unsplit grid (Titarev and Toro 2004; Zingale 2013; Vaidya et al. 2018).

To see how PLUTO uses the RK2 time-stepping method, let's consider a set of conservation laws as shown in Equation 2.6 and rearrange it so that we have :

$$\frac{\partial \mathbf{U}}{\partial t} = -\nabla \cdot \mathbf{F}(\mathbf{U}) + \mathbf{S}(\mathbf{U}), \tag{2.18}$$

If $\Delta t^n = t^{n+1} - t^n$ is the time between consecutive steps and if $\mathcal{L}$ represents the right-hand side's spatial operator (see Mignone et al. (2007) and Vaidya et al. (2018) for more details), then using RK2 we can advance Equation 2.18 from $\mathbf{U}^n$ to $\mathbf{U}^{n+1}$ as follows:

$$\mathbf{U}^* = \mathbf{U}^n + \Delta t^n \mathcal{L}^n, \tag{2.19}$$

$$\mathbf{U}^{n+1} = \frac{1}{2}\Big[\mathbf{U}^n + \mathbf{U}^* + \Delta t^n \mathcal{L}^*\Big]. \tag{2.20}$$

2.3 Additional physics

In PLUTO, additional physics such as radiative cooling and thermal conduction can be included to the set of conservation laws represented by Equation 2.6 via the source term $\mathbf{S}(\mathbf{U})$ in the energy Equation 2.3. If we let $\Psi(\Lambda, \Gamma)$ represent the radiative transfer and $\mathbf{F_c}$ represent the classical thermal conduction flux (Cowie and McKee 1977; Balsara, Tilley, and Howk 2008; Vaidya et al. 2017), then we can write the energy Equation 2.3 as

$$\frac{\partial(\rho E)}{\partial t} + \nabla \cdot (\rho E \mathbf{v}) + \nabla \cdot (P\mathbf{v}) = \Psi(\Lambda, \Gamma) + \nabla \cdot \mathbf{F_c}\,, \tag{2.21}$$

such that

$$\Psi(\Lambda, \Gamma) = \Gamma(T, n_{\rm H}) - \Lambda(T, n_{\rm H}), \tag{2.22}$$

$$\mathbf{F_c} = \kappa \nabla T, \tag{2.23}$$

where T is the temperature, $n_{\rm H}$ is the number density, Λ is the cooling rate, Γ is the heating rate and κ is the thermal conduction coefficient. If $\Psi(\Lambda, \Gamma) < 0$, cooling dominates and if $\Psi(\Lambda, \Gamma) > 0$, heating dominates.

2.3.1 Radiative cooling and heating

Radiative transfer is an important process when modelling bow shocks; it determines the heating and cooling of the materials that make-up bow shocks, in other words, it determines the material temperatures and the emission of the bow shock. This means radiative transfer plays a major role in determining the morphology of the bow shocks as well as the emission properties such as observable wavelengths, because the emitted photons are linked to the composition and physical properties of the sources (Ploeckinger and Schaye 2020). In addition, radiative transfer in any system, including bow shocks, can only be described using properties of matter at an atomic and molecular level (Wiersma, Schaye, and Smith 2009; Ploeckinger and Schaye 2020).

We implement radiative transfer that is associated with atomic cooling; molecular vibrational, collisional and rotational cooling; bremsstrahlung cooling; cosmic ray heating; compton cooling/heating; dust grain cooling/heating and radiation heating from the HVR star. We modify the radiative cooling and heating tables from Ploeckinger and Schaye (2020), such that important processes applicable to the bow shocks of cool and hot stars are as mentioned in Table 2.1, i.e., Collisional Ionization Equilibrium (CIE) processes and photoionization processes, respectively. The latter processes are used to construct the radiative cooling curves as shown in Figure 2.6 for CIE (top) and photoionization (bottom). In addition, heating is the major difference between the photoionization and CIE curves, since at lower temperatures ($T \lesssim 10^4$ K), heating in cool stars is dominated by dust grains and in hot stars is dominated by photoionizing radiation of a typical O-type star, then for cool stars, additional heating due to dust is added by using equation C15 and C5 of Wolfire et al. (2003) along with parameters from Table 2 of Wolfire et al. (2003) for $R = R_0 = 8.5\,$Kpc (distance corresponding to the position of the Sun in our Galaxy), such that equation C15 and C5, respectively reduces to

$$\Gamma_{\rm dust} = \frac{1.1\times10^{-25} n_{\rm H}}{1+3.2\times10^{-2}\Big((T/100\,{\rm K})^{1/2}/n_{\rm e}\times0.5\Big)^{0.73}} \ \ [{\rm erg\ cm^{-3}s^{-1}}], \tag{2.24}$$

and

$$n_{\rm e} = 6.8\times10^{-3}(T/100\,{\rm K})^{1/4} \ \ [{\rm cm^{-3}}]. \tag{2.25}$$

For hot stars, additional heating due to photoionization of pure H is added using equation (2.2) of Osterbrock (1989) as

$$\Gamma_{\rm O-type\,star} = n_{\rm e} n_{\rm p} \alpha_{\rm B} \frac{3}{2} kT_{\rm eff} \ \ [{\rm erg\ cm^{-3}s^{-1}}], \tag{2.26}$$

where $n_{\rm e} = n_{\rm p} = n_{\rm H} = 1\ {\rm cm^{-3}}$, k is the Boltzmann constant, $T_{\rm eff}$ is the effective temperature, $\alpha_{\rm B}$ is the coefficient from Table 1 of Hummer (1994), and the mean energy due to a typical O-type star is $\left\langle \frac{3}{2}kT_{\rm eff} \right\rangle \approx 5$ eV (Meyer et al. 2014; Green et al. 2019).

Cool stars have low temperature and high density dusty winds, that are composed of molecules such as CO whose density can be thought of as being proportional to the density of the wind (Lamers and Cassinelli 1999). The collisions of CO with H_2 causes collisional excitation of the rotational levels of CO, and absorption of lower wavelength photons causes photo-excitation of the vibrational levels of CO. These are some of the collisional, rotational and vibrational processes included in our CIE cooling curve (Lamers and Cassinelli 1999). Hot stars have high temperature and low density winds, and most of the atoms in the atmosphere of their winds are ionized, and the temperatures are so high that molecules hardly form, so that in this case photoionization dominates over CIE (Lamers and Cassinelli 1999). Hot stars radiate high energy photons, which are absorbed by most atoms and electrons in their atmospheres, as a result the outer atmospheres of these hot stars have a lot of absorption lines (Sutherland and Dopita 1993; Lamers and Cassinelli 1999).

TABLE 2.1: Cooling and heating processes for Collisional Ionization Equilibrium (CIE) and Photoionization.

Label	**CIE Processes**
$(\Lambda;\Gamma)_{\rm atomic}$	Cooling and heating due to elements: H, He, C, N, O, Ne, Mg, Si, S, Ca and Fe
$(\Lambda;\Gamma)_{\rm other\ processes}$	Cooling and heating from collisions H_2, Cooling from the rotations of the hydrogen isotope Deuterium, Cooling from other molecules except for H_2 and HD, Heating due to the dissociation of CO molecule, Cosmic ray heating, Cooling due to bremsstrahlung.
$\Gamma_{\rm dust}$	Heating due to dust grains
Label	**Photoionization Process**
$(\Lambda;\Gamma)_{\rm atomic}$	Cooling and heating due to elements: H, He, C, N, O, Ne, Mg, Si, S, Ca and Fe
$(\Lambda;\Gamma)_{\rm other\ processes}$	Cooling due to bremsstrahlung, Cooling and heating due to the compton effects.
$\Gamma_{\rm O-type\,star}$	Heating due to photoionizing radiation from an O-type star

Note: This table was constructed using Ploeckinger and Schaye (2020).

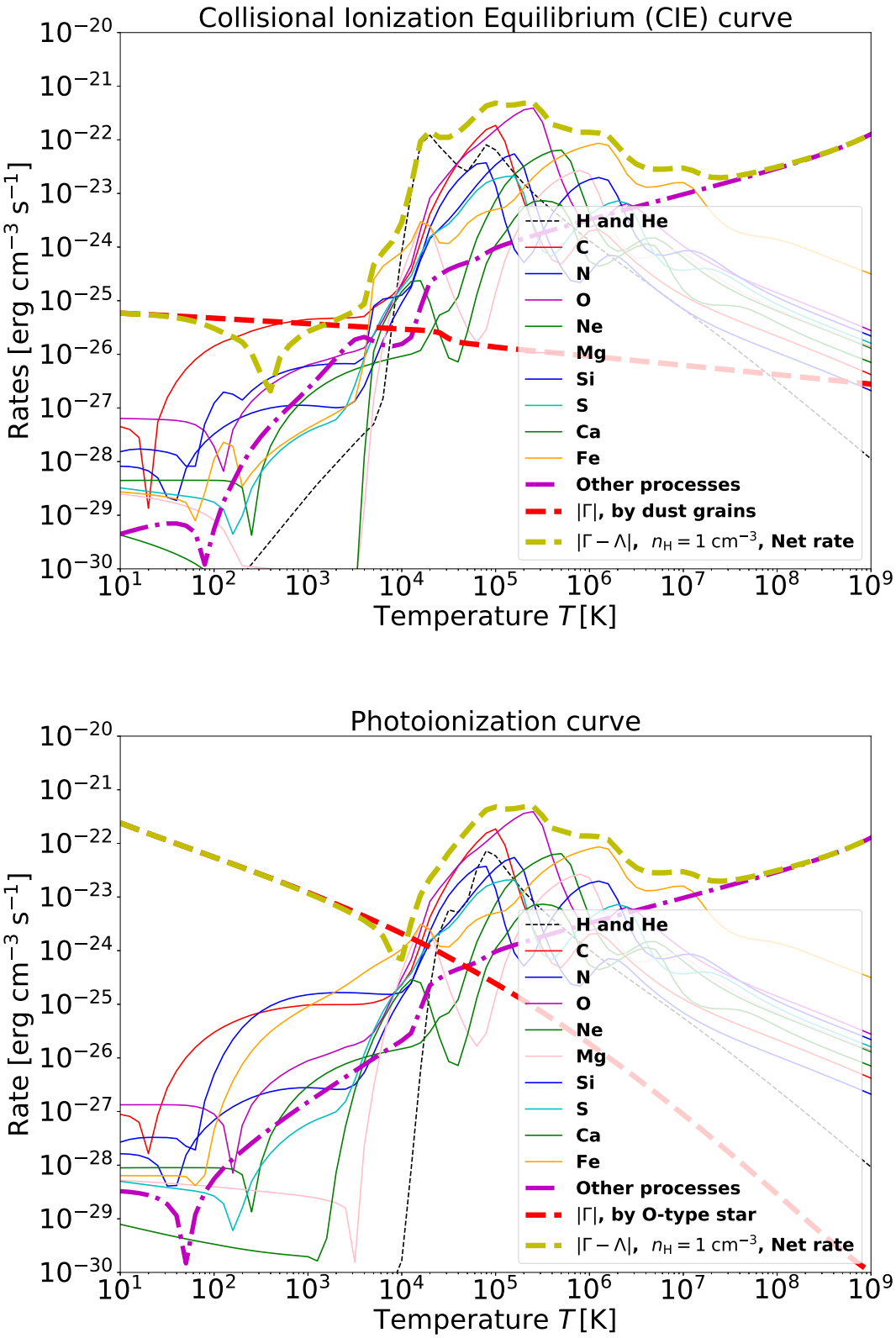

FIGURE 2.6: Radiative cooling and heating rates that were included in our models. The solid curves show the contribution from heavy atoms, while the black dashed curve is the contribution from hydrogen and helium. The purple dashed-dotted curve is the contribution from molecular rotation, vibration and collision, in addition to processes associated with cosmic rays, bremsstrahlung and compton effect. The yellow dashed curve is the continuous net rate. [Top] Collisional Ionization Equilibrium (CIE) curve, where heating (red dashed curve) is mostly due to dust grains. [Bottom] Photoionization curve, where heating (red dashed curve) is mostly due to a typical O-type star.

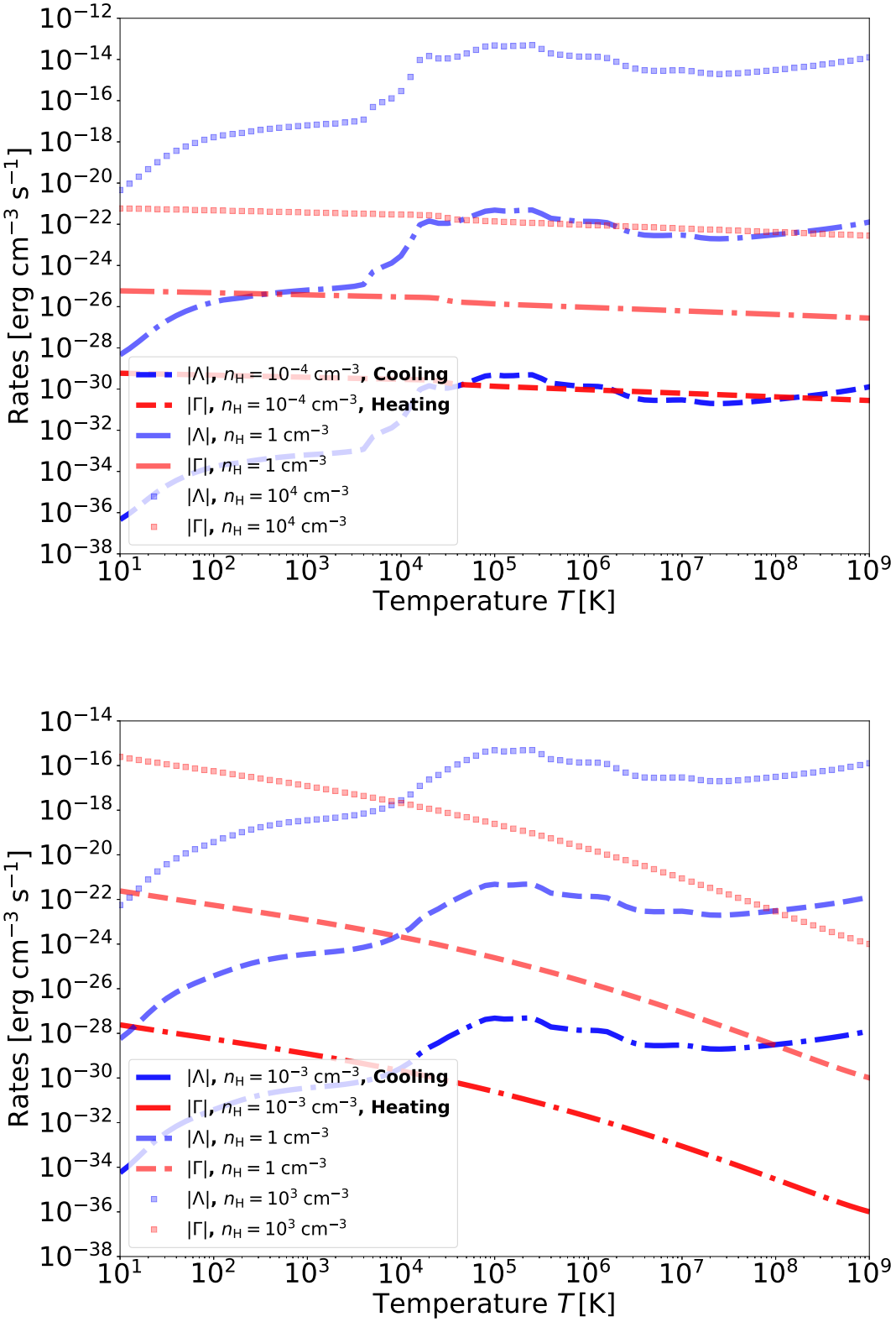

FIGURE 2.7: The corresponding separated cooling (blue) and heating (red) of the net rate curve in Figure 2.6 with respect to number densities (n_H), for both CIE (top) and photoionization (bottom)

.

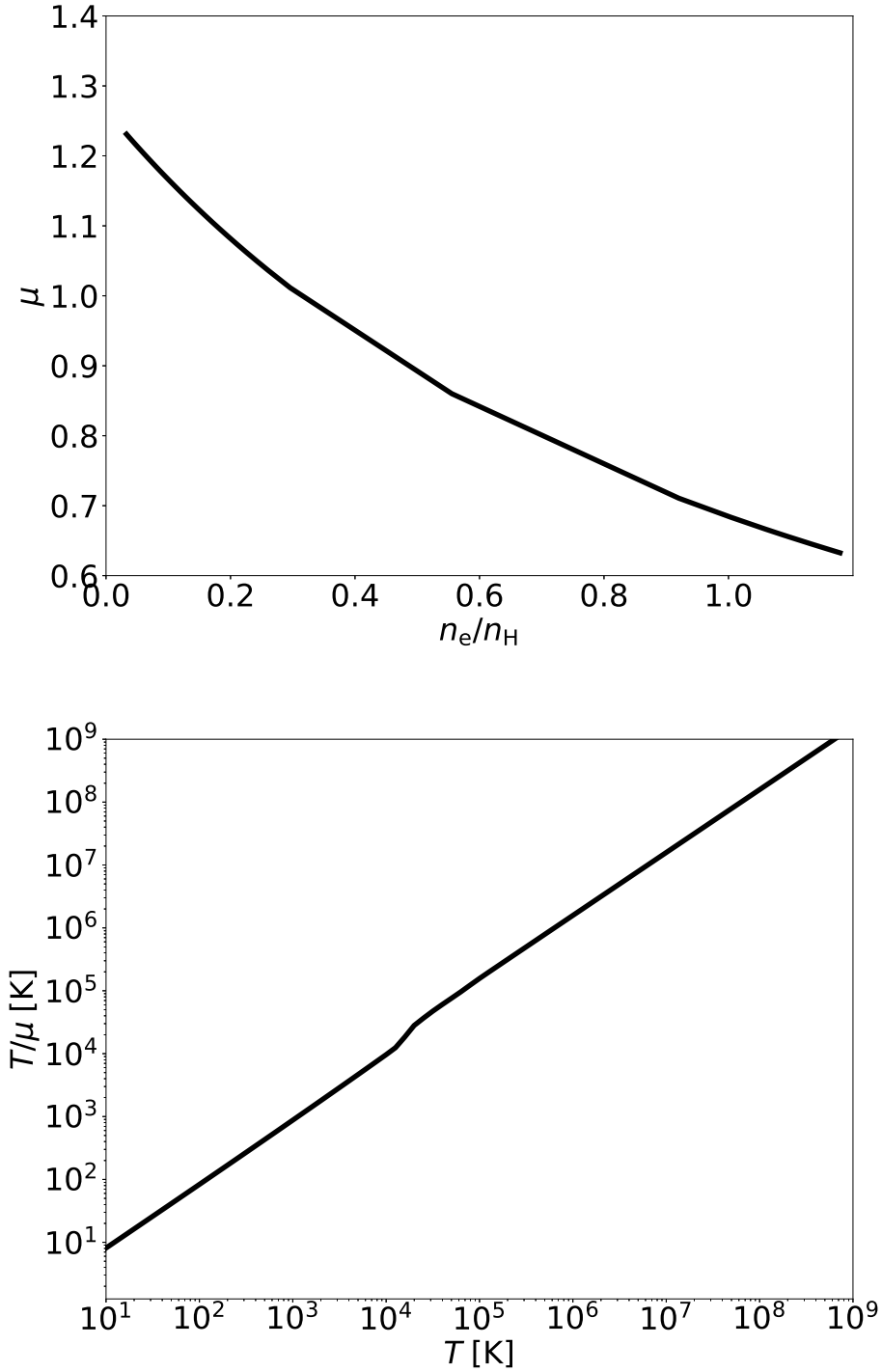

FIGURE 2.8: [Top] Mean molecular weight, μ, as a function of electron fraction, n_e/n_H. [Bottom] The temperature divided by the mean molecular weight as a function of temperature.

2.3.2 Thermal conduction

We use PLUTO's built-in Runge-Kutta Legendre method presented by Vaidya et al. (2017) to compute the thermal conduction throughout the computational domain. It is included only for models of hot stars, because bow shocks around hot stars have a sufficiently large temperature gradient in the reverse shock (see Figure 1.6). This large temperature difference between adjacent fluids drives the heat flux, because

electrons move fast enough to transport energy from the hot medium to the nearby cooler medium (Cowie and McKee 1977; Meyer et al. 2014, and references therein).

The thermal conduction term is determined by finding the solution of (Vaidya et al. 2017)

$$\frac{\partial(\rho E)}{\partial t} = \nabla \cdot \mathbf{F_c}. \tag{2.27}$$

The term $\nabla \cdot \mathbf{F_c}$ is discretised using standard second-order finite difference (Vaidya et al. 2017). For example, for cell i in a 1D grid as shown in Figure 2.1 we have

$$\frac{\partial}{\partial x}\mathbf{F_c}\Big|_i = \frac{(\mathbf{F_c})_{i+\frac{1}{2}} - (\mathbf{F_c})_{i-\frac{1}{2}}}{\Delta x}. \tag{2.28}$$

From Equation 2.28 we have,

$$\frac{\partial}{\partial x}\mathbf{F_c}\Big|_i = \frac{(\kappa\nabla\mathbf{T})_{i+\frac{1}{2}} - (\kappa\nabla\mathbf{T})_{i-\frac{1}{2}}}{\Delta x}, \tag{2.29}$$

since we are now focusing on a 1D grid, then

$$\frac{\partial}{\partial x}\mathbf{F_c}\Big|_i = \frac{\kappa\frac{\partial\mathbf{T}}{\partial\mathbf{x}}\big|_{i+\frac{1}{2}} - \kappa\frac{\partial\mathbf{T}}{\partial\mathbf{x}}\big|_{i-\frac{1}{2}}}{\Delta x}. \tag{2.30}$$

The temperature of the interface is determined from the adjacent cells across the interface as (Mignone et al. 2012)

$$\frac{\partial T}{\partial x}\Big|_{i+\frac{1}{2}} = \frac{T_{i+1} - T_i}{\Delta x}, \tag{2.31}$$

and

$$\frac{\partial T}{\partial x}\Big|_{i-\frac{1}{2}} = \frac{T_i - T_{i-1}}{\Delta x}, \tag{2.32}$$

thus Equation 2.28 becomes

$$\frac{\partial}{\partial x}\mathbf{F_c}\Big|_i = \frac{\kappa\left(\frac{T_{i+1}-T_i}{\Delta x} - \frac{T_i-T_{i-1}}{\Delta x}\right)}{\Delta x}. \tag{2.33}$$

This is an example of how thermal conduction is calculation in a 1D grid. A generalised version is used in our multi-dimensional models.

Chapter 3

Stellar wind and interstellar medium parameters

In this chapter, we describe the initial conditions of the stellar wind and ISM used to investigate the different bow shock models around HVR stars. In future, models will be coupled to a stellar evolution code to get evolving wind parameters, however in this work the stellar wind parameters are fixed, and we consider two cases: stars in the MS and RSG phase. Similarly, while we plan to consider stars moving in a non-homogenous medium (with clumps, gradients, and other structures), in this work we assume the ISM is homogenous and the four different phases, hot ionized medium (HIM), H II region (HII), warm neutral medium (WNM), and cold neutral medium (CNM) are described below. In addition, consideration of the effect of magnetic fields is also planned for future work.

3.1 Wind model

TABLE 3.1: Stellar wind parameters adopted in our models.

Evolutionary phase	$\dot{M}_{\rm w}$ [$M_\odot$/yr]	$v_{\rm w}$ [km/s]	$T_{\rm w}$ [K]
Main-Sequence (MS)	10^{-9} [1]	1000 [1,2]	2.5×10^4 [1,2]
Red-supergiant (RSG)	10^{-6} [1,2]	50 [1,2,3]	2.5×10^3 [1,2]

References: [1] Lamers and Cassinelli (1999). [2] Osterbrock (1989). [3] Bennett (2010).

Stellar wind parameters are very uncertain (Lamers and Cassinelli 1999; Vidotto and Cleary 2020). We consider stars with mass in the range $8\,M_\odot \lesssim M \lesssim 25\,M_\odot$, that is the star is assumed to be massive but not massive enough to become a Wolf-Rayet star; in other words MS stars that can evolve to become RSGs, where the wind mass-loss timescale is greater than the nuclear timescale (Maeder and Meynet 1987; Davies and Beasor 2018). (Note, this is in the non-interacting/single, non-rotating, non-magnetic, solar metallicity stellar evolution scenarios). For hot massive stars that will evolve to the RSG phase, the mass-loss rate of the MS star is typically $10^{-9}\,M_\odot/\mathrm{yr} \lesssim \dot{M}_{\rm w} \lesssim 10^{-7}\,M_\odot/\mathrm{yr}$ (Lamers and Cassinelli 1999), and for the RSG phase it is higher and in the range, $10^{-7}\,M_\odot/\mathrm{yr} \lesssim \dot{M}_{\rm w} \lesssim 10^{-5}\,M_\odot/\mathrm{yr}$ (Osterbrock 1989; Lamers and Cassinelli 1999). The value of the mass-loss rates used at the inner boundary for the wind models in this work are given in Table 3.1.

Even though the mass-loss rates can at some point be the same for MS and RSG

stars, because it also depends on the mass of the star and its luminosity (Osterbrock 1989), the terminal velocity of the winds of hot and cool stars are very different: 1000 km/s $\lesssim v_\infty \lesssim$ 3000 km/s for hot stars (Osterbrock 1989; Lamers and Cassinelli 1999), and 20 km/s $\lesssim v_\infty \lesssim$ 50 km/s for cool stars (Osterbrock 1989; Lamers and Cassinelli 1999; Bennett 2010). The velocity for the RSG wind is chosen to be 50 km/s because this allows for larger bow shocks which are easier to model at lower resolutions (the stand-off distance is greater than the internal stellar wind in-flow boundary). The mass-loss rate and wind velocity selected for the MS phase, results in bow shock radii at the lower end of the possibilities. In addition, the outflow temperatures of hot OB-type stars are 2×10^4 K $\lesssim T_\mathrm{w} \lesssim 3 \times 10^4$ K and 1000 K $\lesssim T_\mathrm{w} \lesssim$ 3000 K for KM-type stars (Osterbrock 1989; Lamers and Cassinelli 1999). As shown in Table 3.1, the selected values are typical for MS and RSG stars and differ by an order of magnitude.

3.2 ISM model

TABLE 3.2: ISM parameters adopted in our models.

ISM phase	T [K]	n_H [cm^{-3}]
Hot ionized medium (HIM)	10^6 [1,2,3,4,5]	0.005 [1,2,4,5]
H II region (HII)	10^4 [1]	0.3 [1]
Warm neutral medium (WNM)	5×10^3 [1,6]	0.6 [1,6]
Cold neutral medium (CNM)	10^2 [1,6]	30.0 [1,6]

References: [1] Draine (2011). [2] McKee (1995). [3] Spitzer (1990). [4] Ferriere (2001) and references therein. [5] Klessen and Glover (2016) and references therein. [6] Wolfire et al. (1995).

The ISM is the material found between stars (Draine 2011), it has different phases depending on its temperature and density (e.g., see Table 3.2). The density of the ISM plays a crucial role in the formation of bow shocks, because it determines the ram pressure of the ISM which affects the R_SOD as shown in Equation 1.7. According to Draine (2011), the ISM phases from lower to higher densities are the HIM, HII region, WNM, CNM and the molecular gas (H_2). The latter is not included in this work because it has very high densities 100 cm$^{-3} \lesssim n_\mathrm{H} \lesssim 10^6$ cm^{-3} which will result in very small R_SOD values which will be smaller than the internal stellar wind in-flow boundary in our model setup.

As discussed in Chapter 1, The HIM is typically produced by blastwaves such as those from supernova explosions. It has temperatures $T \gtrsim 10^{5.5}$ K due to heating by shock waves, and any ISM with temperature greater than this is referred to as hot and also ionized, provided the density is very low about ~ 0.005 cm^{-3} (Spitzer 1990; McKee 1995; Ferriere 2001; Draine 2011; Klessen and Glover 2016). HII regions are typically found around hot stars which emit high energy photons > 13.6 eV which ionize the hydrogen in their surrounding medium, thus heating the gas to temperatures $\sim 10^4$ K, and it has densities in the range 0.3 cm$^{-3} \lesssim n_\mathrm{H} \lesssim 10^4$ cm^{-3} (Draine 2011). The WNM is composed of neutral gas with temperatures in the range 5500 K $\lesssim T \lesssim$ 8700 K and densities in the range 0.1 cm$^{-3} \lesssim n_\mathrm{H} \lesssim 0.59$ cm^{-3} according to the standard models of Wolfire et al. (1995), this ISM phase is heated by photoelectrons from dust and cosmic rays (Field, Goldsmith, and Habing 1969;

Wolfire et al. 1995; Draine 2011; Klessen and Glover 2016). The CNM is also composed of neutral gas. It is also heated by photoelectrons from dust and cosmic rays, and its parameters are also in the range 41 K $\lesssim T \lesssim$ 210 K for temperature and 4.2 cm^{-3} $\lesssim n_{\mathrm{H}} \lesssim$ 80 cm^{-3} for density (Wolfire et al. 1995). The WNM and CNM usually form a two-phase medium which is in pressure equilibrium and they are typically found in cool clouds (Field, Goldsmith, and Habing 1969, and references therein).

The various temperatures and densities selected for the different ISM phases as shown in Table 3.2 are in the respective ranges as discussed in the paragraph above. These temperature and density values will be used as initial conditions for the models with different ISM phases to explore the impact of the ISM on the physical properties of bow shocks, for example, the effect of ISM phase on the morphology, evolution, size of the bow shock, the type of instabilities formed, and the time taken to reach a steady state.

Chapter 4

Runaway stars: Comparison with analytic and literature studies

Given the setup and additional modifications we have made to the PLUTO code, it is important to verify that the code behaves as expected through comparison with exact analytic values where possible, or with similar calculations in the literature. Some models from the literature use different types of numerical codes, e.g., Gadget SPH (Mohamed, Mackey, and Langer 2012), MPI-AMRVAC (van Marle, Decin, and Meliani 2014), PLUTO (Meyer et al. 2014), ENZO (Li, Bryan, and Quataert 2019) and PION (Green et al. 2019). In this work, in addition to testing adiabatic models with respect to the Wilkin (1996) solution for the size and shape of the bow shock, we also compare models including thermal conduction and radiative cooling against similar runs in Meyer et al. (2014) where the PLUTO code was also used.

4.1 The effect of cooling, thermal conduction and stellar evolutionary phase on the bow shock structure

To investigate the effect of stellar evolutionary phase, cooling and thermal conduction, we ran MS and RSG runaway models with parameters and model setup similar to that of Meyer et al. (2014) as shown in Table 4.1. The setup involves using 2D axis-symmetric cylindrical coordinates, the internal boundary with a radius of 20 cells, and the HLL solver. The models from Meyer et al. (2014) that we intend to compare with are those with space velocity, $v_* = 40$ km/s for a 10 $M_\odot$ MS star, and $v_* = 40$ km/s and $v_* = 70$ km/s for a RSG star; and the temperature of the wind is $T_w = 2.52 \times 10^4$ K for the MS and $T_w = 2.5 \times 10^3$ K for the RSG. Note that it was not clear from the Meyer et al. (2014) paper which wind parameters were used since they only state the approximate values using figures, (e.g., see Figure 3 of Meyer et al. (2014)). The ISM is assumed to be WNM with density, $n_H = 0.57$ cm^{-3} and temperature $T = 8000$ K for the MS case, and $T = 3300$ K for RSG case.

For the analysis, we used the density jumps at the reverse shocks (which separates the freely expanding wind and the shocked wind, see Figure 1.6) for which we know that from the Rankine–Hugoniot jump condition, the jump factor of ~ 4 is expected for the adiabatic case. We also use $R(0^o)/R(90^o)$ (where $R(0^o)$ is the distance between the star and the contact discontinuity parallel to the direction of motion (i.e., along the apex), while $R(90^o)$ is similar to $R(0^o)$ but perpendicular to the direction of motion, (see Equation 1.8)). The results for the different models are shown in Table 4.2 and Figures 4.1 - 4.6, and the comparison of the cooling curve used in this work to that of Meyer et al. (2014) in Figure 4.7.

TABLE 4.1: Setup parameters for the MS and RSG runaway test models

EV phase	Model name	Condition	v_* [km/s]	$N_{\rm zones}$	x-axis [pc]	y-axis [pc]
MS	MS_40A	A	40	700×700	$0 \leq x \leq 0.4$	$-0.2 \leq y \leq 0.2$
	MS_40C	C	40	700×700	$0 \leq x \leq 0.4$	$-0.2 \leq y \leq 0.2$
	MS_40T	TC	40	700×700	$0 \leq x \leq 0.4$	$-0.2 \leq y \leq 0.2$
	MS_40CT	C and TC	40	700×700	$0 \leq x \leq 0.4$	$-0.2 \leq y \leq 0.2$
RSG	RSG_40C	C	40	600×600	$0 \leq x \leq 1.4$	$-0.7 \leq y \leq 0.7$
	RSG_70C	C	70	600×600	$0 \leq x \leq 1.4$	$-0.7 \leq y \leq 0.7$

Note: The model setup is similar to Meyer et al. (2014), except for RSG_70C, which is similar to RSG_40C but at 70 km/s in our case. Here EV=evolutionary, A=Adiabatic, C=Cooling, TC=Thermal Conduction, $N_{\rm zones}$ is the resolution in terms of the number of grid zones.

TABLE 4.2: Bow shock properties for MS and RSG runaways

Model name	Density jump factor at the reverse shock	$R(0^o)/R(90^o)$		
		Model value	Wilkin (1996) solution	% Error
MS_40A	3.9	0.612	0.577	5.9
MS_40C	4.1	0.589	0.577	2.1
MS_40T	7.0	0.603	0.577	4.9
MS_40CT	12.3	0.601	0.577	4.1
RSG_40C	3.6	0.509	0.577	11.9
RSG_70C	2.9	0.539	0.577	6.7

The percentage error (% Error) is given by $\left|\frac{Mv-Ws}{Ws}\right| \times 100\%$, where Ws is the Wilkin (1996) analytic solution of $R(0^o)/R(90^o)$ and Mv is the model value.

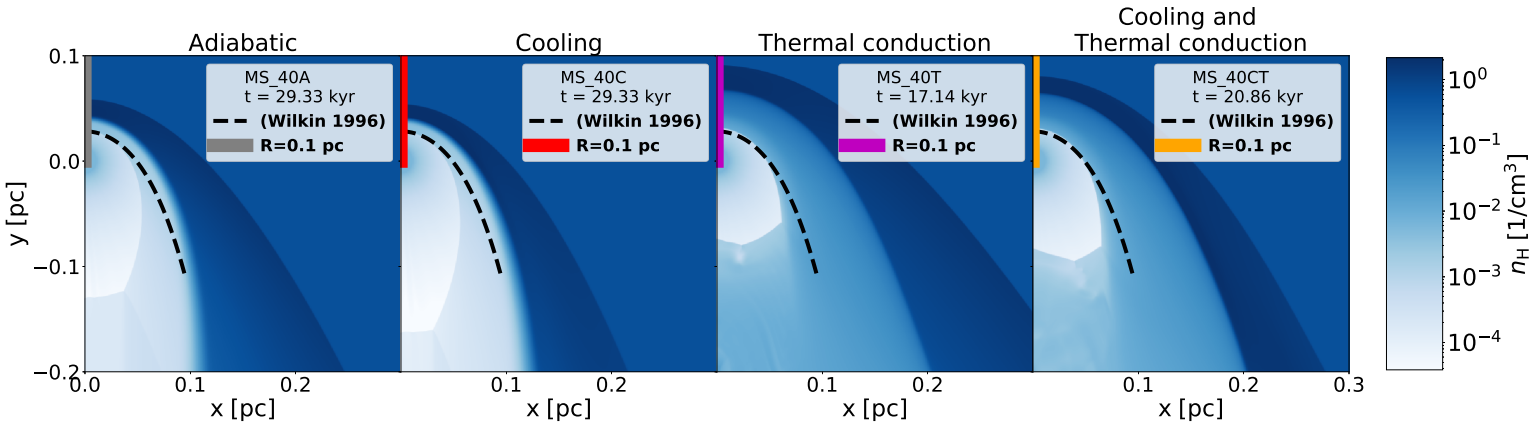

FIGURE 4.1: Density plots for the bow shocks produced by a 10 $M_\odot$ MS star moving at 40 km/s with respect to the ISM of density, $n_{\rm H} = 0.57$ cm^{-3} and temperature, $T = 8000$ K. The stellar wind has $v_{\rm w} = 1000$ km/s, $\dot{M}_{\rm w} = 2.43 \times 10^{-10}$ $M_\odot$/yr and $T_{\rm w} = 2.52 \times 10^4$ K. The first, second, third and fourth column correspond to the models obtained with adiabatic, cooling, thermal conduction, and cooling and thermal conduction conditions, respectively (see Table 4.1). The black-curve corresponds to the Wilkin (1996) analytic solution, while the vertical lines with length R = 0.1 pc are regions of cuts made to generate the Figure 4.2 profiles.

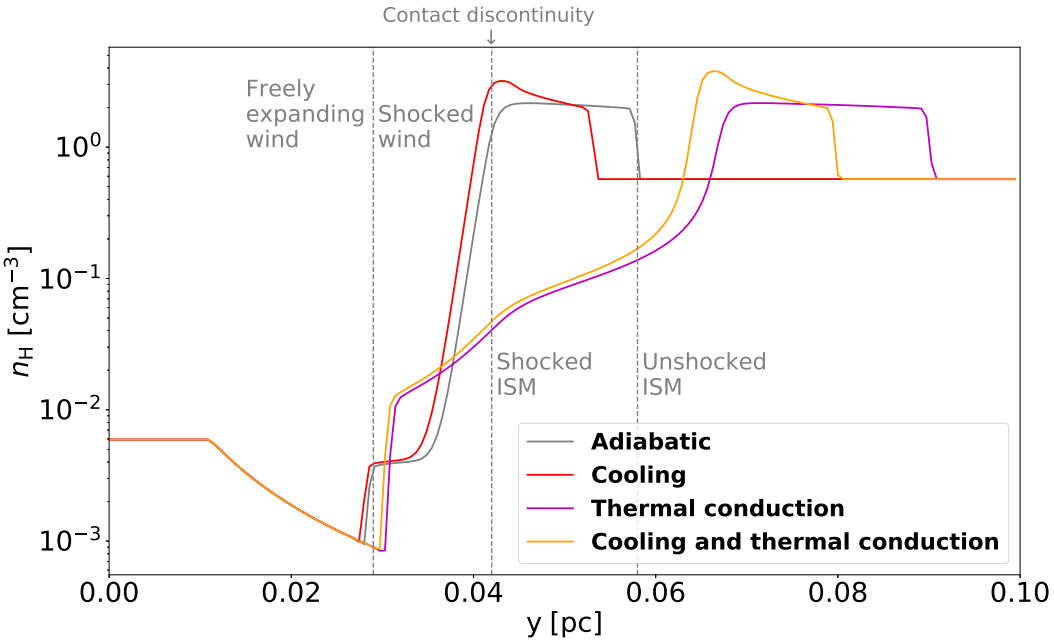

FIGURE 4.2: Density profiles taken along the y-axis from 0 to 0.1 pc of the MS models shown in Figure 4.1, where each color correspond to each cut in the 2D map. The grey vertical lines separating different regions of the bow shock corresponding to the adiabatic model.

For the MS models, Figure 4.1 shows the effect of cooling, thermal conduction and combination of both on the structure of the bow shock, and the comparison with the Wilkin (1996) analytic solution. The $R(0^o)/R(90^o)$ values in Table 4.2, suggest that the bow shock with cooling agrees more with the analytic solution with only a small percentage error of 2.1 % compared to other models which have higher percentage errors. The model MS_40C in Figure 4.1 is a factor of $\sim$ 1.1 smaller than the model MS_40A, because cooling decreases the temperature, which decreases the pressure of the wind, which then results in the decrease in the R_{SOD} and as a result the bow shock size is reduced. Model MS_40T in Figure 4.1 is larger by a factor of $\sim$ 1.6 than the adiabatic model MS_40A, because thermal conduction will enable the flow of electrons since the reverse shock of the bow shock of a hot MS star has a large temperature gradient $\Delta T \sim 10^7$ K, the electrons will have higher kinetic energy, and they will move fast enough to transfer energy from hotter to cooler regions of the bow shock, thus increasing the size of the bow shock (Meyer et al. 2014, and references therein). In Figure 4.1, model MS_40CT is larger than model MS_40A by a factor of $\sim$ 1.4 and MS_40C by a factor of $\sim$ 1.7, because thermal conduction was enabled, but it is smaller than model MS_40T by a factor of $\sim$ 1.1 because cooling was also included.

Table 4.2 also shows the density jump factor at the reverse shock (between the free expanding wind and the shocked wind of models as shown in Figure 4.2) along the apex of the bow shock for each model in Figure 4.1. From the Rankine-Hugoniot jump conditions, we expect a density jump factor of $\sim$ 4 for non-radiative shocks, which fits in well with the adiabatic model MS_40A, which differs only by $\sim$ 2%.

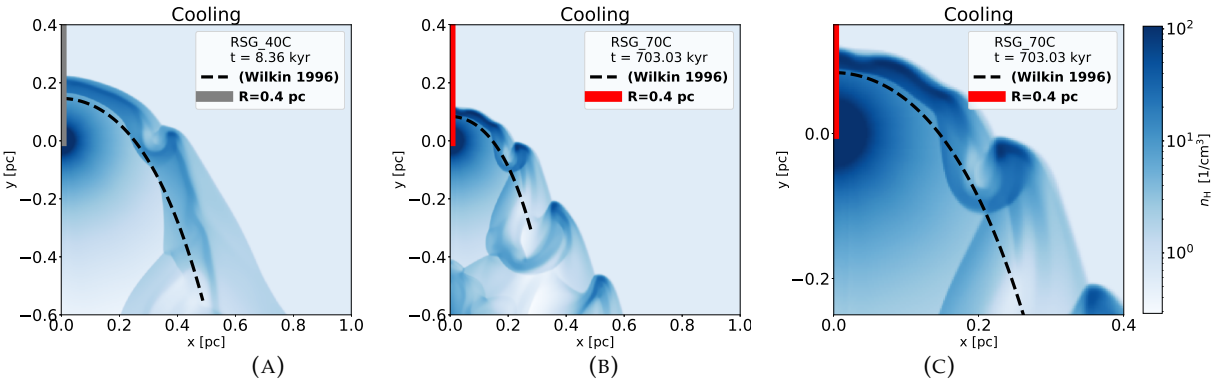

FIGURE 4.3: Density plots for the bow shocks produced by a 10 $M_\odot$ RSG star moving at 40 km/s (left) and 70 km/s (middle and right) with respect to the ISM of density, $n_H = 0.57$ cm^{-3} and temperature, $T = 3300$ K. The stellar wind has $v_{wind} = 10$ km/s, $\dot{M}_w = 7.02\times10^{-7}$ $M_\odot$/yr and $T_w = 2.5\times10^3$ K. The black-curve corresponds to the Wilkin (1996) analytic solution. Both plot (A) and (B) are obtained with radiative cooling included (see Table 4.1). Plot (C) is a zoomed-in view of plot (B).

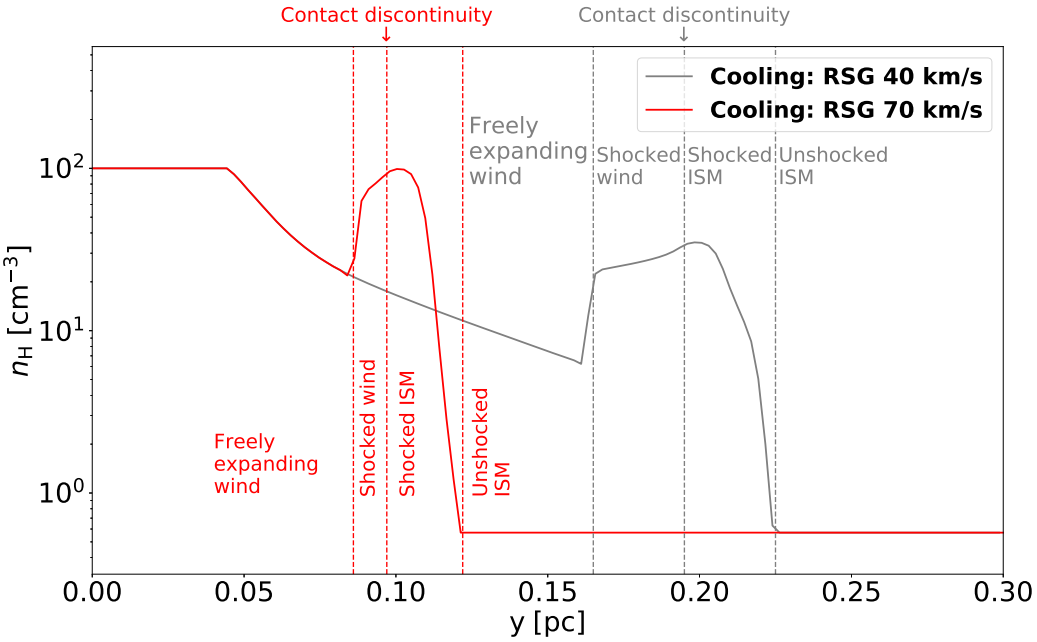

FIGURE 4.4: Density profiles taken along the y-axis from 0 to 0.3 pc for models RSG_40C (grey curve) and RSG_70C (red curve) of Figure 4.3. The vertical dashed lines separate different regions of the bow shock, where the color correspond to the color of the curve.

For the RSG models, thermal conduction is not included because the temperature gradient at the shocks are small $\Delta T \approx 10^3 - 10^4$ K, (Meyer et al. 2014). Similar to Figure 4.1, Figure 4.3 shows the effect of space velocity (the velocity of the central star) on the bow shock structure and comparing with the Wilkin (1996) analytic solution with percentage errors shown in Table 4.2. From $R(0^o)/R(90^o)$ in Table 4.2 of models RSG_40C and RSG_70C of Figure 4.3, increasing the space velocity of the star reduces the bow shock size, because the ram pressure of the ISM increases, which in turn decreases the R_{SOD}. This suggests that we will have significantly smaller bow shocks for HVRs compared to runaways.

4.2 Comparison with the literature

To explore the similarities and differences between this work and the literature, we ran 2D MS and RSG models with parameters similar to those of Meyer et al. (2014) as discussed in the section above. The comparison of our models to that work (which is fairly representative of other literature studies) is shown in Figure 4.5 and 4.6 for the MS and RSG cases, respectively.

We have noticed the following similarities between our models and Meyer et al. (2014). Firstly, the bow shock structure and flow characteristics are similar for the respective evolutionary phases. Secondly, the cooling reduces the bow shock size in both MS and RSG models. Third, for the MS models, thermal conduction makes the bow shock larger. Fourth, the similarity is also in the Kelvin-Helmholtz instabilities in the RSG models, whose growth is more significant for higher space velocities.

Our models differ from Meyer et al. (2014) as follows. Firstly, all of our bow shocks are slightly smaller than those of Meyer et al. (2014), because the wind parameters given in that work are approximations (see Figure 3 of Meyer et al. 2014), as such it was very difficult to determine the actual values that they used. Therefore for the purpose of comparing our models to that work, the wind density for the our MS model that was adopted here is 5.88×10^{-3} cm^{-3} which corresponds to $\dot{M}_{\rm w}$ = 2.43×10^{-10} M$_\odot$/yr and for the RSG model is 1×10^{2} cm^{-3} which corresponds to $\dot{M}_{\rm w}$ = 7.02×10^{-7} M$_\odot$/yr, and the wind velocities that were adopted where $v_{\rm w} = 1000$ km/s and $v_{\rm w} = 10$ km/s, for the MS and RSG, respectively; as a result, our models are slightly different to that of Meyer et al. (2014). Secondly, our models including thermal conduction where run for a shorter time than the Meyer et al. (2014) models due to their high computational cost; as a result, the tail of our bow shock models is different to that of Meyer et al. (2014). Third, the cooling between our models and the literature is different at lower temperatures, $T \lesssim 10^4$ K as shown in Figure 4.7, in Meyer et al. (2014) a lot of assumptions and extrapolations were performed to obtain the net cooling rate, and heating due to H_2 molecules was not included; in our case, we included heating from both the dust grains and H_2 at lower temperatures for the CIE case; in addition, our photoionization cooling curve is slightly different from that of Meyer et al. (2014) because they used tables from Wiersma, Schaye, and Smith (2009), while we used up-to-date tables from Ploeckinger and Schaye (2020).

In addition to not having exact but approximate values of the initial conditions in Meyer et al. (2014), some of the PLUTO code's numerical prescription such as the limiter and reconstruction methods, which are crucial to the simulation outputs such as the definition of shock waves (see Chapter 2 and Appendix B for details) were not mentioned in their paper. This resulted in the differences in the discontinuities and instabilities than can be seen in the models of this work compared to that of Meyer et al. (2014) as shown in Figure 4.5 and 4.6.

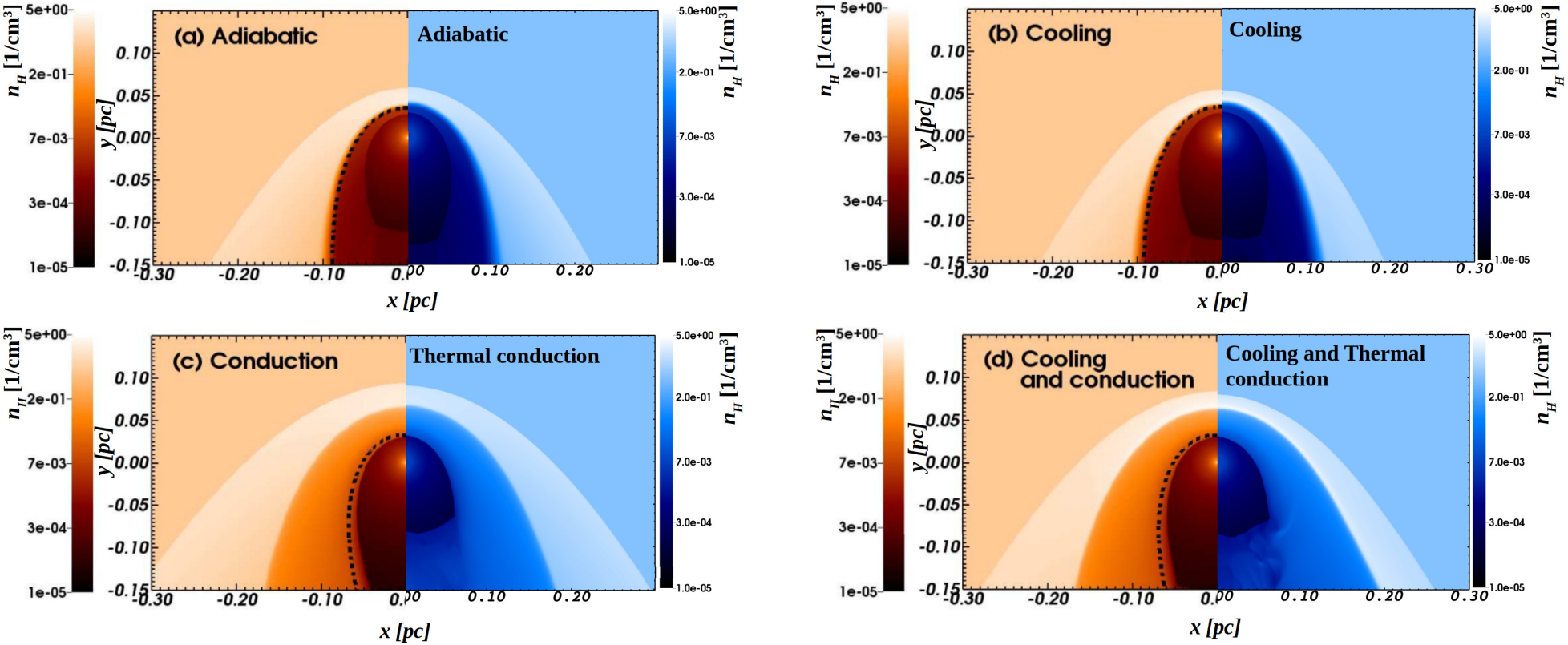

FIGURE 4.5: Density plots of a stellar wind bow shock for a MS 10 $M_\odot$ star from literature (Meyer et al. 2014) in red and this work in blue. Plot (a), (b), (c) and (d) correspond to the models obtained with adiabatic, cooling, thermal conduction, and cooling and thermal conduction conditions, respectively.

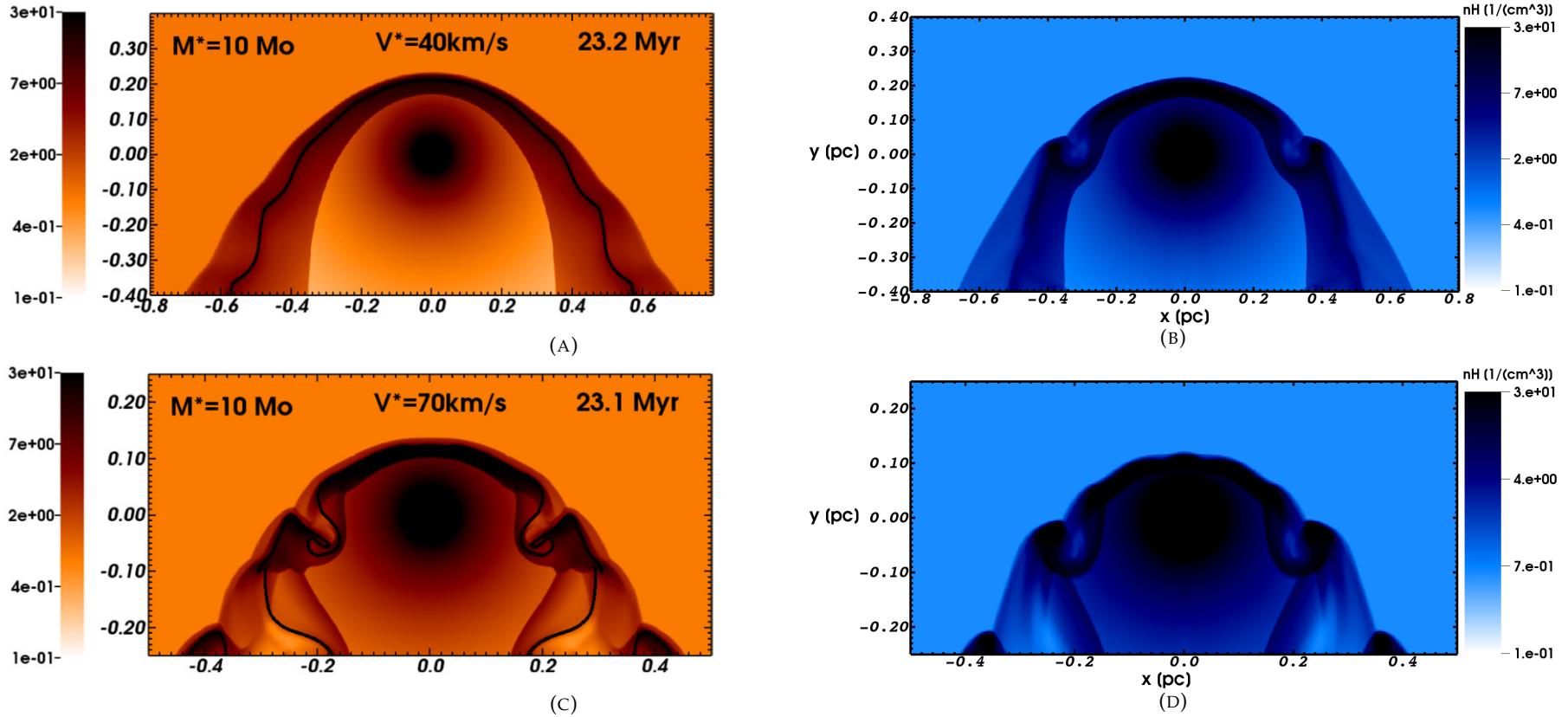

(A) (B) (C) (D)

FIGURE 4.6: Density plots of a stellar wind bow shock around a RSG star with 10 $M_\odot$ from the literature (Meyer et al. 2014) in the (left column) and this work in the (right column). We have $v_{\rm star} = 40$ km/s in the (top row) and $v_{\rm star} = 70$ km/s in the (bottom row).

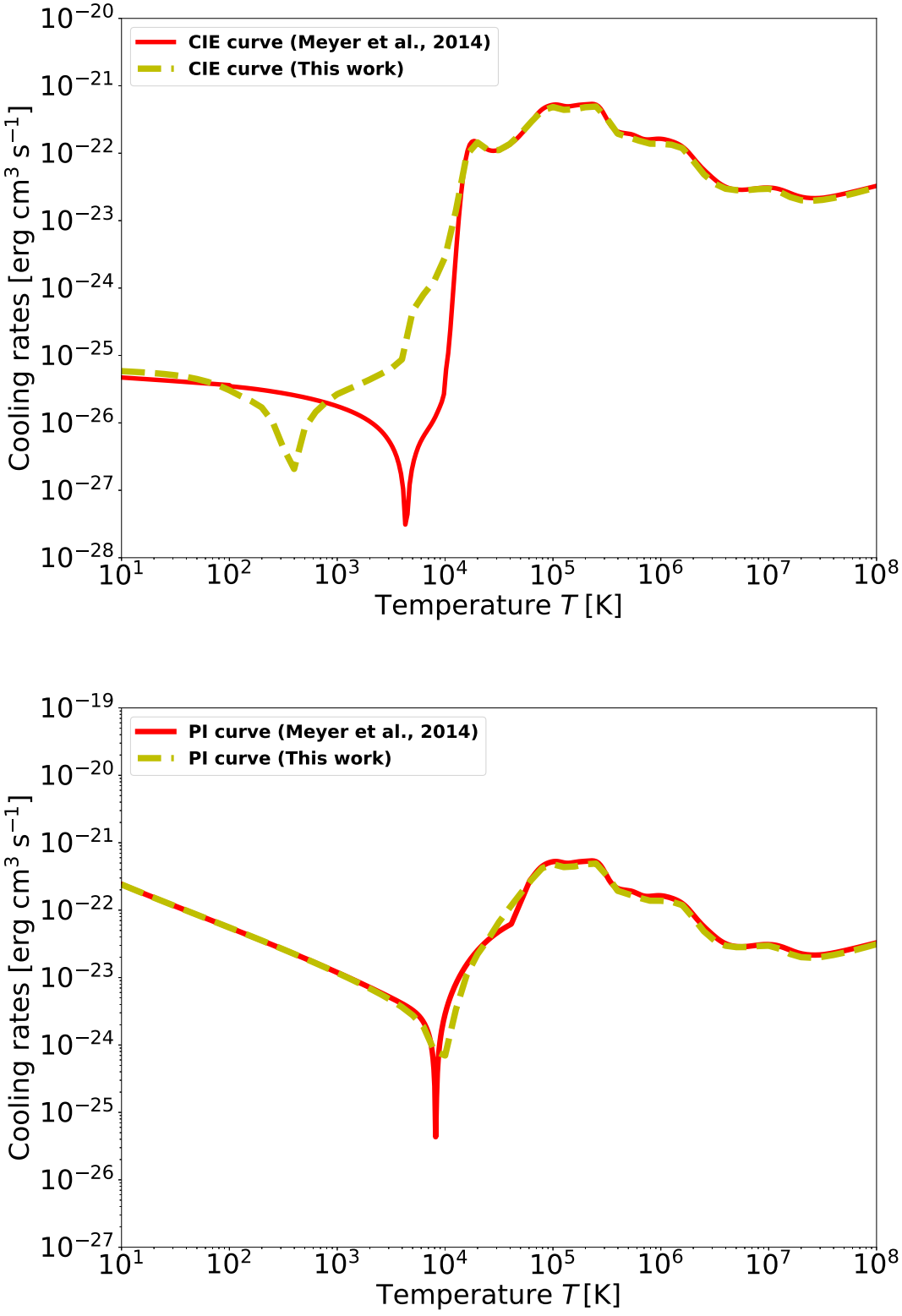

FIGURE 4.7: [Top] Our cooling rates as a function of temperature for CIE case (yellow) compared to that in Meyer et al. (2014) (red). [Bottom] Our photoionization (PI) cooling curve (yellow) compared to that in Meyer et al. (2014) (red).

Chapter 5

Bow shocks from MS and RSG high-velocity runaways

In the previous chapter, we tested the setup and modifications made to the code for 2D bow shocks in the adiabatic, thermal conduction and cooling case. In this chapter, we make further 2D tests investigating the effect of resolution on the bow shocks formed by HVRs, both to aid resolution selection for the full parameter study, and to inform the analysis of our results. We consider the MS and RSG phases of HVRs moving with space velocity, $v_* = 200$ km/s, through a uniform ISM of density $n_{\rm H} = 0.57$ cm^{-3}, and perform the resolution tests for two conditions for each evolutionary phase, i.e., the adiabatic and thermal conduction & radiative cooling for the MS case, and adiabatic and radiative cooling conditions for the RSG phase. The initial and boundary conditions are shown in Section 5.1. The results are discussed in relation to the Wilkin (1996) analytic solution with the MS case in Section 5.2 and the RSG case in Section 5.3. Further analysis and discussion is given in Section 5.4 and 5.5, respectively, and the summary in Section 5.6.

5.1 Initial and boundary conditions

To explore the effect of changing the grid resolution given different evolutionary phases (MS and RSG), and physical conditions (adiabatic, and thermal conduction and/or cooling), we ran 2D models with resolution $N_{\rm zones} = 64 \times 64$, 128×128, 256×256 and 512×512 as shown in Table 5.1 where all the models are axis-symmetric in cylindrical coordinates. The external boundary range for the MS case is $0 \leq$ x ≤ 0.2 pc for the x-axis and $-0.1 \leq$ y ≤ 0.1 pc for the y-axis, while for the RSG case it is $0 \leq$ x ≤ 1.4 pc for the x-axis and $-0.7 \leq$ y ≤ 0.7 pc for the y-axis, with an internal boundary radius of 20 cells. HLL is the solver of choice because of its robustness, efficiency and shock capturing ability. These initial, external and internal boundary conditions are similar to those in Meyer et al. (2014), except for the $v_{\rm w}$ and v_*. See Chapter 3 for the description of the wind and ISM models, where the ISM properties are similar to those in Chapter 4.

TABLE 5.1: MS and RSG HVR resolution test models for ISM density 0.57 cm^{-3} and space velocity 200 km/s

EV phase	Model name	N_{zones}	Zone width [pc]	$\frac{R_{SOD}}{\Delta x}$	TC and/or C	$\dot{M}_w$ [$M_\odot$/yr]	v_w [km/s]	T_w [K]	T_{ISM} [K]
MS	MS_A64	64×64	3.1×10^{-3}	4	No	10^{-9}	1000	2.5×10^4	8×10^3
	MS_A128	128×128	1.6×10^{-3}	11	No	10^{-9}	1000	2.5×10^4	8×10^3
	MS_A256	256×256	7.8×10^{-4}	21	No	10^{-9}	1000	2.5×10^4	8×10^3
	MS_A512	512×512	3.9×10^{-4}	40	No	10^{-9}	1000	2.5×10^4	8×10^3
	MS_C64	64×64	3.1×10^{-3}	3	Yes	10^{-9}	1000	2.5×10^4	8×10^3
	MS_C128	128×128	1.6×10^{-3}	8	Yes	10^{-9}	1000	2.5×10^4	8×10^3
	MS_C256	256×256	7.8×10^{-4}	17	Yes	10^{-9}	1000	2.5×10^4	8×10^3
	MS_C512	512×512	3.9×10^{-4}	32	Yes	10^{-9}	1000	2.5×10^4	8×10^3
RSG	RSG_A64	64×64	2.2×10^{-2}	6	No	10^{-6}	50	2.5×10^3	3.3×10^3
	RSG_A128	128×128	1.1×10^{-2}	15	No	10^{-6}	50	2.5×10^3	3.3×10^3
	RSG_A256	256×256	5.5×10^{-3}	29	No	10^{-6}	50	2.5×10^3	3.3×10^3
	RSG_A512	512×512	2.7×10^{-3}	55	No	10^{-6}	50	2.5×10^3	3.3×10^3
	RSG_C64	64×64	2.2×10^{-2}	4	Yes	10^{-6}	50	2.5×10^3	3.3×10^3
	RSG_C128	128×128	1.1×10^{-2}	8	Yes	10^{-6}	50	2.5×10^3	3.3×10^3
	RSG_C256	256×256	5.5×10^{-3}	16	Yes	10^{-6}	50	2.5×10^3	3.3×10^3
	RSG_C512	512×512	2.7×10^{-3}	34	Yes	10^{-6}	50	2.5×10^3	3.3×10^3

Where EV = Evolutionary, N_{zones} is the number of grid zones, $\frac{R_{SOD}}{\Delta x}$ is the number of cells within the stand-off distance, TC = Thermal conduction and C = Cooling.

5.2 Resolution tests for bow shocks around a MS HVR

We present 2D density, temperature and velocity plots of the bow shocks in Figures 5.1, 5.2 and 5.3, respectively, which include both the adiabatic case, and the thermal conduction and cooling case. We took a single cut through each of the bow shocks at the apex (i.e., from 0 to 0.04 pc of the y-axis) and the resulting 1D profiles are shown in Figure 5.4.

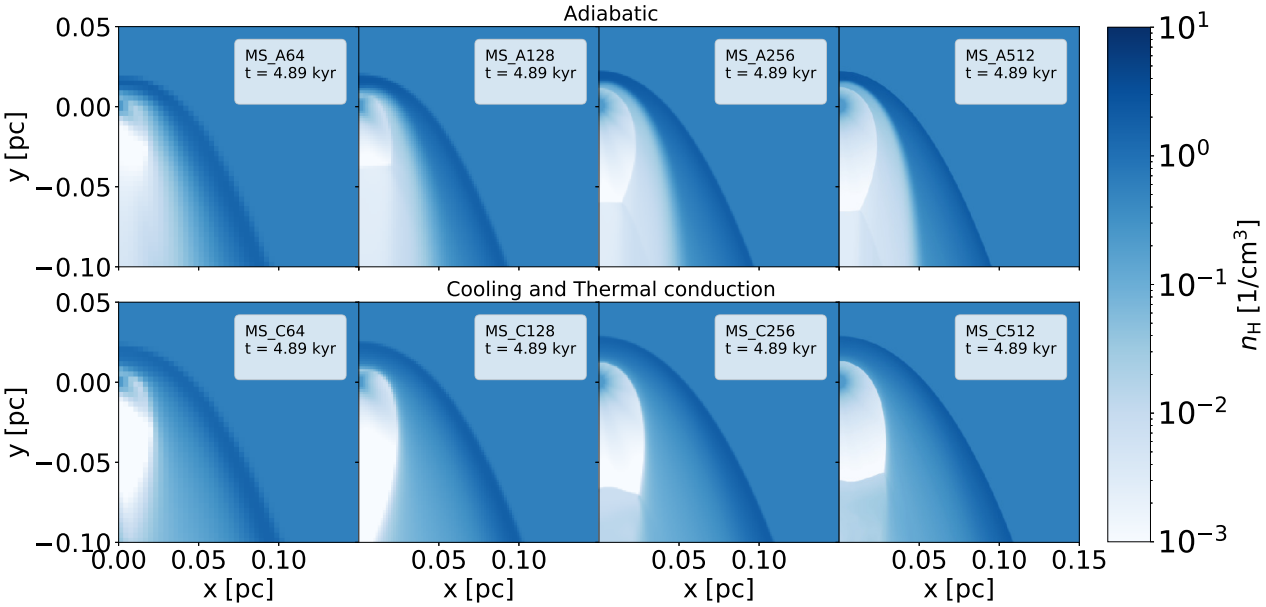

FIGURE 5.1: Density plots at time, t = 4.89 kyr, for the bow shocks produced by MS stars moving at 200 km/s, for the adiabatic case (top row) and for the cooling and thermal conduction case (bottom row) for grid resolutions, $N_{\text{zones}} = 64^2$, 128^2, 256^2 and 512^2 (the first, second, third, and fourth column, respectively).

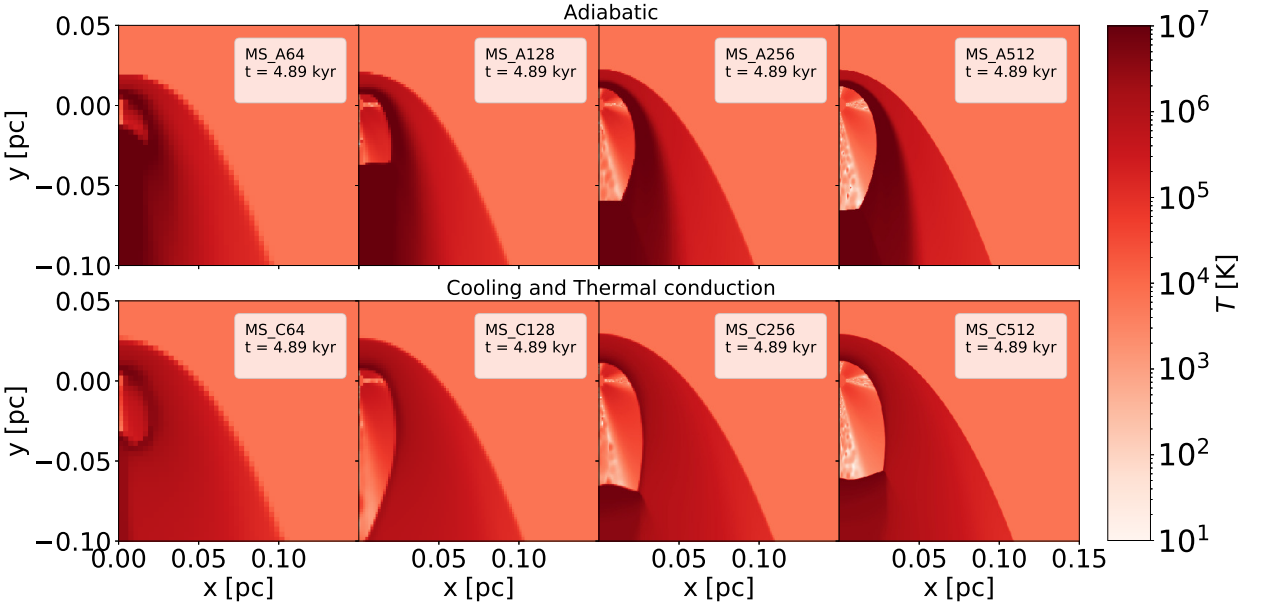

FIGURE 5.2: Temperature plots at time, t = 4.89 kyr, for the bow shocks produced by MS stars moving at 200 km/s, for the adiabatic case (top row) and for the cooling and thermal conduction case (bottom row) for grid resolutions, $N_{\text{zones}} = 64^2$, 128^2, 256^2 and 512^2 (the first, second, third, and fourth column, respectively).

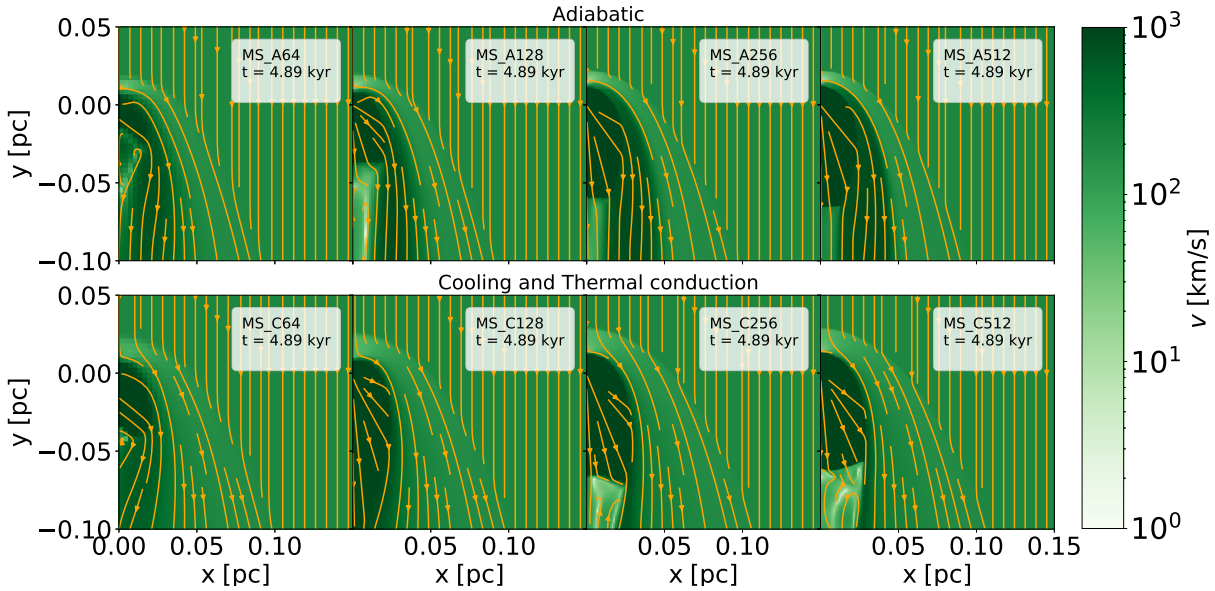

FIGURE 5.3: Velocity plots at time, t = 4.89 kyr, for the bow shocks produced by MS stars moving at 200 km/s, for the adiabatic case (top row) and for the cooling and thermal conduction case (bottom row) for grid resolutions, $N_{\rm zones} = 64^2$, 128^2, 256^2 and 512^2 (the first, second, third, and fourth column, respectively). The orange curves with arrows are the streamlines showing the fluid flow.

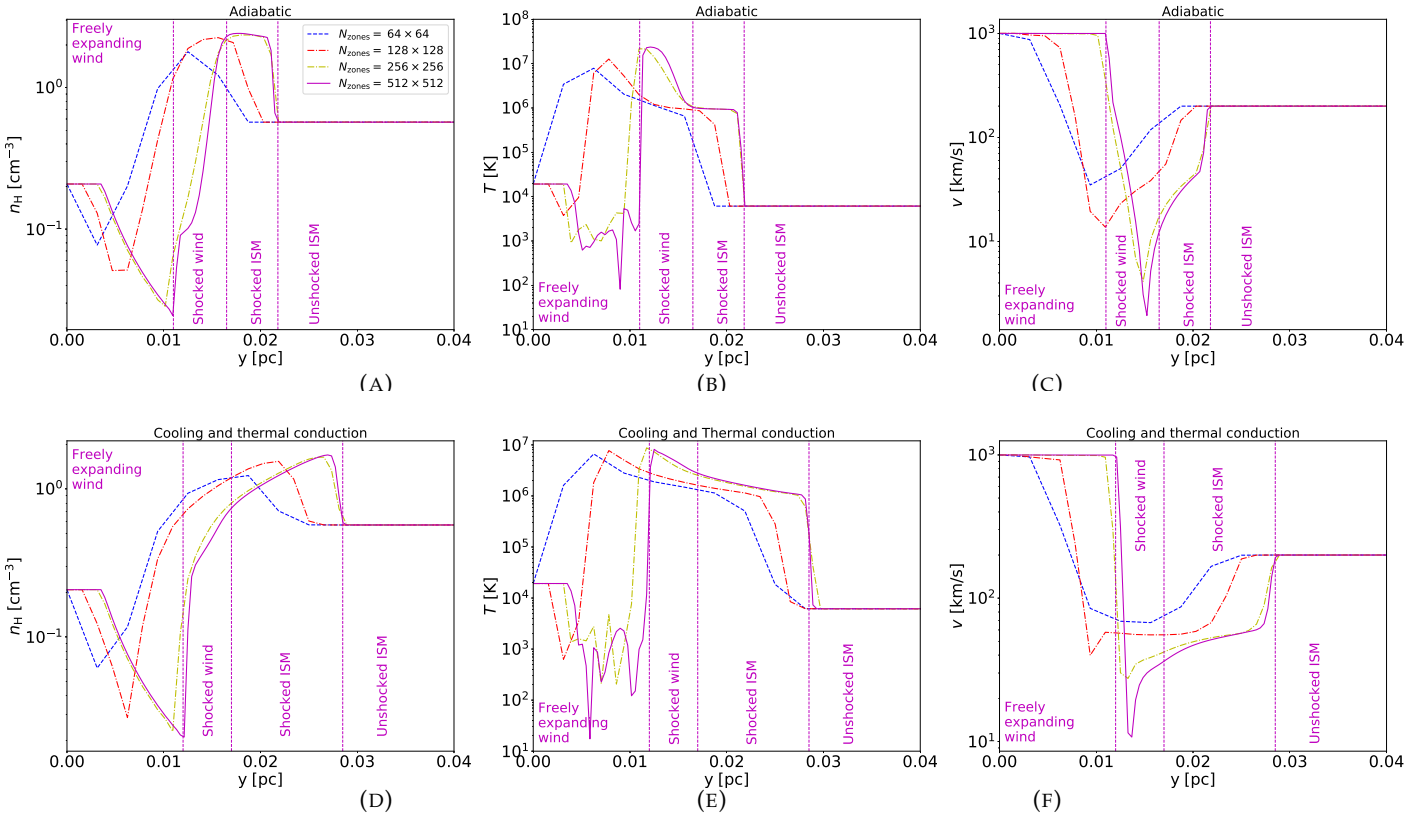

FIGURE 5.4: Profiles extracted along the apex (from 0 to 0.04 pc along the y-axis) of the bow shock of MS models at different resolutions of Figures 5.1, 5.2 and 5.3, for the adiabatic case (top row) and for the cooling and thermal conduction case (bottom row). In the first, second and third column are the density, temperature and velocity profiles, respectively. The magenta vertical dashed lines separate different regions (freely expanding wind, shocked wind, shocked ISM and unshocked ISM) of the bow shock structure for models with resolution $N_{\rm zones} = 512^2$ in each plot.

5.3 Resolution tests for bow shocks around a RSG HVR

We ran similar tests for the RSG case, the 2D density, temperature and velocity plots of the bow shock are shown in Figures 5.5, 5.6 and 5.7, respectively, which include both the adiabatic case and the cooling case. As before, we took a single cut through each of the bow shocks at the apex (i.e., from 0 to 0.2 pc along the y-axis) and the resulting 1D profiles are shown in Figure 5.8.

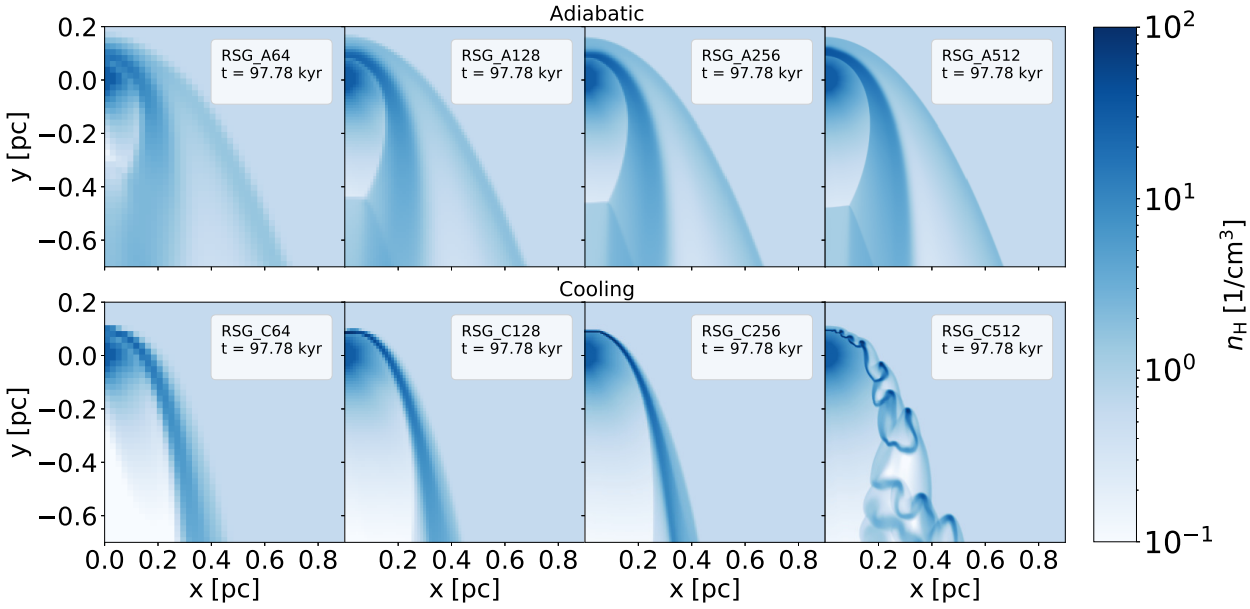

FIGURE 5.5: Same as Figure 5.1 for the RSG case. Density plots at time, t = 97.78 kyr, for the bow shocks produced by RSG stars moving at 200 km/s, for the adiabatic case (top row) and for the cooling case (bottom row) for grid resolutions, $N_{\text{zones}} = 64^2$, 128^2, 256^2 and 512^2 (the first, second, third, and fourth column, respectively).

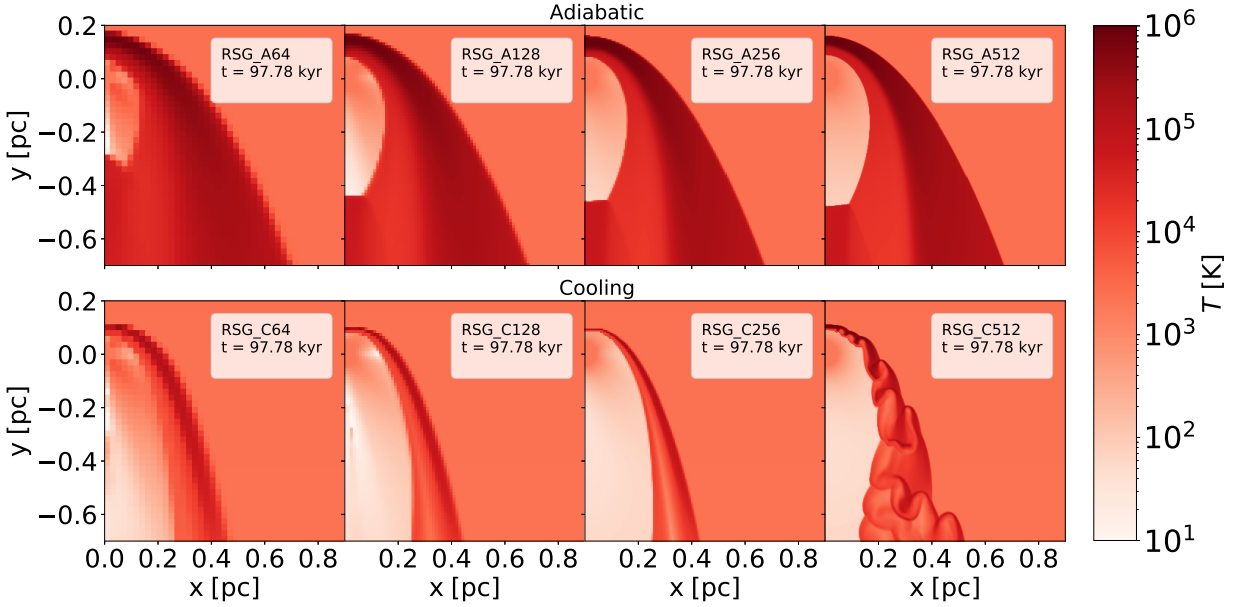

FIGURE 5.6: Same as Figure 5.2 for the RSG case. Temperature plots at time, t = 97.78 kyr, for the bow shocks produced by RSG stars moving at 200 km/s, for the adiabatic case (top row) and for the cooling case (bottom row) for grid resolutions, $N_{\text{zones}} = 64^2$, 128^2, 256^2 and 512^2 (the first, second, third, and fourth column, respectively).

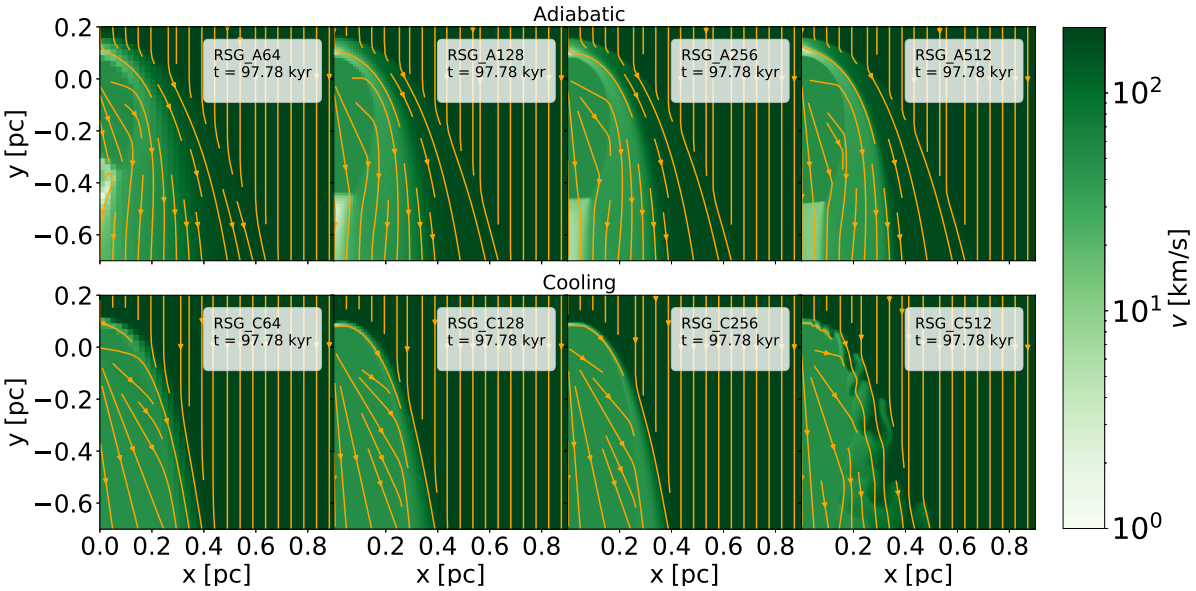

FIGURE 5.7: Same as Figure 5.3 for the RSG case. Velocity plots at time, t = 97.78 kyr, for the bow shocks produced by RSG stars moving at 200 km/s, for the adiabatic case (top row) and for the cooling case (bottom row) for grid resolutions, $N_{\rm zones} = 64^2$, 128^2, 256^2 and 512^2 (the first, second, third, and fourth column, respectively). The orange curves with arrows are the streamlines showing the fluid flow.

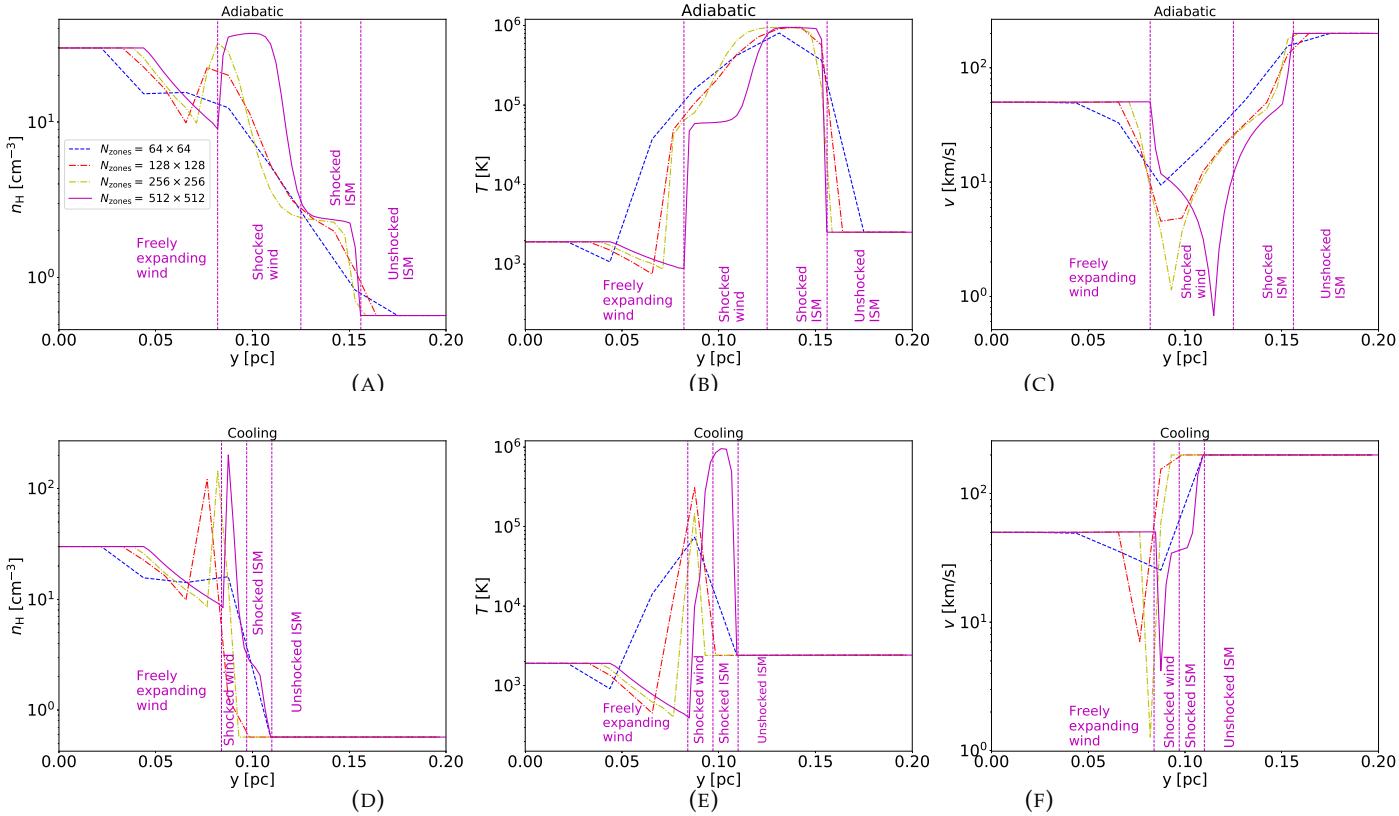

FIGURE 5.8: Same as Figure 5.4 for the RSG case. Profiles extracted along the apex of the bow shock of RSG models in different resolutions (i.e., from 0 to 0.2 pc along the y-axis) of Figures 5.5, 5.6 and 5.7, for the adiabatic case (top row) and for the cooling case (bottom row). In the first, second and third column are the density, temperature and velocity profiles, respectively. The magenta vertical dashed lines separate different regions (freely expanding wind, shocked wind, shocked ISM and unshocked ISM) for bow shock structure for models with resolution $N_{\rm zones} = 512^2$ in each plot.

5.4 Analysis of the HVR MS and RSG test models

To quantitatively investigate how the resolution affects the models, we focused on the reverse shock, which is the region consisting of rapid changes in the physical properties of the bow shock structures presented in Section 5.2 and 5.3. This region separates the freely expanding wind and the shocked wind as shown in Figures 5.4 and 5.8. We also focus on the contact discontinuity which separates the shocked wind and shocked ISM, as its radius can be approximated by the Wilkin (1996) analytic solution. The density jump and the temperature jump (ΔT) at the reverse shock, in addition to the Wilkin (1996) solution, were used to explore the resolution effect, and the results are shown in Table 5.2, and their respective plots in Figure 5.9.

TABLE 5.2: Quantitative analysis of the density and temperature profiles of Figure 5.4 and 5.8.

		Approximate density jump factor at reverse shock		
Evolutionary phase	N_{zones}	Adiabatic	Thermal conduction and/or Cooling	Ratio
MS	64×64	12.8	8.4	~ 0.7
	128×128	22.6	11.8	~ 0.5
	256×256	61.6	15.3	~ 0.2
	512×512	3.9	12.2	~ 3.1
RSG	64×64	1.0	1.0	~ 1.0
	128×128	2.3	12.2	~ 5.3
	256×256	3.3	16.9	~ 5.1
	512×512	4.1	23.9	~ 5.8
		Approximate (ΔT [K]) at reverse shock		
Evolutionary phase	N_{zones}	Adiabatic	Thermal conduction and/or Cooling	Ratio
MS	64×64	7.9×10^6	6.6×10^6	~ 0.8
	128×128	1.3×10^7	7.7×10^6	~ 0.6
	256×256	2.2×10^7	8.7×10^6	~ 0.4
	512×512	2.3×10^7	8.2×10^6	~ 0.4
RSG	64×64	3.6×10^4	1.3×10^4	~ 0.4
	128×128	4.8×10^4	1.2×10^4	~ 0.3
	256×256	4.2×10^4	1.1×10^4	~ 0.3
	512×512	4.6×10^4	9.4×10^3	~ 0.2
		Models compared to Wilkin (1996) solution			
Evolutionary phase	N_{zones}	Adiabatic		Thermal conduction and/or Cooling	
		$R(0^o)/R(90^o)$	% Error	$R(0^o)/R(90^o)$	% Error
MS	64×64	0.203	64.8	0.203	64.8
	128×128	0.367	36.5	0.310	46.3
	256×256	0.522	9.6	0.521	9.8
	512×512	0.626	8.5	0.586	1.5
RSG	64×64	0.423	26.7	0.305	47.2.8
	128×128	0.526	8.9	0.392	32.1
	256×256	0.549	4.8	0.456	21.0
	512×512	0.601	4.1	0.555	3.9

N_{zones} is the number of grid zones, Ratio is the value in the thermal conduction and/or cooling case divided by the value in the adiabatic case. The definition of $R(0^o)/R(90^o)$ and the percentage error (% Error) are as in Table 4.2.

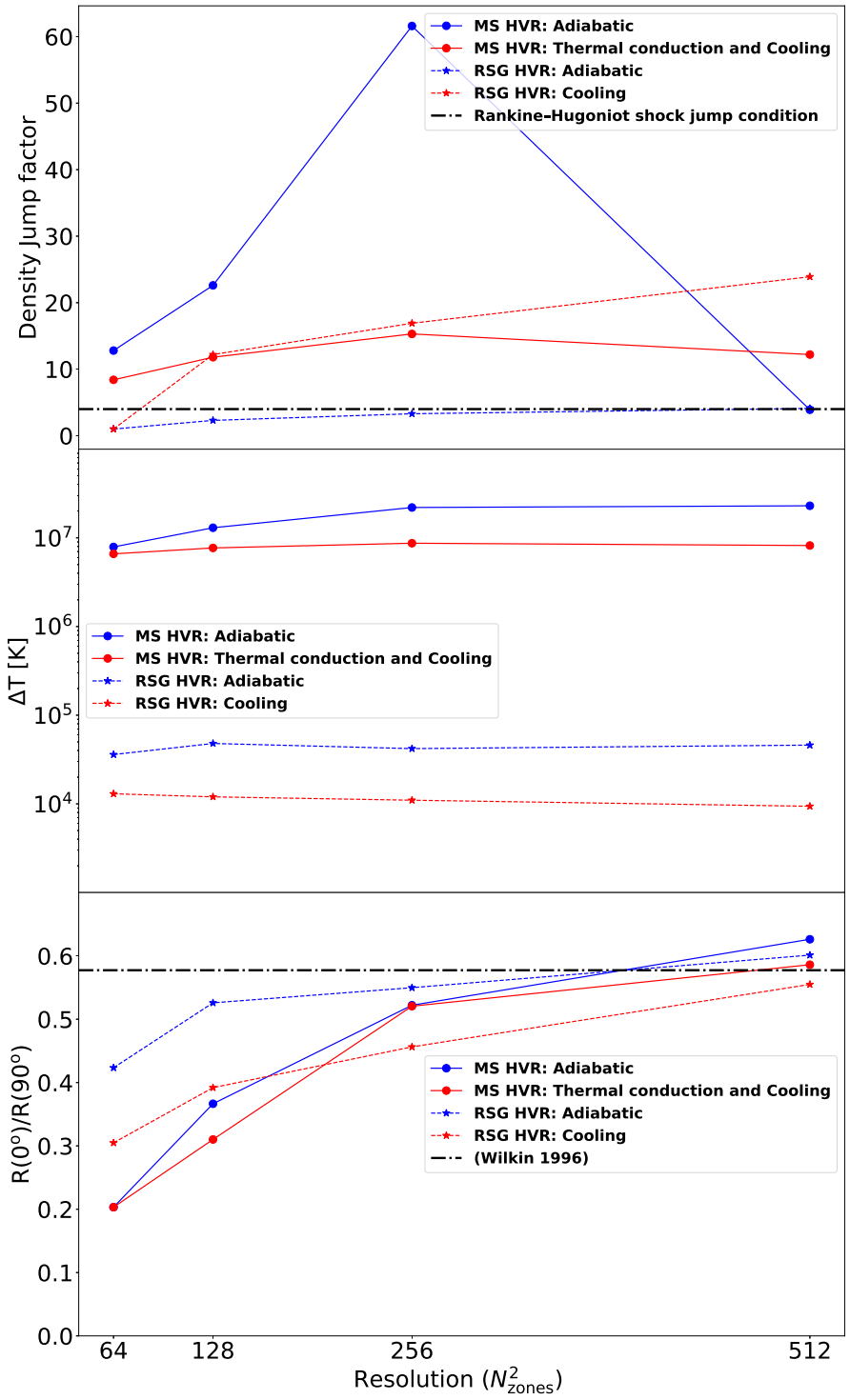

FIGURE 5.9: The effect of resolution on the HVR models for the MS case (dots) and the RSG case (stars), for both the adiabatic case (blue solid line) and thermal conduction and/or cooling case (red dashed line). Note, the lines are only used to help differentiate between cases, rather than represent continuous data. We have the effect on the density jump factor (top plot), temperature jump at the reverse shock (middle plot) and contact discontinuity in comparison with the Wilkin (1996) analytic solution $R(0^{\rm o})/R(90^{\rm o}) = 0.577$ (bottom plot). See the analytic solution on the 2D maps in Figures C.1 (for the MS case) and C.2 (for the RSG case) of Appendix C.1. **Please note** at low resolution $N_{\rm zones} \leq 256^2$ is difficult to determine the reverse shock and the contact discontinuity, as such these measurements are very approximate.

5.5 Discussion of the resolution tests

In this section, we discuss the test results that were presented in the previous sections (i.e., Section 5.2, 5.3, and 5.4), in addition to explaining the similarities and differences between the models with different evolutionary phases, different conditions (adiabatic, cooling and thermal conduction) and different resolutions. We firstly discuss the effect of resolution in the adiabatic models for both the MS and RSG cases simultaneously in Section 5.5.1, followed by the thermal conduction and/or cooling models for the MS and RSG cases in Section 5.5.2.

5.5.1 Resolution tests with adiabatic models

When doing numerical studies of fluids, for simplicity, we start with the adiabatic case, for which we typically have less complex flow characteristics and structures that can be easily described by simple analytic recipes, e.g., the Euler equations in Section 2.1 and the well known Rankine–Hugoniot shock jump conditions.

The first thing to note is that the temperature maps in Figure 5.2 have artifacts, cross-like features in the freely expanding wind. This is due to integration errors in grid codes that occur due to advection at regions of higher kinetic energy, but this does not affect the bow shock because the state of the fluid before and after the shock does not depend on the temperature, see Mackey et al. (2021) for more details. In addition, we should expect this to occur for the MS models because their stellar winds have high temperatures, $\sim$ 25 000 K and move at high velocities, $\sim$ 1000 km/s or higher.

The model MS_A64 of Figures 5.1, 5.2 and 5.3 (for the MS case) and RSG_A64 of Figures 5.5, 5.6 and 5.7 (for the RSG case), shows that at resolution $N_{\rm zones} = 64 \times 64$ the shock regions are smeared-out, and it is difficult to distinguish between discontinuities, but then as the resolution is increased to about $N_{\rm zones} = 256 \times 256$ as shown for model MS_A256 of Figures 5.1, 5.2 and 5.3 (for the MS case) and RSG_A256 of Figures 5.5, 5.6 and 5.7 (for the RSG case); the discontinuities can be clearly distinguished from one another. Thus, for modelling the bow shocks of HVR stars, it would be best to use resolution of at least $N_{\rm zones} = 256 \times 256$ in order to get well-defined shock waves. The 2D maps alone do not give enough information to make a clear suggestion about the convergence of the code, for this we use the 1D profiles extracted from these 2D maps.

As in the 2D maps, the 1D curves at resolution $N_{\rm zones} = 64 \times 64$ as shown in the top row of Figure 5.4 (for the MS case) and Figure 5.8 (for the RSG case) do not show well-defined shock waves which are represented by the discontinuities (i.e., very steep slopes) in these profiles. However, as the resolution increases, the shock wave becomes less smeared-out and the discontinuities are well-defined especially with resolution $N_{\rm zones} = 512 \times 512$. However, the $N_{\rm zones} = 256 \times 256$ models have not yet converged according to the 1D profiles (even though one might think they have converged by considering only the corresponding 2D maps as discussed above).

For the adiabatic 1D profiles, from the Rankine-Hugoniot jump condition a density jump factor of $\sim$ 4 is expected at the reverse shock, and from the top part of Table 5.2 and Figure 5.9, it seems the RSG models shows better agreement with this jump condition than the MS models at lower resolutions $N_{\rm zones} \leq 256^2$, but both

better agree with this jump condition at a higher resolution of $N_{\rm zones} = 512 \times 512$, with density jump factor of 3.9 and 4.1 for the MS and RSG, respectively. Overall the density jumps increase with resolution, but for the MS case the density jump drops from resolution $N_{\rm zones} = 256 \times 256$ to $N_{\rm zones} = 512 \times 512$ because the reverse shock is well resolved and can be properly determined, which leads to the convergence of the model towards the Rankine-Hugoniot jump condition, while for the RSG case the density jump increases and converges towards the Rankine-Hugoniot jump condition with increase in resolution from $N_{\rm zones} = 64 \times 64$ to $N_{\rm zones} = 512 \times 512$, this is all shown in the top part of Figure 5.9. The middle part of Table 5.2, shows how the temperature jump at the reverse shock changes with resolution in the adiabatic case, for the RSG models the temperature jump is lower compared to that of the MS models, which is expected since MS stars have faster winds and that results in stronger reverse shocks than RSG stars. The effect of increasing resolution is shown graphically in the middle part of Figure 5.9, overall the temperature jump is better determined, measured and increases as the reverse shock is better resolved. In addition, the post-shock temperature jump can also be predicted from the Rankine-Hugoniot jump condition as:

$$\Delta T \approx 2.3 \times 10^5 \ {\rm K} \Big(\frac{v_{\rm sh}}{100 \ {\rm km \, s^{-1}}} \Big)^2, \tag{5.1}$$

where $v_{\rm sh}$ is the shock speed. Since we study our simulations after they reached steady state, the shock speed is about 200 km/s, as a result from Equation 5.1, the predicted post-shock temperature jump is about 9.2×10^5 K. It seems the MS models in adiabatic case are an order of magnitude greater than the predicted post-shock temperature jump, while the RSG models in adiabatic case are an order of magnitude lower than the predicted post-shock temperature jump.

The bottom part of Table 5.2, shows the model value of $R(0^{\rm o})/R(90^{\rm o})$ with respect to the resolution for the adiabatic case and the % Error of the model compared to the Wilkin (1996) analytic solution. From this we see that as the resolution is increased, the models agree more with the analytic solution as shown in the corresponding plots in the bottom part of Figure 5.9. This is expected because the contact discontinuity is better determined and measured at higher resolutions, especially at $N_{\rm zones} = 512 \times 512$ for our models. This can be clearly seen in the Mach number plots in Figure C.5 and C.6 for the MS and RSG case, respectively.

Overall, from these adiabatic resolution tests, we develop an understanding of the impact of numerical resolution on the derived physical structure of the bow shock, and we conclude that it would be best to use resolution $N_{\rm zones} \gtrsim 512 \times 512$ for 2D models, and the same for 3D models which will require $N_{\rm zones} \gtrsim 512 \times 512 \times 512$ and even more computational time. Further discussions about the importance of resolution tests when planning simulations can be found in Zingale (2013).

5.5.2 Resolution tests with thermal conduction and/or cooling

Now that we know how resolution affects our model in the less complex adiabatic case as discussed in Section 5.5.1 above, we now explore the resolution effects when additional processes (thermal conduction and/or cooling) are included in the simulations. For the MS models, both thermal conduction and cooling are included, but for the RSG models only cooling is included as the temperatures are not high enough to allow significant transport of energy via electrons.

The MS models when cooling and thermal conduction are included, are impacted similarly by the resolution as in the adiabatic case (see Section 5.5.1). However, the 2D density, temperature and velocity maps as shown in the bottom row of Figures 5.1, 5.2 and 5.3, respectively, illustrate that when both cooling and thermal conduction are included, the net bow shock size becomes larger even though we know that cooling slightly reduces the bow shock size (see Figure 4.1). The bow shock becomes larger when thermal conduction is included because in the bow shock of MS models there is a large temperature jump around the reverse shock, $\Delta T \sim 10^7$ K (see 2D and 1D temperature plots of Figures 5.2 and 5.4, respectively), as a result the electrons move fast enough to act as energy transporters as they travel from the hotter to the nearby lower-temperature fluid (see Meyer et al. (2014), and references therein for more details).

In addition, when thermal conduction and cooling are included for MS case, the density jumps at the reverse shock as shown in the top part of Table 5.2 seems to drop by approximately half compared to the adiabatic case, which is unexpected, but at higher resolution $N_{\rm zones} = 512 \times 512$ it a factor of ~ 3 larger than the adiabatic case, which is expected because of cooling. The unexpected measurements occur at lower resolutions $N_{\rm zones} \leq 256 \times 256$ because it is difficult to determine the reverse shock (see Figure 5.4). The temperature jump at the reverse shock seems to have decreased by approximately half at the reverse shock compared to the adiabatic case as shown in the middle part of Table 5.2. This is expected because thermal conduction reduces the temperature at the reverse shock via electrons as discussed in the paragraph above, while cooling reduces the temperature via radiation. As the resolution increases, the temperature jump at the reverse shock seems to converge towards a larger temperature jump, as shown in the middle part of Figure 5.9. Furthermore, in these conditions, the MS models at higher resolution seem to agree more with the Wilkin (1996) analytic solution as shown in the bottom parts of Table 5.2 and Figure 5.9. In addition, these results of the effect of cooling and thermal conduction for MS HVRs are similar to the results of runaways as shown in Figure 4.2, but the bow shocks of HVRs are smaller because of higher space velocities as expected from Equations 1.7 and 1.8.

For the RSG models as expected, when cooling is included the bow shock becomes smaller compared to the adiabatic case as shown in the bottom row of Figures 5.5 - 5.8. The resolution effects for the RSG models when cooling is included are also the same as in the adiabatic case (see Section 5.5.1). However, when cooling is included, in addition to resolving discontinuities, the resolution is important for resolving the development or growth of instabilities. The bottom row of Figures 5.5, 5.6 and 5.7 show that at lower resolutions (e.g., $N_{\rm zones} \lesssim 256 \times 256$), the instability growth cannot be captured and cannot be resolved due to too much dissipation of the flow, meaning the bow shock's discontinuities as well as its instabilities cannot be captured; this is therefore an important consideration when interpreting the numerical models in order to understand the flow structures and when comparing to observational data (Zhekov and Myasnikov 2000). However, at higher resolutions, such as that for model RSG_C512 of Figures 5.5, 5.6 and 5.7, the development and growth of instabilities is clearly captured. Furthermore, the instabilities that we see in model RSG_C512 are the Rayleigh-Taylor and Kelvin-Helmholtz instabilities, with the latter dominating because of the velocity shear between the stellar wind and the ISM induced by the high space velocities of HVRs relative to the ISM.

In addition, for the RSG case as expected, the reverse shock for the radiative cooling case seem to have a higher density jump, approximately 5 to 6 times compared to that of the adiabatic case as shown in the top parts of Table 5.2 and Figure 5.9, and this jump also increases with resolution. In the middle parts of Table 5.2 and Figure 5.9, similar to the MS case, the temperature jump seems to be lower at the reverse shock in the cooling case than the adiabatic case, which is expected because of radiative cooling. In addition, this temperature jump seems to be slightly nonmonotonic with increasing resolution for the RSG case, however, this is likely due to difficulties in determining the shock properties at low resolution. Furthermore, similar to the MS case, as the resolution is increased, the model converges towards the Wilkin (1996) solution as shown in the bottom parts of Table 5.2 and Figure 5.9.

5.6 Summary

The tests presented and analysis performed in this chapter show that resolution is an important consideration for determining the properties of our HVR bow shocks in both the adiabatic case and thermal conduction and/or cooling case. In addition, it is also important for resolving instabilities, particularly when dealing with processes such as cooling for RSG HVR bow shocks. In other words, with high resolution (e.g., $N_{\rm zones} \gtrsim 512 \times 512$), we can get much sharper well-defined discontinuities and flow characteristics. Given the above results, we have chosen to run the parameter study with the highest resolution feasible $N_{\rm zones} = 512 \times 512$, and we now have a better understanding of the limitations of models with lower resolution.

Chapter 6

HVR bow shocks from different space velocities and ISM phases

In this chapter, we present the main results of this Thesis, i.e, the effect of the ISM properties and stellar space velocities on the bow shock morphology, and evolution in 2D and 3D for MS and RSG HVRs models. The parameters and configurations that are adopted for these models developed from a series of tests, including the investigation of the numerics of PLUTO using 3D models of a freely expanding wind of a stationary star with respect to the ISM (see Appendix B); testing adiabatic, cooling and thermal conduction models for slower-moving runaways and comparing with the literature (see Chapter 4); and 2D resolution tests of MS and RSG HVRs with adiabatic, thermal conduction and/or cooling physics (see Chapter 5). We consider MS and RSG HVRs moving at 200 km/s and 400 km/s, and passing through each of the different ISM phases (HIM, HII region, WNM and CNM).

6.1 MS and RSG model setup

To explore the effect of stellar evolutionary phase, different ISM phases and high space velocities on the bow shocks of HVRs, we ran models using the stellar wind and ISM parameters described in Chapter 3 as initial conditions (see Table 6.1), while varying the resolution and the size of the computational domain depending on the size of the output bow shocks. The 2D results for both MS and RSG HVRs are in Section 6.2, while the comparison of the 2D and 3D RSG HVR models are shown in Section 6.3, and the comparison with previous work in Section 6.4. We did not conduct 3D MS HVR models, because the resolution required (Table 6.1), and the inclusion of thermal conduction, would require computational time beyond what is available to us. Thus, for 3D we only conducted models for the RSG phase, which took about 1-4 months running time on 96 CPUs to produce outputs with sufficient detail needed for our analysis. Future studies using Adaptive Mesh Refinement (AMR) will enable us to overcome some of the computational cost limitations.

TABLE 6.1: 2D and 3D model setup for different stellar evolutionary phases, ISM phases and space velocities

2D									
EV phase	Model name	ISM phase	v_* [km/s]	N_{zones}	Zone width [pc]	x-axis [pc]	y-axis [pc]	R_{SOD} [pc]	IB [pc]
MS	MS_HIM200	HIM	200	512×512	3.1×10^{-3}	$0 \leq x \leq 1.6$	$-0.8 \leq y \leq 0.8$	1.3×10^{-1}	3.1×10^{-2}
	MS_HIM400		400	320×320	3.1×10^{-3}	$0 \leq x \leq 1.0$	$-0.5 \leq y \leq 0.5$	6.3×10^{-2}	3.1×10^{-2}
	MS_HII200	H II	200	512×512	7.8×10^{-4}	$0 \leq x \leq 0.4$	$-0.2 \leq y \leq 0.2$	1.6×10^{-2}	7.8×10^{-3}
	MS_HII400		400	256×256	7.8×10^{-4}	$0 \leq x \leq 0.2$	$-0.1 \leq y \leq 0.1$	8.1×10^{-3}	7.8×10^{-3}
	MS_WNM200	WNM	200	512×512	3.9×10^{-4}	$0 \leq x \leq 0.2$	$-0.1 \leq y \leq 0.1$	1.2×10^{-2}	3.9×10^{-3}
	MS_WNM400		400	256×256	3.9×10^{-4}	$0 \leq x \leq 0.1$	$-0.05 \leq y \leq 0.05$	5.7×10^{-3}	3.9×10^{-3}
	MS_CNM200	CNM	200	512×512	5.9×10^{-5}	$0 \leq x \leq 0.03$	$-0.015 \leq y \leq 0.015$	1.6×10^{-3}	5.9×10^{-4}
	MS_CNM400		400	256×256	5.9×10^{-5}	$0 \leq x \leq 0.015$	$-0.0075 \leq y \leq 0.0075$	8.0×10^{-4}	5.9×10^{-4}
RSG	RSG_HIM200	HIM	200	1024×1024	1.6×10^{-2}	$0 \leq x \leq 16$	$-8.0 \leq y \leq 8.0$	8.9×10^{-1}	3.1×10^{-1}
	RSG_HIM400		400	512×512	1.6×10^{-2}	$0 \leq x \leq 8$	$-4.0 \leq y \leq 4.0$	4.4×10^{-1}	3.1×10^{-1}
	RSG_HII200	H II	200	1024×1024	2.0×10^{-3}	$0 \leq x \leq 2$	$-1.0 \leq y \leq 1.0$	1.2×10^{-1}	3.9×10^{-2}
	RSG_HII400		400	512×512	2.0×10^{-3}	$0 \leq x \leq 1$	$-0.5 \leq y \leq 0.5$	5.7×10^{-2}	3.9×10^{-2}
	RSG_WNM200	WNM	200	512×512	1.7×10^{-3}	$0 \leq x \leq 0.8$	$-0.4 \leq y \leq 0.4$	8.1×10^{-2}	3.1×10^{-2}
	RSG_WNM400		400	320×320	1.7×10^{-3}	$0 \leq x \leq 0.5$	$-0.25 \leq y \leq 0.25$	4.1×10^{-2}	3.1×10^{-2}
	RSG_CNM200	CNM	200	512×512	2.0×10^{-4}	$0 \leq x \leq 0.1$	$-0.05 \leq y \leq 0.05$	1.1×10^{-2}	3.9×10^{-3}
	RSG_CNM400		400	256×256	2.0×10^{-4}	$0 \leq x \leq 0.05$	$-0.025 \leq y \leq 0.025$	6.0×10^{-3}	3.9×10^{-3}
3D									
EV phase	Model name	ISM phase	v_* [km/s]	N_{zones}	Zone width [pc]	x/z-axis [pc]	y-axis [pc]	R_{SOD} [pc]	IB [pc]
RSG	RSG_WNM200	WNM	200	$512 \times 512 \times 512$	1.7×10^{-3}	$0 \leq x \leq 0.8$	$-0.4 \leq y \leq 0.4$	$0 \leq x \leq 0.8$	8.1×10^{-2}
	RSG_WNM400		400	$320 \times 320 \times 320$	1.7×10^{-3}	$0 \leq x \leq 0.5$	$-0.25 \leq y \leq 0.25$	$0 \leq x \leq 0.5$	4.1×10^{-2}

Note: Similar to the setup in Meyer et al. (2014), here the internal boundary (IB) is set to a radius of 10 cells for MS and 20 cells for RSG phase. The definition of EV and N_{zones} are as in Table 5.1. The stellar wind and ISM parameters referred to in this table are described in detail in Chapter 3.

6.2 2D MS and RSG HVR models for different ISM phases and stellar space velocities

We present the bow shocks produced by a MS and RSG HVR star in 2D for the different cases stated in Table 6.1. We analyze and discuss the characteristics of the bow shock structures produced by these stars in Section 6.2.1, their evolution in Section 6.2.2, and their dynamical and cooling timescales in Section 6.2.3.

6.2.1 The characteristics of the MS and RSG HVR bow shock structures

The 2D density, temperature, velocity and emissivity maps are presented in Figures 6.1, 6.3, 6.5 and 6.7, respectively, for the MS and Figures 6.2, 6.4, 6.6 and 6.8 for the RSG case, in order to show how each of these parameters vary throughout the computational domain. For both the MS and RSG cases, the size of the bow shock becomes smaller with an increase in space velocity and/or ISM density as expected from the Wilkin (1996) analytic solution ($R_{\rm SOD}$ in Table 6.1). For the MS case, the 2D plots of the steady state structures and shapes of the bow shocks are similar and due to the stabilising thermal conduction included, do not show any growth of instabilities. This makes them ideal for investigating how different physical parameters such as the ISM density and stellar space velocity affect the size and shape of the bow shock in comparison to the Wilkin (1996) analytic solution. However, for the RSG case, the bow shock changes significantly with the change in ISM properties and velocity of the central star, particularly its stability, as a result only the RSG_HII400 and RSG_WNM400 models reach and remain in steady state.

Furthermore, for bow shock models in the first and fourth columns of Figures 6.2, 6.4, 6.6 and 6.8 corresponding to models where the stellar winds of the RSG collide with the ISM in the HIM and CNM phases, respectively, both 200 km/s and 400 km/s models have distortions at the apex. However, from the second and third columns of Figures 6.2, 6.4, 6.6 and 6.8, which represent models where the stellar wind of the RSG collides with the HII region and WNM, respectively, the bow shock models for 400 km/s reach and remain in steady state, while their corresponding 200 km/s models reach and then diverge from steady state. The 200 km/s models have distorted bow shock structures especially at the tip of the bow shock which are likely due to the carbuncle phenomenon (Quirk 1994). Since some 400 km/s models which have a high velocity reach and remain in steady in the HII region and WNM but not in the HIM and CNM phases, then the carbuncle phenomenon manifests only in some models even though the model setups are similar. It seems the bow shock structure gets distorted regardless of the stellar space velocity if the density of the ISM is too low (e.g., HIM, $n_{\rm H} \sim 0.005$ cm^{-3}) and also if it is too high (e.g., CNM, $n_{\rm H} \sim 30$ cm^{-3}); or if the temperature of the ISM phase is too high (e.g., HIM, $T \sim 10^6$ K) or it is too low (e.g., CNM , $T \sim 100$ K). Detailed study of the carbuncle phenomenon and approaches for avoiding it (e.g., having the star travel at an angle through the grid or using different solvers) will be investigated in future work. However, it is not clear what causes the carbuncle phenomenon or how to avoid it, because the theory behind it is still not well understood (Elling 2006).

In the bow shocks of MS and RSG HVRs shown in Figure 6.1 and 6.2, respectively, the density of the shocked regions increases with the space velocity and ISM density. The density of the shocked regions for the MS case is approximately in the range $10^{-3} - 10^{-2}$, $10^{-2} - 10^{-1}$, $10^{-2} - 10^{0}$ and $10^{0} - 10^{2}$ cm^{-3}, while for the RSG case is

approximately in the range $10^{-2} - 10^{-1}$, $10^{0} - 10^{2}$, $10^{0} - 10^{3}$ and $10^{1} - 10^{4}$ cm^{-3} for the HIM, HII region, WNM and CNM phase, respectively, and higher values in these ranges correspond to shocked regions for higher velocity (400 km/s) models. In addition, we see that the density of these shocked regions is more significantly affected by the ISM phase than the stellar space velocity. For the RSG case, apart from the carbuncle phenomenon numerical artifacts seen in Figures 6.2, 6.4, 6.6 and 6.8, we also see the growth of the Rayleigh–Taylor instabilities as the heavier fluid pushes into the lighter fluid or when the lighter fluid is accelerated into the heavier fluid. This can be clearly seen in the density plots in Figure 6.2.

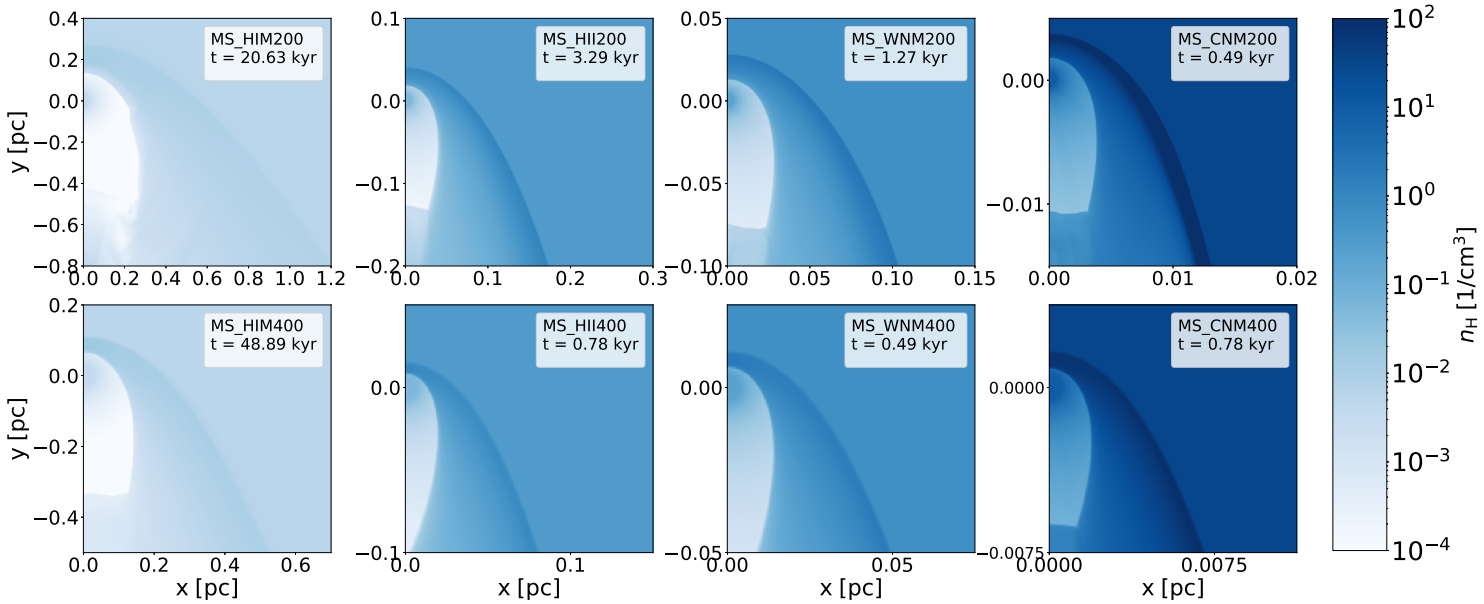

FIGURE 6.1: Density plots of the MS bow shocks for stars moving at 200 km/s (top row) and 400 km/s (bottom row) with respect to the ISM. The ISM phase in the first, second, third and fourth column is the HIM, HII region, WNM and CNM, respectively.

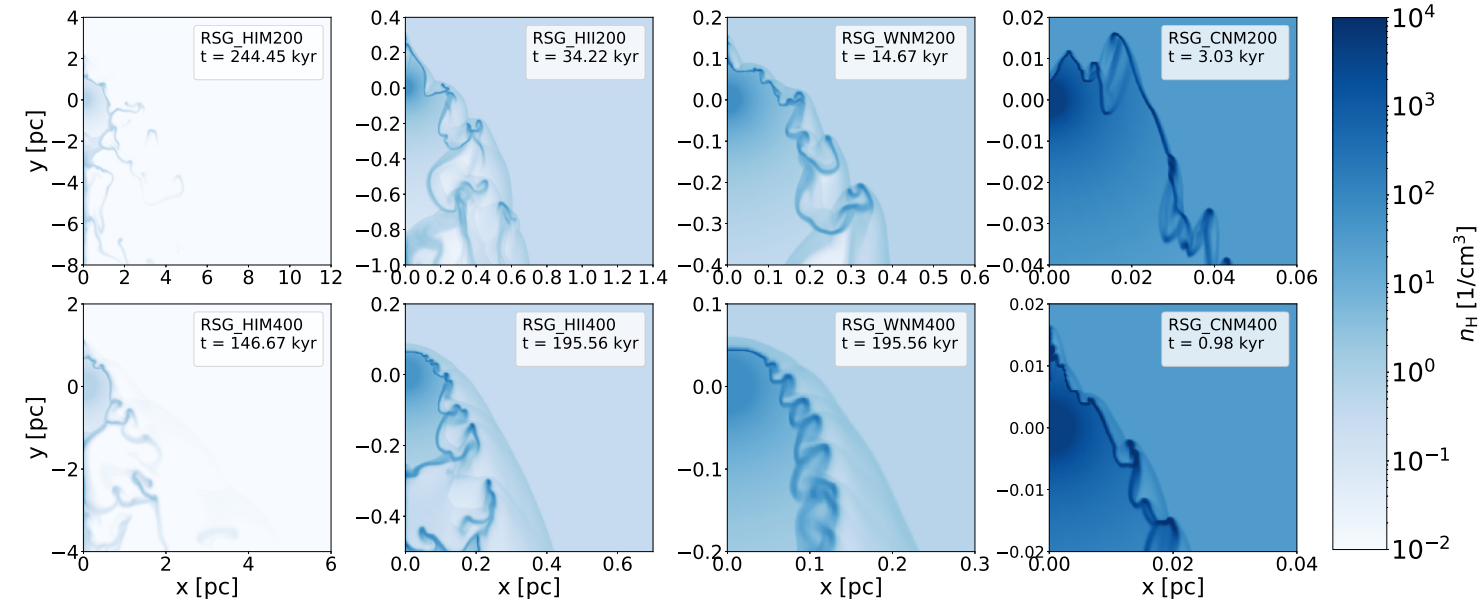

FIGURE 6.2: Density plots of the RSG bow shocks for stars moving at 200 km/s (top row) and 400 km/s (bottom row) with respect to the ISM. The ISM phase in the first, second, third and fourth column is the HIM, HII region, WNM and CNM, respectively.

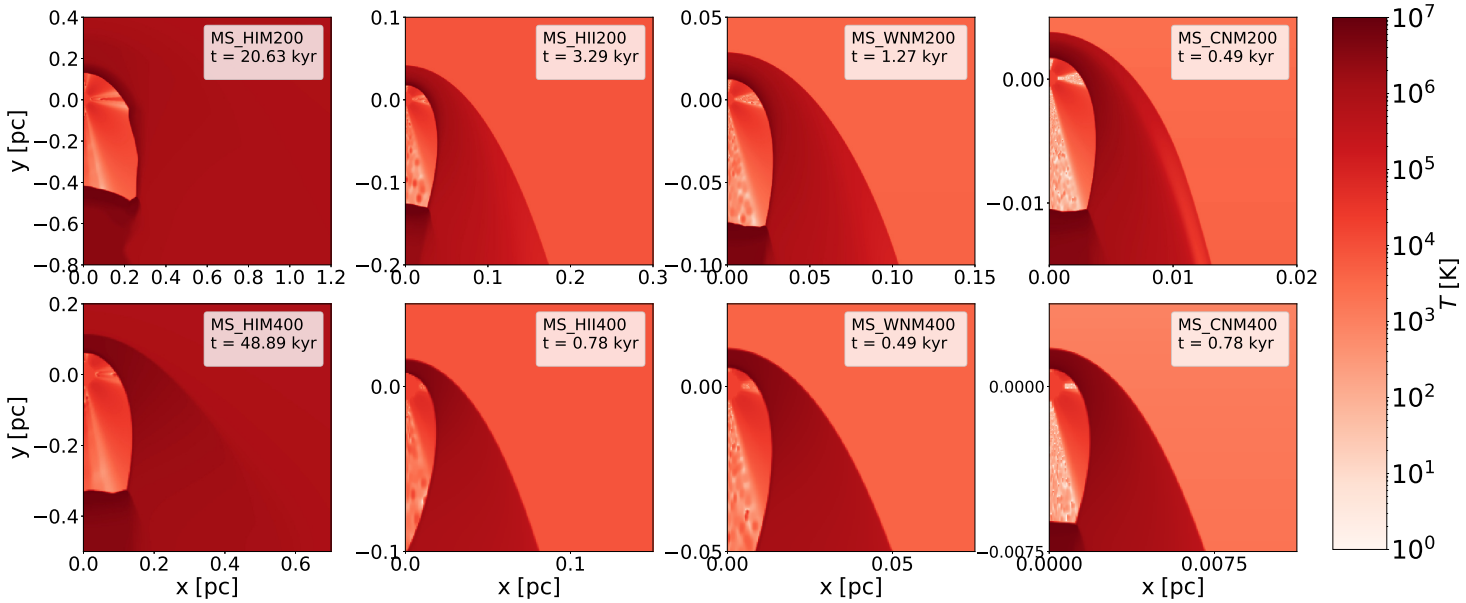

FIGURE 6.3: Temperature plots of the MS bow shocks for stars moving at 200 km/s (top row) and 400 km/s (bottom row) with respect to the ISM. The ISM phase in the first, second, third and fourth column is the HIM, HII region, WNM and CNM, respectively.

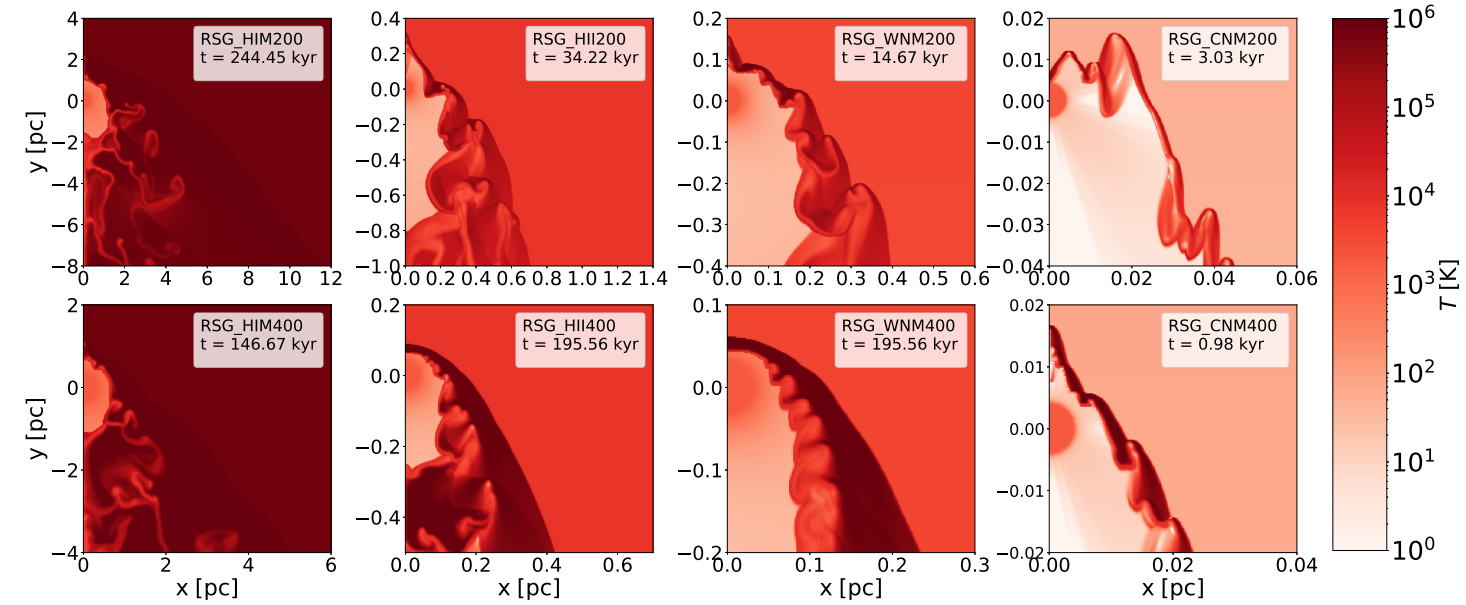

FIGURE 6.4: Temperature plots of the RSG bow shocks for stars moving at 200 km/s (top row) and 400 km/s (bottom row) with respect to the ISM. The ISM phase in the first, second, third and fourth column is the HIM, HII region, WNM and CNM, respectively.

In Figure 6.3 and 6.4 are the corresponding temperature plots for the MS and RSG cases, respectively, and all the MS models have cross-like (horizontal and vertical lines) artifacts in the region where the wind is expanding freely. These artifacts are due to integration errors that result from the advection of thermal energy where the kinetic energy dominating flow is very high (total energy is conserved by the finite-volume method); Mackey et al. (2021) see similar structures. These cross-like features do not affect the resulting bow shock structure, because the properties of the fluid after the shock do not depend on the temperature of the fluid before the shock, provided the shock has a large-Mach-number (Mackey et al. 2021), which is the case for these MS HVR models. However, for the RSG plots, these cross-like artifacts appear only in the CNM models. In this case the cause is less clear, but since

RSG stars have much slower wind speeds compared to MS stars, this might be the reason why most of the RSG models do not exhibit these artifacts.

In addition, the shocked regions and the unshocked ISM are not easily distinguishable in the case of the HIM models compared to other models, because the HIM phase has lower densities and higher temperatures than other ISM phases. The HIM models especially the RSG_HIM200 have a weak forward shock because the velocity of the star relative to the ISM is comparable to the sound speed of the HIM (see the Mach number plot in Appendix C Figure C.8). Similar results to simulation RSG_HIM200 can be seen in (Ballone et al. 2013), where the source of the wind reaches velocities comparable to the sound speed of the hot ambient medium.

In Figures 6.5 and 6.6 for the MS and RSG case, respectively, we see the relative velocity in different regions of the bow shocks. The fluid in the upper part of the shocked regions (y $\gtrsim$ 0 pc) and the tail are subsonic, while all other regions are supersonic, except for the discontinuities which are sonic (see Appendix C.2). We see that the shocked regions have relatively lower velocities than the unshocked regions as expected, with the apex of the shocked region having the lowest velocity ($\sim 10^0 - 10^1$ km/s) in that region because it is where the wind collides head-on with the ISM. This is the case because the shocked regions have higher densities, meaning particles collide and slow down more significantly than in the unshocked regions. Overall, the velocity in the shocked regions is in the range $\sim 10^0 - 10^2$ km/s for the MS case, and it is in the range $\sim 10^0 - 10^2$ km and $\sim 10^0 - 2 \times 10^2$ km for the 200 and 400 km/s models of the RSG case, respectively. For the MS case, the velocity in the region of the freely expanding wind is the highest in the presented computation domains since MS stars have fast winds ($\sim 10^3$ km/s) for our wind models (see Chapter 3), while for the RSG case, the highest velocity is in the unshocked ISM (200 km/s or 400 km/s depending on the space velocity) because its speed is relative to the HVR's speed. For both MS and RSG cases, the tail is the region of lowest velocities which is in the range $\sim 10^0 - 10^2$ km/s.

In addition, for the RSG case in Figure 6.6, it clearly shows the growth of Kelvin-Helmholtz instabilities at the interface separating the faster and slower fluids, for example, the RSG_WNM400 model shows the growth of Kelvin-Helmholtz instabilities because of the velocity shear between the faster ISM (for which its velocity is relative to the HVR star) and the slower wind velocities. These Kelvin-Helmholtz instabilities dominate over the Rayleigh–Taylor instabilities at higher space velocity, while the Rayleigh–Taylor instabilities dominate at lower ISM densities.

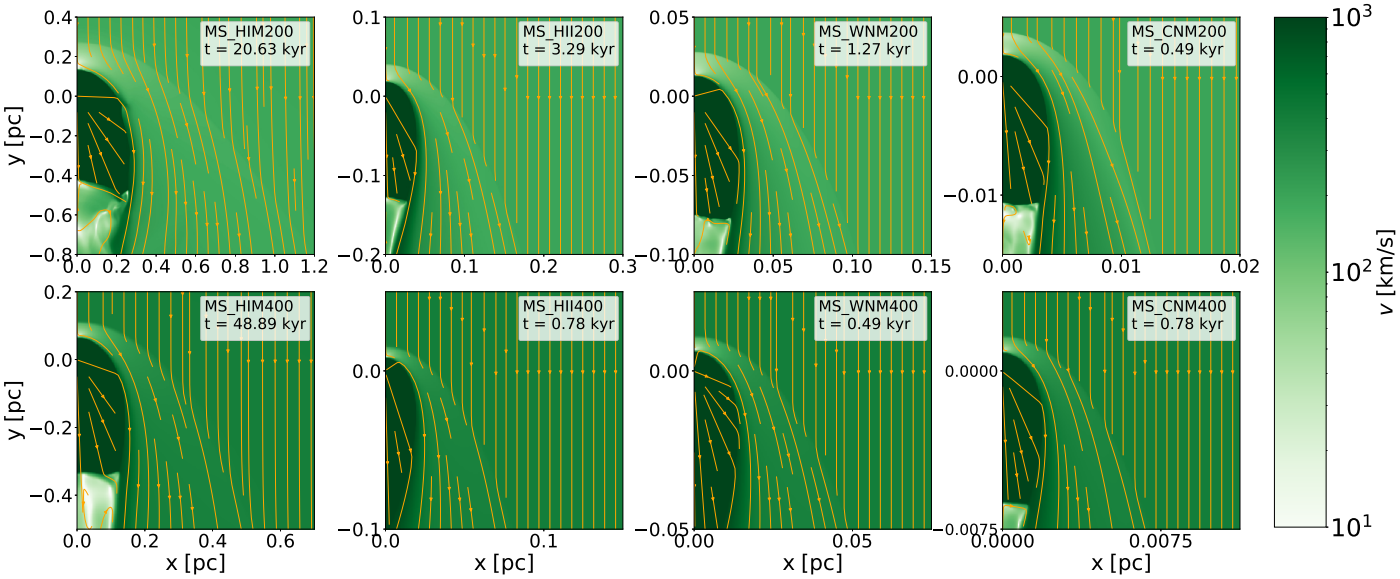

FIGURE 6.5: Velocity plots of the MS bow shocks for stars moving at 200 km/s (top row) and 400 km/s (bottom row) with respect to the ISM. The ISM phase in the first, second, third and fourth column is the HIM, HII region, WNM and CNM, respectively. The orange curves with arrows are the streamlines showing the fluid flow.

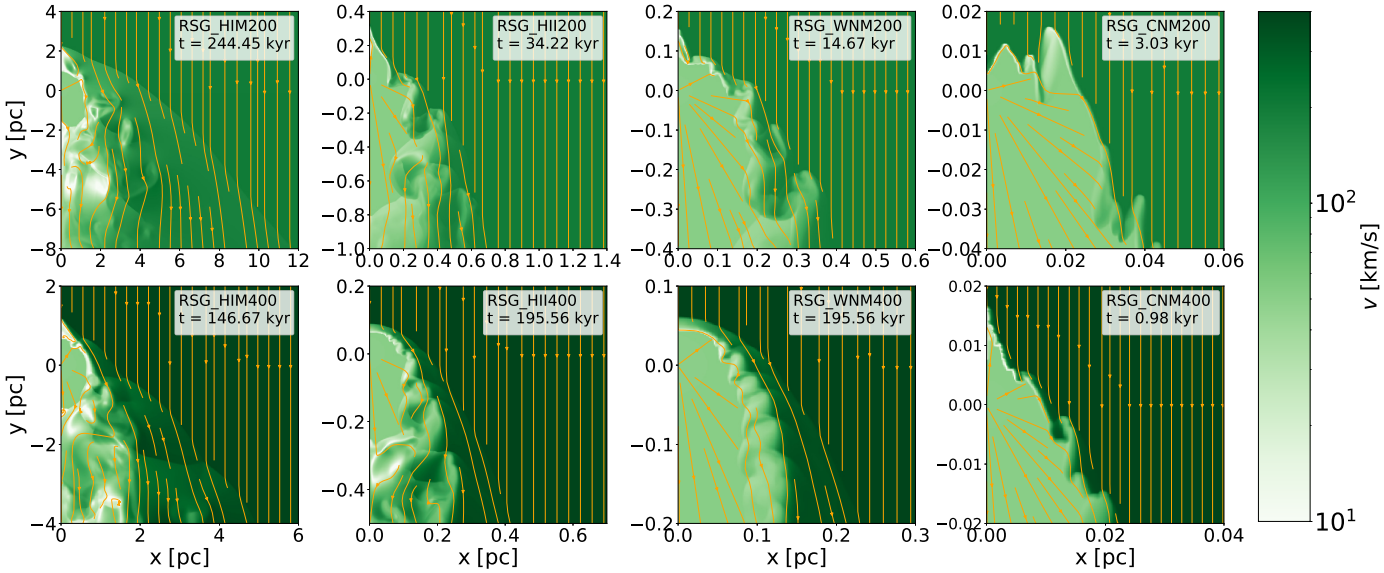

FIGURE 6.6: Velocity plots of the RSG bow shocks for stars moving at 200 km/s (top row) and 400 km/s (bottom row) with respect to the ISM. The ISM phase in the first, second, third and fourth column is the HIM, HII region, WNM and CNM, respectively. The orange curves with arrows are the streamlines showing the fluid flow.

Figure 6.7 and 6.8 for the MS and RSG case, respectively, show the emissivities of these HVR models. The emissivity is calculated by measuring the amount of energy per unit time per unit volume of each zone in the computational domain of each simulation, as given by the sum of everything from the cooling functions (see Figure 2.6 where cooling function are plotted). Since the emissivity scales with density, the emissivity of the shocked regions is higher for higher space velocity and/or ISM density models. Like the temperature plots, for the HIM models the emissivity of the unshocked ISM is approximately similar to that of the shocked regions, but not for other ISM phases. Furthermore, since the emissivity is also derived from the temperature, the cross-like artifacts also appear in these emissivity plots in all the ISM phases for the MS case, but only for the CNM phase for the RSG case. The emissivity

is highest in the shocked regions especially around the apex for both the MS and RSG case. For the MS models the emissivity is in the range $\sim 10^{-26} - 10^{-24}$, $10^{-23} - 10^{-22}$, $10^{-23} - 10^{-21}$ and $10^{-21} - 10^{-20}$ ergs cm^{-3} s^{-1} for the HIM, HII region, WNM and CNM cases, respectively, while for the RSG models it is in the range $\sim 10^{-25} - 10^{-24}$, $10^{-24} - 10^{-22}$, $10^{-24} - 10^{-22}$ and $10^{-23} - 10^{-22}$ ergs cm^{-3} s^{-1}, and for both MS and RSG cases, the higher velocity models (400 km/s) have greater emissivity for each ISM phase.

From these 2D maps, we conclude that the characteristic bow shock structures of the MS and RSG HVRs show similar trends with the physical parameters such as the ISM density and space velocity, however, the RSG models have instabilities that are more profound than the MS models, which is expected based on the theory of the non-linear thin-shell instabilities (Dgani, van Buren, and Noriega-Crespo 1996).

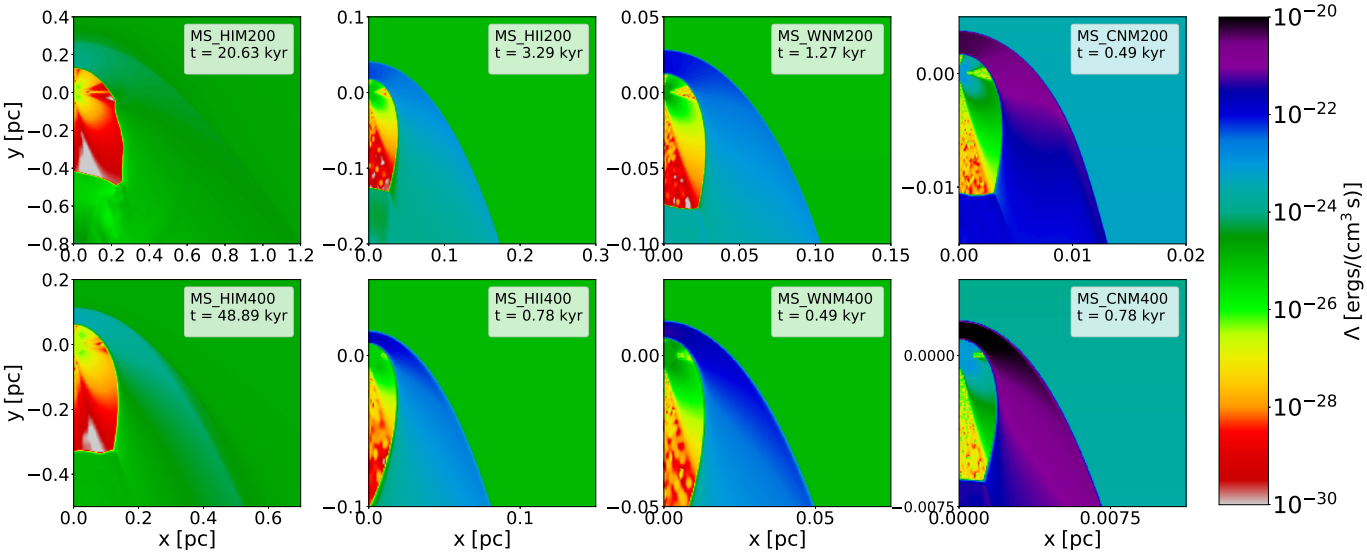

FIGURE 6.7: Emissivity plots of the MS bow shocks for stars moving at 200 km/s (top row) and 400 km/s (bottom row) with respect to the ISM. The ISM phase in the first, second, third and fourth column is the HIM, HII region, WNM and CNM, respectively.

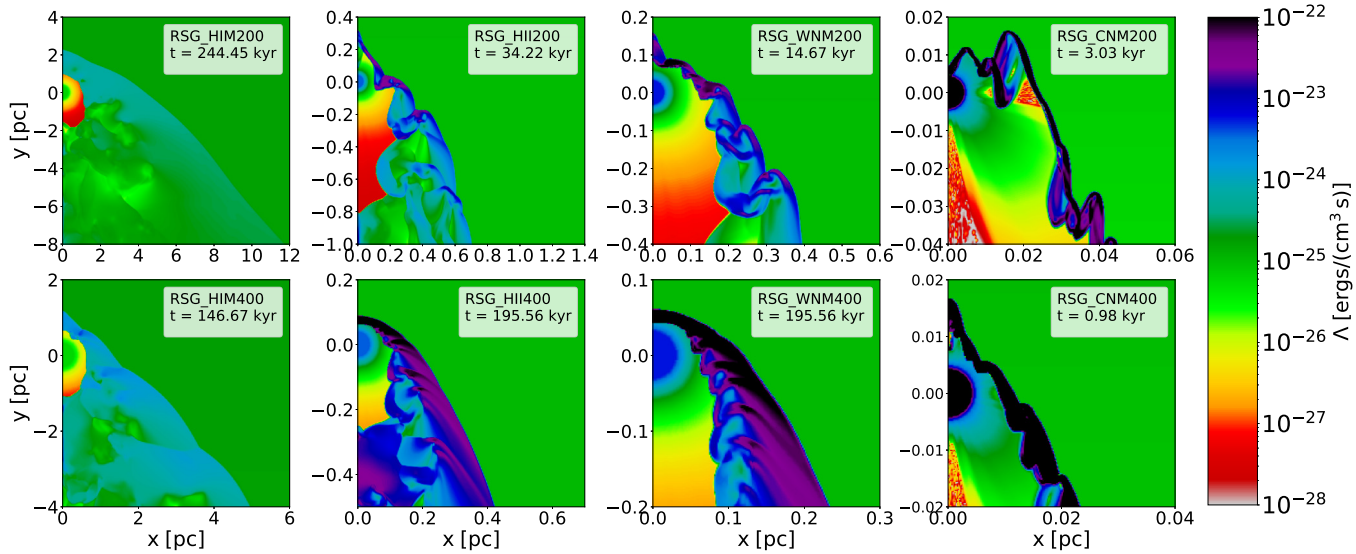

FIGURE 6.8: Emissivity plots of the RSG bow shocks for stars moving at 200 km/s (top row) and 400 km/s (bottom row) with respect to the ISM. The ISM phase in the first, second, third and fourth column is the HIM, HII region, WNM and CNM, respectively.

6.2.2 The evolution of the MS and RSG HVR bow shock structures

The evolution of the shape of the bow shock models presented in Section 6.2.1 is measured using $R(0^o)/R(90^o)$ and is compared to the Wilkin (1996) analytic solution (Equation 1.8) as shown in Figures 6.9 and 6.10 for the MS and RSG case, respectively, where $R(0^o)$ is the distance between the star and the contact discontinuity parallel to the direction of motion (i.e., along the apex), while $R(90^o)$ is similar to $R(0^o)$ but perpendicular to the direction of motion.

The higher the space velocity of the central star and/or the denser the ISM, the quicker the bow shock simulation reaches a steady state as shown in Table 6.2. These changes in structure of the bow shocks as a function of time are also compared to the Wilkin (1996) analytic solution. From Figure 6.9 plots, we see that all the MS models reach a steady state and remain in steady state, while most RSG models reach a steady state and then start to diverse due to the carbuncle phenomenon, which can be seen by the rising curves on the top row of Figure 6.10. Furthermore, from Table 6.2, it seems the 200 km/s MS models takes approximately twice as along to reach a steady state compared to the 400 km/s MS model for the same ISM phase, as would be expected from the crossing times. However, the density of the ISM phase seems to have a more significant effect on how quick the models reach a steady state.

Even though the 2D maps of the MS bow shock models shown in Figures 6.1, 6.3, 6.5 and 6.7 do not show any growth of instabilities, their corresponding evolution plots in Figure 6.9 do show oscillations which are due to very small instabilities; note, the jaggedness seen in some of the plots is due to time sampling and discretization of the fluid, which can be solved by increasing the time and spatial resolution (but in our case this is not possible as due to limited computational resources). In addition, the theory of the non-linear thin-shell instability states that the bow shock is more stable and the rate at which these instabilities grow is lower for smaller values of $\frac{v_*}{v_w}$ (Dgani, van Buren, and Noriega-Crespo 1996). This is the case for these MS HVR models since $v_w >> v_*$, because the MS stars have fast winds of order $\sim$ 1000 km/s or higher (Lamers and Cassinelli 1999; Kippenhahn, Weigert, and Weiss 2012) as discussed in Chapter 3.

However, for the RSG case, the 2D maps in Figures 6.2, 6.4, 6.6 and 6.8 show large growth of instabilities, which cause oscillations in their corresponding evolution curves in Figure 6.10. For the RSG case, most of the models are initially in agreement with the Wilkin (1996) analytic solution, but as they evolve, they diverge from the analytic solution because of the build-up of fluid at the tip of the bow shock. This is a well known limitation of 2D simulations (some of the simulations by Green et al. (2019) also exhibit this issue), and may be due to the carbuncle phenomenon. Some models, specifically the RSG_HII400 and RSG_WNM400 do not exhibit this build-up of fluids, and they remain in steady state and agree well with the analytic solution throughout their evolution, even though they have strong instabilities.

The Kelvin-Helmholtz, Rayleigh–Taylor and non-linear thin-shell instabilities exhibited by these RSG bow shocks have as expected, higher growth rates compared to those of MS stars (see oscillations in Figures 6.9 and 6.10), because for RSG stars the wind velocity is slower (50 km/s) compared to the star's velocity (either 200 km/s or 400 km/s), i.e., ($\frac{v_*}{v_w} >> 1$), which should result in less stable bow shocks (Dgani, van Buren, and Noriega-Crespo 1996).

TABLE 6.2: Time taken for the MS and RSG HVR models to reach a steady state along the apex

Model	Time [kyr]	Model	Time [kyr]	ΔTime [kyr]
MS_HIM200	~ 3	MS_HIM400	~ 1.25	1.75
MS_HII200	~ 0.45	MS_HII400	~ 0.2	0.25
MS_WNM200	~ 0.34	MS_WNM400	~ 0.13	0.21
MS_CNM200	~ 0.06	MS_CNM400	~ 0.015	0.045
RSG_HIM200	-	RSG_HIM400	-	-
RSG_HII200	-	RSG_HII400	~ 6	-
RSG_WNM200	-	RSG_WNM400	~ 4	-
RSG_CNM200	-	RSG_CNM400	-	-

Note: These time values where approximated from the bow shock evolution plots in Figure 6.9 and 6.10 for the MS and RSG case, respectively. The symbol (-) means the models reach steady state and then move out of steady state due the carbuncle phenomenon. ΔTime is the difference between the time taken for the 200 km/s and 400 km/s models to reach a steady state for each ISM phase.

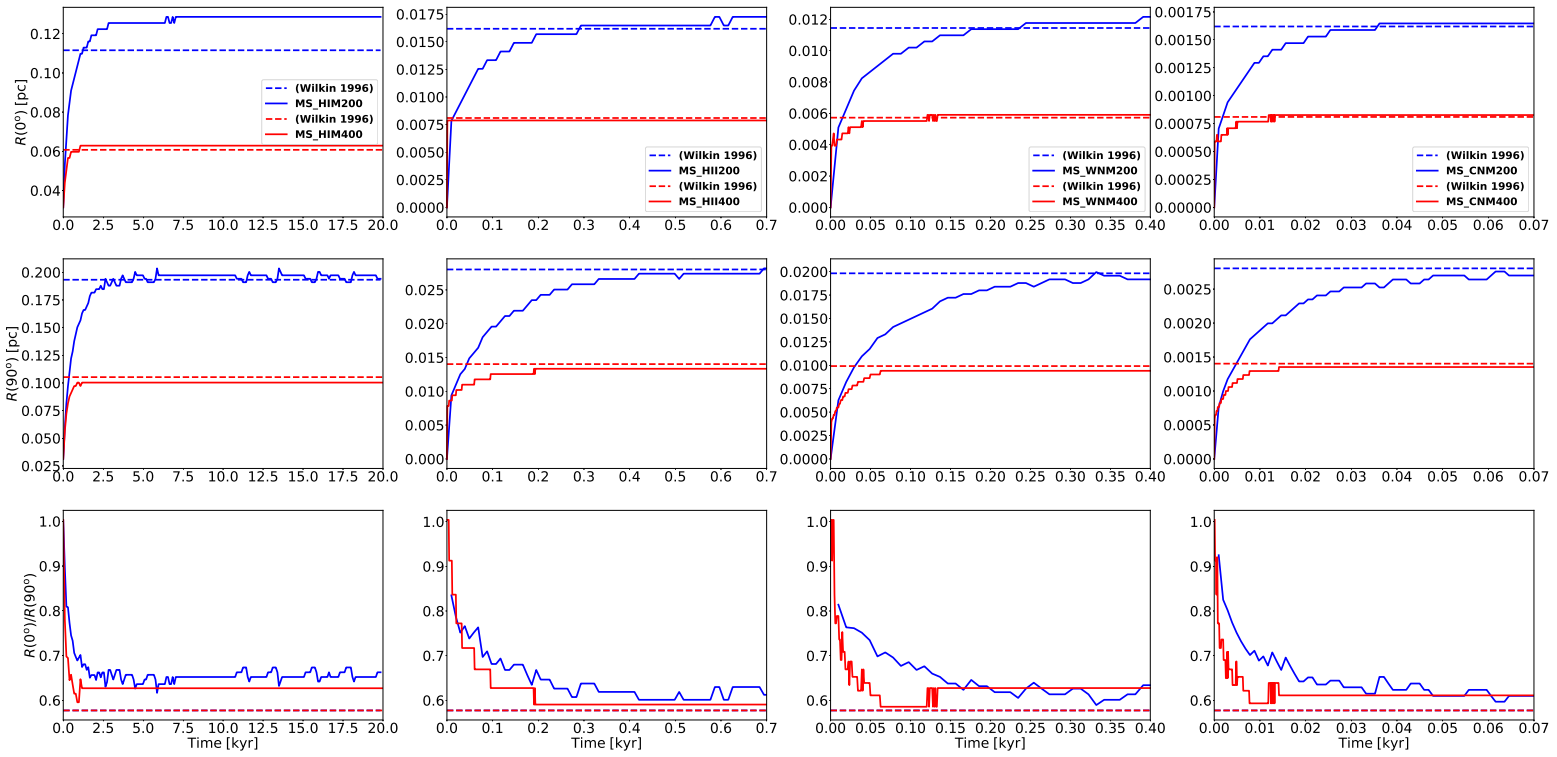

FIGURE 6.9: Evolution of the bow shock around a MS star moving at 200 km/s (red) and 400 km/s (blue) with the respective model (solid) and analytic solution (dashed). The ISM phase in the first, second, third and fourth column is the HIM, HII region, WNM and CNM, respectively. The first, second and third rows are for the $R(0^o)$, $R(90^o)$ and $R(0^o)/R(90^o)$, respectively, where $R(0^o)$ and $R(90^o)$ are the distances between the star and the contact discontinuity, parallel and perpendicular to the direction of motion, respectively.

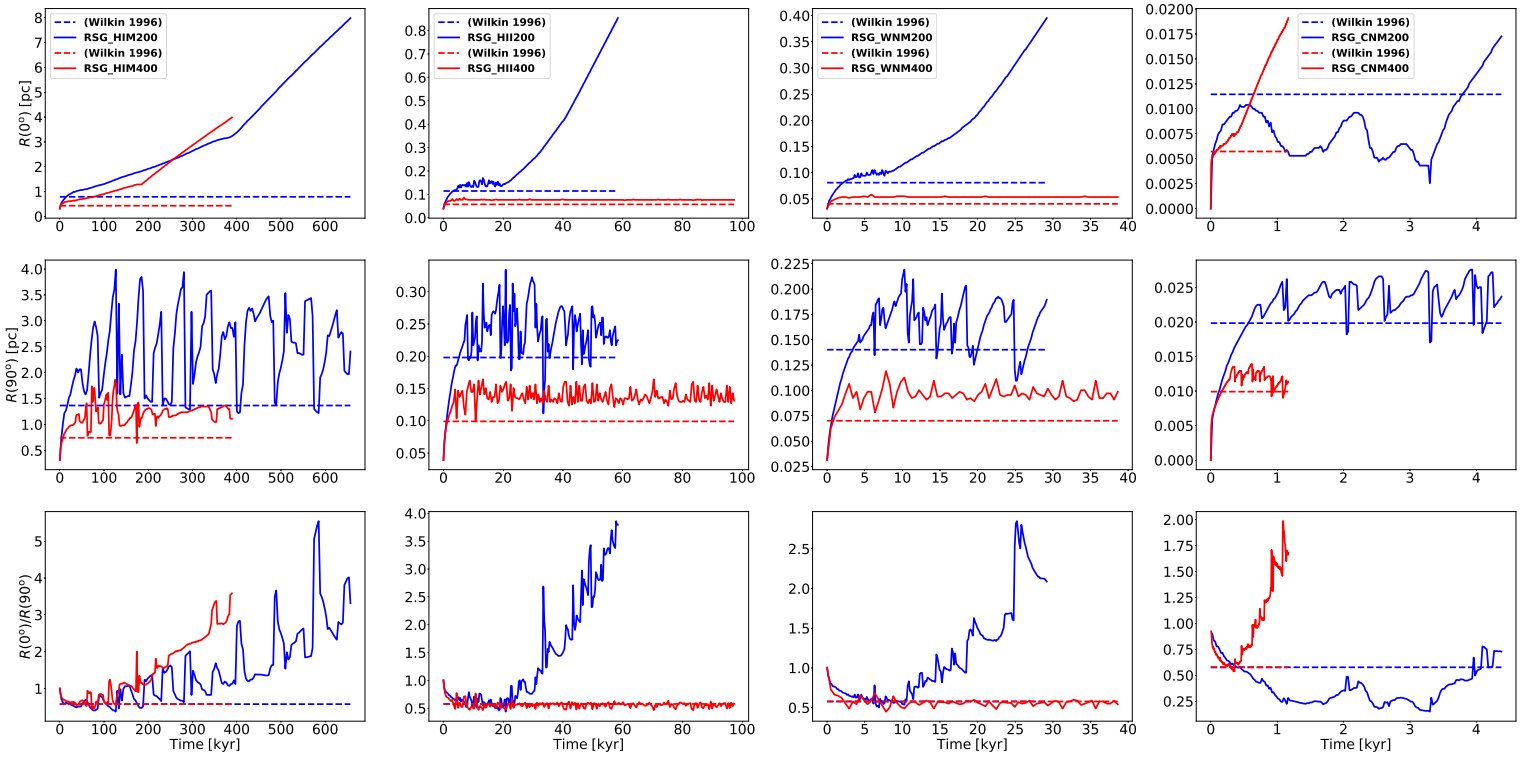

FIGURE 6.10: Evolution of the bow shock around a RSG star moving at 200 km/s (red) and 400 km/s (blue) with the respective model (solid) and analytic solution (dashed). The ISM phase in the first, second, third and fourth column is the HIM, HII region, WNM and CNM, respectively. The first, second and third rows are for the $R(0^o)$, $R(90^o)$ and $R(0^o)/R(90^o)$, respectively, where $R(0^o)$ and $R(90^o)$ are the distances between the star and the contact discontinuity, parallel and perpendicular to the direction of motion, respectively.

6.2.3 Dynamical and cooling timescales

The dynamical and cooling timescales are shown in Figures 6.11 - 1.12 for the models presented in Section 6.2.1.

The definition of the timescales that we use are similar to that of Mohamed, Mackey, and Langer (2012) and Meyer et al. (2014), where the dynamical timescale is calculated as

$$\tau_{\rm dyn} = \frac{R_{\rm SOD}}{v}, \tag{6.1}$$

and the cooling timescale is calculated as

$$\tau_{\rm cool} = \frac{P}{\Lambda}, \tag{6.2}$$

where P, Λ and v are as defined in Chapter 2. When $\tau_{\rm cool} << \tau_{\rm dyn}$, the fluid elements show an isothermal behaviour, and when $\tau_{\rm cool} >> \tau_{\rm dyn}$ the fluid elements would show an adiabatic behaviour (Mohamed, Mackey, and Langer 2012; Meyer et al. 2014).

As shown in Figures 6.11 and 6.12 for MS and RSG case, respectively, $\tau_{\rm cool} \gtrsim \tau_{\rm dyn}$ always, because HVR stars move at such high speed that the $\tau_{\rm dyn}$ is always smaller

than $\tau_{\rm cool}$. We notice an adiabatic behaviour for the MS case in the region of the freely expanding wind for all the models, and the unshocked ISM region for the CNM models, while in the RSG case, it is only in the CNM phases. None of the models in Figures 6.11 and 6.12 exhibit the isothermal behaviour, because $\tau_{\rm cool}$ is always greater than $\tau_{\rm dyn}$.

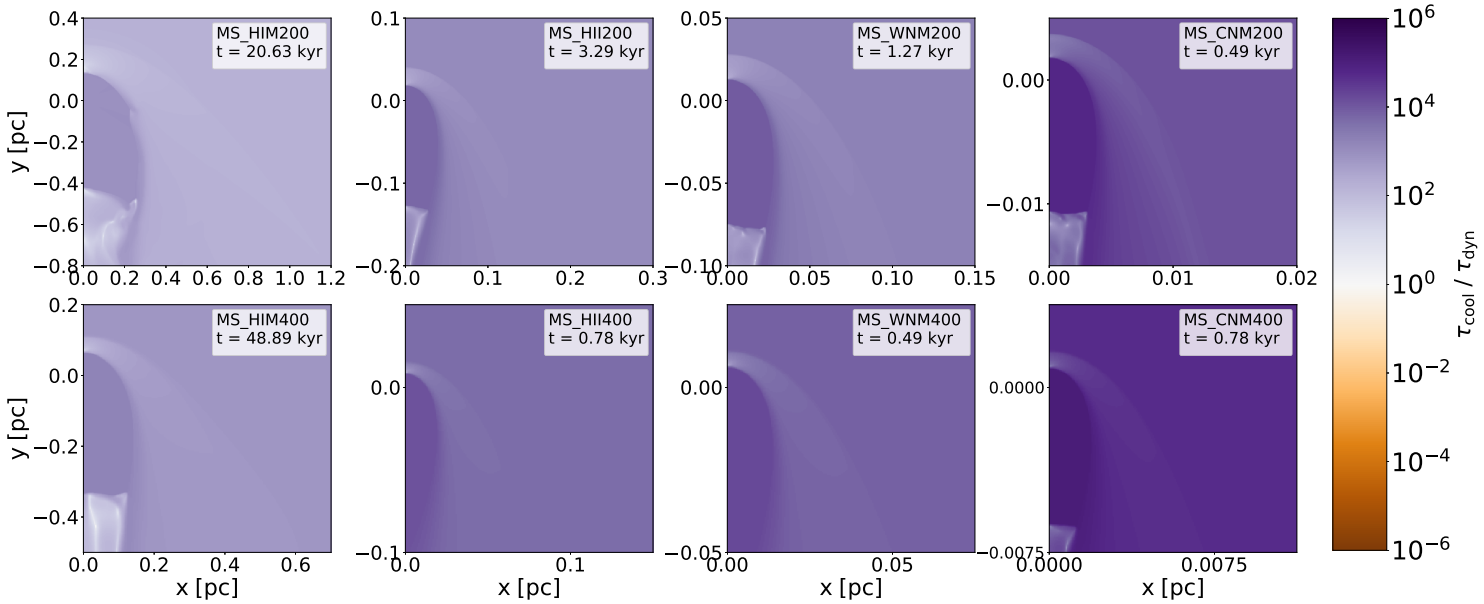

FIGURE 6.11: The ratio of the cooling timescale ($\tau_{\rm cool}$) to the dynamical timescale ($\tau_{\rm dyn}$), for MS case. The stellar space velocity and ISM phase are indicated in the legend along with the bow shock age.

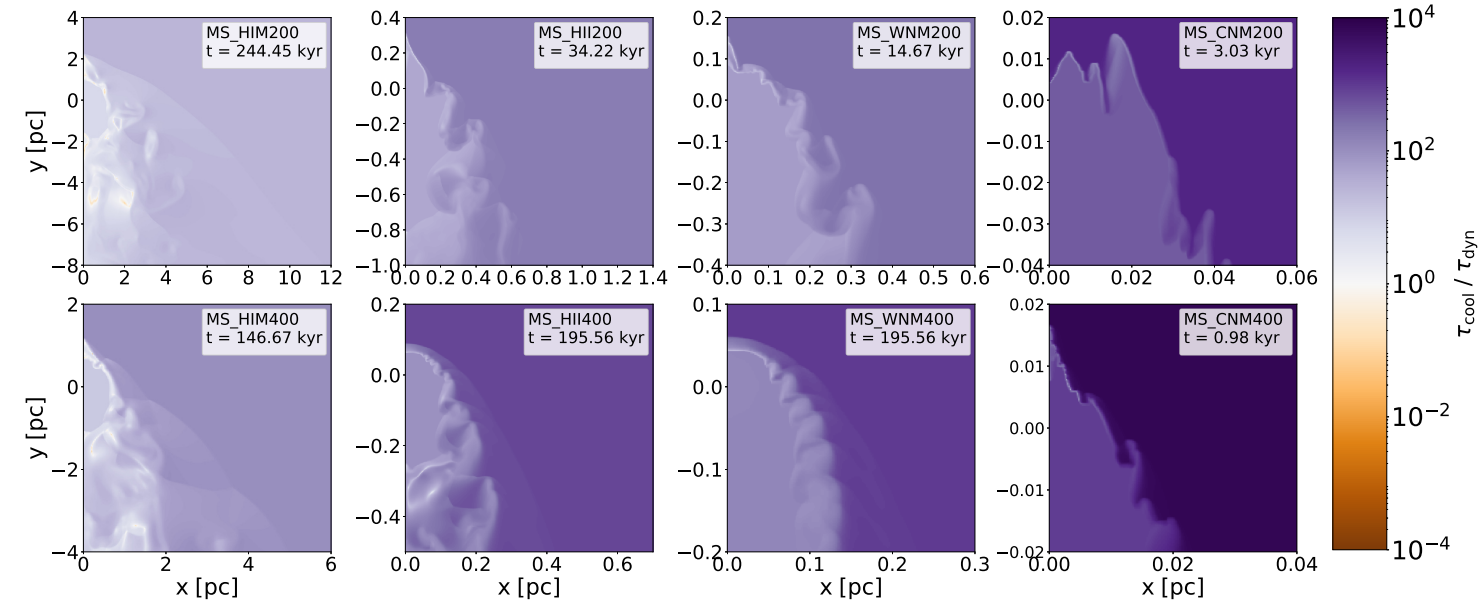

FIGURE 6.12: The ratio of the cooling timescale ($\tau_{\rm cool}$) to the dynamical timescale ($\tau_{\rm dyn}$), for RSG case. The stellar space velocity and ISM phase are indicated in the legend along with the bow shock age.

6.3 Comparing 2D and 3D models

To investigate the effect of dimensionality on the bow shock stability and numerical artifacts, we ran 3D models corresponding to the 2D models of the WNM as shown in Table 6.1. The WNM was chosen because it fills a significant amount ($\sim$ 40%) of the volume of the Galactic disk (Draine 2011), and so is interesting from an observational perspective and one of the 2D models exhibits the carbuncle phenomenon (RSG_WNM200), while the other (RSG_WNM400) does not (see Figures 6.2, 6.4, 6.6 and 6.8). The results for the 2D models and 3D cross-sections are discussed in Section 6.3.1 and see Appendix C.4 for the 3D plots.

6.3.1 Comparing 2D and 3D RSG_WNM200 and RSG_WNM400 models

To explore the similarities and differences between 2D and 3D RSG_WNM200 and RSG_WNM400 models, we sliced the 3D models in order to obtain the x-y 2D plane with similar dimensions to the 2D model and the results are shown in the 2D maps in the left and middle columns, respectively, of Figures 6.13 - 6.14 for RSG_WNM200 and Figures 6.15 - 6.16 for RSG_WNM400. We took cuts along the apex of both models shown in the left and middle columns of Figure 6.13 for RSG_WNM200 and Figure 6.15 for RSG_WNM400, and the resulting profiles are shown in the corresponding right-hand column of these figures. Additional cuts were made along the horizontal as indicated in the left and middle columns of Figure 6.14 for RSG_WNM200 and Figure 6.16 for RSG_WNM400 which pass through the smooth regions and clumpy regions, and their profiles are shown in the right column of the corresponding figures.

For model RSG_WNM200, the similarities between the 2D and 3D models demonstrate that they both experience the carbuncle phenomenon. In addition, the profiles extracted along the apex are different for 2D and 3D as shown in the right column of Figure 6.13, because 2D and 3D models have different instabilities. The differences in the instabilities were investigated further by making horizontal cuts which are represented by (black lines) as shown in Figure 6.14 (left and middle columns). The major difference can be noticed in the 2D maps around x $\approx$ 0.2 pc at the region where the y ≈ -0.07 pc and y ≈ -0.11 pc horizontal cuts pass through, whereby the 3D cross-section map has a more clumpy region than the 2D model. In addition, there is a more spread out vortex around x $\approx$ 0.2 pc at the region where the y ≈ -0.21 pc and y ≈ -0.24 pc horizontal cuts pass through.

For model RSG_WNM400, the instabilities are also the main difference when going from 2D to 3D as shown in the density, temperature, velocity and emissivity maps of Figure 6.15. In the top part of the maps (y $\gtrsim -0.1$ pc), the 2D and 3D plots are similar in their instabilities, but in the bottom part (y $\lesssim -0.1$ pc) they are not. Further analysis of the top and bottom part of the maps is carried out in Figure 6.16. The extracted profiles in the smooth regions of the maps, represented by the black lines (i.e., y ≈ -0.01 pc and y ≈ -0.04 pc), have corresponding profiles that are very similar for both the 2D and 3D model. The profiles extracted in the clumpy regions of the maps, represented by the white lines (i.e., y ≈ -0.065 pc and y ≈ -0.095 pc), have profiles that are also similar for both the 2D and 3D model for y ≈ -0.065 pc, but very different for y ≈ -0.095 pc, i.e., small scale instabilities are similar but on large scales their growth differs. This can be seen in the down stream profiles in the right column of Figure 6.16.

Overall results from both 2D and 3D of RSG_WNM200 and RSG_WNM400, suggest that the 3D model is about 1.8% larger than the 2D model, which can be seen from the extraction plots along the apex, and the major difference between 2D and 3D are in their instabilities, which can be seen from the extraction plots along the horizontal. This difference in instabilities in 2D and 3D models is expected and happens because an extra dimension allows for more complex internal flows for the 3D models (Blondin and Koerwer 1998), as a result the profiles from the 3D cross-sections have larger or smaller parameter (density, temperature, velocity and emissivity) values compared to the profiles from the 2D models as shown in the 1D plots in Figures 6.14 and 6.16 (right column). Furthermore, the 2D and 3D of models RSG_WNM200 both exhibit similar numerical artifacts, and the 2D and 3D of model RSG_WNM400 have similar instabilities on small scales which then differ on large scales. Overall for both RSG_WNM200 and RSG_WNM400, the 2D and 3D models are at least as unstable as one another, similar to findings by Blondin and Koerwer (1998).

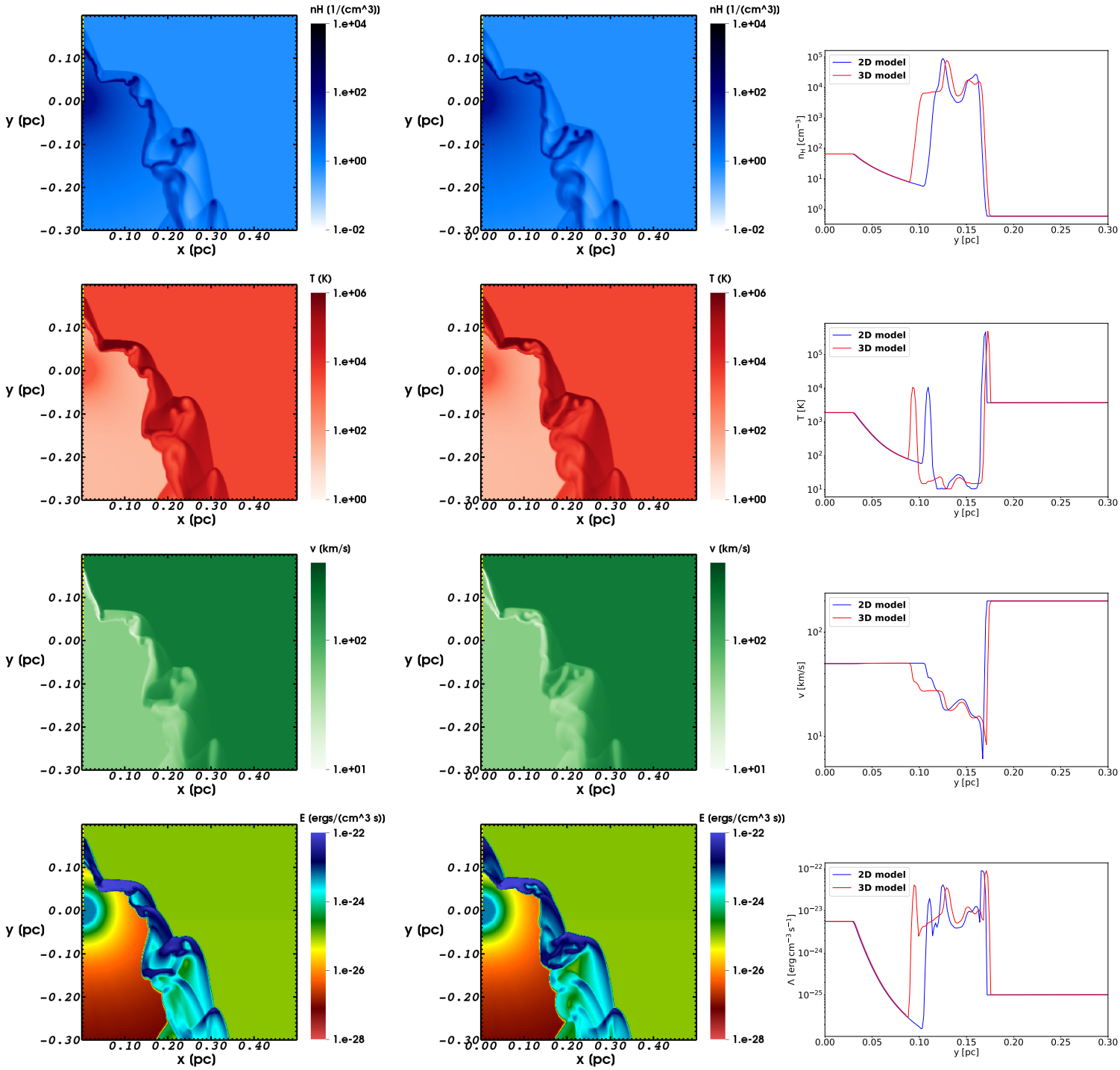

FIGURE 6.13: The bow shocks of model, RSG_WNM200, with the density, temperature, velocity and emissivity plots in the first, second, third and fourth row, respectively. We have the 2D map in the left column and the cross-section from the 3D model in the middle column, with the respective profiles extracted along the apex (i.e., $0 \leq y \leq 0.3$ pc) in the right column.

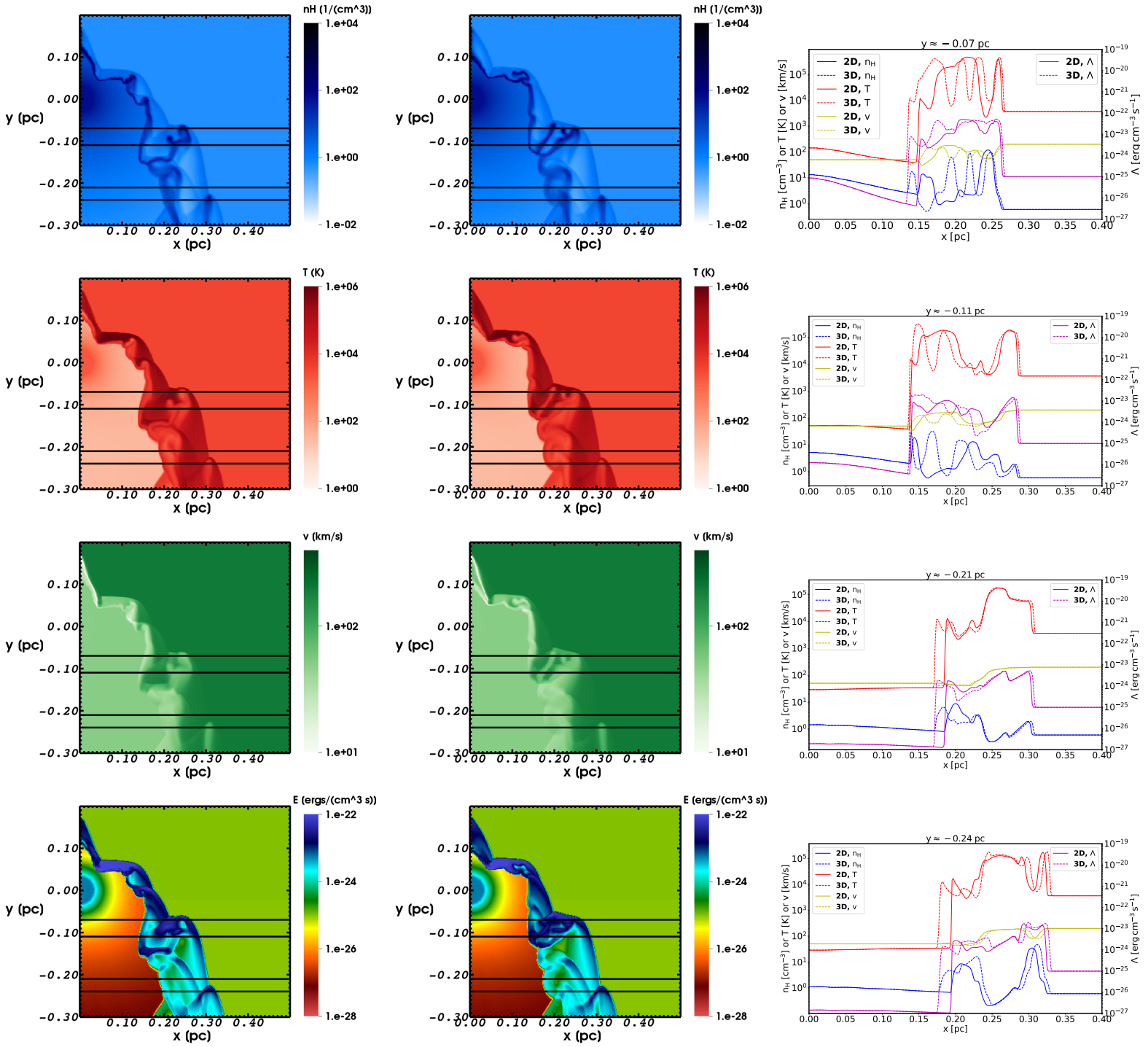

FIGURE 6.14: The bow shocks of model RSG_WNM200 showing the regions of the extracted profiles (the black horizontal lines) for the 2D model (left column) and 3D cross-section (middle column). The extracted lines in format (x1, y1) to (x2, y2) are (0, -0.07) to (0.4, -0.07), (0, -0.11) to (0.4, -0.11), (0, -0.21) to (0.4, -0.21) and (0, -0.24) to (0.4, -0.24). [Right column] The profiles corresponding to the extracted regions, i.e., y ≈ -0.07 pc (first row), y ≈ -1.1 pc (second row), y ≈ -0.21 pc (third row), and y ≈ -0.24 pc (fourth row).

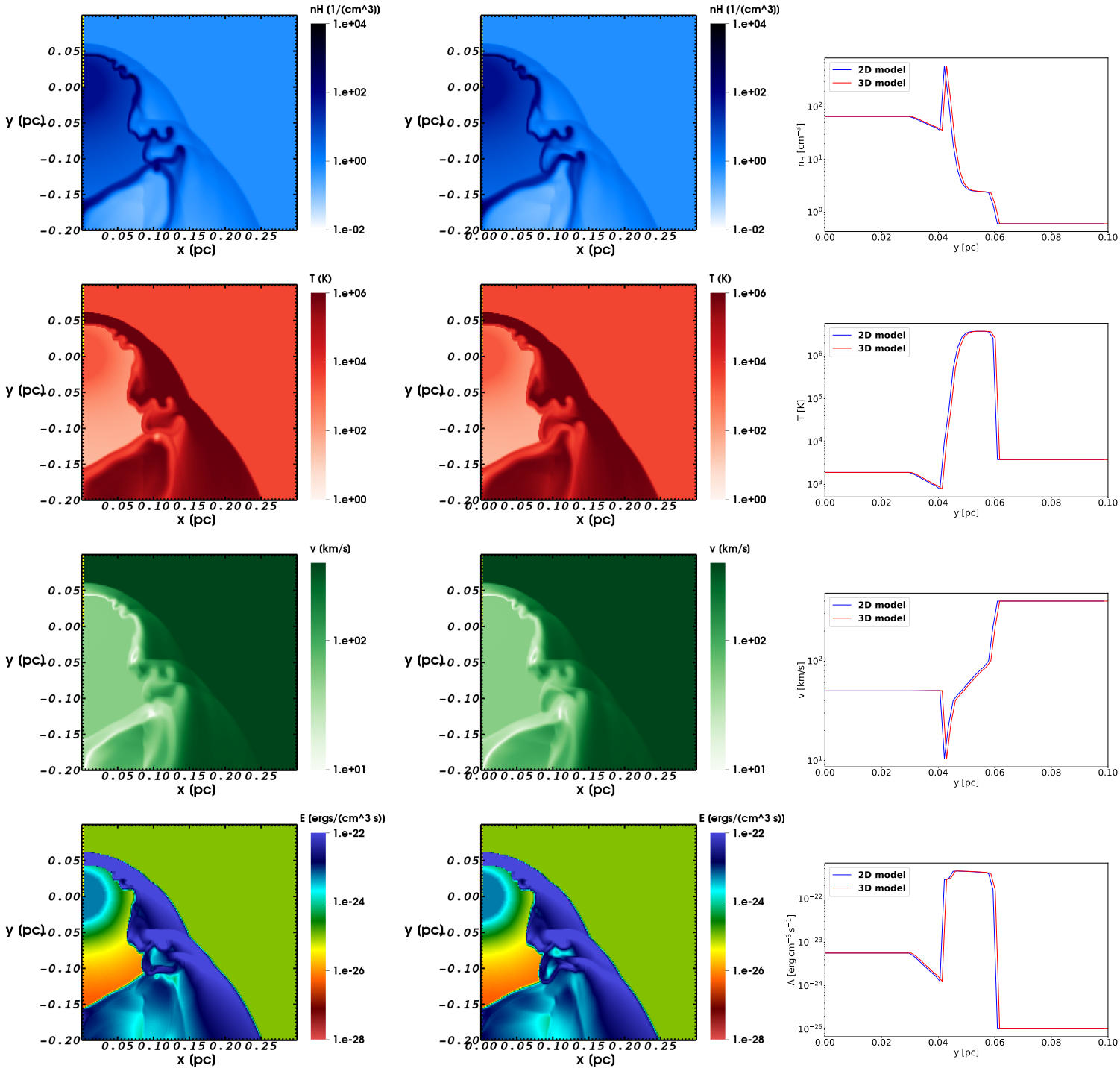

FIGURE 6.15: The bow shocks of model, RSG_WNM400, with the density, temperature, velocity and emissivity plots in the first, second, third and fourth row, respectively. We have the 2D map in the left column and the cross-section from the 3D model in the middle column, with the respective profiles extracted along the apex (i.e., $0 \leq y \leq 0.1$ pc) in the right column.

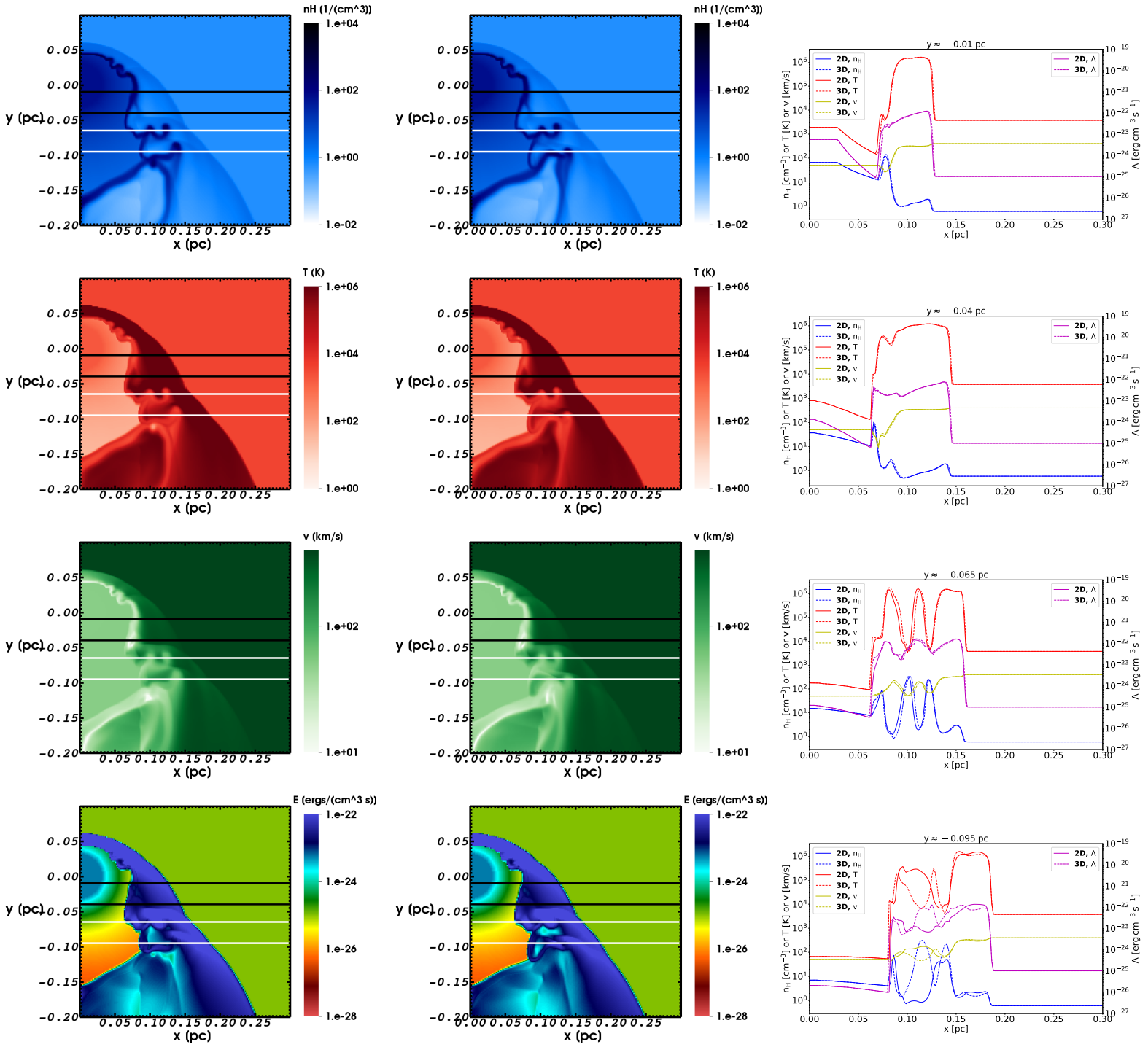

FIGURE 6.16: The bow shocks of model RSG_WNM400 showing the regions of the extracted profiles (the black and white horizontal lines for the clumpy and smooth regions, respectively) for the 2D model (left column) and 3D cross-section (middle column). The extracted lines in format (x1, y1) to (x2, y2) are (0, -0.01) to (0.3, -0.01), (0, -0.04) to (0.3, -0.04), (0, -0.065) to (0.3, -0.065) and (0, -0.095) to (0.3, -0.095). [Right column] The profiles corresponding to the extracted regions, i.e., y ≈ -0.01 pc (first row), y ≈ -0.04 pc (second row), y ≈ -0.065 pc (third row), and y ≈ -0.095 pc (fourth row).

The bow shock structures and shapes of the MS models for the space velocities and ISM phases explored here, all converge towards the Wilkin (1996) analytic solution, while for the RSG models, all the bow shocks have large instabilities and diverge away from the Wilkin (1996) analytic solution due to the carbuncle phenomenon, except for the RSG_HII400 and RSG_WNM400 which reach and remain in steady state (i.e., no carbuncle phenomenon), and they are in agreement with the Wilkin (1996) analytic solution. All the RSG models exhibit mostly the Kelvin-Helmholtz instabilities at higher space velocities and Rayleigh–Taylor instabilities at lower ISM densities. However, for both the MS and RSG models, the bow shock size becomes smaller with the increase in the space velocity and/or ISM density, because increasing one or both of these parameters results in an increase in the ram pressure of the ISM, which results in the decrease in the stand-off distance, $R_{\rm SOD}$, which characterises the bow shock size.

From the comparison of the 2D and 3D models, we see that they both have similar structures and if there are artificial flow characteristics due to the carbuncle phenomenon, then they will be present in both the 2D and 3D models. The major difference between the 2D and 3D models is in their instabilities. In 3D there is an extra spatial dimension which allows for the fluid flow to be more realistic, while in 2D one of the dimensions is acting as a barrier which restrict the fluid from passing through. This results in the instabilities of the 2D models being different to those of the 3D models.

6.4 Comparison with previous studies

We first checked our modifications to the PLUTO code by comparing runaway models with analytic values and previous studies. The 40 and 70 km/s 2D test models are similar to the models of Meyer et al. (2014) as shown in Chapter 4, Figure 4.5 and 4.6 for MS and RSG stars, respectively. The similarity in the 40 km/s MS models is in the bow shock size and flow characteristics which depend on whether the conditions are adiabatic, cooling or thermal conduction; while for the 40 and 70 km/s RSG models, the similarities are in the Kelvin-Helmholtz instabilities and the dependence of the bow shock size on the space velocity. In addition, our MS 40 km/s model with cooling and thermal conduction is consistent with case A model of Comerón and Kaper (1998) where thermal conduction and cooling are also included. The structure of our 40 km/s MS model with cooling differs from the 40 km/s BD $+ 60^{\rm o}2522$ bow shock models of Green et al. (2019), with a smooth stable flow rather than Kelvin-Helmholtz and Rayleigh-Taylor instabilities. This is likely due to the lower ISM density, $n_{\rm H} = 0.57$ cm^{-3} in addition to thermal conduction in our case, while the star moved through much higher densities in the range $n_{\rm H} = 50 - 200$ cm^{-3} and no thermal conduction was included. The vortices that appear in our 40 and 70 km/s RSG bow shock models in Figure 4.3, are formed as a result of velocity shear at the front region of the bow shock. The development of Kelvin-Helmholtz instabilities, which forms vortices as they propagate downstream to the tail of the bow shock, are similar to the 75 km/s AGB bow shock model by Wareing, Zijlstra, and O'Brien (2007b).

The early stages of the formation of the bow shocks of our RSG HVR models shown in Figures 6.2, 6.4, 6.6 and 6.8, are consistent with the bow shock model of an evolved star moving at 28.3 km/s of van Marle et al. (2011), the Betelgeuse double bow shock

models of Mackey (2012) and the runaway AGB bow shock models of Wareing, Zijlstra, and O'Brien (2007a), in their morphology, flow characteristics and instabilities, (see Appendix C.3, for the early stages of our Table 6.1 HVR models); and the very unstable bow shock of our RSG_CNM200 and RSG_CNM400 models with huge instabilities are similar to those of high Mach number bow shock models of Blondin and Koerwer (1998), and also similar to the instabilities of models by Brighenti and D'Ercole (1995). The Kelvin-Helmholtz and Rayleigh-Taylor instabilities of our RSG HVR models, are consistent with non-magnetic field simulations of Betelgeuse bow shock by van Marle, Decin, and Meliani (2014). The stability of our 2D models with respect to its corresponding 3D models are similar, which is consistent to the findings of Blondin and Koerwer (1998).

The Li, Bryan, and Quataert (2019), 3D adiabatic bow shock models of an AGB star moving at 350 km/s through both the low and high pressure ISM phases, correspond to our 2D cooling bow shock models of RSG stars moving at 400 km/s through the HIM, e.g., in their instabilities at the tail of the bow shock near the star and similarities in the bow shock sizes. In addition, our 2D model of a RSG star moving at 200 km/s in cooling conditions, is consistent with the 3D bow shock model of Mira moving at 125 km/s also in cooling conditions of Li, Bryan, and Quataert (2019), in their flow structures and instabilities.

The detection of Mira's bow shock and tail by the *Galaxy Evolution Explorer (GALEX)* ultraviolet space telescope (Martin et al. 2007) and also in the infrared by *Herschel* (Mayer et al. 2011), suggest the possibility of observing the bow shocks of RSG HVRs in the infrared and ultraviolet. This is also supported by Betelgeuse's (a RSG) bow shock observed by *AKARI* and *Herschel* in the infrared (Ueta et al. 2008; Decin et al. 2012). The 2D bow shock models of MS HVRs moving at 200 km/s in conditions where both cooling and thermal conduction are included, are relevant for the *Wide-field Infrared Survey Explorer (WISE)* observations by Gvaramadze et al. (2019), of the "horseshoe-shaped" bow shock around CPD $-64^{o}2731$, a massive O-type HVR star moving through the ISM at $\sim$ 160 km/s. The bow shock around an O-type star BD $+60^{o}2522$, was also observed by *Spitzer* an infrared Space Telescope (Green et al. 2019).

The majority of stellar bow shocks are discovered in the infrared (Gvaramadze et al. 2013), and it is likely this will also be the case for HVRs, (perhaps even with the newly launched *James Webb Space Telescope (JWST)*), however, detailed studies will be necessary to determine e.g., whether it is heated dust in the ISM or in the shocked wind (the reverse shock) that produce the emission (Ueta et al. 2006), with a large number of X-ray missions, the high energy emission even from the smallest bow shocks may be detectable perhaps as point source emission. Similarly with such high Mach number shocks emission at radio wavelengths may also be generated. The details of potential observability is beyond the scope of this thesis, but planned for future work.

Chapter 7

Conclusion

7.1 Summary and Conclusion

We have presented 2D and 3D axis-symmetric hydrodynamic models in cylindrical coordinates of the interaction of the stellar winds of massive MS and RSG HVRs with the ISM. The focus was on massive HVR stars moving with space velocities of 200 km/s and 400 km/s, which can most likely be produced via dynamical ejections. The MS and RSG evolutionary phases have different stellar wind parameters (e.g., mass-loss rates and wind velocities), which resulted in different ram pressures of the stellar wind, and thus significantly different stand-off distances ($R_{\rm SOD}$). The stellar winds of these HVRs were investigated when colliding with different ISM phases (HIM, HII region, WNM, and CNM), which have different temperatures and densities, which also resulted in different ram pressures for the ISM. The presented models were simulated while taking into account thermal conduction and radiative cooling for the MS HVRs and only radiative cooling for the RSG HVRs. The implemented thermal conduction was based on Vaidya et al. (2017), while the implemented radiative cooling was based on Ploeckinger and Schaye (2020), appropriately modified for stellar wind bow shocks. The processes that were taken into account for radiative transfer were atomic cooling; molecular vibrational, collisional and rotational cooling; bremsstrahlung cooling; cosmic ray heating; Compton cooling/heating; dust grain cooling/heating and radiation heating from the HVR star. The photoionization and collisional ionization equilibrium (CIE) cooling curves were used when modelling bow shocks of MS and RSG stars, respectively.

The resolution, initial and boundary conditions of the presented 2D and 3D models of the bow shock structures of the HVRs were chosen based on our PLUTO code test results. Firstly, we performed extensive 3D AGB star's freely expanding stellar wind models for testing the numerics in PLUTO, i.e., testing different static grid geometries, solvers, limiters and convergence with resolution, while comparing with the analytic models from Gawryszczak, Mikołajewska, and Różyczka (2002), (see Appendix B). Secondly, we tested the effect of including additional physics to our models by conducting 2D adiabatic, thermal conduction and radiative cooling bow shock models for runaways stars moving with 40 km/s, which were then verified through comparison with the analytic models (i.e., the Wilkin 1996 analytic solution) and the literature (i.e., the Meyer et al. 2014 models), (see Chapter 4). Finally, further 2D resolution tests were performed for bow shocks around MS and RSG HVRs moving at 200 km/s through the WNM of density 0.57 $\rm cm^{-3}$ in adiabatic, thermal conduction and/or cooling conditions (see Chapter 5).

Our results agree well with the work by Meyer et al. (2014). Thermal conduction

was important when modelling bow shocks around MS stars, because it significantly affected its size (by making it larger) and structure (by making it more stable with little or no instabilities). However, cooling was important for both MS and RSG models, since it made the bow shock smaller, because it decreased the thermal pressure of the wind and resulted in a smaller stand-off distance ($R_{\rm SOD}$). The bow shocks around RSG HVRs had significant growth of instabilities compared to the bow shocks around MS HVRs, which was expected according to the non-linear thin-shell instabilities by Dgani, van Buren, and Noriega-Crespo (1996), which states that the instability growth rate is low for the $\frac{v_*}{v_{\rm w}} << 1$ case (e.g., MS HVR stars) and high for the $\frac{v_*}{v_{\rm w}} >> 1$ case (e.g., RSG HVR stars).

In addition, because of these high space velocities of HVRs and the velocity shear between the stellar wind and the ISM, Kelvin-Helmholtz instabilities were excited, which dominated in models with higher space velocities; while owing to the high density contrast between the stellar wind and the ISM, Rayleigh–Taylor instabilities were excited, which dominated in models with lower ISM densities. All the models of the bow shocks around MS HVRs converged toward the Wilkin (1996) analytic solution, while most of the bow shocks around RSG HVRs diverged away from the Wilkin (1996) analytic solution because of the carbuncle phenomenon, (see Chapter 6 and Appendix C.1). The 2D maps of the HVR models showed that the bow shock becomes smaller with increase in ISM density or space velocity while keeping other parameters unchanged, as expected from the Wilkin (1996) analytic solution. An increase in one or both of these two parameters also resulted in the bow shock models reaching steady state much quicker, in addition, the high space velocities resulted in a shorter dynamical timescale ($\tau_{\rm dyn}$) than the cooling timescale ($\tau_{\rm cool}$).

The 3D HVR models were only conducted for RSG WNM models, due to the limited computational time available, and the high cost of necessary resolution and the inclusion of thermal conduction for the MS case. In addition, because of limited computational resources, only the WNM was chosen because it fills a significant volume of the Galactic disk (Draine 2011), and so is interesting from an observational perspective. Furthermore, the 200 km/s model exhibited the carbuncle phenomenon while the 400 km/s models did not. The comparison between the 2D and 3D models showed that the major difference between the two is in their bow shock size and instabilities. The 3D models were $\sim$ 1.8% larger than the 2D models and the flow characteristics were more realistic because of the extra dimension, which permitted more movement of the fluid and thus differences in the formation and growth of instabilities. The similarity between the 2D and 3D models was that they both exhibited the carbuncle phenomenon.

7.2 Final remarks

The models presented in this work have some limitations; firstly, possibly due to the axis-symmetric cylindrical coordinates both the 2D and 3D models of RSGs exhibited the carbuncle phenomenon, an artificial and unphysical build-up of fluid at the apex of the bow shocks; possible approaches for addressing this in future work would be to use an asymmetric geometry, or to have the star travel at an angle through the grid, however according to Elling (2006), ways of avoiding it are trial and error because the theory behind it is poorly understood. Secondly, higher resolution is computationally costly, but this can be solved by applying adaptive mesh

refinement (AMR), which will enable an increase in resolution only at the shocked regions of the bow shock structures with reasonable computational cost. Third, the initial conditions of the stellar wind and ISM parameters remain constant throughout the simulations, as such, we did not get bow shocks with evolving stellar wind parameters and changing ISM properties; in future work this will be corrected by coupling these hydrodynamic models to stellar evolutionary codes (e.g., MESA (Paxton et al. 2011)) and considering a heterogeneous ISM. Finally, for simplicity we did not include the effects of magnetic fields (e.g., the interstellar magnetic field can inhibit the instabilities (van Marle, Decin, and Meliani 2014)) and stellar rotation (e.g., rotation of stars results in the polar region being hotter than other regions of the surface of the stars, which in turn results in anisotropic stellar winds (Maeder and Meynet 2011)), but we consider including them in future work.

Studying stellar wind bow shocks is important because it can help constrain stellar wind properties (e.g., mass-loss rates and wind velocities), and ISM properties (e.g., ISM densities and temperatures). In addition, studying bow shocks produced by HVRs has one major advantage over runaway stars, because HVRs move at higher speeds which will enable them to interact with more of the ISM in their paths before reaching the end of their lives, for example, HVRs can interact with other ISM phases that are different to that of their origin, thus enabling us to study the properties of ISM phases further away from where the HVRs were formed. Furthermore, the high space velocities of HVRs which are comparable to the Galactic escape velocity can also enable these stars to leave their host galaxies and interact with mediums outside of it, which would be interesting for studies of the mediums in the outskirts of galaxies. The major disadvantage of studying bow shocks of HVRs is that they are very small compared to that of runaways, which raises the question of the observability (in terms of resolution) of HVR bow shocks, for example, it would be difficult to identify whether or not the emission is from a bow shock if they are observed as point sources.

These HVRs' bow shocks are small with stand-off distances ($R_{\rm SOD}$) $\sim 8.0 \times 10^{-4} - 1.3 \times 10^{-1}$ pc for MS stars and $\sim 6.0 \times 10^{-3} - 8.9 \times 10^{-1}$ pc for RSGs. The larger value of the stand-off distances in these ranges correspond to HVR models for which the ISM phase is the HIM, and as seen from Figures 6.1 - 6.8 of their models, the densities and temperatures of the unshocked ISM are comparable to that of the shocked regions, suggesting it might be difficult to observe them, even though their stand-off distances are in agreement with the previous observations (for example, the bow shocks of Betelgeuse, Vela X-1 and CPD $-64^{\circ}2731$ have stand-off distances ~ 0.3, 0.57 and 0.9 pc, respectively (Mohamed, Mackey, and Langer 2012; Gvaramadze et al. 2018; Gvaramadze et al. 2019, and references therein)). In addition, the small values of stand-off distances in these ranges result in the bow shocks being closer to the central star, meaning most of the bow shocks may be difficult to make direct observations even with current high resolution telescopes, however, their strong shock interactions result in high emissivities ($\sim 10^{-30} - 10^{-20}$ erg cm^{-3} s^{-1} and $\sim 10^{-28} - 10^{-22}$ erg cm^{-3} s^{-1} for MS and RSG stars, respectively), which may contribute to, and need to be taken into account, when investigating the stellar (point source) emission.

In future work, the potential of observing these bow shocks of HVRs will be investigated by making multi-wavelength estimates using radiative transfer codes (e.g., TORUS (Harries 2000)), in addition to producing synthetic images of the emissions of

these bow shocks in different wavelengths (e.g., ultraviolet, Hα, infrared and radio). Future observations by advanced telescopes such as the *James Webb Space Telescope (JWST)* which is mainly designed for infrared observations, promises to find more bow shocks since they are mostly observed in the infrared (Gvaramadze et al. 2013, and references therein), and high resolution radio telescopes such as the *Square Kilometre Array (SKA)* might find more radio emitting bow shocks similar to the recently discovered radio emission from the bow shock of Vela X-1 by MeerKAT, an *SKA* pathfinder (van den Eijnden et al. 2022).

Appendix A

Solving the Riemann problem

In this appendix, we describe in detail each of the different solvers tested and discussed in Chapter 2, for which the test results are presented in Appendix B. In addition, equations and figures are used to show how each solver works when tackling the Riemann problem. The details for the TWO-SHOCK, ROE, AUSM+, HLL, HLLC and TVDLF solvers are described in Sections, A.1, A.2, A.3, A.4, A.5 and A.6, respectively.

A.1 TWO-SHOCK Riemann solver

To better understand how the two-shock approximate Riemann solver works as shown in Colella and Glaz (1985), let's first start by writing Equation 2.7 in 1D and set $\mathbf{U} = \mathbf{A}$ and $\mathbf{F} = \mathbf{B}$ so that we have

$$\frac{\partial \mathbf{A}}{\partial t} + \frac{\partial \mathbf{B}(\mathbf{A})}{\partial x} = 0, \tag{A.1}$$

Then the Riemann problem is the initial value problem for the Equation A.1 with initial data (Colella and Glaz 1985) as

$$\mathbf{A}(\mathbf{x}, \mathbf{0}) = \begin{cases} \mathbf{A_L}, & x < 0, \\ \mathbf{A_R}, & x > 0, \end{cases} \tag{A.2}$$

where $\mathbf{A_L}$ and $\mathbf{A_R}$, respectively, represents the left and right interface states as shown in Figures (2.5 and A.1), as $\mathbf{U_L}$ and $\mathbf{U_R}$ respectively, where the $*$ in Figure A.1 represents the region of the contact discontinuity (Colella and Glaz 1985).

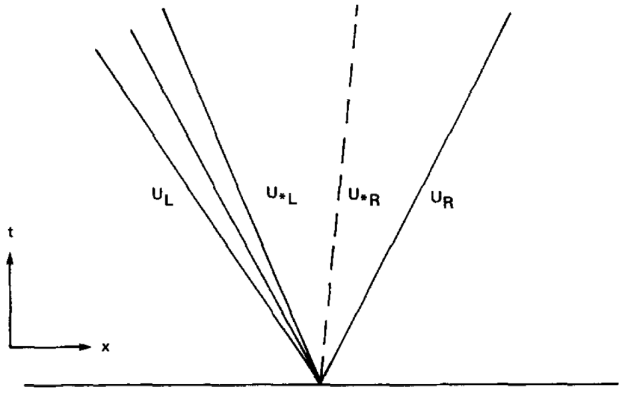

FIGURE A.1: The $x - t$ space showing the solution of the Riemann problem, where x is position and t is time. [Credit: Colella and Glaz (1985)].

Figure A.2 shows in simple terms what Figure A.1 illustrates, which is when the left state $\mathbf{A_L}$ and right state $\mathbf{A_R}$ are treated as shock waves when we have a two-shock approximate Riemann solver, and the wave at the center across which pressure and velocity remain constant is referred to as the contact, such that we have shock-contact-shock Riemann in the $x-t$ plane (Colella and Glaz 1985; Rider 1999).

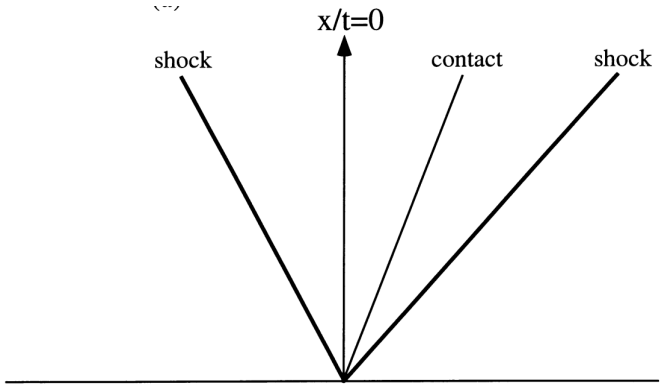

FIGURE A.2: The physical representation of the two-shock approximate Riemann problem with the two shock waves. [Credit: Rider (1999)].

A.2 ROE Riemann solver

To better understand how the Roe solver works, let's consider a 1D advection equation as shown in Equation A.1, such that $M = \frac{\partial \mathbf{B}}{\partial \mathbf{A}}$, which is a matrix of a jacobian form so that we have only the real eigenvalues (Roe 1981). Since $\mathbf{B}$ is a function of $\mathbf{A}$, the Roe solver finds the solution of the Riemann problem by considering an approximate solution of the approximate problem of Equation A.1 by using a matrix as follows:

$$\frac{\partial \mathbf{A}}{\partial t} + \tilde{M}\frac{\partial \mathbf{A}}{\partial x} = 0, \tag{A.3}$$

where $\tilde{M}$ is a constant matrix, the advantage is that it results in the unaltered data of the interface states $(\mathbf{A_L}, \mathbf{A_R})$ (Roe 1981) as shown in Equation A.2. In addition, $\tilde{M}$ is chosen in such as way that it suits the local condition and the only matrix $\tilde{M}(\mathbf{A_L}, \mathbf{A_R})$ that is acceptable must satisfy the following conditions: (1) The matrix must map linearly from vector space $\mathbf{A}$ to $\mathbf{B}$ (Roe 1981). (2) The matrix $\tilde{M}(\mathbf{A_L}, \mathbf{A_R}) \rightarrow M(\mathbf{A})$ as $\mathbf{A_L} \rightarrow \mathbf{A_R} \rightarrow \mathbf{A}$, where $M = \frac{\partial \mathbf{B}}{\partial \mathbf{A}}$. (3) $\tilde{M}(\mathbf{A_L}, \mathbf{A_R}) \times (\mathbf{A_L} - \mathbf{A_R}) = \mathbf{B_L} - \mathbf{B_R}$ for any values of $\mathbf{A_L}, \mathbf{A_R}$. (4) The linearly independent eigenvectors of matrix $\tilde{M}$. In simple terms, the matrix $\tilde{M}$ must be a "property U" matrix, see Roe (1981) for more details about the Roe solver.

A.3 AUSM+ Riemann solver

Equation A.4 shows how the AUSM+ works, it illustrates for example how we can determine the flux $\mathbf{B}$ of Equation A.1 for the interface $i + \frac{1}{2}$ of Figure 2.5 whose interface states are represented in Equation A.2 as

$$\mathbf{B}_{i+\frac{1}{2}} = M_{i+\frac{1}{2}}\frac{1}{2}\Big[a\mathbf{A}_L + a\mathbf{A}_R\Big] - \frac{1}{2}|M_{i+\frac{1}{2}}|\Big[a\mathbf{A}_R - a\mathbf{A}_L\Big] + P_{i+\frac{1}{2}}, \tag{A.4}$$

where a is a constant, $M_{i+\frac{1}{2}}$ is the Mach number of the interface, and they are related through the velocity $u_{i+\frac{1}{2}} = aM_{i+\frac{1}{2}}$, while $P_{i+\frac{1}{2}}$ is the pressure, see Liou and Steffen (1993) for the full derivation of this equation.

In simple terms, the RHS of Equation A.4 shows the left and right states as a Mach-number-weighted average instead of the traditional simple average of the interface states (Liou and Steffen 1993), so this method uses the speed to alter and represent the interface state as a way of tackling the Riemann problem, while treating the conservative and pressure terms separately (Liou and Steffen 1993; Foo et al. 1995).

A.4 HLL solver

To see how the HLL solver handles the Riemann problem, let's consider a set of conservation laws as shown in (A.1). Since in numerical methods the conservative laws are based directly on the integral form (Toro, Spruce, and Speares 1994) then the differential conservation law of form (A.1) can be written in integral form as

$$\oint \Big(\mathbf{A}dx - \mathbf{B}(\mathbf{A})dt \Big) = 0. \tag{A.5}$$

The interface states which form the Riemann problem are as shown in Equation A.2, and Figure A.3 below shows the Riemann problem's structure of the solution.

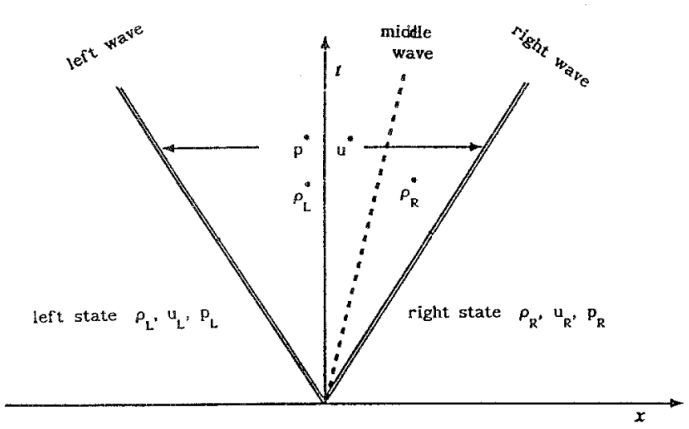

FIGURE A.3: The structure of the solution of the Riemann problem with $\mathbf{A_L}$ and $\mathbf{A_R}$ as the data for the left and right separated by $x = 0$ in the $x - t$ plane, showing three waves (the left, middle and right waves). The middle wave is the contact discontinuity, while the left and right waves are non-linear, which can either be shocks or rarefactions. The region where the variables have the $(^*)$, is called the star region and it is where we want to determine the flux, by solving the Riemann problem. [Credit: Toro, Spruce, and Speares (1994)].

The solution of the Riemann problem shown in Figure A.3 can be approximated by the HLL solver as in Figure A.4 by assuming that there is no middle wave, but only the two non-linear left and right waves, i.e., there is no contact wave in the star region as shown in the Riemann fan of Figure A.3 (Toro, Spruce, and Speares 1994).

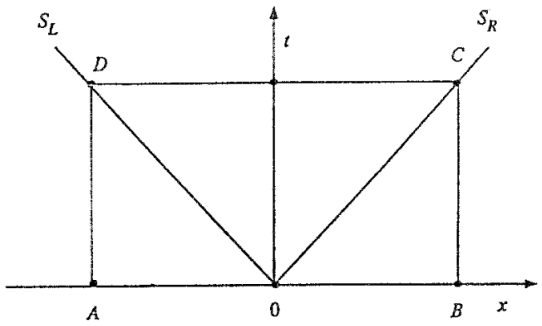

FIGURE A.4: The wave structure for the HLL approximate Riemann solver for the case where we have a subsonic flow, where $S_\mathbf{L}$ and $S_\mathbf{R}$ are the estimates for the lower and upper bound wave speed estimates. [Credit: Toro, Spruce, and Speares (1994)].

From Figures A.3 - A.4 and the basic assumptions of the HLL solver, we can evaluate Equation A.5 for the rectangle ABCD which basically gives the star region's constant vector, $\mathbf{A}^*_{\mathbf{i}+\frac{1}{2}}$, and its corresponding flux vector, $\mathbf{B}^*_{\mathbf{i}+\frac{1}{2}}$, directly as

$$\mathbf{A}^*_{i+\frac{1}{2}} = \frac{S_R\mathbf{A}_R - S_L\mathbf{A}_L - (\mathbf{B}_R - \mathbf{B}_L)}{S_R - S_L}, \tag{A.6}$$

and

$$\mathbf{B}^*_{i+\frac{1}{2}} = \frac{S_R\mathbf{B}_L - S_L\mathbf{B}_R + S_LS_R(\mathbf{A}_R - \mathbf{A}_L)}{S_R - S_R}, \tag{A.7}$$

where cell i and interface $i+\frac{1}{2}$ are replaced by the L and R respectively as subscripts in the right hand side (RHS) of Equations A.6 - A.7, with $\mathbf{B}_R = \mathbf{B}(\mathbf{A}_R)$, $\mathbf{B}_L = \mathbf{B}(\mathbf{A}_L)$ as shown in Toro, Spruce, and Speares (1994). This function of the flux forms the basis of the Godunov-type method (Godunov 1959) with the numerical flux of the HLL solver for the intercell given as

$$\mathbf{B}^{\text{HLL}}_{i+\frac{1}{2}} = \begin{cases} \mathbf{B}_i, & \text{for } S_L \geq 0, \\ \mathbf{B}^*_{i+\frac{1}{2}}, & \text{for } S_L \leq 0 \leq S_R, \\ \mathbf{B}_{i+1}, & \text{for } S \leq 0. \end{cases} \tag{A.8}$$

See Toro, Spruce, and Speares (1994) for the full derivation of Equations A.6 - A.8.

A.5 HLLC solver

The HLLC solver works in similar way to the HLL solver, but with an improvement such that three wave speed estimates are assumed as shown in Figure A.5, instead of only two as shown in Figure A.4 for the HLL solver (Toro, Spruce, and Speares 1994). The assumed wave speed estimates are S_L, S_M and S_R, and Figure A.5 shows the solution of the structure for the HLLC Riemann solver for the case of a subsonic flow which is similar to Figure A.4 but with S_M (see Toro, Spruce, and Speares (1994) for sonic and supersonic flow cases).

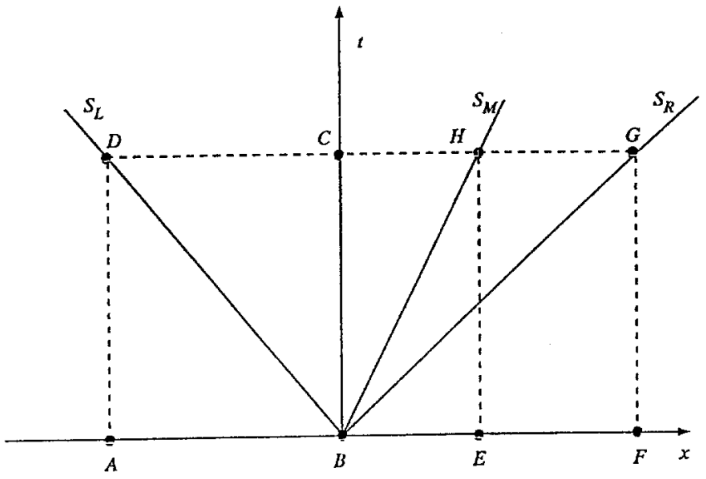

FIGURE A.5: Structure of the waves shown in the HLLC approximate Riemann solver, with wave speed estimates S_L, S_M and S_R for the case of a subsonic flow. [Credit: Toro, Spruce, and Speares (1994)].

Similar to the HLL solver, we evaluate Equation A.5 in the quadrilateral ABCD of Figure A.5, we get the fluxes in the star region (see Figure A.3 for the star region) as

$$\mathbf{B}_L^* = \mathbf{B}_L + S_L(\mathbf{A}_L^* - \mathbf{A}_L), \tag{A.9}$$

similarly for the right (R) evaluated focusing on the rectangle EFGH we have

$$\mathbf{B}_R^* = \mathbf{B}_R + S_R(\mathbf{A}_R^* - \mathbf{A}_R), \tag{A.10}$$

what's left is to find the vector $\mathbf{A}_{L/R}^*$, where the Equations A.9 - A.10 can be expressed as

$$S_{L/R}\mathbf{A}_{L/R}^* - \mathbf{B}_{L/R}^* = S_{L/R}\mathbf{A}_{L/R} - \mathbf{B}_{L/R} = \mathbf{Q}, \tag{A.11}$$

where $()_{L/R} = ()_L$ or $()_R$ depending on whether we are dealing with left (L) or right (R) of Figure A.5. The equation above can be written in full as

$$S_{L/R} = \begin{pmatrix} \rho_{L/R}^* \\ \rho_{L/R}^* u^* \\ E_{L/R}^* \end{pmatrix} - \begin{pmatrix} \rho_{L/R}^* u^* \\ \rho_{L/R}^* u^{*2} + p^* \\ u^*(E_{L/R}^* + p^*) \end{pmatrix} = \begin{pmatrix} q_1 \\ q_2 \\ q_3 \end{pmatrix} \tag{A.12}$$

in addition, at the contact discontinuity the speed is $u^* = S_M$, and the unknown vector of conserved variables in the star region can be given as

$$\mathbf{A}_{L/R}^* = \left[\rho_{L/R}^*,\ \rho_{L/R}^* u^*,\ E_{L/R}^*\right]^T, \tag{A.13}$$

which when determined can be substituted into Equations A.9 and A.10 to give the direct determination of the flux in the star region of Figure A.3. See Toro, Spruce, and Speares (1994) for detailed derivation of Equations A.9 - A.13.

A.6 TVDLF solver

To see how the TVDLF scheme works and why it does not require a Riemann solver, let's consider a system of conservation laws as shown in Equation A.1 with interface state as shown in Equation A.2. To advance the solution cross the cell interface $i + \frac{1}{2}$

in a 1D grid as shown in Figure 2.5, from level n to $n+1$ in one transport step T such that for cell i we have:

$$\mathbf{A}_i^T = \mathbf{A}_i^n - \frac{\Delta t}{\Delta x}\left(\mathbf{B}_{i+\frac{1}{2}}^{LR} - \mathbf{B}_{i-\frac{1}{2}}^{LR}\right) \tag{A.14}$$

$$\mathbf{A}_i^{n+1} = \mathbf{A}_i^T - \frac{1}{2}\left(\mathbf{\Phi}_{i+\frac{1}{2}}^{LR} - \mathbf{\Phi}_{i-\frac{1}{2}}^{LR}\right). \tag{A.15}$$

Note that terms of the form $\Delta\mathbf{A}^{LR} = \mathbf{A}^R - \mathbf{A}^L$ denotes the difference, with the term $\mathbf{\Phi}^{LR}$ denoting the dissipative limiter, which is a function of some symmetric average $\mathbf{A}^{LR}$ (Tóth and Odstrčil 1996). For TVD, the flux $\mathbf{B}$ and the dissipative limiter $\mathbf{\Phi}$ could be combined in a single modified flux (Tóth and Odstrčil 1996).

Yee (1994) multiplied the term $\mathbf{\Phi}_{i+\frac{1}{2}}^{LR}$ by the local Courant value in order to reduce the diffusivity of the original TVD scheme, resulting in a method that is computationally efficient and consistent with the solution of the schemes that use Riemann solvers (Yee 1994; Tóth and Odstrčil 1996). In addition, this TVDLF scheme preserves many of the important properties of the original TVD scheme and it is given as

$$\mathbf{\Phi}_{i+\frac{1}{2}}^{\text{TVDLF}} = \frac{\Delta t}{\Delta x} c_{i+\frac{1}{2}}^{max} \Delta\mathbf{A}^{LR}, \tag{A.16}$$

where $c_{i+\frac{1}{2}}^{max}$ is the local Courant number (Tóth and Odstrčil 1996). This equation is how the TVDLF scheme finds the flux at interface $i+\frac{1}{2}$ without using a Riemann solver. See Tóth and Odstrčil (1996) for the full derivation of Equations A.14 - A.16.

Appendix B

Exploring the PLUTO code with models of spherical winds

In this appendix, we present our exploration of the PLUTO CODE USING A model of a freely expanding stellar wind generated by a stationary (asymptotic giant branch (AGB)) star with respect to the ISM. The results are compared to the analytical solution shown in Figure 2 of Gawryszczak, Mikołajewska, and Różyczka (2002). The expansion of the stellar wind from near the surface of the star ($\sim$ 2 AU) to the outer distances away from the star ($\sim$ 10 AU) is simulated in 3D for different coordinate systems (cartesian, spherical and polar-cylindrical). For each coordinate system, we investigate the effect of resolution and different solvers, in addition to other parameters such as the limiter for the reconstruction process and the CFL value for stability and efficiency.

We conducted a resolution/convergence test in which we compared the analytic solutions to models with increasing resolution. A model would be considered to have converged if the increase in resolution did not significantly affect the results; see Zingale (2013) for detailed discussion about convergence with resolution. We used these tests to optimize the performance of the code for our specific problem, to check that our resolution was sufficient to properly capture the physics and to be as computationally efficient as possible.

In addition, for each coordinate system we tested different solvers (TWO-SHOCK, ROE, AUSM+, HLLC, HLL and TVDLF) at a specific resolution (i.e., resolution found to be useful from resolution tests). Testing different solvers is important because every solver performs best for specific types of problems. For the purpose of this project we need a solver that can easily resolve and capture shock waves, a key component of bow shock models. In the literature, they mention which solvers are best to use for specific problems as well as their advantages and disadvantages, as discussed in the Chapter 2 and Appendix A. The additional advantage of testing solvers here is that their limitations and efficiency can be checked for specific problems, instead of general problems mentioned in the literature.

All the tests were performed in 3D, and run with 240 processors. Based on the literature and discussions in Chapter 2 and Appendix A, we chose to start doing our tests using the following configuration, i.e., the default parameter settings were: grid resolution $N_{\text{zones}} = 128^3$, HLL solver, VANLEER limiter and $CFL = 0.1$, except for the tests involving that parameter. The analytic solutions from the literature are derived in Section B.1, and the test results are presented in Sections B.2 - B.9 with the summary in B.10.

B.1 The analytical solution of the free expanding stellar wind

As in Gawryszczak, Mikołajewska, and Różyczka (2002), let's consider a symmetric stellar wind which is spherical and stationary, then the density, ρ, velocity, v and pressure, P, are all a function of only the radius, r. This means the continuity equation becomes

$$\rho = \frac{\alpha}{r^2 v}, \tag{B.1}$$

where α is a variable related to the mass-loss rate $\dot{M}$ as $\alpha = \frac{\dot{M}}{4\pi}$, and in addition the momentum equation reduces to

$$v\frac{dv}{dr} = -\frac{1}{\rho}\frac{dP}{dr}. \tag{B.2}$$

In order to eliminate P, let's consider the polytropic equation of state:

$$P = \kappa\rho^{\gamma}, \tag{B.3}$$

where κ is the polytropic constant and γ is the adiabatic index. Since we are dealing with the freely expanding wind, the pressure at the surface of the star can be given as

$$P = (\gamma - 1)\rho u, \tag{B.4}$$

where u is the internal energy, and is related to the temperature, T, as follows

$$u = \frac{3}{2}\frac{k_B T}{\mu}, \tag{B.5}$$

where k_B is the Boltzmann constant and μ is the mean molecular weight. Combining Equations B.3, B.4 and B.5 gives the polytropic constant as a function of density and temperature as

$$\kappa = \left(\frac{3}{2}\frac{k_B T}{\mu}\right)(1-\gamma)\rho^{(1-\gamma)}. \tag{B.6}$$

Now substituting Equation B.3 into B.2, we get

$$v\frac{dv}{dr} = -\frac{1}{\rho}\frac{d(\kappa\rho^{\gamma})}{dr}, \tag{B.7}$$

which reduces to

$$v\frac{dv}{dr} = \kappa\gamma\rho^{(\gamma-2)}\frac{d\rho}{dr}. \tag{B.8}$$

Differentiating Equation B.1 using the quotient rule results in

$$\frac{d\rho}{dr} = -\left[\frac{\alpha}{r^2 v^2}\frac{dv}{dr} + \frac{2\alpha}{r^3 v}\right]. \tag{B.9}$$

From the combination of Equations B.8 and B.9 we can get the analytical solution of the density as

$$\frac{d\rho}{dr} = \frac{\rho}{r}\frac{2}{\kappa\alpha^{-2}\gamma r^4\rho^{(\gamma+1)} - 1}, \tag{B.10}$$

or the analytical solution of the velocity as

$$\frac{dv}{dr} = \frac{\kappa\gamma\rho^{(\gamma-2)}}{v}\left[\frac{\rho}{r}\frac{2}{\kappa\alpha^{-2}\gamma r^4\rho^{(\gamma+1)} - 1}\right]. \tag{B.11}$$

We can then derive the temperature as a function of radius by considering the equation of state relating the density and temperature as

$$P = \frac{k_B T}{\mu}, \tag{B.12}$$

Combination of B.3 and B.12 gives the analytical solution of the temperature as

$$T = \frac{\kappa\mu}{k_B}\rho^{\gamma}. \tag{B.13}$$

Equations B.10, B.11 and B.13 are the analytical solutions that will be compared to the models during our code tests of a freely expanding stellar wind. See Gawryszczak, Mikołajewska, and Różyczka (2002) for more details about the analytical solution of the spherical-symmetric stationary wind.

B.2 Cartesian coordinates

B.2.1 Testing different resolutions

We can see from Figure B.1 that as the resolution is increased, the wind becomes more spherical, this shows the importance of resolution to our stellar wind problem. At low resolution of $N_{\text{zones}} = 64^3$ the wind outflow is symmetric but not spherical, instead we get artifacts which form a cross like structure extending to the outer boundaries. This behavior is unphysical, but as the resolution is increased to $N_{\text{zones}} = 128^3$ and then to 256^3, the models become more and more reliable, which is also shown in Figure B.2 where higher resolution models agree more with the analytical solution than low resolution models.

In addition, the velocity plots of Figure B.1 are a good way to see the impact of cartesian coordinates and resolution on spherical winds, because as the resolution is increased, the yellow cross like structure which is clearly due to this cartesian coordinate system becomes even less prominent. This means increasing the resolution, can reduce the influence of the grid structure on the fluid flow, but of course at the expense of computational efficiency (see Figure B.16).

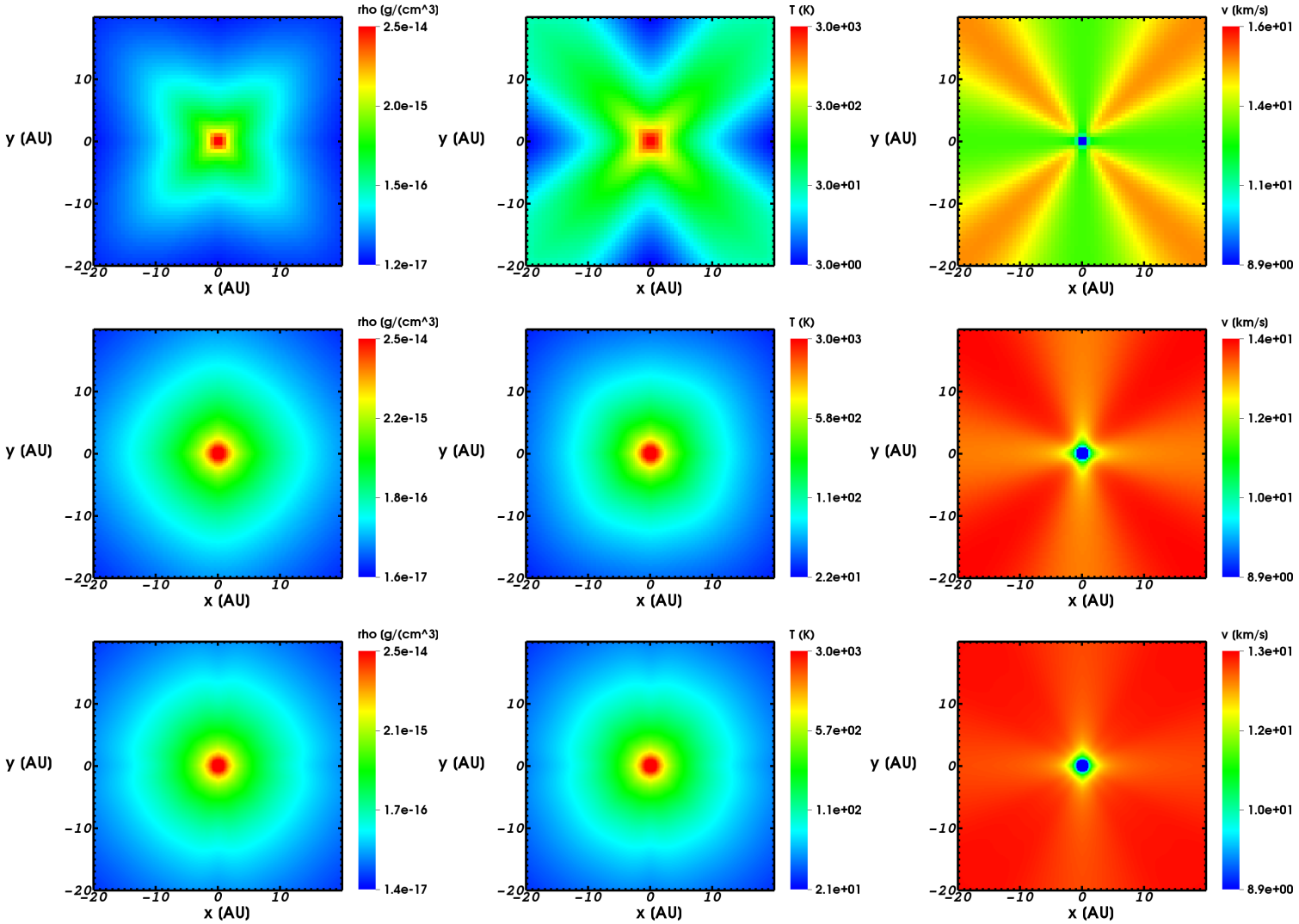

FIGURE B.1: Convergence tests of the stellar wind models in cartesian coordinates using the HLL solver. The top, middle and bottom row represents grid resolution $N_{\text{zones}} = 64^3$, 128^3 and 256^3, respectively. The left, middle and right columns represent density, temperature and velocity, respectively.

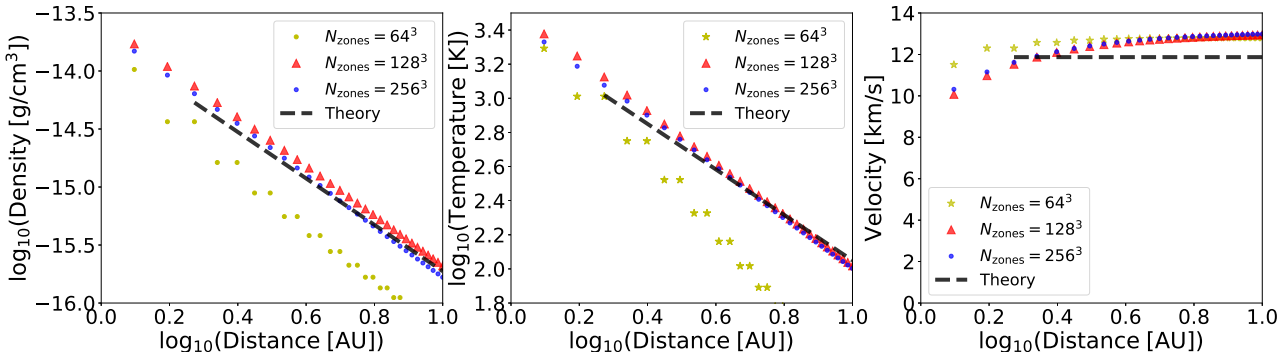

FIGURE B.2: 1D plots of the models in Figure B.1 taken from 1 AU to 10 AU and compared to the analytic solution (black-dashed line) from 2 AU to 10 AU. The yellow stars, the red triangles and the blue dots represents the models with grid resolution $N_{\text{zones}} = 64^3$, 128^3 and 256^3, respectively.

B.2.2 Testing different solvers

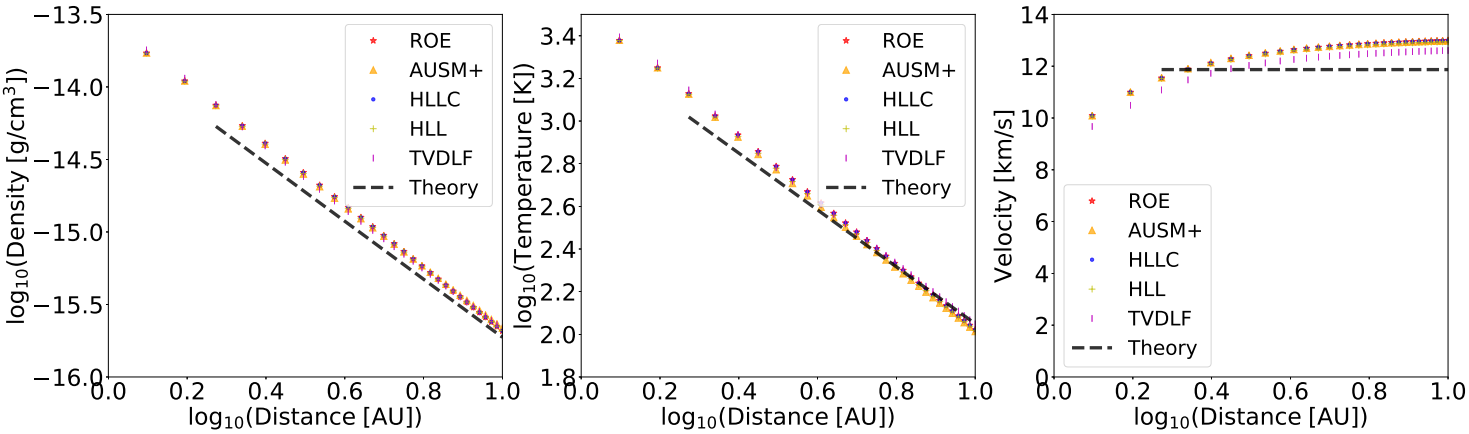

FIGURE B.3: 1D plots of the different solver models, which are taken from 1 AU to 10 AU and compared to the analytic solution (black, dashed line) which ranges from 2 AU to 10 AU. The red star, the orange triangle, the blue dot, the yellow cross and the purple vertical line represent the ROE, AUMS+, HLLC, HLL, and TVDLF solvers, respectively.

The efficiencies of the different solver were found to be similar (see Table B.1 and Figure B.16), however, from the temperature and the velocity profiles in cartesian coordinates for each case as shown in Figure B.3, the result with TVDLF solver show better agreement with the analytic solution; even though it is the most dissipative (Vaidya et al. 2018).

B.3 Spherical coordinates

B.3.1 Testing different resolutions

The advantage of using the spherical coordinate system is that we get a spherical and symmetric stellar wind outflow with no numerical artifacts at every resolution, and for each solver, as shown in Figure B.4. The resolution $N_{\text{zones}} = 256^3$ is too computationally expensive which is why it is not included, but from resolution 64^3 and 128^3 it is clear that higher resolution models show closer agreement with the analytic solution (see Figure B.5).

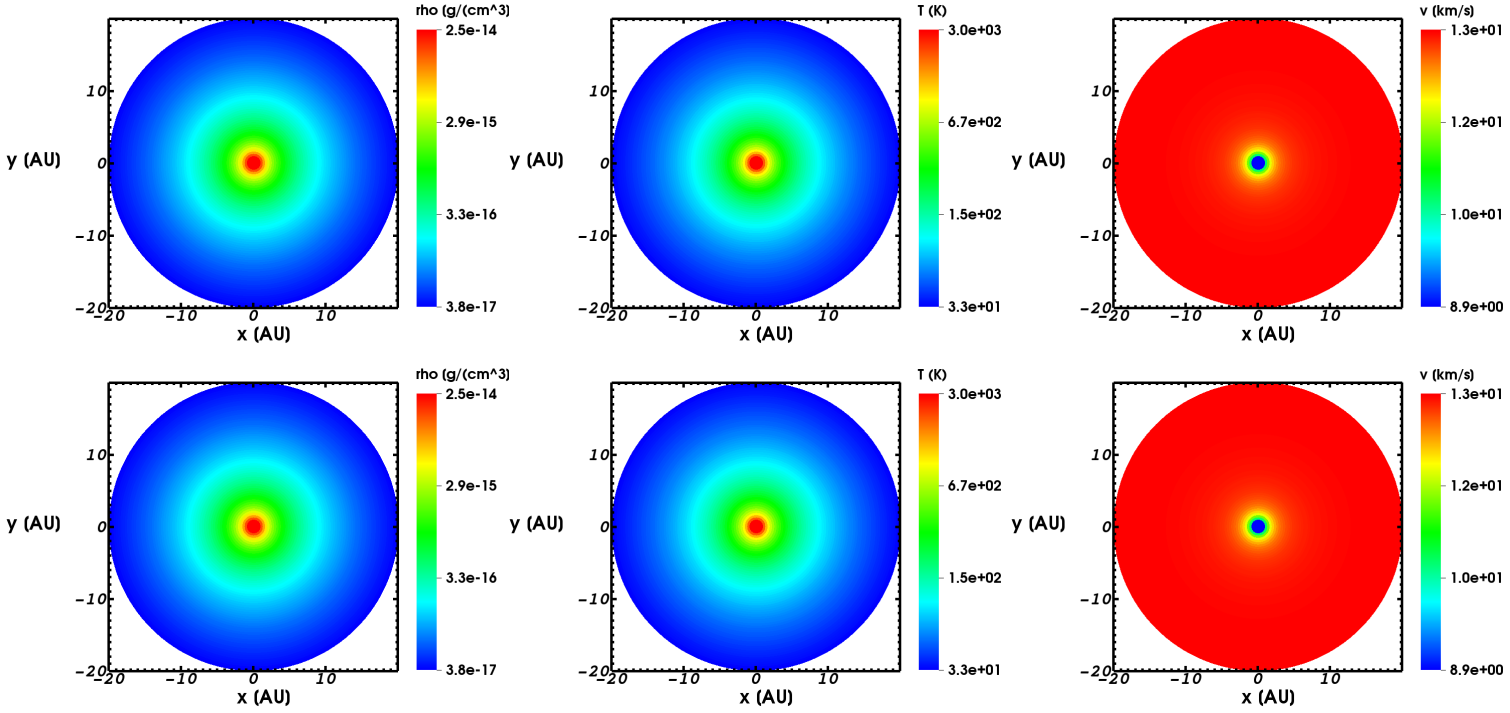

FIGURE B.4: The same as figure B.1 but for spherical coordinates.

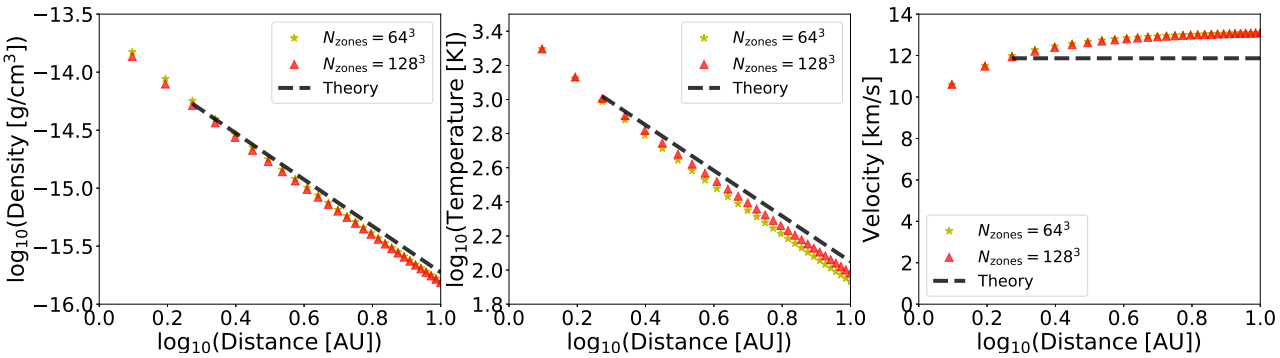

FIGURE B.5: The same as Figure B.2 but for models in spherical coordinates.

B.3.2 Testing different solvers

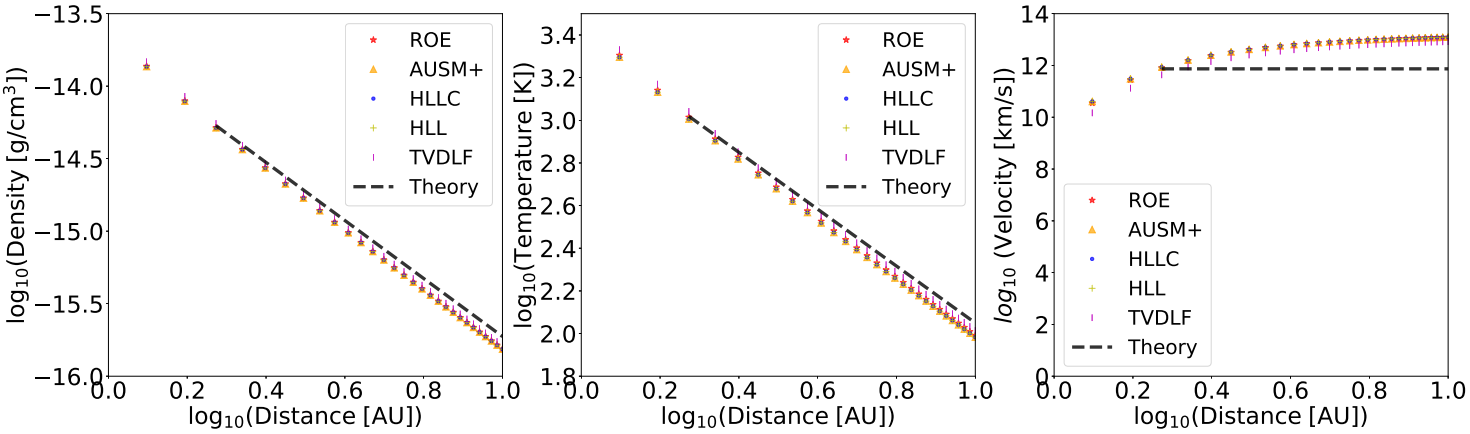

FIGURE B.6: The same as Figure B.3 but for spherical coordinates.

For this coordinate system, looking at the density, temperature and velocity profiles in Figure B.6, the models obtained using different solvers produce very similar results, with the TVDLF solver in slightly better agreement with the analytic solution. In addition, looking at the efficiencies of solvers in spherical coordinates in Table B.1, TVDLF is more efficient than the other solvers.

B.4 Polar-cylindrical coordinates XY-plane

B.4.1 Testing different resolutions

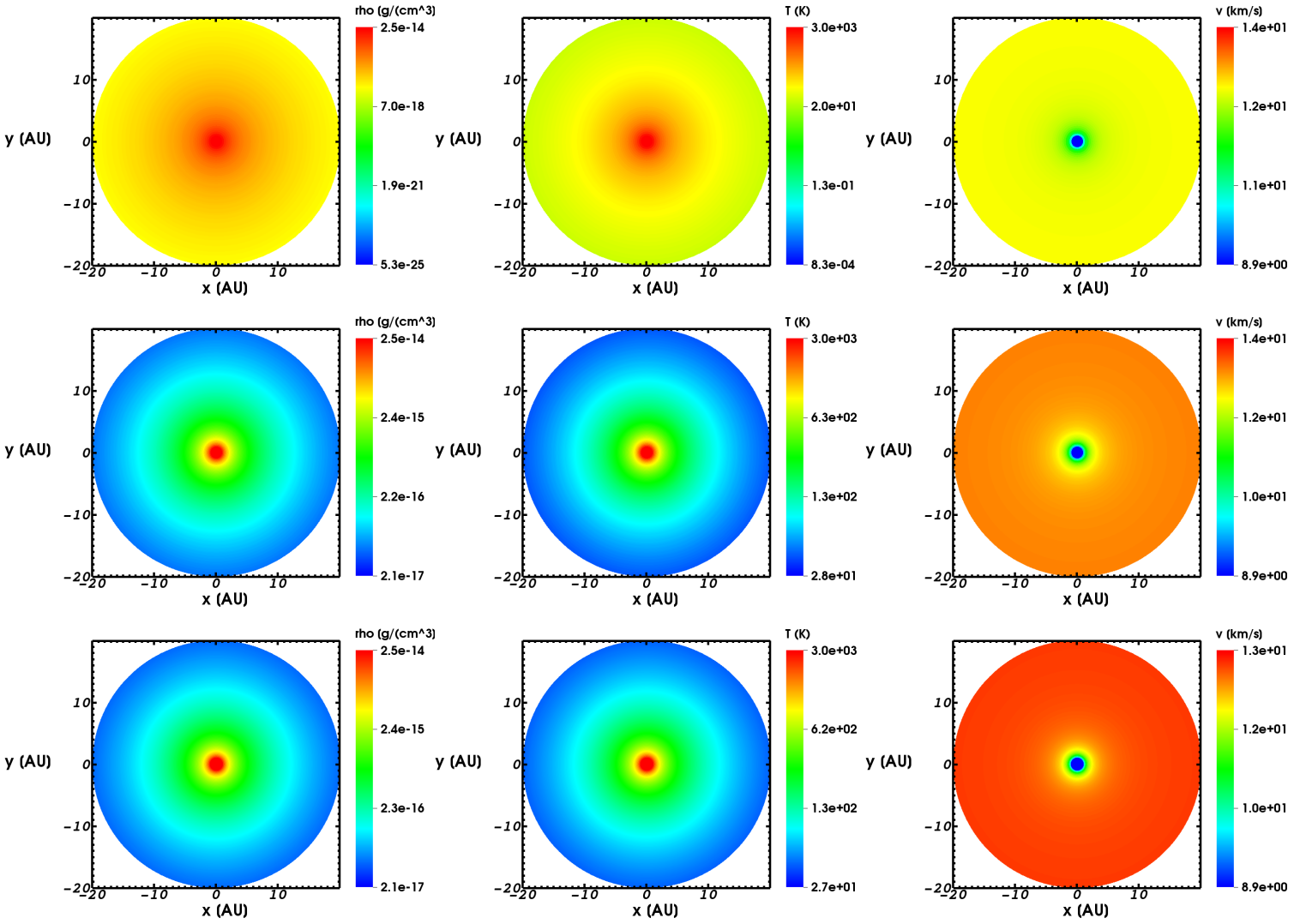

FIGURE B.7: The same as figure B.1 but for polar-cylindrical coordinates.

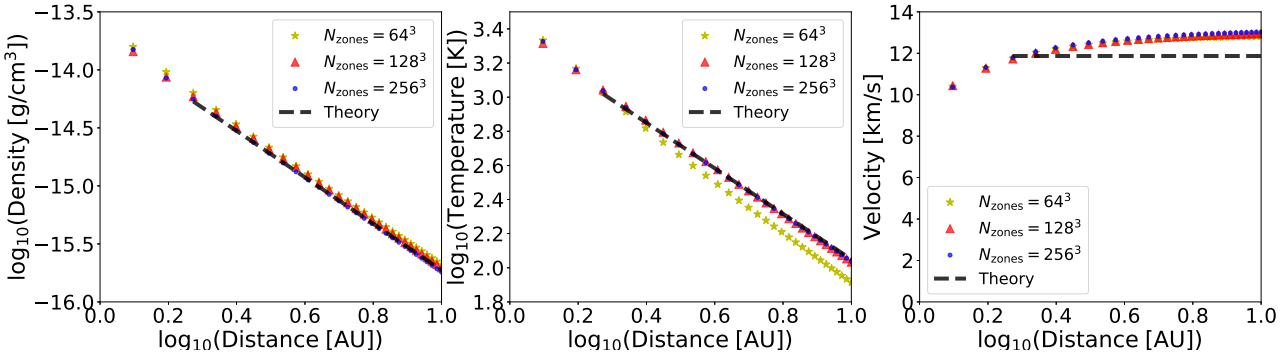

FIGURE B.8: The same as Figure B.2 but for models in polar-cylindrical coordinates.

Looking first at the XY-plane with the Z as the normal in Figure B.10, we see a symmetric and spherical wind outflow, with similar advantages for different resolutions and solvers as mentioned in the previous section of spherical coordinates. However, at the lower resolution of $N_{\text{zones}} = 64^3$, the wind is more smeared-out than at higher resolution, and the density, temperature and velocity profiles for lower resolution shows poor agreement with the analytical solution (see Figure B.8), especially in the temperature profile. Even though the winds are spherical and symmetric, we see the importance of higher resolution in order to obtain numerical models that are consistent with the analytic solutions.

B.4.2 Testing different solvers

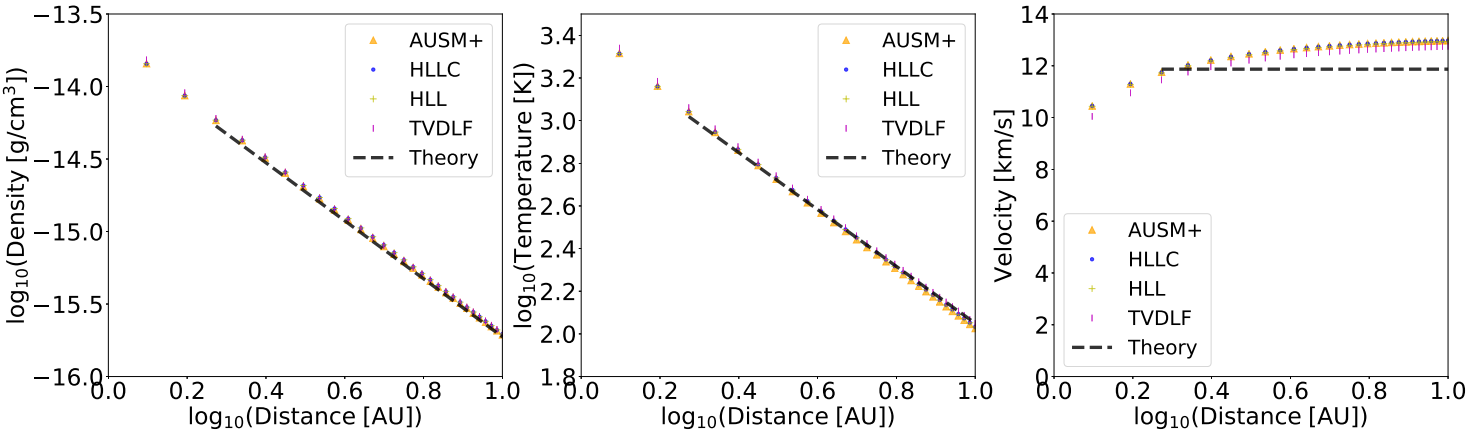

FIGURE B.9: The same as Figure B.3 but for polar-cylindrical coordinates.

A disadvantage of this coordinate system is that, as indicated in Table B.1, only four solvers were compatible. In the XY-plane of this coordinate system, all the models obtain using the different solvers are symmetric and spherical as shown in Figure B.7 for the density, temperature and velocity cross-sections. The profiles of the different solver models are shown in Figure B.9, and all show good agreement with the analytical solution, again with the TVDLF performing slight better as shown in Table B.1 and Figure B.16, the solvers have very similar efficiencies.

B.5 Polar-cylindrical coordinates XZ-plane

B.5.1 Testing different resolutions

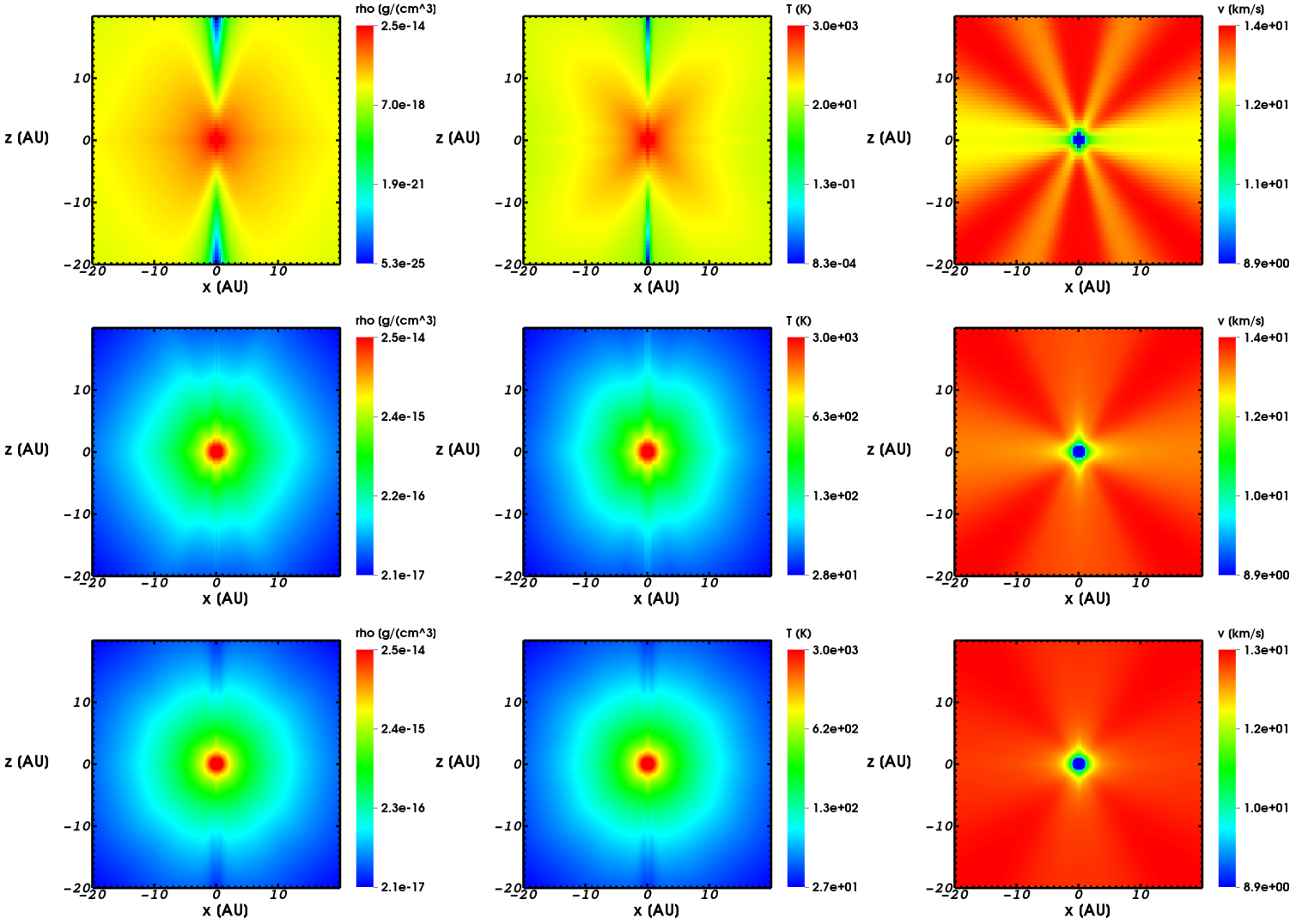

FIGURE B.10: The same as figure B.7 but in the XZ-plane of the polar-cylindrical coordinates.

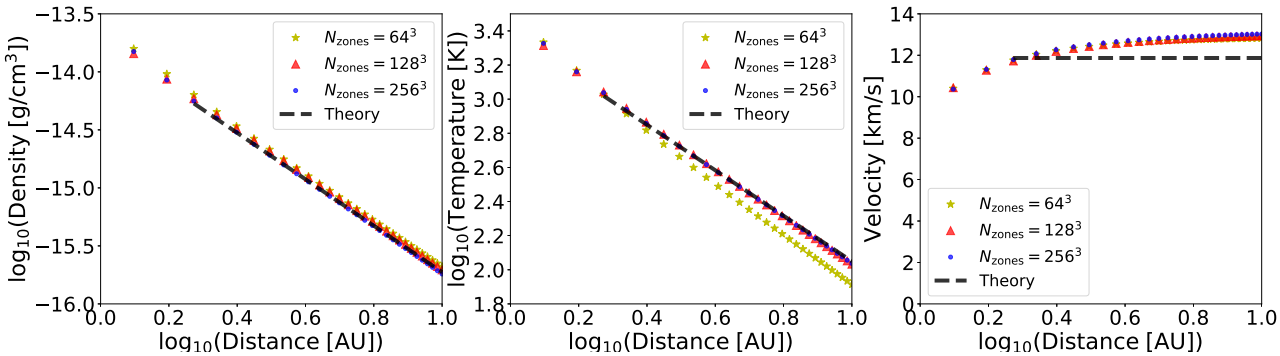

FIGURE B.11: The same as Figure B.8 but for the XZ-plane of the polar-cylindrical coordinates models shown in Figure B.10.

The XZ-plane of this coordinate system as shown in Figure B.10, is similar to the cartesian case, with disadvantages such as aspherical winds and artifacts dues to

the grid. In addition, the axis of the cylindrical grid is visible in every model, but it becomes less prominent at higher resolution, again this shows the importance of resolution. In addition, the cross-like structures that appear in the velocity plots also disappear at higher resolution similar to the cartesian case, In addition, agreement with the these models agree more with the analytical solution improves with increasing resolution (see Figure B.11).

B.5.2 Testing different solvers

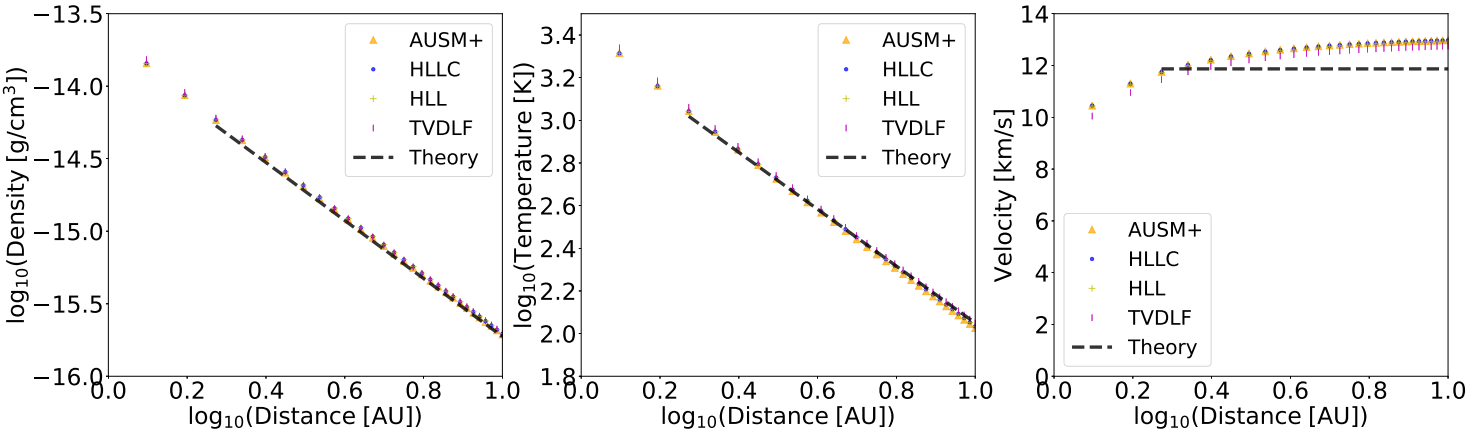

FIGURE B.12: The same as Figure B.9 but for XZ-plane of the polar-cylindrical coordinates.

For the different solvers in the XZ-plane of this coordinate system, the model obtained with the TVDLF solver seemed to be more spherical compared to the other solvers, and as shown in Figure B.12, followed the analytic solution more closely.

B.6 Comparison of cartesian, spherical and polar-cylindrical coordinates for resolution 64^3 and 128^3 with HLL solver

To illustrate how the model of the freely expanding wind in different coordinate systems compares to the analytic solutions, we present in Figure B.13 the plots showing how the density, temperature and velocity at each radial coordinate changes for each coordinate system compared to the analytic solution. The results show that on overall using our default parameter setting, the polar-cylindrical coordinates is the best performing coordinate systems for modelling spherical stellar wind. In addition, at lower resolution $N_{\text{zones}} = 64^3$ the spherical coordinate system performs better than the cartesian, however, at higher resolution $N_{\text{zones}} = 123^3$ their performance is similar.

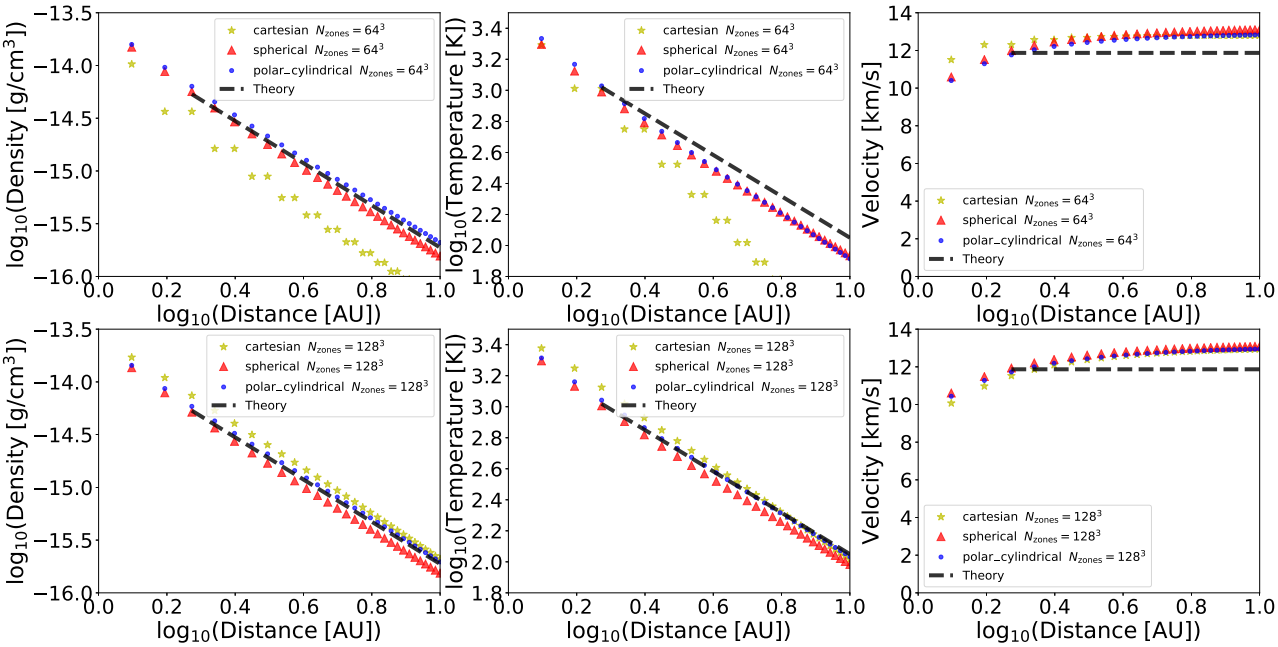

FIGURE B.13: Comparing different coordinates system using the same HLL solver at the same resolution. The yellow star, red triangle and blue dot represents the model obtained using the cartesian, spherical and polar-cylindrical coordinates system, respectively. The top and bottom row is for grid resolution $N_{\text{zones}} = 64^3$ and 128^3, respectively.

B.7 Different limiters

Limiters, as discussed in detail in Chapter 2, function to make sure that there is no overshoot and undershoot in each cell of the grid and no oscillations at discontinuities. The OSPRE and VANLEER were the only compatible limiters for the problem under investigation (i.e., the symmetric and spherical outflowing wind). The tests of these limiters were performed in 3D cartesian coordinates, resolution $N_{\text{zones}} = 128^3$ and solver HLL because we wanted a more robust and efficient configuration for conducting the tests. The results compared to the analytic solution turned out to be very similar as shown in Table Figure B.14, as were their efficiencies (Table B.1 and Figure B.16). The goal was to check if the limiter can have a huge impact on the model output, but it turns out no significant impact was found. This is the case because limiters are important in regions of the grid where discontinuities arise (Zingale 2013), and these are absent from the stellar wind problem chosen. Fully testing the limiters is thus left for future work.

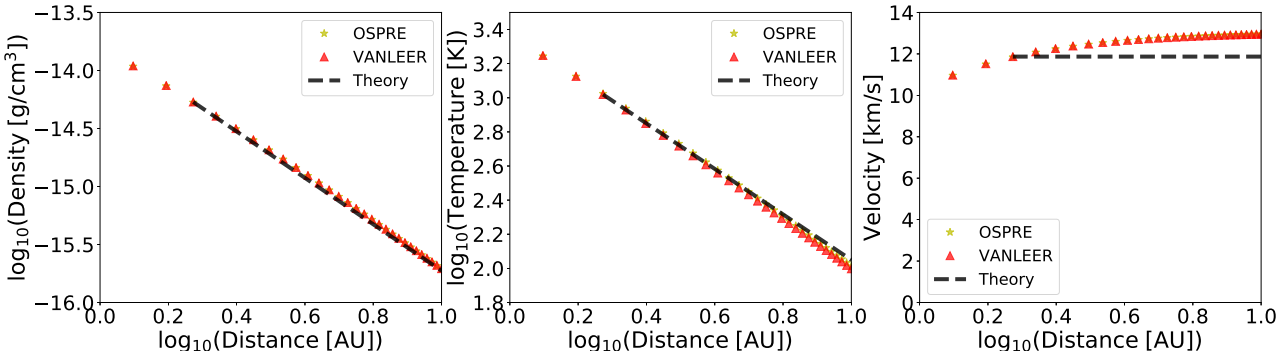

FIGURE B.14: The yellow stars and the red triangles represent models obtained using the OSPRE and VANLEER limiter from 1 AU to 10 AU of the models, respectively, compared to the analytical solution from 2 AU to 10 AU (black dashed line).

B.8 Different CFL value

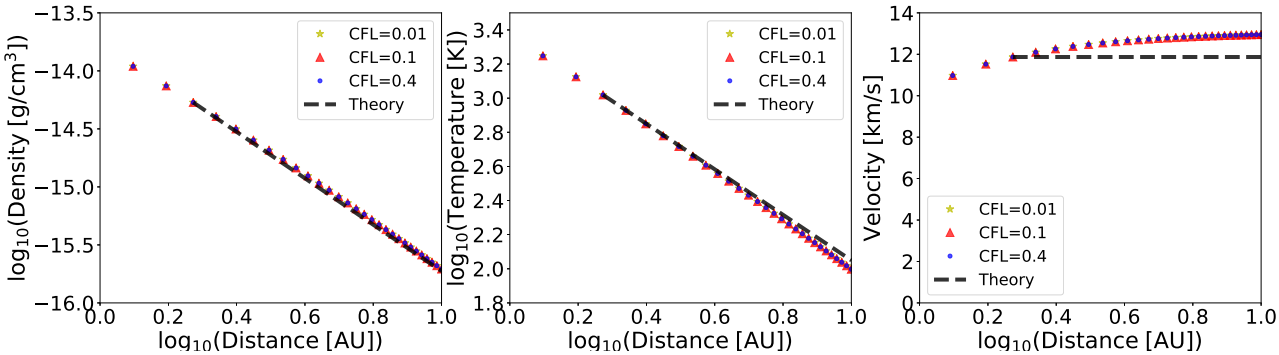

FIGURE B.15: These plots compare the models obtained using the CFL value of 0.01, 0.1 and 0.4 which are represented by the yellow star, red triangle and blue dot, respectively. These plots are taken from 1 AU to 10 AU of the models, and they are compared with the analytical solution represented by the back dashed line.

Different CFL values were tested using the same configuration as that above for section B.7 with the VANLEER limiter set. CFL values are important for the stability of the code, and indeed as mentioned in Beckers (1992), Mignone et al. (2007), Zingale (2013), and Vaidya et al. (2018), in 3D for stability $0 < CFL < 0.5$, models with CLF values of -0.1 and 0.6 were tested and did not converge. From our tests, as $CFL \to 0$, the simulation becomes more stable but also because the timestep is smaller more computationally expensive, and that as $CFL \to 0.5$ the simulation becomes less stable but more computationally efficient, which is consistent with the literature (Mignone et al. 2007; Zingale 2013; Vaidya et al. 2018). In addition, for the small values tested here the results compared to the analytic values were similar as shown in Figure B.15. Overall we found its best to use $CFL = 0.1$ to guarantee stability and efficiency.

B.9 Computational cost for different model parameters

In this section, we present the efficiency of the different configurations of each test models in terms of the N_{zones} per core per second for each model to reach a steady state (i.e., until the physical properties of the stellar wind at each radial coordinate no-longer changes with time). The results are shown in Table B.1 and Figure B.16, where firstly we have the time taken for the wind simulation to reach a steady state while using a $N_{\text{zones}} = 128^3$ resolution and for different solvers. Secondly, while using the cartesian coordinates, resolution $N_{\text{zones}} = 128^3$, and the HLL solver for different limiters. Third, while using the cartesian coordinates, resolution $N_{\text{zones}} = 128^3$, the HLL solver and the VANLEER limiter for different CFL values.

TABLE B.1: The performance of the code measured in N_{zones} per core per second for the stellar wind simulation to reach a steady state while using 240 processors for the test models.

		Coordinate system		
		Cartesian	Spherical	Polar-cylindrical
Grid Resolution (N_{zones})	64^3	3.79	0.674	2.02
	128^3	16.2	0.325	4.41
	256^3	29.9	-	4.32
Solver	TWO-SHOCK	-	-	-
	ROE	16.2	0.299	-
	AUSM+	16.2	0.347	4.57
	HLLC	16.2	0.331	4.50
	HLL	16.2	0.347	4.33
	TVDLF	15.2	0.361	4.50
Limiter	OSPRE	17.3	-	-
	VANLEER	17.3	-	-
CFL value	0.01	10.1	-	-
	0.1	17.3	-	-
	0.4	17.3	-	-

Note: Parts with (-) are not compatible with our testing configuration or are too computationally expensive.

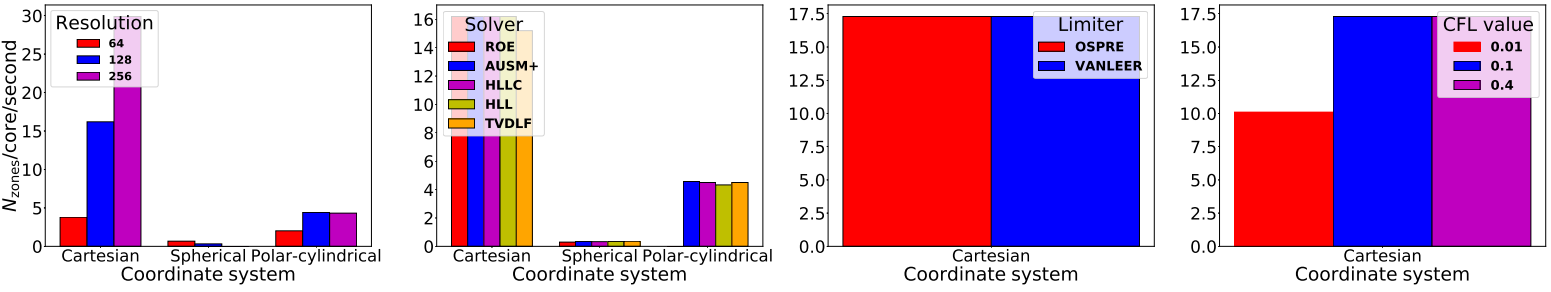

FIGURE B.16: Plots showing the performance of PLUTO code, while testing its numerics with respect to the N_{zones} per core per second by using a freely expanding stellar wind produced by a stationary star, the runtime is the time taken for the simulated stellar wind to reach a steady state. Presented in this figure is the runtime of cases in Table B.1 with respect to the coordinate system. We have the resolution tests, solver tests, limiter tests and CFL value tests, in the first, second, third and fourth columns, respectively.

B.10 Summary of code tests

All the tests were performed in 3D, and ran with 240 processors. The default parameter settings were: grid resolution $N_{\text{zones}} = 128^3$, HLL solver, VANLEER limiter and CFL=0.1, except for the tests involving that parameter. The density, temperature and velocity profiles of the models are plotted from 1 to 10 AU, while the corresponding analytical solutions, represented by equations B.10, B.11 and B.13 are plotted from 2 to 10 AU with the initial conditions taken from the respective models at 2 AU.

Overall, we conclude that the best coordinate system to use for spherical winds is the spherical, but at a lower resolution of $N_{\text{zones}} = 128^2$ because it is computationally intensive. However, for bow shocks, where we go into the frame of reference of the moving star, and have the ISM medium flowing past, the polar-cylindrical system is used instead because then we can easily define the inflow material and have a spherical wind in the direction of motion, but using resolution $N_{\text{zones}} \geq 256^3$, to guarantee that we eliminate the artifacts that occur at the axis due to the geometry (see Figure B.10). We set the star to move parallel to the XY-plane and perpendicular to the XZ-plane as shown in Figures B.7 and B.10, respectively. In addition, the advantage of this coordinate system is that it is more computationally efficient than the spherical case (but it is less efficient than the cartesian as shown in Table B.1 and Figure B.16). The density, temperature and velocity profiles of its models as shown in Figure B.13, also agree well with the analytical solution in all the resolutions compared to the other coordinate systems.

So in conclusion, the best configuration to use for the spherical stellar winds in 3D is the polar-cylindrical coordinates, with resolution $N_{\text{zones}} = 256^3$, the TVDLF solver, any of the limiters and the $CFL = 0.1$. The concerns about the TVDLF is that it is not a good shock capturing solver, it is more dissipative, and it does not use a Riemann solver. Since the second best performing solver is HLL, for modelling bow shocks we chose it instead as it is a good shock capturing solver which uses the Riemann solver. A full exploration of the different configurations for bow shocks will be carried out in the future. For example, the MINMOD limiter which was not tested here, maybe used when modelling bow shocks because of its shock capturing ability and efficiency (Zingale 2013).

It is important to note that this freely expanding wind test problem may not be ideal for showing the differences between solvers, but the main purpose of this freely expanding wind test problem was to explore the code. Only a small number of test problems could be conducted within a certain period of time given our limited computational resources. In future work, shock test problems will be used to further investigate the different solvers, to see how the solvers are able to resolve the contact discontinuity, shocks, and how good the different schemes are at capturing KH/RT instabilities.

Appendix C

Supplementary plots

As discussed in Chapter 5, resolution is an important consideration when conducting numerical simulations in adiabatic, thermal conduction and/or cooling conditions, and as discussed in Chapter 6, stellar evolutionary phase, space velocity and ISM phase have a significant impact on the morphology and evolution of stellar bow shocks. Here we present additional plots to support arguments made in Chapter 5 (for the HVR resolution tests) and Chapter 6 (for the HVR studies of the effect of space velocity and ISM phase on the bow shock). We compare the HVR models to the Wilkin (1996) analytic solution in Section C.1. We present the corresponding Mach number plots in Section C.2. For studying the effect of space velocity and ISM phase on the bow shock, we also present the models at their early stages before reaching steady state or before exhibiting the carbuncle phenomenon in Section C.3. And in Section C.4, we present 3D projections of the WNM models for the study of the effect of space velocity and ISM phase on the bow shock.

C.1 Comparing model to Wilkin (1996) analytic solution in 2D maps

To clearly show how the Wilkin (1996) analytic solution traces the shocked region of the bow shock, we plot it on top of the 2D maps as shown in Figures C.1 - C.2 for the resolution study, and Figures C.3 - C.4 for the studies of the effect of space velocity and ISM phase on the bow shock.

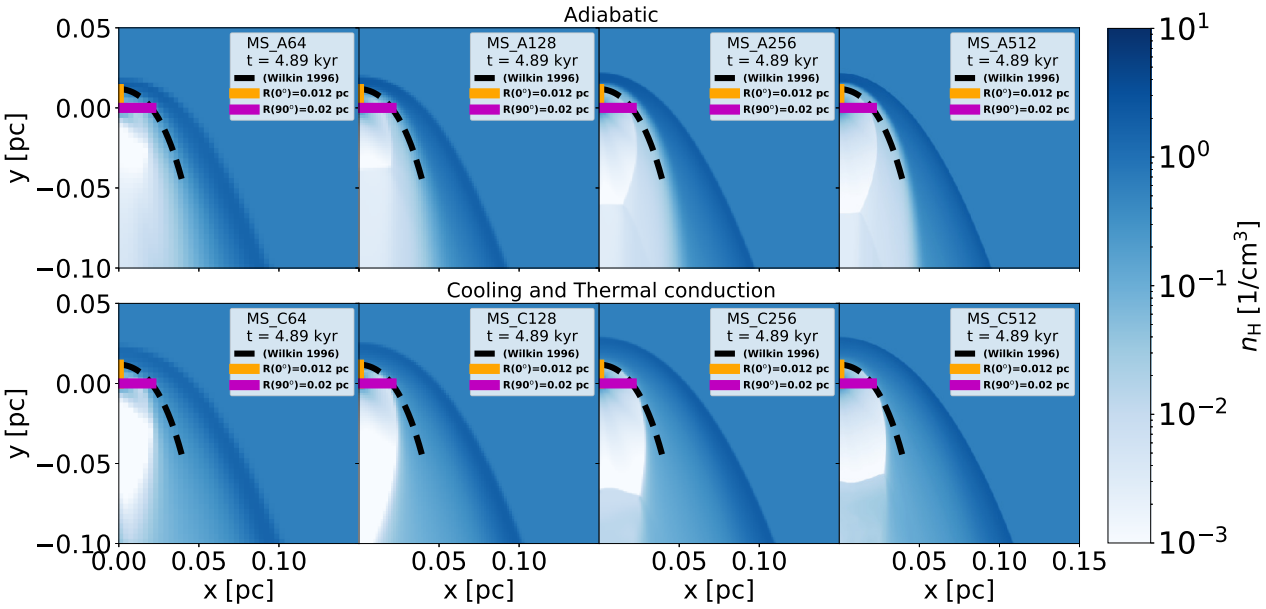

FIGURE C.1: Comparing the Wilkin (1996) analytic solution (black-dashed-curve) to the density plots at steady state, for the bow shocks produced by MS stars moving at 200 km/s, for the adiabatic case (top row) and for the cooling & thermal conduction case (bottom row) for grid resolutions, $N_{\rm zones} = 64^2$, 128^2, 256^2 and 512^2 (the first, second, third, and fourth column, respectively).

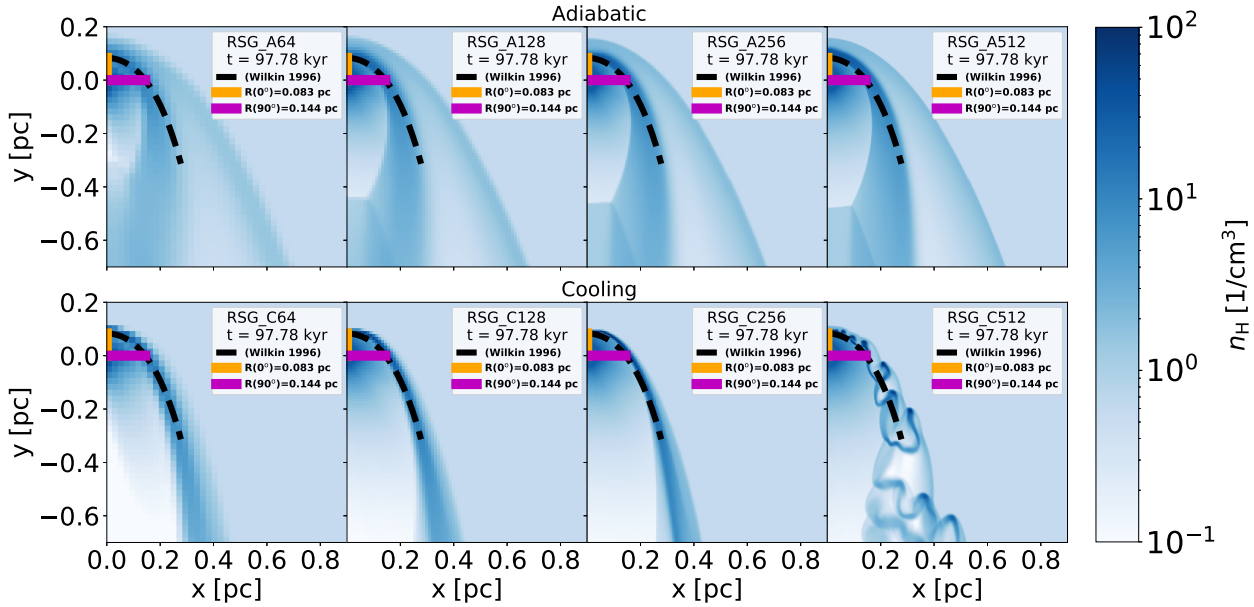

FIGURE C.2: Comparing the Wilkin (1996) analytic solution (black-dashed-curve) to the density plots at steady state, for the bow shocks produced by RSG stars moving at 200 km/s, for the adiabatic case (top row) and for the cooling & thermal conduction case (bottom row) for grid resolutions, $N_{\rm zones} = 64^2$, 128^2, 256^2 and 512^2 (the first, second, third, and fourth column, respectively).

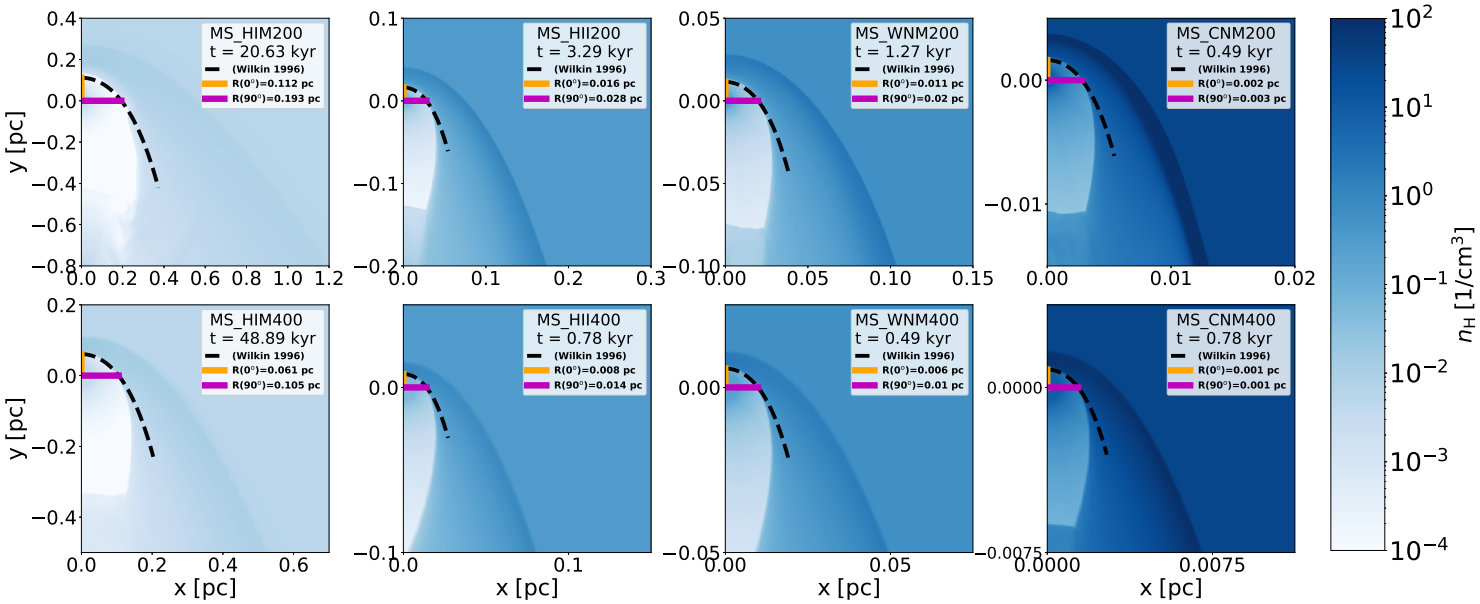

FIGURE C.3: Comparing the Wilkin (1996) analytic solution (black-dashed-curve) to the density plots of the MS bow shocks for stars moving at 200 km/s (top row) and 400 km/s (bottom row) with respect to the ISM. The ISM phase in the first, second, third and fourth column is the HIM, HII region, WNM and CNM, respectively.

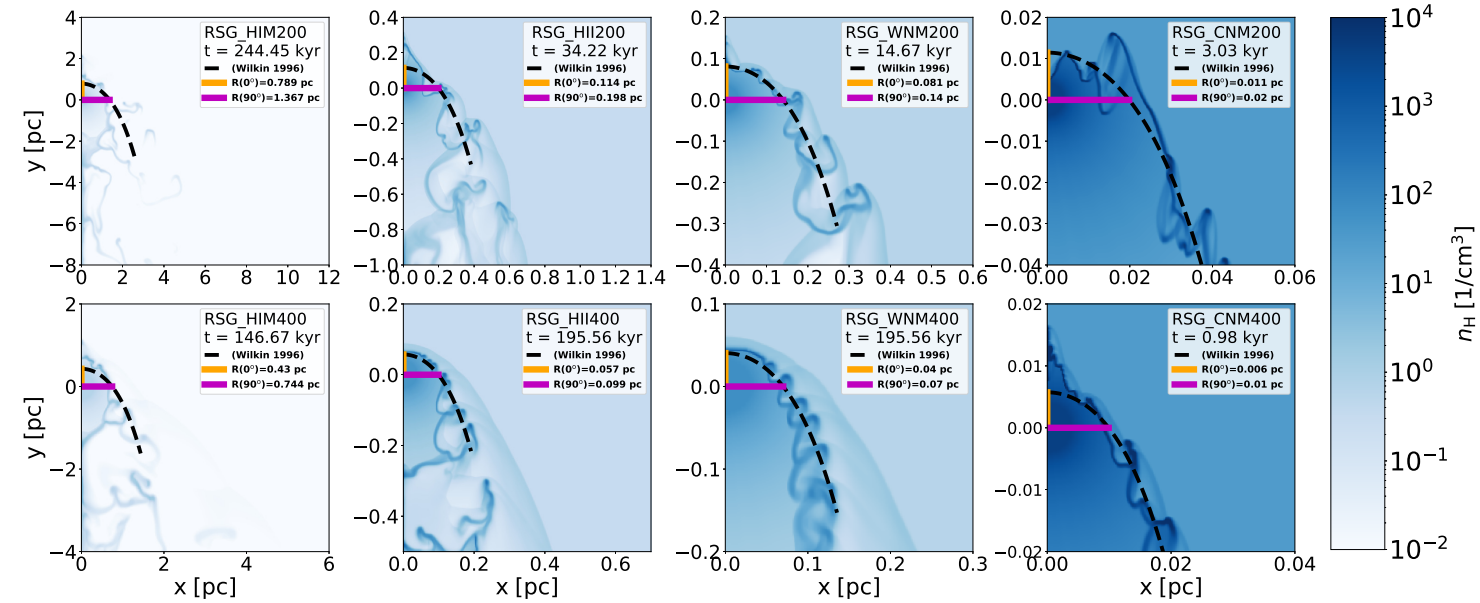

FIGURE C.4: Comparing the Wilkin (1996) analytic solution (black-dashed-curve) to the density plots of the RSG bow shocks for stars moving at 200 km/s (top row) and 400 km/s (bottom row) with respect to the ISM. The ISM phase in the first, second, third and fourth column is the HIM, HII region, WNM and CNM, respectively.

C.2 Mach number

To clearly show how the velocity of the fluid compares to that of the sound speed, we use the Mach number plots, which show regions of the bow shock where the fluid flow is supersonic ($> 10^0$), sonic ($\approx 10^0$) and subsonic ($< 10^0$) for the resolution study in Figures C.5 - C.6 and for studies focusing on the effect of space velocity and ISM phase on the bow shock in Figures C.7 - C.8. These plots clearly show that the fluid is subsonic at the apex where the wind collides head-on with the ISM and the

the tail, and that the fluid is sonic at the contact discontinuity and supersonic in the freely expanding wind and unshocked ISM regions.

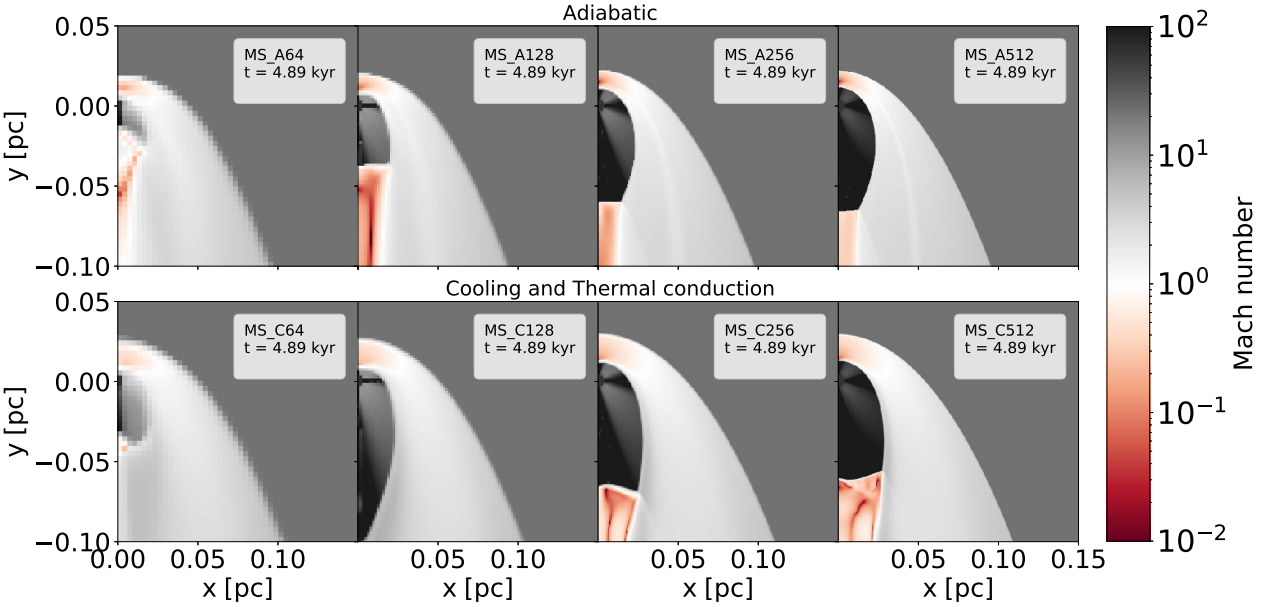

FIGURE C.5: Mach number plots at time, t = 4.89 kyr, for the bow shocks produced by MS stars, respectively, moving at 200 km/s, for the adiabatic case (top row) and for the cooling and/or thermal conduction case (bottom row) for grid resolutions, $N_{\text{zones}} = 64^2$, 128^2, 256^2 and 512^2 (the first, second, third, and fourth column, respectively).

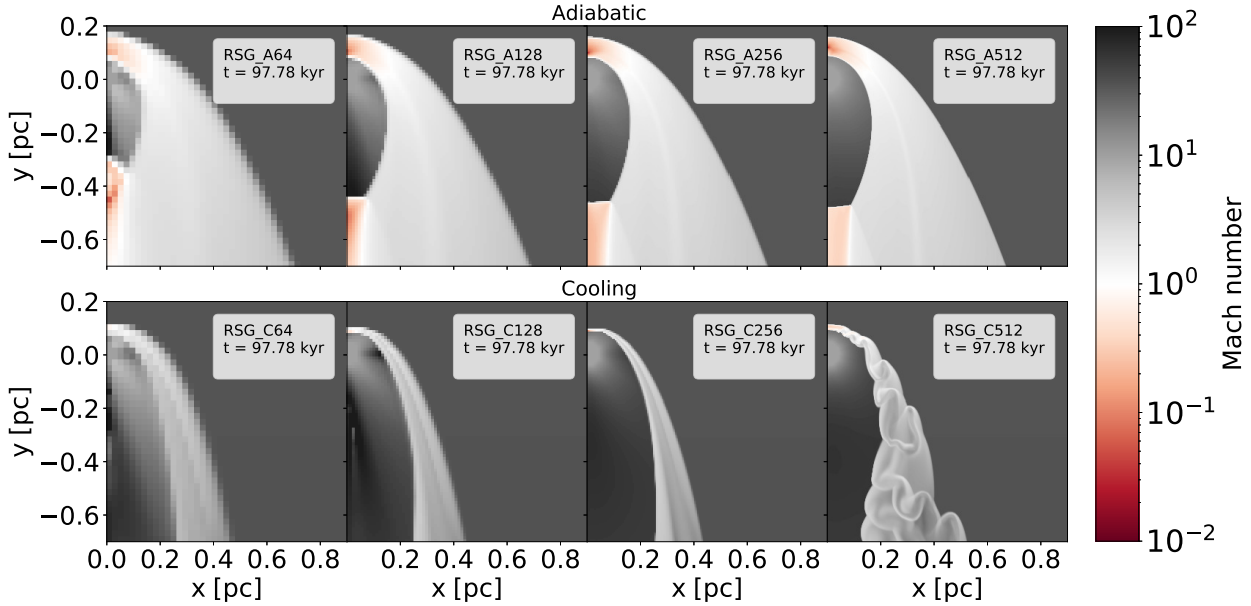

FIGURE C.6: Mach number plots at time, t = 97.78 kyr, for the bow shocks produced by RSG stars, respectively, moving at 200 km/s, for the adiabatic case (top row) and for the cooling and/or thermal conduction case (bottom row) for grid resolutions, $N_{\text{zones}} = 64^2$, 128^2, 256^2 and 512^2 (the first, second, third, and fourth column, respectively).

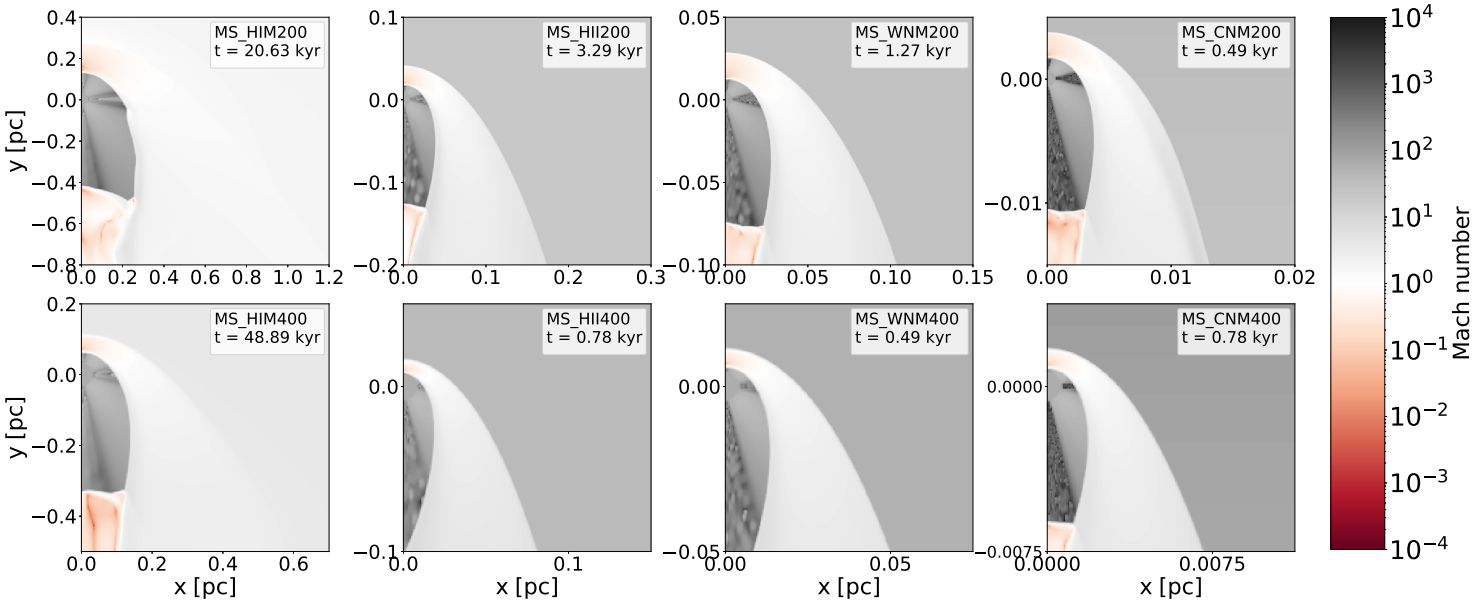

FIGURE C.7: Mach number plots of the MS bow shocks for stars moving at 200 km/s (top row) and 400 km/s (bottom row) with respect to the ISM. The ISM phase in the first, second, third and fourth column is the HIM, HII region, WNM and CNM, respectively.

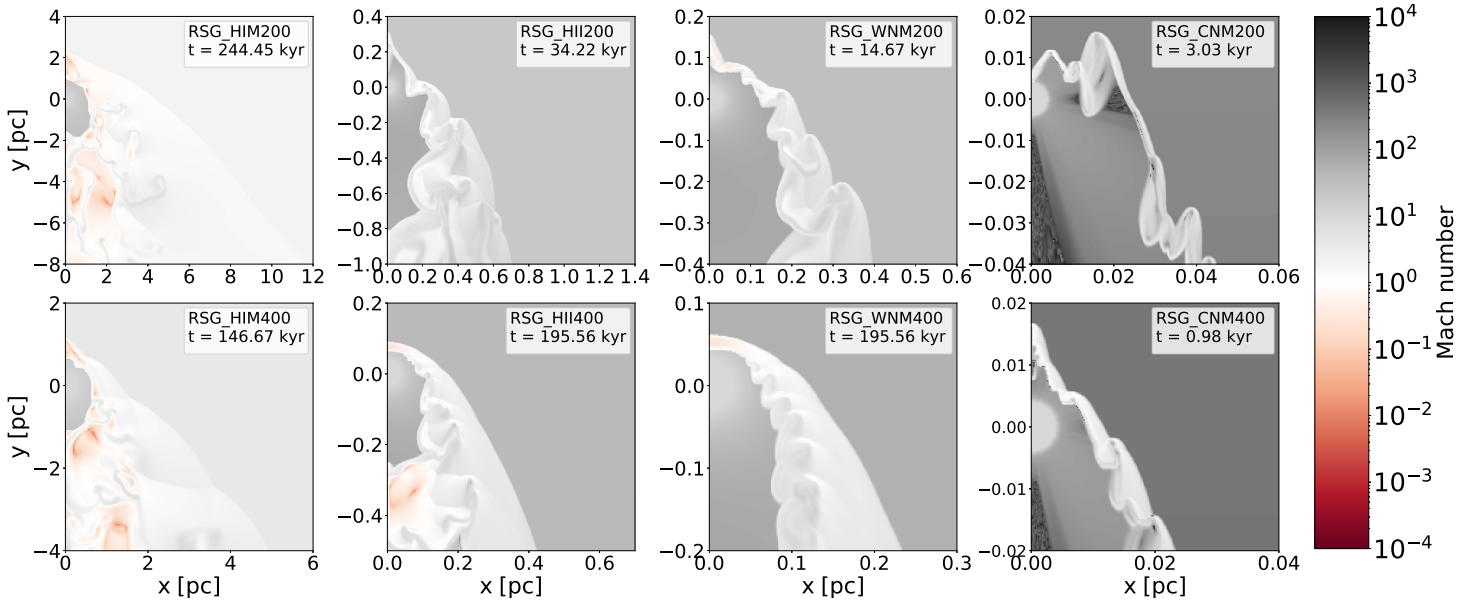

FIGURE C.8: Mach number plots of the RSG bow shocks for stars moving at 200 km/s (top row) and 400 km/s (bottom row) with respect to the ISM. The ISM phase in the first, second, third and fourth column is the HIM, HII region, WNM and CNM, respectively.

C.3 Bow shock formation

To demonstrate that all the models during the investigation of the effect of space velocity and ISM phase on the bow shock did not immediately exhibit the carbuncle phenomenon, in Figures C.9 - C.10 we present the models in their early stages before reaching a steady state or before the build-up of fluid at the tip of the bow shock.

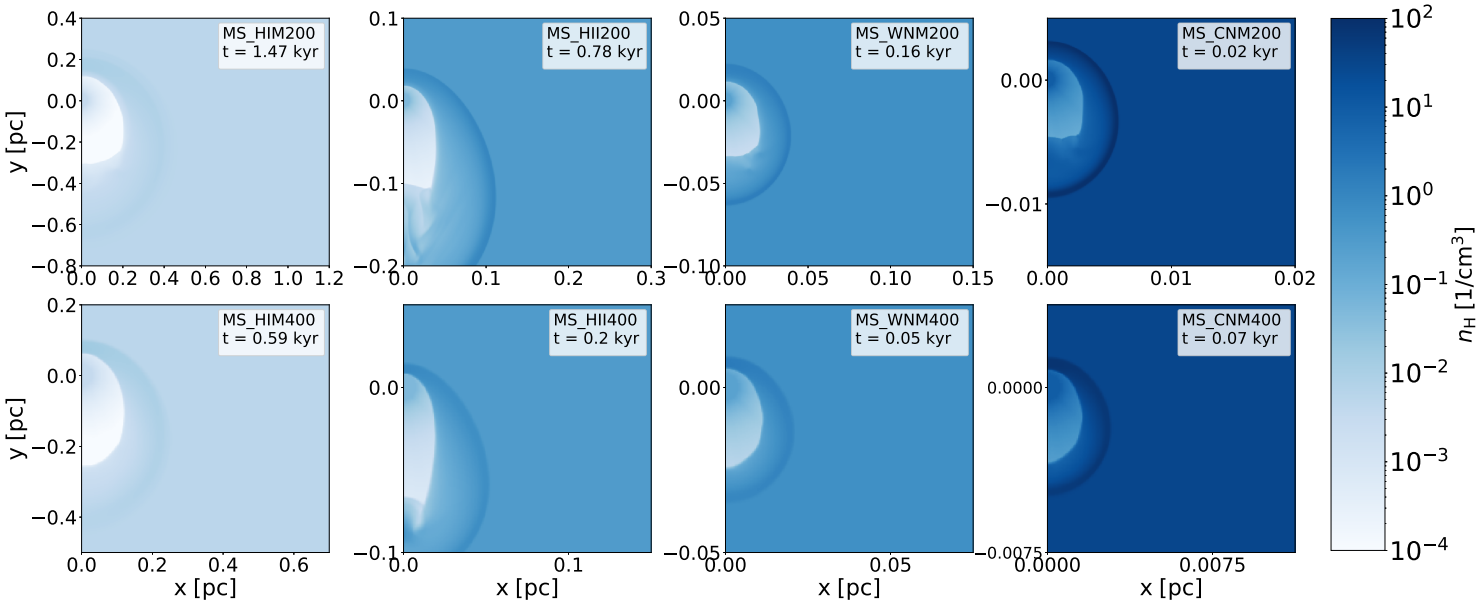

FIGURE C.9: Density plots of the MS bow shocks for stars moving at 200 km/s (top row) and 400 km/s (bottom row) with respect to the ISM. The ISM phase in the first, second, third and fourth column is the HIM, HII region, WNM and CNM, respectively. Similar to models presented in Figure 6.1.

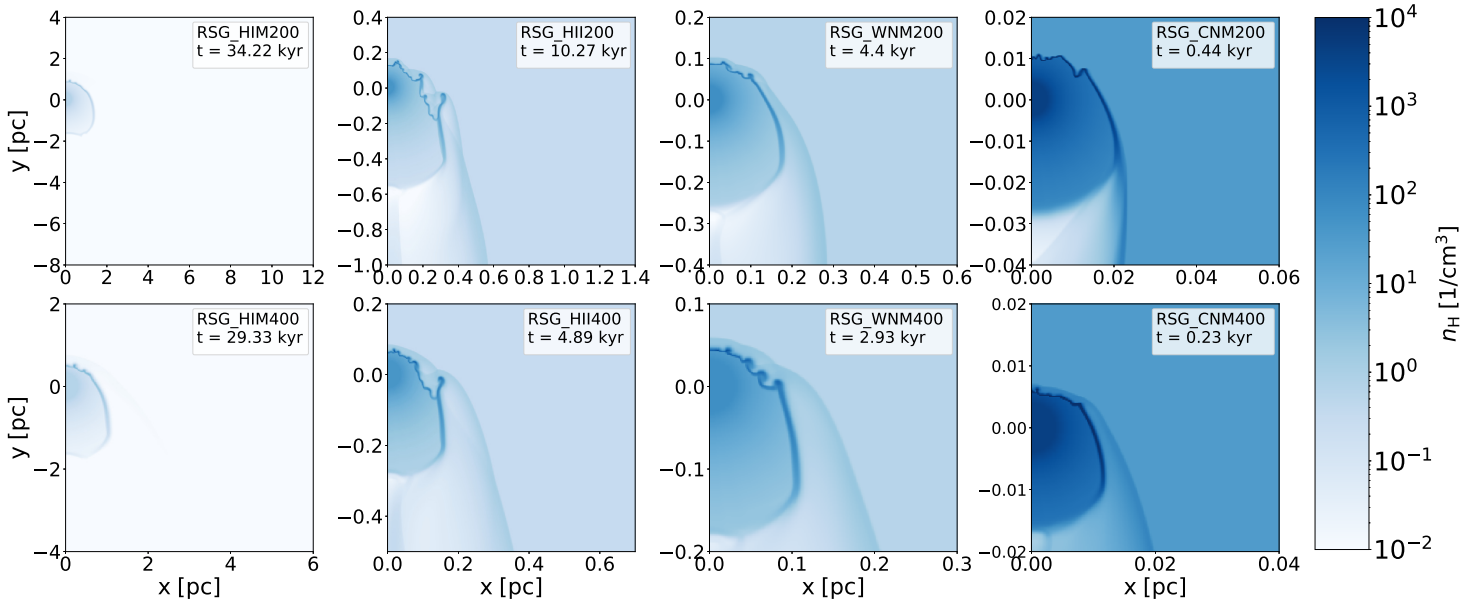

FIGURE C.10: Density plots of the RSG bow shocks for stars moving at 200 km/s (top row) and 400 km/s (bottom row) with respect to the ISM. The ISM phase in the first, second, third and fourth column is the HIM, HII region, WNM and CNM, respectively. Similar to models presented in Figure 6.1.

C.4 3D plots

Here we present the 3D views of the models that where sliced and presented in Chapter 6 for the density, temperature, velocity and emissivity plots in Figure C.11.

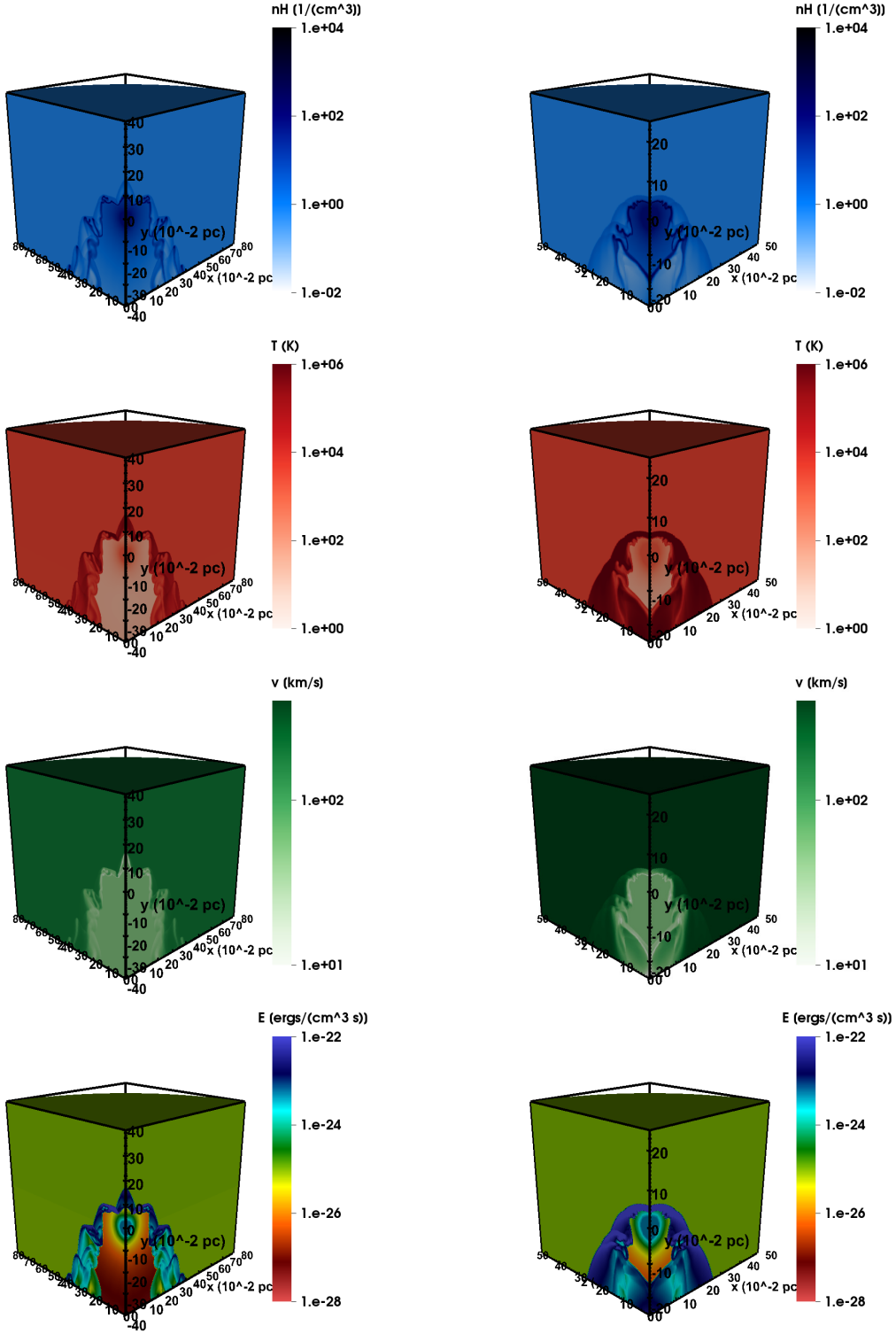

FIGURE C.11: 3D projections of the bow shocks of models, RSG_WNM200 (left) and RSG_WNM400 (right), which where sliced to produce the 3D (2D slice) maps in Section 6.3. We have the density, temperature, velocity and emissivity plots in the first, second, third and fourth row, respectively.

Bibliography

Abbott, R. et al. 2020. GW190521: A Binary Black Hole Merger with a Total Mass of 150 $M_{\odot}$, *PhRvL*, 125, 101102.

Agertz, Oscar et al. 2007. Fundamental differences between SPH and grid methods, *MNRAS*, 380, 963–978.

Anosova, J., J. Colin, and L. Kiseleva. 1996. Triple Star Systems as Producers of High Velocity Stars in the Galaxy, *Ap&SS*, 236, 293–294.

Ballone, A. et al. 2013. Hydrodynamical Simulations of a Compact Source Scenario for the Galactic Center Cloud G2, *ApJ*, 776, 13.

Balsara, Dinshaw S., David A. Tilley, and J. Christopher Howk. 2008. Simulating anisotropic thermal conduction in supernova remnants - I. Numerical methods, *MNRAS*, 386, 627–641.

Baranov, V. B., K. V. Krasnobaev, and A. G. Kulikovskii. 1971. A Model of the Interaction of the Solar Wind with the Interstellar Medium, *Soviet Physics Doklady*, 15, 791.

Batten, P. et al. 1997. On the Choice of Wavespeeds for the HLLC Riemann Solver, *SIAM J. Sci. Comput.*, 18, 1553–1570.

Beckers, J. M. 1992. Analytical linear numerical stability conditions for an anisotropic three-dimensional advection-diffusion equation, *SJNA*, 29, 701–713.

Benaglia, P. et al. 2010. Detection of nonthermal emission from the bow shock of a massive runaway star, *A&A*, 517, L10.

Bennett, P. D. 2010. Chromospheres and Winds of Red Supergiants: An Empirical Look at Outer Atmospheric Structure, *Hot and Cool: Bridging Gaps in Massive Star Evolution*. Ed. by C. Leitherer et al. Vol. 425. Astronomical Society of the Pacific Conference Series, 181.

Blaauw, A. 1961. On the origin of the O- and B-type stars with high velocities (the "run-away" stars), and some related problems, *BAIN*, 15, 265.

Blaauw, Adriaan. 1993. Massive Runaway Stars, *Massive Stars: Their Lives in the Interstellar Medium*. Ed. by Joseph P. Cassinelli and Edward B. Churchwell. Vol. 35. Astronomical Society of the Pacific Conference Series, 207.

Blondin, John M. and Joel F. Koerwer. 1998. Instability of isothermal stellar wind bowshocks, *NewA*, 3, 571–582.

Bond, Howard E. and Brent Miszalski. 2018. Spectroscopy of V341 Arae: A Nearby Nova-like Variable Inside a Bow Shock Nebula, *PASP*, 130, 094201.

Brighenti, F. and A. D'Ercole. 1995. Evolution of WR ring nebulae generated by a moving central star - II. The influence of the red supergiant bow shock, *MNRAS*, 277, 53–69.

Brott, I. et al. 2011. Rotating massive main-sequence stars. I. Grids of evolutionary models and isochrones, *A&A*, 530, A115.

Brown, Warren R. 2015. Hypervelocity Stars, *ARA&A*, 53, 15–49.

Carruthers, George R. 1970. Rocket Observation of Interstellar Molecular Hydrogen, *ApJL*, 161, L81.

Chieffi, Alessandro and Marco Limongi. 2013. Pre-supernova Evolution of Rotating Solar Metallicity Stars in the Mass Range 13-120 M $_{\odot}$ and their Explosive Yields, *ApJ*, 764, 21.

Choudhuri, Arnab Rai. 1998. The physics of fluids and plasmas : an introduction for astrophysicists.

Colella, P. and H. M. Glaz. 1985. Efficient Solution Algorithms for the Riemann Problem for Real Gases, *JCoPh*, 59, 264–289.

Comerón, F. and L. Kaper. 1998. Numerical simulations of wind bow shocks produced by runaway OB stars, *A&A*, 338, 273–291.

Conlon, E. S. et al. 1990. The runaway nature of distant early-type stars in the galactic halo. *A&A*, 236, 357.

Cowie, L. L. and C. F. McKee. 1977. The evaporation of spherical clouds in a hot gas. I. Classical and saturated mass loss rates. *ApJ*, 211, 135–146.

Cowie, L. L., C. F. McKee, and J. P. Ostriker. 1981. Supernova remnant revolution in an inhomogeneous medium. I - Numerical models. *ApJ*, 247, 908–924.

Davies, Ben and Emma R. Beasor. 2018. The initial masses of the red supergiant progenitors to Type II supernovae, *MNRAS*, 474, 2116–2128.

de Jager, C., H. Nieuwenhuijzen, and K. A. van der Hucht. 1988. Mass loss rates in the Hertzsprung-Russell diagram. *A&AS*, 72, 259–289.

de Mink, S. E. et al. 2013. The Rotation Rates of Massive Stars: The Role of Binary Interaction through Tides, Mass Transfer, and Mergers, *ApJ*, 764, 166.

Decin, L. et al. 2012. The enigmatic nature of the circumstellar envelope and bow shock surrounding Betelgeuse as revealed by Herschel. I. Evidence of clumps, multiple arcs, and a linear bar-like structure, *A&A*, 548, A113.

Dgani, Ruth, Dave van Buren, and Alberto Noriega-Crespo. 1996. The Transverse Acceleration Instability for Bow Shocks in the Nonlinear Regime, *ApJ*, 461, 372.

Dorigo Jones, J. et al. 2020. Runaway OB Stars in the Small Magellanic Cloud: Dynamical versus Supernova Ejections, *ApJ*, 903, 43.

Draine, Bruce T. 2011. Physics of the Interstellar and Intergalactic Medium.

Elling, Volker. 2006. Carbuncles as self-similar entropy solutions, *arXiv Mathematics e-prints*, math/0609666.

Ferland, G. J. et al. 1998. CLOUDY 90: Numerical Simulation of Plasmas and Their Spectra, *PASP*, 110, 761–778.

Ferriere, Katia M. 2001. The interstellar environment of our galaxy, *RvMP*, 73, 1031–1066.

Field, G. B., D. W. Goldsmith, and H. J. Habing. 1969. Cosmic-Ray Heating of the Interstellar Gas, *ApJL*, 155, L149.

Foo, C. J.H. et al. 1995. Two-Way Calling Public CT2 Telepoint System, *IEEE Journal on Selected Areas in Communications*, 13, 923–931.

Gawryszczak, A. J., J. Mikołajewska, and M. Różyczka. 2002. Morphology of planetary nebulae with binary cores. The effect of gravitational focusing by the companion to the mass-losing star, *A&A*, 385, 205–215.

Gies, D. R. 1987. The kinematical and binary properties of association and field O stars, *ApJS*, 64, 545.

Gies, D. R. and C. T. Bolton. 1986. The Binary Frequency and Origin of the OB Runaway Stars, *ApJS*, 61, 419.

Godunov, S. K. 1959. A difference method for numerical calculation of discontinuous solutions of the equations of hydrodynamics. Russian, *Mat. Sb., Nov. Ser.*, 47, 271–306.

Gottlieb, S. and C. W. Shu. 1998. Total variation diminishing Runge-Kutta schemes, *MaCom*, 67, 73–85.

Green, Samuel et al. 2019. Thermal emission from bow shocks. I. 2D hydrodynamic models of the Bubble Nebula, *A&A*, 625, A4.

Gull, T. R. and S. Sofia. 1979. Discovery of two distorted interstellar bubbles. *ApJ*, 230, 782–785.

Gvaramadze, V. V. 2009. HD 271791: Dynamical versus binary-supernova ejection scenario, *MNRAS*, 395, 85–89.

Gvaramadze, V. V. and D. J. Bomans. 2008. Search for OB stars running away from young star clusters. I. NGC 6611, *A&A*, 490, 1071–1077.

Gvaramadze, V. V. et al. 2011. 4U 1907+09: an HMXB running away from the Galactic plane, *A&A*, 529, A14.

Gvaramadze, V. V. et al. 2013. IRC -10414: A bow-shock-producing red supergiant star, *MNRAS*, 437, 843–856.

Gvaramadze, V. V. et al. 2018. Modelling interstellar structures around Vela X-1, *MNRAS*, 474, 4421–4431.

Gvaramadze, V. V. et al. 2019. CPD-64°2731: a massive spun-up and rejuvenated high-velocity runaway star, *MNRAS*, 482, 4408–4421.

Harries, Tim J. 2000. Synthetic line profiles of rotationally distorted hot-star winds, *MNRAS*, 315, 722–734.

Harten, Amiram, Peter D. Lax, and Bram van Leer. 1983. On Upstream Differencing and Godunov-Type Schemes for Hyperbolic Conservation Laws, *SIAM Review*, 25, 35–61.

Hollis, J. M. et al. 1992. The 0623+71 Bow Shock Nebula, *ApJ*, 393, 217.

Hoogerwerf, R., J. H. J. de Bruijne, and P. T. de Zeeuw. 2000. The Origin of Runaway Stars, *AJ*, 544, L133–L136.

Howarth, Ian D. and Raman K. Prinja. 1989. The Stellar Winds of 203 Galactic O Stars: A Quantitative Ultraviolet Survey, *ApJS*, 69, 527.

Hoyle, F. and G. R. A. Ellis. 1963. On the Existence of an Ionized Layer about the Galactic Plane, *AuJPh*, 16, 1.

Hubber, D. A., S. A.E.G. Falle, and S. P. Goodwin. 2013. Convergence of AMR and SPH simulations - I. Hydrodynamical resolution and convergence tests, *MNRAS*, 432, 711–727.

Hummer, D. G. 1994. Total Recombination and Energy Loss Coefficients for Hydrogenic Ions at Low Density for 10<T/E/Z/2<10/7K, *MNRAS*, 268, 109.

Huthoff, F. and L. Kaper. 2002. On the absence of wind bow-shocks around OB-runaway stars: Probing the physical conditions of the interstellar medium, *A&A*, 383, 999–1010.

Kaper, L. et al. 1997. Discovery of a Bow Shock around VELA X-1, *ApJL*, 475, L37–L40.

Kippenhahn, Rudolf and Alfred Weigert. 1990. Stellar Structure and Evolution.

Kippenhahn, Rudolf, Alfred Weigert, and Achim Weiss. 2012. Stellar Structure and Evolution.

Klessen, Ralf S. and Simon C. O. Glover. 2016. Physical Processes in the Interstellar Medium, *Saas-Fee Advanced Course*, 43, 85.

Köhler, K. et al. 2015. The evolution of rotating very massive stars with LMC composition, *A&A*, 573, A71.

Kuiper, G. P. 1935. Problems of Double-Star Astronomy. II, *PASP*, 47, 121.

Lamers, H. J. G. L. M. 1981. Mass loss from O and B stars. *ApJ*, 245, 593–608.

Lamers, H. J. G. L. M. et al. 2000. The Dependence of Mass Loss on the Stellar Parameters, *Thermal and Ionization Aspects of Flows from Hot Stars*. Ed. by Henny Lamers and Arved Sapar. Vol. 204. ASPC, 395.

Lamers, Henny J. G. L. M. and Joseph P. Cassinelli. 1999. Introduction to Stellar Winds.

Lamers, Henny J. G. L. M. and Claus Leitherer. 1993. What are the Mass-Loss Rates of O Stars?, *ApJ*, 412, 771.

Le Bertre, T. et al. 2012. Discovery of a detached H I gas shell surrounding α Orionis, *MNRAS*, 422, 3433–3443.

LeVeque, Randall J. 2002. Finite Volume Methods for Hyperbolic Problems. Cambridge Texts in Applied Mathematics. Cambridge University Press.

Li, Yuan, Greg L. Bryan, and Eliot Quataert. 2019. The Fate of Asymptotic Giant Branch Winds in Massive Galaxies and the Intracluster Medium, *ApJ*, 887, 41.

Liou, Meng-Sing and Christopher J. Steffen. 1993. A New Flux Splitting Scheme, *JCoPh*, 107, 23–39.

López-Santiago, J. et al. 2012. AE Aurigae: First Detection of Non-thermal X-Ray Emission from a Bow Shock Produced by a Runaway Star, *ApJL*, 757, L6.

Mackey, J. 2012. Accuracy and efficiency of raytracing photoionisation algorithms, *A&A*, 539, A147.

Mackey, Jonathan et al. 2015. Wind bubbles within H ii regions around slowly moving stars, *A&A*, 573, A10.

Mackey, Jonathan et al. 2016. Detecting stellar-wind bubbles through infrared arcs in H II regions, *A&A*, 586, A114.

Mackey, Jonathan et al. 2021. PION: simulating bow shocks and circumstellar nebulae, *MNRAS*, 504, 983–1008.

Maeder, A. and G. Meynet. 1987. Grids of evolutionary models of massive stars with mass loss and overshooting - Properties of Wolf-Rayet stars sensitive to overshooting. *A&A*, 182, 243–263.

Maeder, André. 2009. Physics, Formation and Evolution of Rotating Stars.

Maeder, Andre and Georges Meynet. 2011. Rotating massive stars through the ages, with applications to WR stars, Pop III stars and Gamma Ray Bursts, *arXiv e-prints*, arXiv:1109.6171.

Martin, D. Christopher et al. 2007. A turbulent wake as a tracer of 30,000years of Mira's mass loss history, *Nature*, 448, 780–783.

Mauron, N. and E. Josselin. 2011. The mass-loss rates of red supergiants and the de Jager prescription, *A&A*, 526, A156.

Mayer, A. et al. 2011. Herschel's view into Mira's head, *A&A*, 531, L4.

McKee, C. F. 1995. The Multiphase Interstellar Medium, *The Physics of the Interstellar Medium and Intergalactic Medium*. Ed. by A. Ferrara et al. Vol. 80. Astronomical Society of the Pacific Conference Series, 292.

McKee, C. F. and J. P. Ostriker. 1977. A theory of the interstellar medium: three components regulated by supernova explosions in an inhomogeneous substrate. *ApJ*, 218, 148–169.

McKee, Christopher F. and Eve C. Ostriker. 2007. Theory of Star Formation, *ARA&A*, 45, 565–687.

Meyer, D. M. A. et al. 2014. Models of the circumstellar medium of evolving, massive runaway stars moving through the Galactic plane, *MNRAS*, 444, 2754–2775.

Meynet, G. et al. 1994. Grids of massive stars with high mass loss rates. V. From 12 to 120 M_{sun}_ at Z=0.001, 0.004, 0.008, 0.020 and 0.040, *A&AS*, 103, 97–105.

Meynet, Georges and André Maeder. 2017. Supernovae from Rotating Stars, *Handbook of Supernovae*. Ed. by Athem W. Alsabti and Paul Murdin, 601.

Mignone, A. and G. Bodo. 2005. An HLLC Riemann solver for relativistic flows -I. Hydrodynamics, *MNRAS*, 364, 126–136.

Mignone, A., T. Plewa, and G. Bodo. 2005. The Piecewise Parabolic Method for Multidimensional Relativistic Fluid Dynamics, *ApJS*, 160, 199–219.

Mignone, A. et al. 2007. PLUTO: A Numerical Code for Computational Astrophysics, *ApJS*, 170, 228–242.

Mignone, A. et al. 2012. The PLUTO Code for Adaptive Mesh Computations in Astrophysical Fluid Dynamics, *ApJS*, 198, 7.

Miyoshi, Takahiro and Kanya Kusano. 2005. A multi-state HLL approximate Riemann solver for ideal magnetohydrodynamics, *JCoPh*, 208, 315–344.

Moffat, A. F. J. et al. 1998. Wolf-Rayet stars and O-star runaways with HIPPARCOS. I. Kinematics, *A&A*, 331, 949–958.

Mohamed, S., J. Mackey, and N. Langer. 2012. 3D simulations of Betelgeuse's bow shock, *A&A*, 541, A1.

Neugent, Kathryn F. et al. 2018. A Runaway Yellow Supergiant Star in the Small Magellanic Cloud, *AJ*, 155, 207.

Osterbrock, Donald E. 1989. Astrophysics of gaseous nebulae and active galactic nuclei.

Paxton, Bill et al. 2011. Modules for Experiments in Stellar Astrophysics (MESA), *ApJS*, 192, 3.

Peri, C. S., P. Benaglia, and N. L. Isequilla. 2015. E-BOSS: An Extensive stellar BOw Shock Survey. II. Catalogue second release, *A&A*, 578, A45.

Peri, C. S. et al. 2012. E-BOSS: an Extensive stellar BOw Shock Survey, *A&A*, 538, A108.

Ploeckinger, Sylvia and Joop Schaye. 2020. Radiative cooling rates, ion fractions, molecule abundances, and line emissivities including self-shielding and both local and metagalactic radiation fields, *MNRAS*, 497, 4857–4883.

Poveda, A., J. Ruiz, and C. Allen. 1967. Run-away Stars as the Result of the Gravitational Collapse of Proto-stellar Clusters, *Boletín de los Observatorios de Tonantzintla y Tacubaya*, 4, 86–90.

Puls, J. et al. 1996. O-star mass-loss and wind momentum rates in the Galaxy and the Magellanic Clouds Observations and theoretical predictions. *A&A*, 305, 171.

Quirk, James J. 1994. A contribution to the great Riemann solver debate, *IJNMF*, 18, 555–574.

Rangelov, Blagoy et al. 2019. Runaway O-star Bow Shocks as Particle Accelerators? The Case of AE Aur Revisited, *ApJ*, 885, 105.

Reimers, D. 1975. Circumstellar absorption lines and mass loss from red giants. *Memoires of the Societe Royale des Sciences de Liege*, 8, 369–382.

Renzo, M. et al. 2018. Massive Runaway and Walkaway Stars A study of the kinematical imprints of the physical processes governing the evolution and explosion of their binary progenitors, *arXiv*, 66, 1–28.

Rider, W.J. 1999. An adaptive Riemann solver using a two-shock approximation11This work performed under the auspices of the US Department of Energy by Los Alamos National Laboratory under contract W-7405-ENG-36. *Computers & Fluids*, 28, 741–777.

Roberts, Thomas W. 1990. The behavior of flux difference splitting schemes near slowly moving shock waves, *JCoPh*, 90, 141–160.

Roe, P. L. 1981. Approximate Riemann Solvers, Parameter Vectors, and Difference Schemes, *JCoPh*, 43, 357–372.

Rosen, Alexander and Joel N. Bregman. 1995. Global Models of the Interstellar Medium in Disk Galaxies, *ApJ*, 440, 634.

Rosswog, Stephan. 2009. Astrophysical smooth particle hydrodynamics, *NewAR*, 53, 78–104.

Scherer, K. et al. 2015. Cosmic rays in astrospheres, *A&A*, 576, A97.
Scherer, K. et al. 2016. Shock structures of astrospheres, *A&A*, 586, A111.
Schroder, K. P. and M. Cuntz. 2005. A New Version of Reimers' Law of Mass Loss Based on a Physical Approach, *ApJL*, 630, L73–L76.
Sedlmayr, E. and C. Dominik. 1995. Dust Driven Winds, *SSRv*, 73, 211–272.
Spitzer Lyman, Jr. 1990. Theories of the hot interstellar gas. *A&AA*, 28, 71–101.
Stone, Ronald C. 1991. The Space Frequency and Origin of the Runaway O and B Stars, *AJ*, 102, 333.
Strang, Gilbert. 1968. On the Construction and Comparison of Difference Schemes, *SJNA*, 5, 506–517.
Sutherland, Ralph S. and M. A. Dopita. 1993. Cooling Functions for Low-Density Astrophysical Plasmas, *ApJS*, 88, 253.
Titarev, V. A. and E. F. Toro. 2004. Finite-volume WENO schemes for three-dimensional conservation laws, *JCoPh*, 201, 238–260.
Toonen, S., T. C. N. Boekholt, and S. Portegies Zwart. 2021. Stellar triples on the edge; Comprehensive overview of the evolution of destabilised triples leading to stellar and binary exotica, *arXiv*, arXiv:2108.04272.
Toro, E. F., M. Spruce, and W. Speares. 1994. Restoration of the contact surface in the HLL-Riemann solver, *Shock Waves*, 4, 25–34.
Tóth, Gábor and Dušan Odstrčil. 1996. Comparison of some flux corrected transport and total variation diminishing numerical schemes for hydrodynamic and magnetohydrodynamic problems, *JCoPh*, 128, 82–100.
Townsend, R. H. D. 2009. An Exact Integration Scheme for Radiative Cooling in Hydrodynamical Simulations, *ApJS*, 181, 391–397.
Ueta, T. et al. 2006. Detection of a Far-Infrared Bow Shock Nebula around R Hya: The First MIRIAD Results, *ApJL*, 648, L39–L42.
Ueta, Toshiya et al. 2008. AKARI/FIS Mapping of the ISM-Wind Bow Shock around α Orionis, *PASJ*, 60, S407.
Vaidya, B et al. 2018. User's Guide, URL: http://plutocode.ph.unito.it/documentation.html,
Vaidya, Bhargav et al. 2017. Scalable explicit implementation of anisotropic diffusion with Runge-Kutta-Legendre super-time stepping, *MNRAS*, 472, 3147–3160.
van Buren, Dave and Richard McCray. 1988. Bow Shocks and Bubbles Are Seen around Hot Stars by IRAS, *ApJL*, 329, L93.
van Buren, Dave, Alberto Noriega-Crespo, and Ruth Dgani. 1995. An IRAS/ISSA Survey of Bow Shocks Around Runaway Stars, *AJ*, 110, 2914.
van den Eijnden, J. et al. 2022. MeerKAT discovery of radio emission from the Vela X-1 bow shock, *MNRAS*, 510, 515–530.
van Loon, J. Th. 2006. On the metallicity dependence of the winds from red supergiants and Asymptotic Giant Branch stars, *Stellar Evolution at Low Metallicity: Mass Loss, Explosions, Cosmology*. Ed. by Henny J. G. L. M. Lamers et al. Vol. 353. ASPC, 211.
van Loon, J. Th. et al. 1999. Mass-loss rates and luminosity functions of dust-enshrouded AGB stars and red supergiants in the LMC, *A&A*, 351, 559–572.
van Loon, J. Th. et al. 2005. An empirical formula for the mass-loss rates of dust-enshrouded red supergiants and oxygen-rich Asymptotic Giant Branch stars, *A&A*, 438, 273–289.
van Marle, A. J., L. Decin, and Z. Meliani. 2014. Can the magnetic field in the Orion arm inhibit the growth of instabilities in the bow shock of Betelgeuse?, *A&A*, 561, A152.
van Marle, A. J. et al. 2011. Computing the Dust Distribution in the Bow Shock of a Fast-moving, Evolved Star, *ApJL*, 734, L26.

Vidotto, A. A. and A. Cleary. 2020. Stellar wind effects on the atmospheres of close-in giants: a possible reduction in escape instead of increased erosion, *MNRAS*, 494, 2417–2428.

Vink, J. S. 2006. Massive star feedback – from the first stars to the present, *Stellar Evolution at Low Metallicity: Mass Loss, Explosions, Cosmology*. Ed. by Henny J. G. L. M. Lamers et al. Vol. 353. ASPC, 113.

— 2008a. Mass loss and evolution of hot massive stars, *The Art of Modeling Stars in the 21st Century*. Ed. by L. Deng and K. L. Chan. Vol. 252, 271–281.

— 2008b. Mass loss and the evolution of massive stars, *NewAR*, 52, 419–422.

— 2011. Mass-loss Rates for Very Massive Stars Up to 300 Solar Masses, *UP2010: Have Observations Revealed a Variable Upper End of the Initial Mass Function?* Ed. by M. Treyer et al. Vol. 440. ASPC, 83.

Vink, J. S. and A. de Koter. 2002. Predictions of variable mass loss for Luminous Blue Variables, *A&A*, 393, 543–553.

Vink, J. S., A. de Koter, and H. J. G. L. M. Lamers. 1999. On the nature of the bi-stability jump in the winds of early-type supergiants, *A&A*, 350, 181–196.

— 2000a. New theoretical mass-loss rates of O and B stars, *A&A*, 362, 295–309.

— 2000b. The Bi-Stability Jump of Radiation Driven Winds, *Thermal and Ionization Aspects of Flows from Hot Stars*. Ed. by Henny Lamers and Arved Sapar. Vol. 204. ASPC, 427.

— 2001. Mass-loss predictions for O and B stars as a function of metallicity, *A&A*, 369, 574–588.

Vink, J. S. and G Gräfener. 2012. The Transition Mass-loss Rate: Calibrating the Role of Line-driven Winds in Massive Star Evolution, *ApJL*, 751, L34.

Vink, J. S. et al. 2015. Very Massive Stars in the local Universe, *HiA*, 16, 51–79.

Wareing, C. J., Albert A. Zijlstra, and T. J. O'Brien. 2007a. The interaction of planetary nebulae and their asymptotic giant branch progenitors with the interstellar medium, *MNRAS*, 382, 1233–1245.

— 2007b. Vortices in the Wakes of Asymptotic Giant Branch Stars, *ApJL*, 660, L129–L132.

Wiersma, Robert P. C., Joop Schaye, and Britton D. Smith. 2009. The effect of photoionization on the cooling rates of enriched, astrophysical plasmas, *MNRAS*, 393, 99–107.

Wilkin, Francis P. 1996. Exact Analytic Solutions for Stellar Wind Bow Shocks, *ApJL*, 459, L31.

Wolfire, M. G. et al. 1995. The Neutral Atomic Phases of the Interstellar Medium, *ApJ*, 443, 152.

Wolfire, Mark G. et al. 2003. Neutral Atomic Phases of the Interstellar Medium in the Galaxy, *ApJ*, 587, 278–311.

Woodward, Paul and Phillip Colella. 1984. The numerical simulation of two-dimensional fluid flow with strong shocks, *JCoPh*, 54, 115–173.

Yee, H. C. 1994. A Class of High-Resolution Explicit and Implicit Shock-Capturing Methods, *NASA Technical Memorandum*,

Yusof, Norhasliza et al. 2010. Life and Death of Very Massive Stars, *arXiv*, arXiv:1012.3649.

Zank, G. P. 1999. Interaction of the solar wind with the local interstellar medium: a theoretical perspective, *SSRv*, 89, 413–688.

Zhekov, S. A. and A. V. Myasnikov. 2000. Physics and Gas Dynamics of Wind-Blown Bubbles, *Ap&SS*, 274, 243–255.

Zingale, Michael. 2013. Introduction to Computational Astrophysical Hydrodynamics, 298.

Zinnecker, Hans and Harold W. Yorke. 2007. Toward Understanding Massive Star Formation, *ARA&A*, 45, 481–563.